T2R2 東京科学大学 リサーチリポジトリ
Science Tokyo Research Repository

論文 / 著書情報
Article / Book Information

題目(和文)	光無線給電システムのシステムレベル要件と太陽電池の差分吸収イメージングによるトラッキングに関する研究
Title(English)	A Study on Optical Wireless Power Transmission System and Its Photovoltaic Target Tracking Based on Differential Absorption Imaging
著者(和文)	浅葉薫
Author(English)	Kaoru Asaba
出典(和文)	学位:博士(工学), 学位授与機関:東京科学大学, 報告番号:甲第272号, 授与年月日:2025年3月26日, 学位の種別:課程博士, 審査員:宮本 智之,中村 健太郎,植之原 裕行,德田 崇,宮島 晋介,丸山 武男
Citation(English)	Degree:Doctor (Engineering), Conferring organization: Institute of Science Tokyo, Report number:甲第272号, Conferred date:2025/3/26, Degree Type:Course doctor, Examiner:,,,,,
学位種別(和文)	博士論文
Type(English)	Doctoral Thesis

Powered by T2R2 (Science Tokyo Research Repository)

A Study on Optical Wireless Power Transmission System and Its Photovoltaic Target Tracking Based on Differential Absorption Imaging

(光無線給電システムのシステムレベル要件と太陽電池の差分吸収イメージングによるトラッキングに関する研究)

22D10178 Kaoru Asaba (浅葉　薫)

Department of Electrical and Electronic Engineering

School of Engineering

Institute of Science Tokyo

DOCTORAL DISSERTATION 1 March 2025

Supervisor: Associate Professor Tomoyuki MIYAMOTO, Dr. Eng.

ABSTRACT

Among the wireless power transmission technologies, Optical Wireless Power Transmission (OWPT) has the strength of its directivity because it utilizes short-wavelength electromagnetic waves. Besides that, the opportunity impacting the future OWPT is that the recent significant technology development towards long-distance optical communication in space. In this thesis, to maximize the value of OWPT, such strength and opportunity are focused on, OWPT intended for long-range and high-power is investigated.

There are many demonstration studies in OWPT. In one study, the range between the transmitter and the receiver is fixed, and the beam shape is predetermined. In another, the transmitter is fixed, and the receiver moves under control from the transmitter. However, in the real operation of OWPT, the transmitter must align its beam dynamically depending on the position and attitude of the receiver.

To address this issue, requirements for beam alignment and shaping based on a performance model of the general OWPT system are necessary. This thesis proposes a methodology to determine system-level requirements for beam alignment and shaping for general configurations of non-cooperative and cooperative OWPT systems. In the former configuration, the receiver is fixed, and the transmitter aligns its beam with the receiver. In the latter one, the transmitter and the receiver mutually align. The derived requirements for the non-cooperative model were generally much stronger than for the cooperative system, and the longer the distance to the receiver, the stronger these requirements were. Further relaxation of the system-level requirement of a cooperative OWPT system was realized with a module utilizing the fly-eye lens surrounded by reflective walls.

In traditional OWPT research, a photovoltaic device (PV) contained in the receiver was recognized by detecting its figure, outline, and specific marker through image processing. Trials have been reported as successful in certain conditions. However, recognition is reported to become unstable, especially when outdoor background illumination varies by weather or diurnally. This study proposes differential absorption imaging to recognize PV and estimate its position and attitude under varying illuminating conditions. Generally, PVs are semiconductors such as Si or GaAs, and their light absorption changes rapidly within a narrow range including their band gap wavelengths. On the other hand, compared with PV, the background illumination of the environment surrounding the PV is expected to be sufficiently flat in the above narrow wavelength range. By utilizing this inherent feature of PV, a more robust detection is realizable than other methods using much more general features such as shapes or colors. Images are captured in two wavelengths. One is strongly absorbed by the PV , and the other is not. Then the unnecessary common background in these images is canceled in the differential image of these two, and the PV image is extracted from it. A concept-proof experiment was conducted, and the

“detectability criteria” were defined as the accuracy requirements for the X and Y center coordinates and the area size derived from the system-level requirements study. The experiment was followed by exploiting a GaAs substrate exhibiting a diffuse reflection characteristic and a real thin-film GaAs PV with a non-diffuse one. Two infrared wavelengths 850nm and 940nm were utilized in the experiments. The “threshold equation” which holds at the threshold was derived and verified by experiments. Combined with the SNR discussions, the “detectable range” was derived as the performance limit of this image sensor.

Position estimation was studied mainly by utilizing stereo imagery, which is a scalable technology widely used in small equipment to much larger systems. This method can directly generate the coordinates of the targets on the 2D plane. The results were not strongly affected by the target’s attitude angle in the GaAs substrate experiments, whereas the results were quite different in the GaAs PV case. It is noted that direction is not so affected as position estimation by the target’s attitude. A condition, the “integrity measure”, was defined to avoid inconsistencies between the center coordinates estimations by the left/right optical sensors. It was suggested experimentally that the integrity measure is closely related to the detectability. The “integrity measure” rapidly converges when the exposure time of the image sensor exceeds a certain threshold, and this minimum exposure time depends on the target’s attitude angle. When the target is non-diffuse, the reflection characteristic becomes sharp. Using this characteristic of the minimum exposure time, the target’s attitude angles for the non-diffuse target were estimated with 10 degrees error within a range of approximately 60 degrees, including its normal.

Three algorithms were evaluated to investigate tracking moving non-diffuse GaAs PV targets, and a score function based on the mean position estimation error over tracking was defined to compare the performances of the three algorithms. Among the three, the supervised one performed better.

A concept of operation for a cooperative OWPT system was proposed, and it was shown to be consistent with the results derived from the requirements study. The discussions with regard to detectability criteria and differential absorption imaging in the thesis are scale invariant way, which means their discussions are based on the functions such as SNR whose value can be scale invariant, even when the scale of systems is changed, by scaling parameters of the functions. Using this nature, some examples of OWPT system design of various scale ranges are presented. The models in the thesis depend on parameters in the simulations and experiments, and the values used in the analysis depend on the conditions and apparatus in the experiment study. Moreover, there would be an OWPT system that utilizes other PV materials. However, the methodologies in this thesis are general, and they easily derive new models and values accommodating a new experiment and its apparatus. The author hopes that the results in this thesis exhibit an advancement toward the practical implementation of the operational OWPT system.

TABLE OF CONTENTS

1. INTRODUCTION 1-1

1.1. General Background 1-1

1.1.1. Optical Wireless Power Transmission and Its Study Towards an Operational System 1-3

1.1.2. Wireless Power Transmission Technology 1-3

1.1.2.1. Near-Field Type 1-3

1.1.2.2. Far-Field Type 1-6

1.1.3. Cross SWOT Analysis and Business Case for Optical Wireless Power Transmission 1-12

1.1.4. Status of R&D on Optical Wireless Power Transmission 1-15

1.1.4.1. OWPT Start-Ups in the U.S. and Israel 1-15

1.1.4.2. OWPT International Conference 1-18

1.1.4.3. Status of OWPT R&D in Individual Areas 1-19

1.1.4.3.1. Efficiency 1-19

1.1.4.3.2. Safety 1-22

1.1.4.3.3. Availability 1-23

1.2. Objectives of the research 1-24

1.3. Structure of the thesis 1-25

References 1 1-26

2. OUTLINE OF THE RESEARCH 2-1

2.1. Outline 2-1

2.1.1. System-Level Requirement Study to Maximize Power Transmission Efficiency (Section 3) 2-1

2.1.2. Detection of PV by Differential Absorption Imaging (Section 4) 2-3

2.1.3. The Position and Attitude Estimation of the Photovoltaic Targets (Section 5) 2-6

2.1.4. Real-Time Tracking of the Photovoltaic Targets (Section 6) 2-8

2.1.5. Operational Concept of a Cooperative OWPT System (Section 7) 2-9

References 2 2-10

3. SYSTEM-LEVEL REQUIREMENTS ANALYSIS FOR BEAM ALIGNMENT AND SHAPING 3-1

3.1. Definition of OWPT System Model for Requirement Analysis 3-1

3.2. Beam Shaping and Beam Alignment Requirement in Non-Cooperative OWPT 3-4

3.2.1. Geometrical Configuration 3-4

3.2.2. Orthogonal Cylindrical Beam Expander Optics 3-5

3.2.3. Requirement for Focus Adjustment (Beam Size Control) 3-7

3.2.4. Requirement for Beam Alignment 3-10

3.3. Beam Shaping and Beam Alignment Requirement in Cooperative OWPT 3-13

3.3.1. Geometrical Configuration and Optics 3-13

3.3.2. Requirement for Focus Adjustment 3-15

3.3.3. Requirement for Beam Alignment 3-16

3.4. Summary of the requirement for Focus Adjustment and Beam Alignment 3-19

3.5. Relaxation of the System-Level Requirements using a Fly Eye Module 3-20

3.5.1. The Fly-Eye Module and Its Qualitative Characteristics 3-20

3.5.2. Geometrical, and Optical Configuration of the Analysis 3-22

3.5.3. Power Generation Ratio, Homogenization by Fly Eye Module 3-23

3.5.4. Requirement for Focus Adjustment of Transmitter Beam Expander 3-29

3.5.5. Requirement for Beam Alignment 3-30

3.5.5.1. X(Y) Direction Beam Alignment 3-30

3.5.5.2. Rotational Alignment around Beam Direction 3-31

3.5.6. Requirement for Solar Cell Tilt and Beam Energy Confinement in the Fly Eye Module 3-32

3.5.6.1. Upper Wall Mirror and lower Wall Mirror configurations 3-32

3.5.7. Beam Acceptance Angle and Beam Confinement Effect in Fly Eye Module with Uppwe/Lower Wall Mirror 3-33

3.5.8. Miniaturization of the Fly-Eye Module 3-37

Appendix 3 **3-39**

A.3.1. Ray transfer matrices of the optics used in this study 3-39

A.3.2. Beam propagation and power generation ratio calculation 3-39

A.3.3. Power generation ratio calculation including perturbations 3-40

A.3.3.1. Focus perturbation 3-40

A.3.3.2. Rotational perturbations 3-41

References 3 3-42

4. DETECTION OF PHOTOVOLTAICS BY DIFFERENTIAL ABSORPTION IMAGING 4-1

4.1. The Proof-of-Concept Experiments using $\lambda = 532$ nm and Si substrate 4-1

4.1.1. The Design of the Experiments 4-1

4.1.1.1. The Captured Raw Data in the Experiments 4-2

4.1.1.2. The Data Processing and Software Tools 4-4

4.1.2. Robustness of the Method 4-5

4.1.3. Calibration of the Experiment System 4-7

4.1.3.1.1. Estimation of the γ Parameter 4-8

4.1.3.1.2. Estimation of the intensity reduction factor 4-9

4.1.4. The Data Processing of Captured Image 4-13

4.1.5. Supplemental Information and Data 4-15

4.1.5.1. Differential Images and Binarized Images of Trimming Size 48 × 49 px, Exposure Time 10,000 μs 4-15

4.1.5.2. Determination Error of the X, Y Center Coordinates, and the Area Size of the target 4-16

4.2. Detectability Criteria 4-18

4.2.1. Definition of the Detectability 4-18

4.2.1.1. Cooperative System with the Fly Eye Module 4-19

4.2.1.2. Cooperative/Non-Cooperative System without the Fly Eye Module 4-20

4.2.2. Assessment of the Detectable Range 4-20

4.2.2.1. Improvement by Increase of the Effective Diameter of the Camera Optics 4-23

4.2.2.2. Improvement by the Beam Size (Beam Divergence) Control 4-24

4.2.3. Effect of the Background 4-26

4.3. Reflectivity Characterization of the GaAs Targets 4-27

4.3.1. Configuration of the Experiments 4-27

4.3.2. GaAs Substrate Detection by the Differential Absorption Imaging 4-28

4.3.4. GaAs PV Detection by Infrared Differential Absorption Imaging 4-37

Appendix 4 **4-44**

A.4.1. Derivation of the received power model equation 4-44

A.4.2. Estimation of Diffuse Reflectivity of Si, GaAs Substrate 4-46

A.4.2.1. Reflectivity model (RDP) of material of DP surfaces 4-47

A.4.2.1.1. Diffuse reflectivity model (Red, Rid) 4-47

A.4.2.1.2. Reflectivity model of diffused rays (Rif) 4-48

A.4.2.1.3. Calculation of reflectivity model (RDP) 4-48

A.4.2.2. The reflectivity model (RPD) of the material consists of PD surfaces 4-49

A.4.2.3. Reflectivity model ($RPDDP$) of PDDP composite surface 4-51

A.4.2.4. The ratio of diffuse reflectivity of visible experiments to infrared 4-53

A.4.3. Excerpt from Data Reduction Products (Example of Differential Image, Binarized Image of GaAs Substrate) 4-54

A.4.4. Excerpt from Data Reduction Products (Example of Differential Image, Binarized Image of GaAs Solar of Cell) 4-55

References 4 **4-56**

5. POSITION AND ATTITUDE ESTIMATION OF PHOTOVOLTAICS 5-1

5.1. The Positioning Experiments using a GaAs Substrate 5-1

5.1.1. The Experiment Configuration and the Coordinate System Definition 5-1

5.1.2. Integrity Measure 5-4

5.2. Positioning Experiments using a GaAs Substrate 5-7

5.2.1. Introducing The Coaxial Optics 5-9

5.2.2. GaAs Substrate Experiments Using the Coaxial Optics 5-13

5.3. PV Positioning Experiments 5-14

5.3.1. Positioning of the PV at a Fixed Position 5-15

5.3.2. Positioning of the PV at Position Sets 1, 2, and 3 5-17

5.4. Position Estimation by the methods other than the Stereo Imagery 5-21

5.4.1. Position Estimation by the Apparent Size of the Target 5-21

5.4.1.1. GaAs Substrate 5-22

5.4.1.2. GaAs PV 5-23

5.4.1.2.1. Positioning of the PV at a Fixed Position 5-23

5.4.1.2.2. Positioning of the PV at Position Sets 1, 2, and 3 5-25

5.4.2. Position Estimation with External Ranging Information 5-27

5.5. Attitude Estimation of the GaAs Photovoltaics Target 5-28

5.5.1. The Attitude Estimation by the Integrity Measure 5-28

5.5.2. The Physical Model of the Integrity Measure's Minimum Exposure Time and Attitude Estimation 5-29

5.5.2.1. Derivation of the Integrity Measure's Minimum Exposure Time 5-29

5.5.2.2. Reflectivity model of the PV 5-31

5.5.2.3. Relationship of the Integrity Measure with the Detectability 5-35

5.5.2.4. Error Model of the Minimum Exposure Time Method 5-36

5.5.3. Attitude Estimation by the Apparent Size of the Target 5-37

Appendix 5 **5-40**

A.5.1. Mathematical Formulation of PV Positioning 5-40

A.5.1.1. The Positioning Formula with the Stereo Imagery 5-40

A.5.1.2. Estimation of the Constant ($\Delta\theta$) of Pixel (px) to Angle Conversion 5-42

A.5.2. The Positioning Formula without the Stereo Imagery 5-43

A.5.3. Position and Direction Determination of the GaAs PV (On-Axis and Off-Axis for $\boldsymbol{\phi}$ = 45 deg, 65 deg, 105 deg, and 125 deg) 5-45

A.5.3.1. On-Axis 5-45

A.5.3.2. Off-Axis 5-47

A.5.4. Position Determination based on range estimation by the apparent size of the target combined with direction estimation. 5-53

A.5.4.1. On-Axis 5-53

A.5.4.2. Off-Axis 5-55

A.5.5. Position Determination with External Ranging Information 5-59

References 5 **5-61**

6. REAL-TIME TRACKING OF PHOTOVOLTAICS 6-1

6.1. Experiments of Real-Time Successive Positioning and Attitude Determination of PV 6-1

6.1.1. Experiments Configuration and Tuning of Camera Parameters 6-1

6.1.2. Realtime Positioning of PV 6-5

6.1.3. Successive Attitude Determination of PV 6-6

6.2. Tracking of the PV 6-8

6.2.1. Tracking Algorithms 6-8

6.2.2. Assessment of the three algorithms 6-11

6.3. Accuracy improvement of the three algorithms 6-17

6.4. Assessment of the algorithms for Position Set 2 6-19

6.5. Demonstration of the PV Tracking Using the Algorithm 6-22

6.6. Consistency between system-level requirement study 6-22

Appendix 6 6-24

References 6 6-26

7. A CONCEPT OF OPERATIONS (CONOPS) OF A COOPERATIVE OWPT SYSTEM 7-1

7.1. A Concept of the Operation of an OWOPT 7-1

7.1.1. A ConOps of the cooperative OWPT 7-1

7.1.2. Consistency between Detectability Criteria and Differential Absorption Imaging 7-3

7.2. Scalability of OWPT Systems 7-6

7.2.1. Designing OWPT Systems of Various Power Transmission Ranges 7-6

7.2.2. Scale Transformation of OWPT System Parameters 7-6

7.2.3. Maximum Detectable Range of the GaAs Substrate and the PV 7-7

7.2.4. Examples of OWPT System Design with Scale Transformation 7-8

8. CONCLUSION 8-1

ACKNOWLEDGMENTS

LIST OF PUBLICATIONS

1. Published Journal Papers

2. International Conferences

3. Domestic Conferences

4. Meetings

1. Introduction

1.1. General Background

Wireless power transmission[1] was initially conceived by Nikola Tesla for long-distance power transmission, but its widespread use has progressed from contact-type power transmission. Wireless power transfer by electromagnetic induction has been applied to electric toothbrushes, shavers, cordless phones, etc., and has been integrated into our daily lives. Especially, contactless IC cards have become an indispensable part of our everyday life. On the other hand, early experiments on long-distance wireless power transmission were unsuccessful, despite a huge experimental facility (Figure 1-1). Since then, it has not appeared until now. The reasons for this may be that the power transmission efficiency is lower than that of contact transmission, the cost of infrastructure development is high, and there are concerns about the impact on the environment, including the human body.

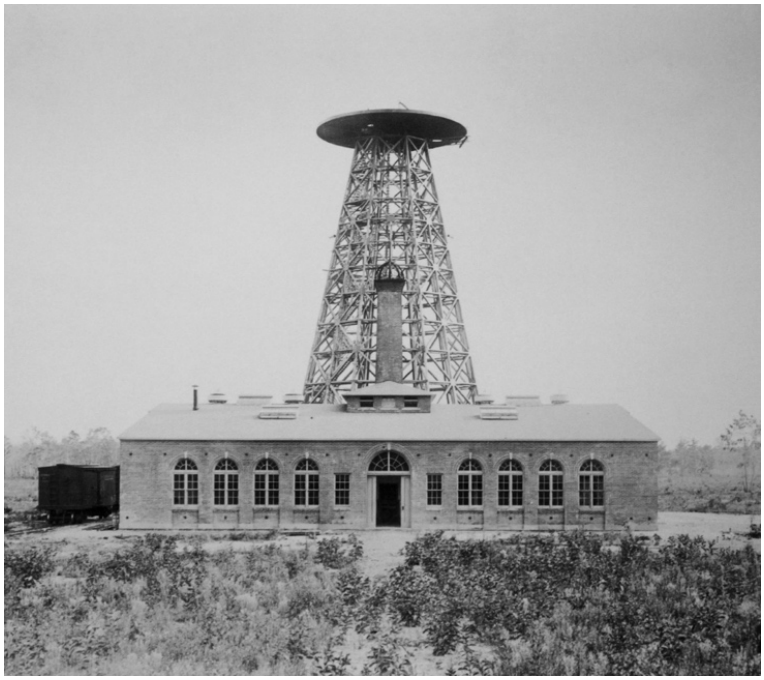


Figure 1-1 The first wireless power transfer experiment facility.[2]

In the future, the development of wireless power transfer technology will continue to move toward non-contact and further away from the contact point. In addition, research and development of higher power supply will be conducted. Examples include wireless power supply for EVs (Electric Vehicles) and AGVs (Automated Guided Vehicles), wireless power supply for remote sites where ground

infrastructure is difficult to install, and wireless power supply for temporary sites during disasters. A system that generates electricity from solar power in space and transmits it to the ground is also being investigated [3], which could also be a type of wireless power transmission.

Social development is not brought about by technology alone. It is important to have a consensus on how society will be enriched by technology, its economic rationality, and the level of risk society can accept. It is appropriate to evaluate each wireless power transfer technology in terms of Efficiency, Safety, Availability, and Cost. Efficiency means the efficiency of power transmission, Safety means no danger to (mainly) humans, and Availability means the spatial (area) ratio of wireless power transfer services is available. Availability can also be defined as the percentage of time in a year that the service is available. Cost is the cost of operational system development, operation, and risk countermeasures, but it is not considered in this thesis because it is a concept-level study.

This thesis is about optical wireless power transmission, which uses light for power transfer. In general, no single technology can cover all wireless power transfer applications. Each technology has its own positive and negative characteristics, and it is appropriate to cover various application areas with various technologies after evaluating them fairly. Based on current information, optical wireless power transmission is examined from the SWOT (Strength, Weakness, Opportunity, Threat) point of view. To conduct a SWOT analysis, optical wireless power transmission is analyzed in terms of efficiency, safety, and availability, and compared with other wireless power transmission technologies. As a result, the business cases of optical wireless power transfer will be extracted.

Based on these results, the current research and development status of optical wireless power transfer is analyzed. The issues will be addressed, and research will be conducted to solve them.

1.1.1. Optical Wireless Power Transmission and Its Study Towards an Operational System

1.1.2. Wireless Power Transmission Technology

Wireless power transfer can be broadly divided into near-field and far-field types (Figure 1-2)[4]. In this subsection, various forms of wireless power transfer technologies are briefly reviewed.

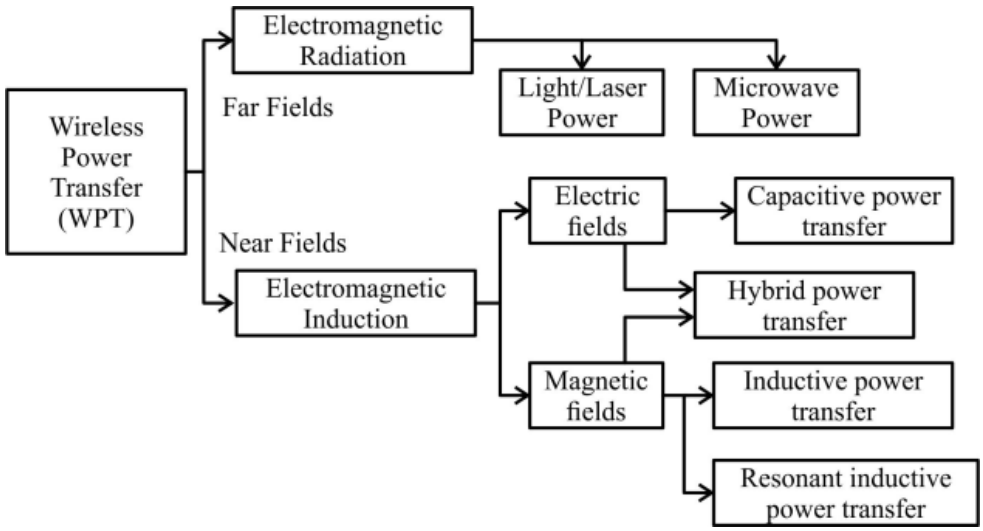


Figure 1-2 Near field and Far field Wireless Power Transfer Scheme[5]

1.1.2.1. Near-Field Type

There are capacitive and inductive WPT in the near-field type [6]. All contact-type WPTs currently in practical use are classified as inductive WPTs. The operational distance by the near-field type is approximately up to 2 m. The near-field type has already been put into practical use, and research and development for higher power transmission efficiency are in progress. Inductive WPT is being evaluated at the operational level.

Capacitive WPT transmits power by high-frequency current from the transmitter to the receiver via electrodes on the transmitter and the receiver (Figure 1-3)[7].

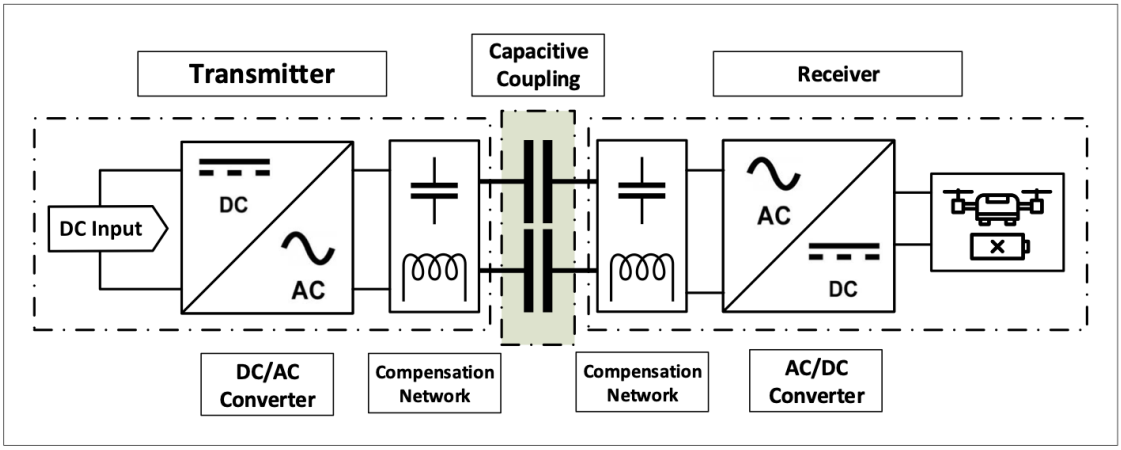


Figure 1-3 Capacitive WPT Scheme [7]

It can be used for small devices implanted in the human body as well as large devices such as EVs and drones. For example, one side of the electrode is attached to the bottom of the EV, and power is transmitted to the EV from the other electrode buried in the ground. The efficiency is as high as 80～90% [8], and power can also be supplied underwater [9]. Although the system requires a ground infrastructure with embedded electrodes, the availability will be sufficient if the system is installed together with the current gas stations and EV stands. Insulation measures and safety measures against leakage electric field are necessary. The exposure limit for leakage electric field is specified by ICNIRP (Figure 1-4) [10].

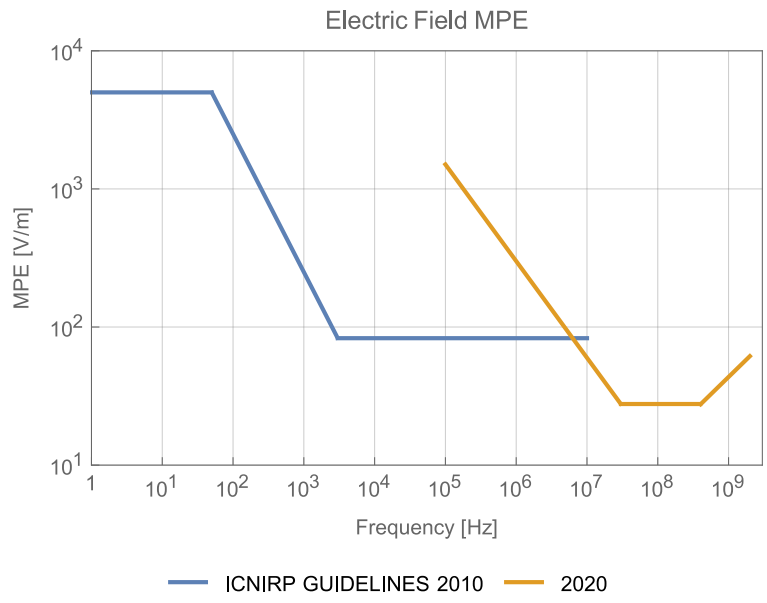


Figure 1-4 Induced Electric Field MPE from ICNIRP Guidelines 2010[10]

Although it has been confirmed that electric field leakage is below the ICNIRP recommendation for small devices implanted in the human body [11], there seem to be no confirmed results for large devices such as EVs. Research and development continue to improve transmission power and efficiency and to reduce leakage.

Inductive WPT has coils on both the transmitter and receiver sides and transmits power from the transmitter side to the receiver side by electromagnetic induction (Figure 1-5).

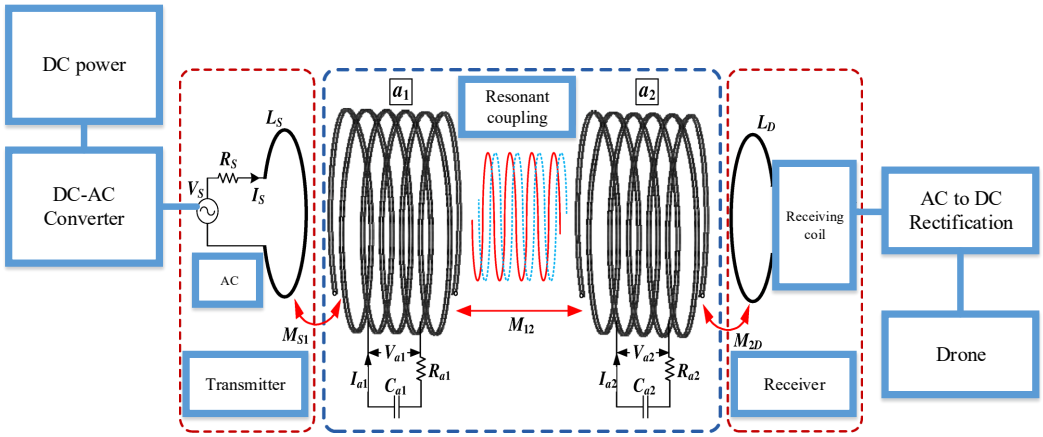


Figure 1-5 Inductive WPT Scheme[7]

The Q-value of the resonance can be enhanced by using an LC circuit instead of a simple coil on the transmitter and receiver sides, thereby improving the efficiency [12]. The efficiency is as high as 80 ～90%. As with capacitive WPT, a ground infrastructure with embedded coils is required [13]. As for safety, ICNIRP defines exposure limits for magnetic field leakage (Figure 1-6), and countermeasures against this are necessary. At a social experiment level, evaluations have been conducted using public buses, in which leakage magnetic fields have been measured. It is reported that the leakage field is within the ICNIRP standard with magnetic shielding [14]. Simulation for evaluation of the magnetic leakage field has also been conducted and was reported to be within the standard [15].

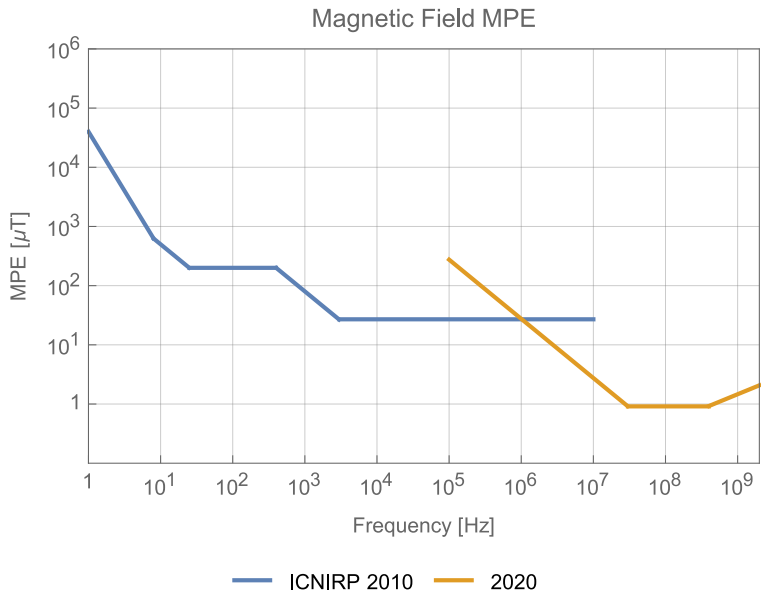


Figure 1-6 Magnetic Field MPE from ICNIRP Guidelines 2010[10]

1.1.2.2. Far-Field Type

Microwave and optical power transmission have been studied for a long time [16,17]. In principle, both methods can be used in kW～GW-class large-scale systems for wireless power transmission without the need for terrestrial infrastructure. Takeda et al. have conducted field demonstrations of optical wireless power transmission for drones and EVs using laser beam [18–20].

As for microwave power transmission, research is underway to generate solar power in geostationary orbit and transmit it to the ground (space solar power generation), and a demonstration system and an actual satellite launch experiment are being studied (Figure 1-7) [21].

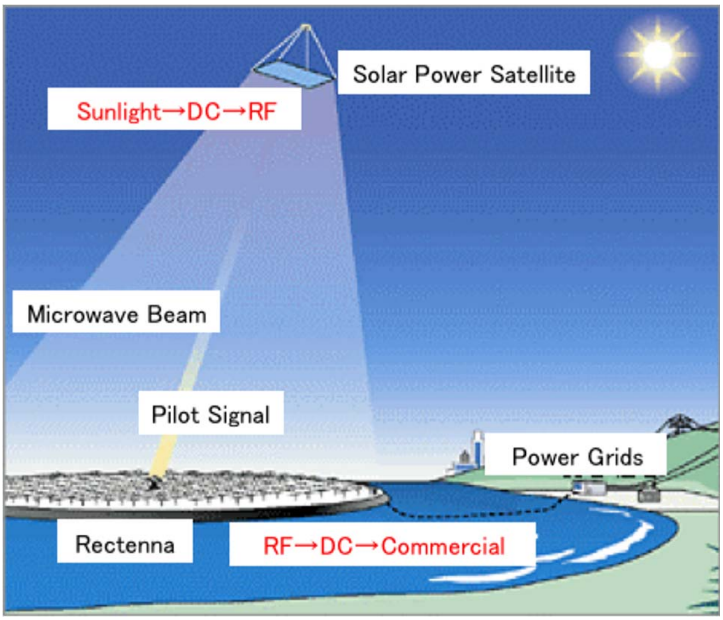


Figure 1-7 Concept of Microwave Space Solar Power System[21]

Laser systems are being studied for space solar power (Figure 1-8), and concept-level studies and demonstrations are underway for ground-based optical wireless power supply.

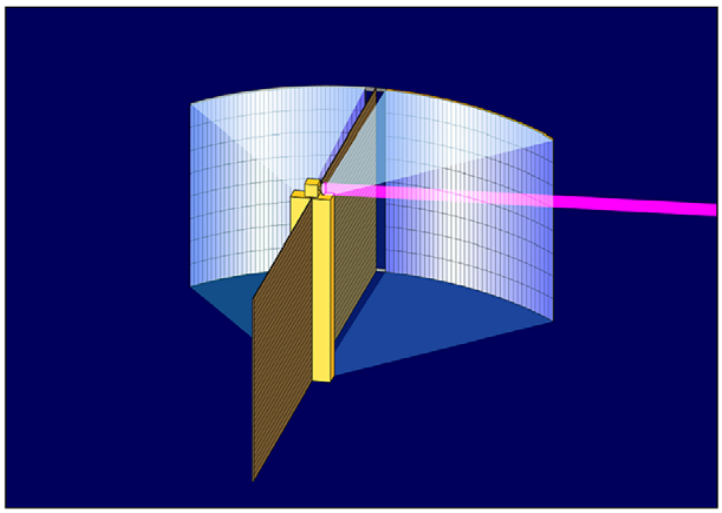


Figure 1-8 Concept of Laser Space Solar Power System[3]

Neither of the two methods has been put into practical use. Qualitative evaluation of Efficiency, Safety, and Availability will be conducted for both systems, and the characteristics of each system will

be extracted. When numerical data are required, we cite data from JAXA's research on space photovoltaics [3,21,22] as a model case.

Differences in diffraction angles due to the wavelengths of microwaves and light affects directivity. Regarding physical size of the system, the laser system has a much higher frequency than microwaves, which is advantageous for the miniaturization of the receiving system. Microwave frequencies of 2.45 and 5.8 GHz are possible, but 5.8 GHz was chosen for its technical maturity. The diffraction angles of microwaves and lasers are very different because the wavelength of microwaves is about 5 cm and the wavelength band considered for lasers is the 1 μm band, respectively, thus, the laser method can reduce the physical size of the receiver system.

In terms of power transmission efficiency, the microwave method is reported to have an efficiency of 70 % for microwave generation and over 80% for power transmission at the rectina level. Even though specific figures are not disclosed for the laser method, it will be lower than these.

Atmospheric transmission is 92 % in the rainy season when using a frequency of 5.8 GHz. Efficiency is almost independent of weather conditions. On the other hand, optical wireless power transmission cannot avoid the influence of weather; JAXA reports that the atmospheric transmittance averages 30～50% per year around Japan [23].

Availability also depends on the number (density) of transmitting devices (satellites) in space. This situation is similar for both microwave and optical wireless power transmission.

Next, we will evaluate both methods concerning safety. In the case of microwaves, the frequency used may be 2.45 or 5.8 GHz, and the exposure limit (Maximum Permissible Exposure (MPE)) is determined to be 10 W/m^2 by the ICNIRP standard (Figure 1-9) [24].

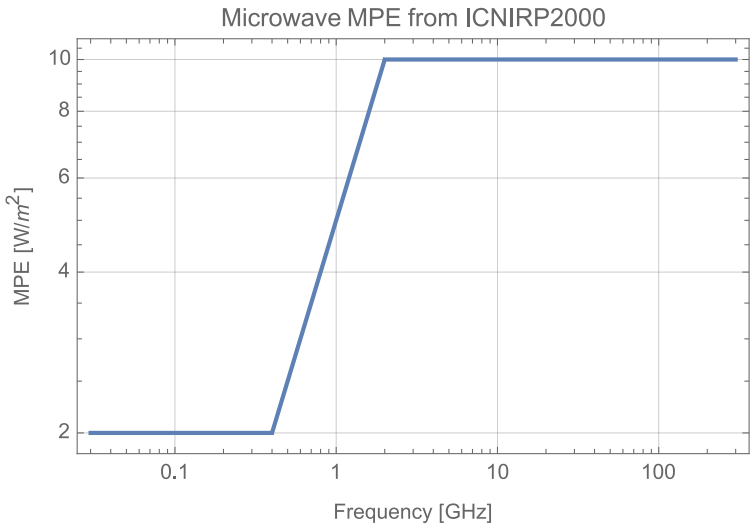


Figure 1-9 Microwave MPE from ICNIRP Guidelines 2020

On the other hand, ICNIRP has established MPE for lasers (Figure 1-10). Note that Figure 1-10 is plotted for 100 s exposure time for continuous wave (CW) laser beam.

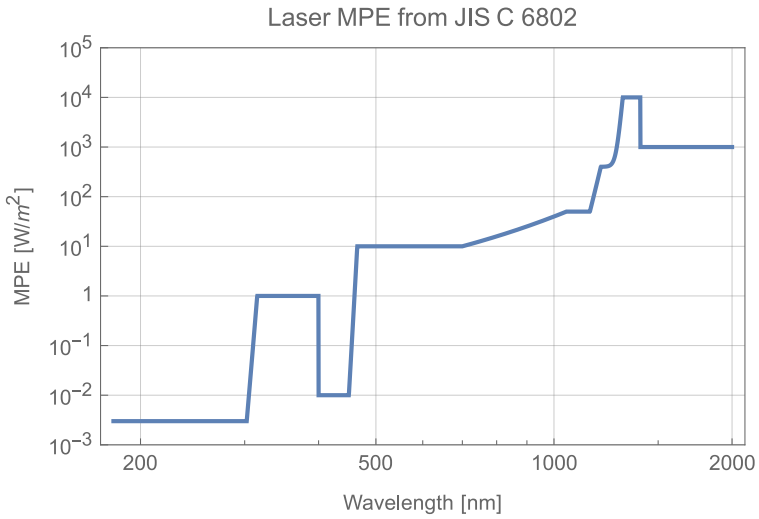


Figure 1-10 Laser MPE from ICNIRP Guidelines 2014

The ICNIRP microwave safety standard is written in W/m^2. The high-frequency limit of the standard is 300 GHz (λ =1 mm). On the other hand, the safety standard for lasers is written in W/m^2, J/m^2 and the long wavelength limit is 1 mm. At λ =1 mm, the two standards must coincide, but in practice, they are 10 W/m^2 for microwaves and 1000 W/m^2 for lasers. They are contradictory.

The MPE for microwaves is normalized to an exposure time of 30 min and an exposure area of 4 cm^2. On the other hand, for laser MPE, the standard exposure time for continuous wave (CW) is 100 s, and

the exposure area used for normalization varies depending on the wavelength. The Limiting Exposure [J] is defined tentatively here as the exposure time × the normalized exposure area × the MPE, and when compared, the high-frequency limit of microwaves and the long-wavelength limit of light are almost equal (Figure 1-11). This suggests that the damage to the human body caused by microwaves and lasers, at least in the wavelength longer than the near-infrared region where burns are believed to occur, is influenced by 'energy', 'not power density'. In fact, JIS C 6802, which cites ICNIRP, states in Table A.5, note c) for MPE to skin, "Between 0.01 m^2 and 0.1 m^2, MPE is inversely proportional to the skin area irradiated," which means that MPE × skin area is constant and is consistent with above view. On the other hand, there is no such note for the eye, which may be because MPE for the eye is defined as power or energy through a ϕ7 mm aperture.

Figure 1-11 also shows a sharp drop in Limiting Exposure to the eye at visible light frequencies. This is due to the focusing effect of light on the retina by the eye, and the specificity and vulnerability of the eye to light are clear.

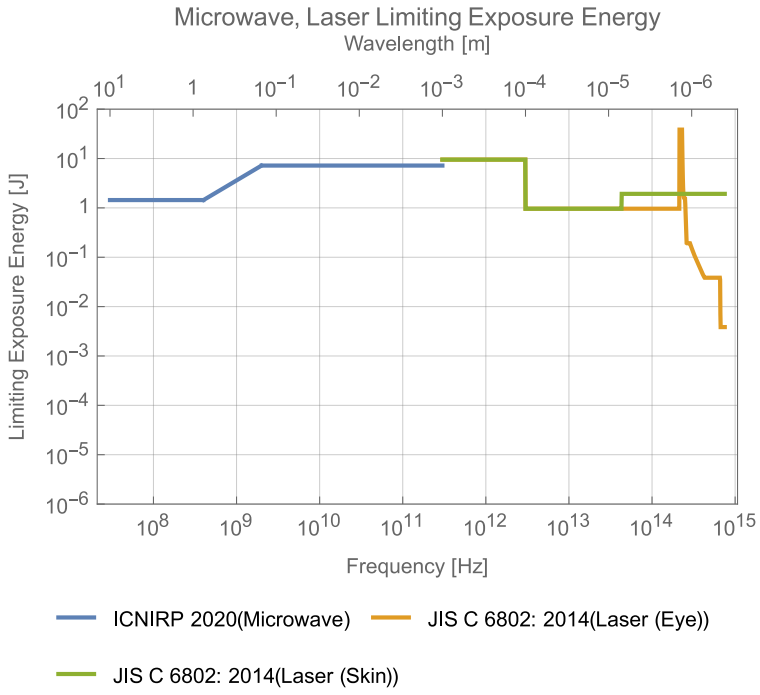
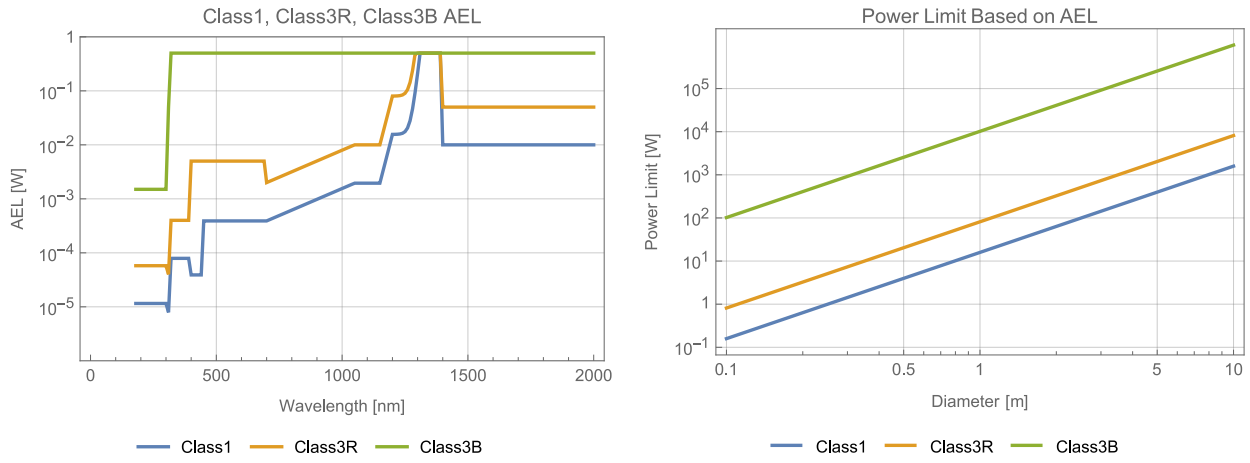


Figure 1-11 Microwave, Laser Limiting Exposure

Based on the ICNIRP exposure limits, JIS C 6802 classifies lasers into Class 1～Class 4 in terms of their safety to the eye and recommends measures to be taken [25]. The classifications are determined by the ALE (Accessible Emission Limit) defined for each class shown in Figure 1-12(a).

In the 400～1400 nm wavelength region, important for OWPT, AEL is defined by the power or energy that passes through a $\phi 7$ mm aperture. Class 3R is a level that 'may be hazardous' for direct observation in the beam, and Class 3B is a level that 'is hazardous' for direct observation in the beam. Assuming that the power output from an OWPT system is P [W] and the beam diameter is D [m], and the exposure time 100s, the power limit considering AEL [W] can be written as $P/\left(\frac{\pi}{4}D^2\right) \leq AEL/\left(\frac{\pi}{4}(7\times10^{-3})^2\right)$. The AEL and power limit P [W] are shown in Figure 1-12(b), where the wavelength is calculated at 850 nm. In OWPT, the diameter of the power beam is approximately the size of the PV, and the PV size can be roughly considered as a typical scale parameter of the target to be powered. Therefore, Figure 1-12(b) shows the relationship between the transmitting power limits and the typical target size based on laser safety. For example, if the device size is 1m and the power exceeds 10kW, it is categorized as Class 4. Then, according to JIS C 6802, consideration must be given to both scattered light and direct incident light. If 10W power is to be supplied, Class 3B measures are required if the device size is 10cm.



(a) (b)

Figure 1-12 AEL [25] and Power Limit. (a) AEL; (b) Power Limit.

In the space solar power generation study, even though the power density of JAXA's microwave system is below the MPE in the neighborhood of the ground-based rectina, it will reach 100 times of the MPE in the central area. It is necessary to keep the surrounding are, which is estimated to be 3.5 km, free of living. The laser system also needs safety assessment adapted to the beam size, but no specific studies have been conducted so far.

1.1.3. Cross SWOT Analysis and Business Case for Optical Wireless Power Transmission

In this section, we continue from the previous section by clarifying the strengths, weaknesses, opportunities, and threats of optical wireless power transmission and conducting a Cross SWOT analysis. The analysis then identifies business cases where the strengths and opportunities of optical wireless power transmission can be maximized, and application areas where the weaknesses can be minimized, and the opportunities can be exploited.

- Strength (Positive × Internal)

  The strength of optical wireless power transmission is its directivity due to the use of short-wavelength electromagnetic waves. The use of electromagnetic waves makes it possible to transmit power over distances that cannot covered by the near-field type. Also, compared to the microwave method, which is also a long-distance type of power transmission, the shorter wavelengths allow the beam with less divergence angle, contributing to a more compact system.

- Weakness (Negative × Internal)

  One of the weaknesses of optical wireless power transmission is eye-safety. From the viewpoint of efficiency, another weak point of optical wireless power transmission is that its power transmission efficiency is lower than that of near-field type and microwave systems. In addition, due to its short wavelength, its availability is more affected by atmospheric transmissivity than microwave systems.

- Opportunity (Positive × External)

  The opportunity for optical wireless power transmission is that future technological development trends will be toward long-distance, high-power wireless power transmission. Another opportunity is the advancement of space development. In fact, long-distance inter-satellite optical communications in space are being demonstrated at the system level and might be available for practical use within 10 years [26,27]. These long-distance optical communication technologies will impact significantly on a future optical wireless power transmission technology. Long-range, high-power wireless power transfer systems will be necessary for lunar and planetary exploration, and powering satellite from orbit. Long-range powering for military drones will also be an application. There would be long-range, high-power transmissions to emergency temporary

stations in disaster areas, or mobile stations for military applications. In these cases, trained personnel wearing protective goggles as safety measures can be expected.

- Threat (Negative × External)

  The threat to optical wireless power transmission is the deployment of terrestrial infrastructure for near-field type WPT. Petrol stations, and EV charging stations proliferating rapidly, can easily be used for near-field WPT stations. They can also be used as take-off/landing sites for drone flights and charging stations by near-field WPT. It will be easy to build and operate a new charging facility of near-field WPT.

The following strategies are obtained from the cross SWOT analysis based on the above SWOTs: Opportunity-Strength Strategy is a strategic area that maximizes each of the above, and Opportunity-Weakness Strategy is the area that overcomes weakness while taking advantage of opportunity. Threat-Weakness Strategy and Threat-Strength Strategy are the areas that makes the most of strategy or minimizing weakness while avoiding the risk of threats.

- Opportunity-Strength Strategy

  - Wireless Power Transmission on Lunar and Planetary Exploration
  - Solar power generation in orbit and then power transmission to the moon/planet

  These are areas where the strength of optical wireless power transfer can be maximized avoiding the ‘weaknesses’ of the system, as they require wireless power transmission in environments without terrestrial infrastructure. The presence of humans in outer space, on the moon, and on planets is exceptional, and safety concerns with high-power lasers are nonexistent or can be controlled. Atmospheric transmissivity is also not an issue except on planets with atmospheres.

- Opportunity-Weakness Strategy

  - Wireless power transmission to large drones for military applications
  - Wireless power for temporary and mobile stations for disaster, and military applications

  These are areas where ground infrastructure is expected to be inadequate, and where the opportunity of optical wireless power can be utilized while minimizing the risks associated with

weaknesses. In this case, since the operation will be conducted by trained personnel, it is expected to be easy to take safety measures such as wearing safety goggles, thus minimizing safety risks. In this situation, opportunity can be utilized.

- Threat-Weakness Strategy, Threat-Strength Strategy

  This area stresses a strategy to minimize the risk of threats in an environment where a terrestrial infrastructure exists while taking advantage of the strength of optical wireless power transmission. Small devices can mitigate the weakness regarding eye-safety because they can utilize irradiation with reasonably low power narrow beam. Also, if a small scale indoor system is concerned, the effect of atmospheric transmittance will be ignored.

The summary is shown in the next table (Figure 1-13).

			Internal	
			Strength	Weakness
			Small Divergence Angle	Eye-Safety, Efficiency, Atmospheric Transmission
External	Oportinity	R&D towards high-power and long-range	Strength is maximized, Weakness are avoided Power transmission in space environment	Opportunity is maximized, Weakness are minimized Power transmisson to where the ground infrastrucutre is inadequate
	Threat	Current gound infrastructure is easily transformed to near field WPT purpose	Threats, Weakness are minimized or avoided Strength is utilized Small systems limiting laser power within Class 1, 3R or 3B and avoid direct incidence to human eyes	

Figure 1-13 Cross SWOT Analysis of OWPT

1.1.4. Status of R&D on Optical Wireless Power Transmission

1.1.4.1. OWPT Start-Ups in the U.S. and Israel

The current status of individual projects and industries can be seen from the status of two startups, Power Light Technologies in the U.S. and Wi-Charge in Israel.

We extracted an article about their contract awards after 2022 from a Power Light Technologies press release and quoted their title and summaries [28].

i. Yahoo Life: PowerLight and Ericsson demonstrate laser beaming system to power 5G Base Station(2022.1.26)

   - PowerLight Technologies and Ericsson have shown how it can become a reality for 5G wireless service.

ii. TelecomPaper: Ericsson, PowerLight demonstrate world's first wireless powered 5G base station(2022.1.26)

- Ericsson has partnered with PowerLight Technologies to achieve a safe, fully wireless-powered 5G base station. The proof-of-concept demo milestone was achieved using optical beaming.

iii. PowerLight Technologies is First to Capture and Convert Wireless Energy from a DE Class Weapons System(2023.7.1)

- "Dual-use" weapons systems demonstration conducted as part of the U.S. Naval Research Laboratory's Safe and Continuous Power Beaming Optical (SCOPE-O) initiative.

iv. PowerLight Ships the First Long Distance Power over Fiber Prototype for Powering Telecom 5G Networks to a Major US Telecom(2023.8.1)

- A long-distance wireless power beaming solution for kilowatt class power levels over kilometers of distance was shipped the first-ever power over fiber (PoF) prototype for telecom applications to a major US telecom company.

v. PowerLight Selected to Partner on DARPA "POWER" Program to develop a Wireless Laser Energy Relay Transfer Supply System for Global Operations(302.8.22)

- While DARPA seeks to enable a near-instantaneous energy transport system for U.S. military operations with contested logistics and/or multi-domain operations, PowerLight laser power-beaming technology provides a key component.

vi. The Debrief Celebrates PowerLight Technologies Along with DARPA for Advancements in Battlefield Power Beaming(2023.9.9)

- DARPA wants to use lasers to send energy directly to war zones. This is the wireless power-beaming technology that will make it happen.

vii. “DARPA Hopes to Beam Power Across 200 Kilometers” – Great Insight about DARPA’s POWER Program(2024.1.9)

- DARPA’s aim is not to bring electricity to homes but to deliver energy to places where it would prove difficult, expensive, or dangerous to reach with grid infrastructure or fuel or battery shipments.

viii. PowerLight’s Role in Blue Origin’s LunA-10 Team Featured in GeekWire Press Release(2024.1.16)

- They joined a team headed by Jeff Bezos’ Blue Origin space venture to design a power-beaming system that might someday charge up robots on the moon.

ix. PowerLight Featured in EEPower.com Article for LunA-10(2024.2.22)(Figure 1-14)

- EEPower.com published an article regarding PowerLight’s endeavor with Blue Origin for DARPA’s LunA-10 program.

The 5G Base station for Ericsson is an optical wireless power supply for locations where power supply by terrestrial infrastructure is not feasible. Power Light's business after 2022 is an Opportunity-Strength, Opportunity-Weakness strategy focused on space, defense, and 5G base stations.

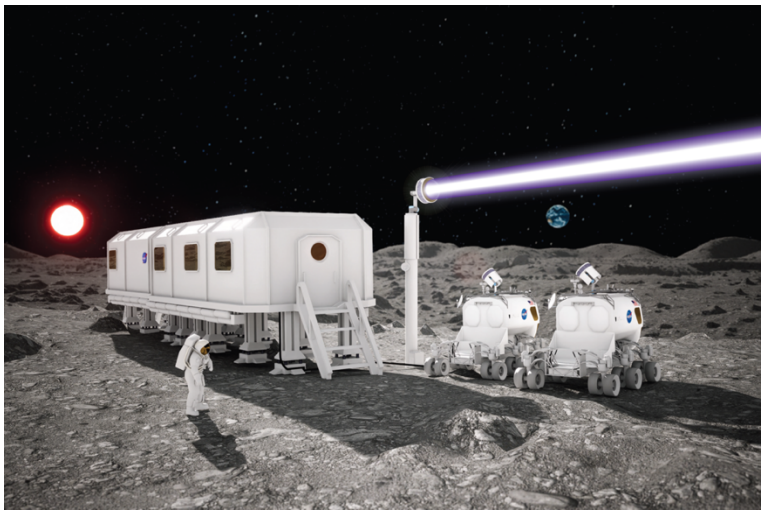


Figure 1-14 Concept of OWPT on Luna [28]

Israeli startup Wi-Charge is shipping its own OWPT system [29], the movable display in a store. As the beam diameter is unknown, the class cannot be specified. However, the output powers are 100mW

and 300mW, and assuming a 100-second CW exposure, their system might have a chance to be classified as Class 1 laser product. The product is at most Class 3B, so the scattered light is not at a dangerous level. The company has shipped six products to Israel, the U.S., Germany, and Brazil, with four mini-displays, smart locks, and small lighting devices. The products are shown on YouTube. The laser beam is emitted from the top of ceiling to the small monitor so that the reflected light does not enter the visitor's eye (Figure 1-15). This company's business is like the Threat-Weakness Strategy, Threat-Strength Strategy concept. While they mitigate the weakness to the safety of the laser beam by limiting the class within 3B, they counter the threat of the terrestrial fixed position infrastructure by allowing a free positional relationship between the terminal and the target.



Figure 1-15 Wi - Charge's OWPT to a small display[29]

1.1.4.2. OWPT International Conference

An international conference of the OWPT is held annually in Japan. The number of oral and poster presentations during 2022～2024 is shown in Figure 1-16. The trend of presentations does not change significantly from year to year. Demonstrations and reports from the industry are small, indicating that mainly university researchers are leading the current R&D. Many of the small-scale demonstrations and experiments in the classification belong to the Opportunity-Strength, Opportunity-Weakness strategy described above.

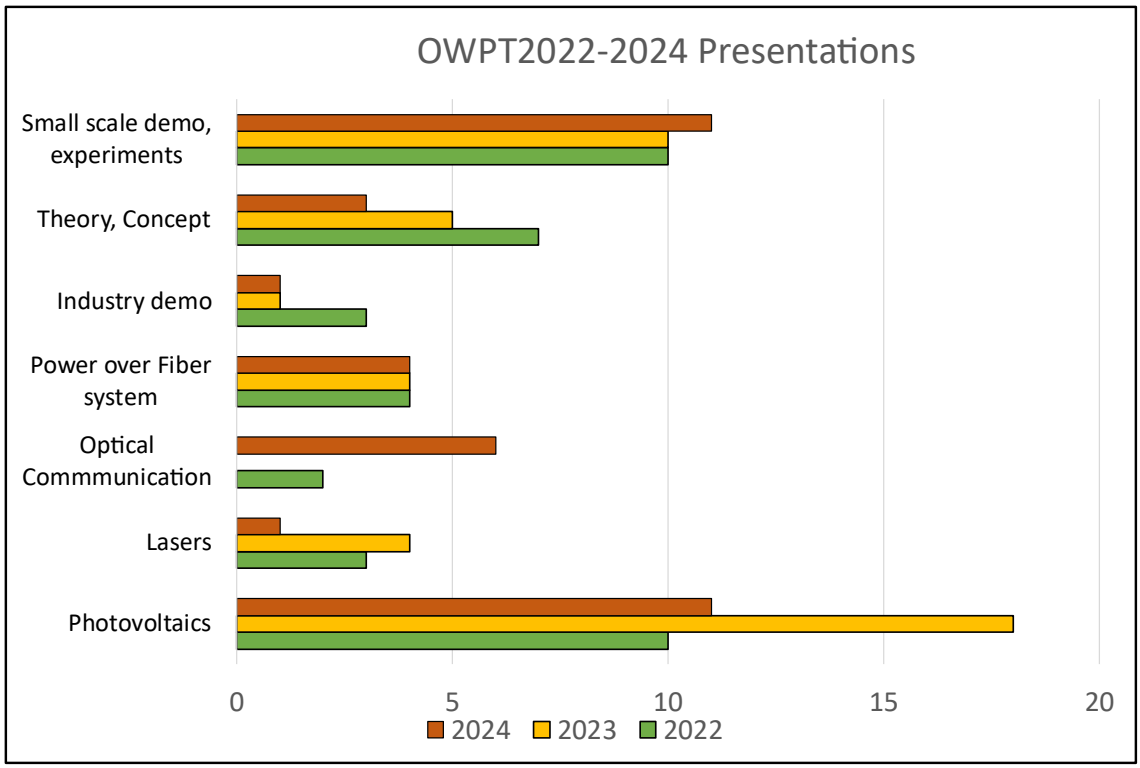


Figure 1-16 OWPT 2022-2024 Presentations

1.1.4.3. Status of OWPT R&D in Individual Areas

1.1.4.3.1. Efficiency

The efficiency of optical wireless power transfer η_{system} is written as,

$$\eta_{system} = \eta_{Light\ Source} \times \eta_{Transmission} \times \eta_{Power\ Generation} \times \eta_{Photovoltaic} \quad (1\text{-}1)$$

where $\eta_{Light\ Source}$ is the electrical-to-optical conversion efficiency of the light source, $\eta_{Transmission}$ is the transmission of the power feed path, $\eta_{Power\ Generation}$ is the ratio of the incident light power entering the PV contributing to the power transmission, and $\eta_{SolarCell}$ is the photoelectric conversion efficiency in the PV.

- $\eta_{Light\ Source}$

  Light source devices would be LEDs and lasers; LED efficiency is around 50% in the near-infrared wavelength [30]. In terms of efficiency, semiconductor lasers and fiber lasers are representative. Semiconductor lasers are of the surface-emitting type and the edge-emitting type, each of which has an efficiency of about 60-70% [31,32]. The efficiency of fiber lasers is about 25-30% [33], but there are reports of

achieving 50% [34].

- $\eta_{Photovoltaic}$

  A comprehensive review of laser-based space photovoltaics by Ren et al [35] summarizes the results of a paper survey on PV efficiency. According to the results, the efficiency of Si, GaAs, PSCs (Perovskite Solar Cells), CIGS (Cu, In, Ga, Se Solar Cells), and CZTS (Cu2ZnSnS4) were about 26.7%, 29.1～47.1%, 25.7～31.3%, 23.35%, and 10%, respectively. GaAs have excellent efficiency and radiation resistance, but it is high cost. PSC, CIGS, and CZTS are newer types of PV compared to Si and GaAs, each with higher efficiency, lower cost, and thinner films, and are expected to be widely used for PV power generation. Although each has not been tested in the space environment, CIGS is said to have an on-orbit lifetime of 30 years, while GaAs have an on-orbit lifetime of 15 years [21].

  $\eta_{Photovoltaic}$ is usually evaluated under the condition of perpendicular incidence to the PV. However, it is conceivable that $\eta_{Photovoltaic}$ depends on the angle of incidence.

- $\eta_{Transmission}$

  Consider atmospheric transmissivity with wavelength λ [μm] and visibility V [km], then a formula of atmospheric transmissivity is derived based on discussions of the scattering theory of light. Let the sum of scattering and absorption cross-section of the atmosphere for a given wavelength λ be $\sigma(\lambda)$. The change dP in flux P [W] with beam propagation dx is,

$$dP = -\sigma P n dx \tag{1-2}$$

  where n the number density of molecules involved in scattering and absorption,

  The change in flux with distance L is therefore

$$P = P_0 exp(-\sigma n L)$$

  σn is rewritten as attenuation coefficient α

$$P = P_0 exp(-\alpha L) \tag{1-3}$$

For a small $2\pi a/\lambda$ where a is a size parameter of the scatterer, σ, thus α, can be approximated as $(2\pi a/\lambda)^n$. When $2\pi a/\lambda \ll 1$, the incident beam will be Rayleigh-scattered ($n = 4$), and for $2\pi a/\lambda \sim 1$, Mie-scattered ($0 < n < 4$) . Thus, $\alpha \propto \lambda^{-n}, 0 < n \leq 4$ is assumed. The reference wavelength is set as 0.55μm, and from the definition of visibility, where the atmospheric transmissivity is 2% at the range equals the visibility,

$$\alpha = -\frac{3.91}{V}\left(\frac{0.55}{\lambda}\right)^n \tag{1-4}$$

Thus, the atmospheric transmissivity $\eta_{Transmission}$ to distance R [km] is

$$\eta_{Transmission} = exp\left\{-3.91\frac{R}{V}\left(\frac{0.55}{\lambda}\right)^n\right\} \tag{1-5}$$

n takes various functional forms depending on the measurement conditions, and several forms have been proposed by Masaki et al [36]. A widely applicable form below is often used.

$$n = 0.585V^{\frac{1}{3}} \tag{1-6}$$

For more precise calculations, simulation tools such as LOWTRAN are available and have been introduced by Miyagawa [37]. Plots of (1-5) and (1-6) are shown in Figure 1-17, showing that the effect of visibility is not so significant at distances of around 100 m.

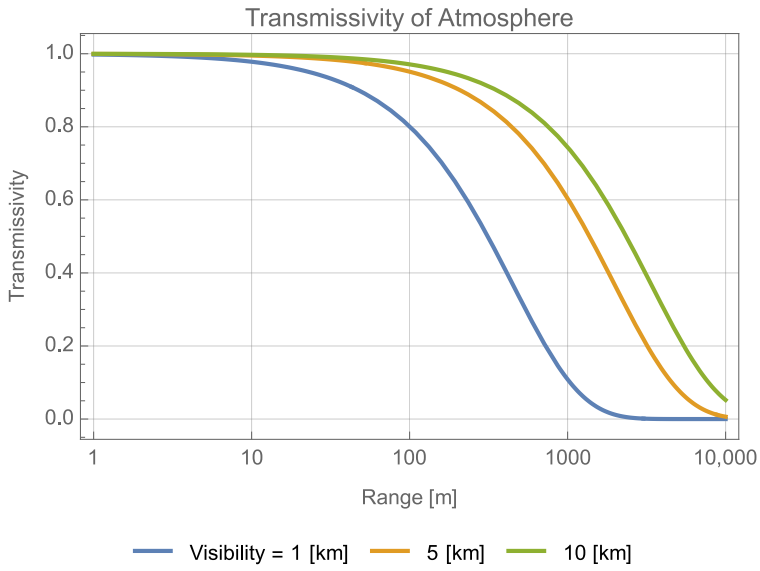


Figure 1-17 Transmissivity of Atmosphere

The atmospheric transmissivity of the entire atmospheric layer can be estimated from the solar radiation values published by the Japan Meteorological Agency in Japan. The atmospheric transmissivity around Japan has been assessed by Nakamura et al. to be 60～80% in cloud-free conditions on an annual average [12]. The assessment in the USA is cited by Degnan [39] based on data, where $\eta_{Transmission}$ is higher than in Japan. For OWPT operations in space environment, this factor is 1.

- $\eta_{Power\ Generation}$

  When we design an OWPT system, a major issue is how to shape the transmitted beam to be irradiated on the PV. Tan [40] et al. introduced $\eta_{Power\ Generation}$ in the definition of the OWPT efficiency and determined its functional form regarding the geometric matching of the incident beam shape and the shadowing effect for a given configuration of the PV. Similar work has been conducted by Wagner et al.[41]. These are examples of active beam alignment of the transmitter and receiver, while passive methods have also been proposed [29,42].

1.1.4.3.2. Safety

In the OWPT, most laser beams are classified as Class 3R, Class 3B, or Class 4, except for transmitting power to small objects. Although there is literature that assesses the safety of laser

beams using MPE [42], there is no research on safety assurance for laser beams at a level significantly higher than MPE. Studies are limited to the case of direct observation of the beam [43,44], and in particular, there looks no studies that discuss safety in the environment of Class 4 lasers, where reflection and scattering of the emitted beam are also classified as hazardous. In considering the application of optical wireless power transfer, safety is an important issue at the stage of social infrastructure development beyond the research stage. Whether to adopt a Threat-Strength / Threat-Weakness strategy by dealing with safety or to adopt an Opportunity-Strength or Weakness strategy by moving into areas where safety is not a decisive factor, seems to be a major issue.

1.1.4.3.3. Availability

There are studies regarding optical wireless power transmission to drone systems [45,46] similar to the ground and airborne power supply infrastructure for capacitive, inductive WPT. An idea to feed power to EVs from the air has been presented [47].

1.2. Objectives of the research

The following research directions were established.

- The Strength-Opportunity and Strength-Weakness strategies described in 1.1.3 are adopted
- While a high-power optical wireless power transmission is investigated, the study is intended to be scalable
- The study is to explore the research areas that are essential for the construction of OWPT systems but have not yet been deepened.

There are many studies regarding OWPT from basic performance calculation [48] to system concept [46,49,50] and from device level experiments [51,52] to demonstrations of power transmission [53] so far. In one demonstration, the range between the transmitter and receiver is fixed and the beam shape is predetermined [54]. In another one, the transmitter is fixed, and the receiver moves under control from the transmitter [19].

In the real operation of OWPT, dynamical beam alignment and shaping by the transmitter are necessary. Considering safety, controlling the beam actively from the transmitter side is preferable. Before and while the light source transmits the beam, accurate target (PV) position estimation is necessary. Also, the target's attitude angle estimation is needed for appropriate beam shaping. For a moving target, they should be conducted in real-time.

Following the above policies, the following individual sub-research themes were established.

1. System-Level Requirements for Beam Alignment and Shaping Optics

Since requirements for optics such as beam alignment and shaping are essential parameters for OWPT system design and they are quite effective for feasibility, cost, scale, etc. of the system, it is necessary to discuss such requirements in more general configurations and to clarify trade-off items. Subitem 1 of this study focuses on filling a gap between the initial concept/demonstration and an operational system. The objectives of subitem 1 are:

1. To propose a methodology based on a simple model to simulate and evaluate the system-level performance of OWPT in a general configuration.

2. To clarify the system-level requirements regarding beam alignment and shaping based on a particular parameter set such as the beam divergence angle and the size of the PV.

2. Recognition, Position and Attitude Estimation, and Tracking of Photovoltaics (PV)

In traditional OWPT research, PV was recognized by detecting its figure or outline by image processing [55–61], etc. Trials have been reported as successful in certain conditions. However, especially in the case that outdoor background illumination varies by weather or diurnally, recognition is reported to become unstable.
A study on the recognition of PV is the second subitem in this thesis. The third subitem is position and attitude estimation, and tracking and real-time attitude estimation is the fourth subitem.

3. A Concept of a Cooperative OWPT System

The last (fifth) subitem is that a concept of a cooperative OWPT system, including the beam alignment concept, is proposed based on the discussions so far. Consistency between the system-level requirement and the position estimation results is also discussed. Then, scalability of the OWPT system parameter is discussed and examples of the OWPT system parameter for various scales are presented.

1.3. Structure of the thesis

Section 2 describes the outline of this study, and Sections 3 to 7 are devoted to the individual subthemes. In Section 3, system-level requirements are discussed. Sections 4, 5, and 6 report PV detection, position estimation, and real-time attitude estimation (tracking). The consistency between a cooperative OWPT concept and the results of Section 3 and Sections 4-6 are discussed in Section 7, including a discussion of the functional block diagrams. Section 8 summarizes the outcomes. Acknowledgments and a list of published papers are included at the end of this paper.

References 1

1. Nikola Tesla. *Wikipedia* 2024.
2. Wardenclyffe Tower. *Wikipedia* 2024.
3. Mori, M.; Kagawa, H.; Saito, Y. Summary of Studies on Space Solar Power Systems of Japan Aerospace Exploration Agency (JAXA). *Acta Astronautica* **2006**, *59*, 132–138, doi:10.1016/j.actaastro.2006.02.033.
4. Frolova, E.; Dobroskok, N.; Morozov, A. Critical Review of Wireless Electromagnetic Power Transmission Methods.; Atlantis Press: Dordrecht, The Netherlands, 2022; pp. 14–20.
5. Huda, S.M.A.; Arafat, M.Y.; Moh, S. Wireless Power Transfer in Wirelessly Powered Sensor Networks: A Review of Recent Progress. *Sensors* **2022**, *22*, 2952, doi:10.3390/s22082952.
6. Chandrasekar Rao, T.S.; Geetha, K. Categories, Standards and Recent Trends in Wireless Power Transfer: A Survey. *Indian Journal of Science and Technology* **2016**, *9*, doi:10.17485/ijst/2016/v9i20/91041.
7. Nguyen, M.T.; Nguyen, C.V.; Truong, L.H.; Le, A.M.; Quyen, T.V.; Masaracchia, A.; Teague, K.A. Electromagnetic Field Based WPT Technologies for UAVs: A Comprehensive Survey. *Electronics* **2020**, *9*, 461, doi:10.3390/electronics9030461.
8. Lecluyse, C.; Minnaert, B.; Kleemann, M. A Review of the Current State of Technology of Capacitive Wireless Power Transfer. *Energies* **2021**, *14*, 5862, doi:10.3390/en14185862.
9. Tamura, M.; Naka, Y.; Murai, K.; Nakata, T. Design of a Capacitive Wireless Power Transfer System for Operation in Fresh Water. *IEEE Trans. Microwave Theory Techn.* **2018**, *66*, 5873–5884, doi:10.1109/TMTT.2018.2875960.
10. GUIDELINES FOR LIMITING EXPOSURE TO TIME-VARYING ELECTRIC AND MAGNETIC FIELDS (1 Hz TO 100 kHz). *Health Physics* **2010**, *99*, 818–836, doi:10.1097/HP.0b013e3181f06c86.
11. Al-Kalbani, A.I.; Yuce, M.R.; Redoute, J.-M. A Biosafety Comparison Between Capacitive and Inductive Coupling in Biomedical Implants. *Antennas Wirel. Propag. Lett.* **2014**, *13*, 1168–1171, doi:10.1109/LAWP.2014.2328375.
12. Soni, S.; Gupta, S. WPT Techniques Based Power Transmission: A State-of-Art Review. In Proceedings of the 2022 13th International Conference on Computing Communication and Networking Technologies (ICCCNT); October 2022; pp. 1–6.
13. Rajitha, M.; Sai, M.Y.; Uday, A.; Balakrishna, A. WIRELESS POWER TRANSFER FOR ELECTRICAL VEHICLE APPLICATIONS.

14. Brecher, A.; Arthur, D. *Review and Evaluation of Wireless Power Transfer (WPT) for Electric Transit Applications*; Federal Transit Administration;
15. Wen, F.; Huang, X. Human Exposure to Electromagnetic Fields from Parallel Wireless Power Transfer Systems. *Int J Environ Res Public Health* **2017**, *14*, 157, doi:10.3390/ijerph14020157.
16. Strassner, B.; Chang, K. Microwave Power Transmission: Historical Milestones and System Components. *Proc. IEEE* **2013**, *101*, 1379–1396, doi:10.1109/JPROC.2013.2246132.
17. Kwon, H.; Walker, G.H.; Humes, D.H. Diode Laser Satellite Systems for Beamed Power Transmission. **1990**, 34.
18. Hajimiri, A. Wireless Power Transfer at Distance. In Proceedings of the 2023 IEEE Custom Integrated Circuits Conference (CICC); April 2023; pp. 1–4.
19. Kawashima, N.; Takeda, K.; Matsuoka, H.; Fujii, Y.; Yamamoto, M. Laser Energy Transmission for a Wireless Energy Supply to Robots.; Ferrara (Italy), September 2005; p. 4.
20. Takeda K.; Kawashima N.; Yabe K. Laser Energy Transmission to a Small-Unmanned Aerial Vehicle. *SPACE TECHNOLOGY JAPAN, THE JAPAN SOCIETY FOR AERONAUTICAL AND SPACE SCIENCES* **2008**, *7*, 27–32, doi:10.2322/stj.7.27.
21. Sasaki, S.; Tanaka, K.; Maki, K. Microwave Power Transmission Technologies for Solar Power Satellites. *Proc. IEEE* **2013**, *101*, 1438–1447, doi:10.1109/JPROC.2013.2246851.
22. Hiroaki S. JAXAにおける宇宙太陽光利用システム（SSPS）開発の現状. 4.
23. Fujita, K.; Arimoto, Y.; Shimada, S.; Yoshino, J.; Kobayashi, T.; Shiratama, K.; Nagayama, H.; Saito, Y.; Suzuki, H.; Imaizumi, M.; et al. Progress in Research on Laser Transmission Systems, Atmospheric Influence on Laser Transmission, and Laser Photovoltaics in Laser Space Solar Power System. *AEROSPACE TECHNOLOGY JAPAN* **2014**, *12*, Tq_5-Tq_10, doi:10.2322/tastj.12.Tq_5.
24. *Guidelines for Limiting Exposure to Electromagnetic Fields (100 kHz to 300 GHz)*; **2020**. DOI: 10.1097/HP.0000000000001210.
25. *JISC6802:2018　レーザ製品の安全基準*;
26. Wayne, D.T.; Rahimzadeh, S.; Cote, N.; Kepler, D.; Butterfield, M.; Smith, J.; Lacy, S. Connecting the Warfighter with Lasers in Space: The Space Development Agency and the Optical Communications Terminal Standard. In Proceedings of the Free-Space Laser Communications XXXVI; Hemmati, H., Robinson, B.S., Eds.; SPIE: San Francisco, United States, March 12 2024; p. 37.
27. Kotake, H.; Saito, Y.; Araki, T.; Makino, K.; Koga, M.; Tanabe, K.; Sato, N.; Tsuji, H.; Toyoshima, M. Preliminary Design of Key Optical Components Onboard Laser

Communication Terminal of GEO Data Relay Satellite for Cislunar Optical Communication System. In Proceedings of the Free-Space Laser Communications XXXVI; Hemmati, H., Robinson, B.S., Eds.; SPIE: San Francisco, United States, March 12 2024; p. 38.
28. PowerLight Technologies Available online: https://powerlighttech.com/ (accessed on 23 May 2022).
29. The Wireless Power Company Available online: https://www.wi-charge.com (accessed on 9 May 2022).
30. Stanley Electronic Components Available online: https://www.stanley-components.com/jp/ (accessed on 3 April 2024).
31. Crump, A.T., Paul Diode Lasers: Research Gives High-Power Diode Lasers New Capabilities Available online: https://www.laserfocusworld.com/lasers-sources/article/16556280/diode-lasers-research-gives-high-power-diode-lasers-new-capabilities (accessed on 3 April 2024).
32. Xiao, Y.; Wang, J.; Liu, H.; Miao, P.; Gou, Y.; Zhang, Z.; Deng, G.; Zhou, S. Multi-Junction Cascaded Vertical-Cavity Surface-Emitting Laser with a High Power Conversion Efficiency of 74%. *Light Sci Appl* **2024**, *13*, 60, doi:10.1038/s41377-024-01403-7.
33. Hecht, J. FIBER LASERS: Fiber Lasers: The State of the Art Available online: https://www.laserfocusworld.com/test-measurement/spectroscopy/article/16549567/fiber-lasers-fiber-lasers-the-state-of-the-art (accessed on 3 April 2024).
34. Systems, I.L. Highest-Efficiency High-Power Fiber Lasers Available online: https://lasersystems.ipgphotonics.com/Technology/high-efficiency-fiber-lasers (accessed on 3 April 2024).
35. Ren, X.-N.; Ge, C.-C.; Chen, Z.-P.; Tu, Y.; Zhang, Y.-C.; Wang, L.; Liu, Z.-L.; Guan, Y.-Q. Energy Conversion Materials for Space Solar Power Station. *Chinese Physics B* **2023**.
36. Masaki, H.; Tanaka, H. Estimation of the Extinction Coefficient of Light Through Atmosphere. *Journal of the Illuminating Engineering Institute of Japan* **1963**, *47*, 6.
37. Miyagawa, M. LOWTRAN用バンドモデルを使用した大気透過率の計算. *J. Jpn. Soc. Infrared Scence & Technology* **2004**, *14*, 4.
38. Nakamura, K.; Mitani, M. 大気透過率の長期変動とその最近の傾向. *Tenki* **2018**, *65*, 4.
39. Degnan, J.J. Millimeter Accuracy Satellite Laser Ranging: A Review. In *Contributions of Space Geodesy to Geodynamics: Technology*; 1993; Vol. 25.

40. Tang, J.; Matsunaga, K.; Miyamoto, T. Numerical Analysis of Power Generation Characteristics in Beam Irradiation Control of Indoor OWPT System. *Opt Rev* **2020**, *27*, 170–176, doi:10.1007/s10043-020-00590-z.
41. Wagner, L.; Bett, A.W.; Helmers, H. On the Alignment Tolerance of Photovoltaic Laser Power Converters | Elsevier Enhanced Reader. *Optik* **2017**, *131*, 5, doi:10.1016/j.ijleo.2016.11.072.
42. Liu, Q.; Xiong, M.; Liu, M.; Jiang, Q.; Fang, W.; Bai, Y. Charging A Smartphone Over the Air: The Resonant Beam Charging Method. 10.
43. Rizzo, L.; Duncan, K.J.; Zunino, J.L.; Federici, J.F. Direct Beam Hazard Analysis of Large Beam Diameters for Laser Power Beaming. *Journal of Laser Applications* **2018**, *30*, 032017, doi:10.2351/1.5042166.
44. Bai, Y.; Liu, Q.; Chen, R.; Zhang, Q.; Wang, W. Long-Range Optical Wireless Information and Power Transfer. *IEEE Internet Things J.* **2023**, *10*, 1617–1627, doi:10.1109/JIOT.2022.3209588.
45. Abubakar, A.I.; Ahmad, I.; Omeke, K.G.; Ozturk, M.; Ozturk, C.; Abdel-Salam, A.M.; Mollel, M.S.; Abbasi, Q.H.; Hussain, S.; Imran, M.A. A Survey on Energy Optimization Techniques in UAV-Based Cellular Networks: From Conventional to Machine Learning Approaches. *arXiv:2204.07967 [cs, eess]* **2022**.
46. Zhu, K.; Yang, J.; Zhang, Y.; Nie, J.; Lim, W.Y.B.; Zhang, H.; Xiong, Z. Aerial Refueling: Scheduling Wireless Energy Charging for UAV Enabled Data Collection. *IEEE Trans. on Green Commun. Netw.* **2022**, 1–1, doi:10.1109/TGCN.2022.3164602.
47. Hassan, M.R. Theory of Dronized Laser Source for Next Generation of Optical Wireless Power Transmission. *IEEE J. Select. Topics Quantum Electron.* **2022**, *28*, 1–9, doi:10.1109/JSTQE.2022.3162170.
48. Setiawan Putra, A.W.; Tanizawa, M.; Maruyama, T. Optical Wireless Power Transmission Using Si Photovoltaic Through Air, Water, and Skin. *IEEE Photon. Technol. Lett.* **2019**, *31*, 157–160, doi:10.1109/LPT.2018.2887081.
49. Rathod, Y.; Hughes, L. Simulating the Charging of Electric Vehicles by Laser. *Procedia Computer Science* **2019**, *155*, 527–534, doi:10.1016/j.procs.2019.08.073.
50. Iyer, V.; Bayati, E.; Nandakumar, R.; Majumdar, A.; Gollakota, S. Charging a Smartphone Across a Room Using Lasers. *Proc. ACM Interact. Mob. Wearable Ubiquitous Technol.* **2018**, *1*, 143:1-143:21, doi:10.1145/3161163.
51. Nguyen, D.H.; Tumen-Ulzii, G.; Matsushima, T.; Adachi, C. Performance Analysis of a Perovskite-Based Thing-to-Thing Optical Wireless Power Transfer System. *IEEE Photonics J.* **2022**, *14*, 1–8, doi:10.1109/JPHOT.2022.3146365.

52. Zhou, J.; He, X.; Kato, T.; Yoshikawa, K.; Yamada, H. Power Generation Characteristics of Si PV Cell under Extremely High-Intensity near-Infrared Light Irradiation. *IEICE Electron. Express* **2022**, *19*, 20210476–20210476, doi:10.1587/elex.19.20210476.
53. Takeda K.; Kawashima N. 100 m Laser Energy Transportation Experiment to a Model Rover to Explore the Ice on the Moon. *JOURNAL OF THE JAPAN SOCIETY FOR AERONAUTICAL AND SPACE SCIENCES* **2003**, *51*, 393–396, doi:10.2322/jjsass.51.393.
54. Mukherjee, J.; Wulfken, W.; Hartje, H.; Steinsiek, F.; Perren, M.; Sweeney, S.J. Demonstration of Eye-Safe (1550 Nm) Terrestrial Laser Power Beaming at 30 m and Subsequent Conversion into Electrical Power Using Dedicated Photovoltaics. In Proceedings of the 2013 IEEE 39th Photovoltaic Specialists Conference (PVSC); IEEE: Tampa, FL, USA, June 2013; pp. 1074–1076.
55. Setiawan Putra, A.W.; Kato, H.; Adinanta, H.; Maruyama, T. Optical Wireless Power Transmission to Moving Object Using Galvano Mirror. In Proceedings of the Free-Space Laser Communications XXXII; Hemmati, H., Boroson, D.M., Eds.; SPIE: San Francisco, United States, March 2 2020; p. 50.
56. Setiawan Putra, A.W.; Kato, H.; Maruyama, T. Infrared LED Marker for Target Recognition in Indoor and Outdoor Applications of Optical Wireless Power Transmission System. *Jpn. J. Appl. Phys.* **2020**, *59*, SOOD06, doi:10.35848/1347-4065/ab9489.
57. Sovetkin, E.; Steland, A. Automatic Processing and Solar Cell Detection in Photovoltaic Electroluminescence Images. *ICA* **2019**, *26*, 123–137, doi:10.3233/ICA-180588.
58. Imai, H.; Watanabe, N.; Chujo, K.; Hayashi, H.; Yamauchi, A. Beam-Tracking Technology Developed for Free-Space Optical Communication and Its Application to Optical Wireless Power Transfer. In Proceedings of the 4th Optical Wireless and Fiber Power Transmission Conference (OWPT2022); Yokohama, Japan.
59. XiaoJie, M.; Tomoyuki, M. Safety System of Optical Wireless Power Transmission by Suppressing Light Beam Irradiation to Human Using Camera. **2021**, 2.
60. He, T.; Yang, S.-H.; Zhang, H.-Y.; Zhao, C.-M.; Zhang, Y.-C.; Xu, P.; Muñoz, M.Á. High-Power High-Efficiency Laser Power Transmission at 100 m Using Optimized Multi-Cell GaAs Converter. *Chinese Phys. Lett.* **2014**, *31*, 104203, doi:10.1088/0256-307X/31/10/104203.
61. Liu, Y.; Miyamoto, T. Numerical Analysis of Multi-Particle Mie Scattering Characteristics for Improvement of Solar Cell Appearance in OWPT System. **2021**, 2.

2. Outline of the research

2.1. Outline

This section describes the outline of the thesis, each subsection corresponds to subitems described in Section 1.3. The detail of each subsection is presented in the subsequent sections.

2.1.1. System-Level Requirement Study to Maximize Power Transmission Efficiency (Section 3)

Generally, in the OWPT system, the “cooperative” system configuration and the “non-cooperative” one can be classified and defined as follows. In a non-cooperative OWPT configuration, the PV is fixed on the ground, etc., and the power transmitter aligns its beam with the face of the PV. In a cooperative OWPT configuration, the PV and the power transmitter mutually align. Even though the cooperative configuration is more complex than non-cooperative one in system design, its advantages are clarified in this study.

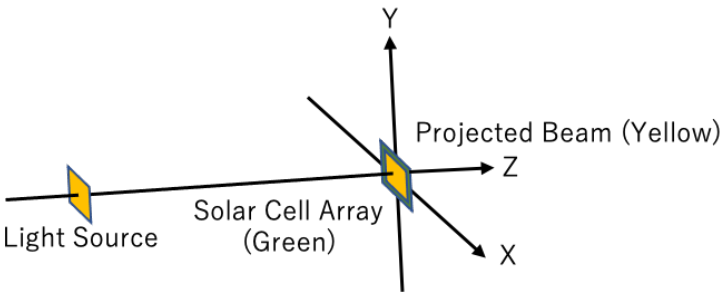


Figure 2-1 Cooperative OWPT configuration.

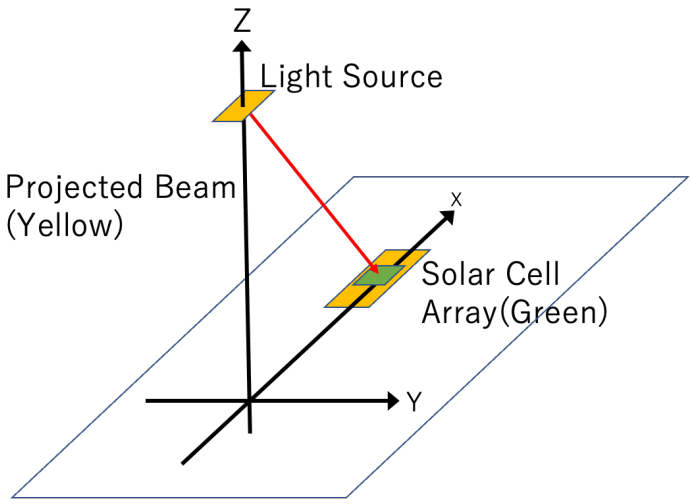


Figure 2-2 Non-Cooperative OWPT configuration.

Studies of beam alignment and shaping based on a mathematical efficiency model of OWPT have not been mature. Theoretical analysis, trade-off based on a mathematical model, and consolidation of system level requirement and design are essential to fill a gap between the initial concept/demonstration and the operational system. An OWPT system-level requirements are analyzed for beam shaping and alignment by a simple geometry and an optics model. A general result is that misalignment and beam shape tolerance become quite demanding for both configurations, and there will be cases that some relaxation is necessary to build operational systems. Relaxation of system requirements for cooperative OWPT with the fly-eye module is investigated.

A fly-eye lens has been utilized to generate uniform irradiance [3]. Since this feature is favorable to OWPT, its adaptation to transmitter optics and receiver optics has been proposed, and preliminary experiment results and its usefulness were reported [4]. There is a critical angle for a fly-eye lens. For a beam with an incident angle larger than this, the fly-eye lens projects the image of the incident beam, not to the array but to the adjacent area. To avoid this problem, introducing reflective walls around the space between the fly-eye lens and the PV array was proposed, and preliminary experiments were reported [5,6]. While the fly-eye lens has been discussed regarding its beam homogenization effect, this study analyzes it mainly from a beam alignment and shaping point of view. It is shown that a module utilizing the fly-eye lens (hereafter the fly-eye module) relaxes misalignment and beam shaping requirements. Trade-offs among two kinds of reflective wall structures and wall-less structures are discussed, and their advantages and disadvantages are clarified.

2.1.2. Detection of PV by Differential Absorption Imaging (Section 4)

Once the beam alignment and shaping requirements were derived for non-cooperative and cooperative configurations, the next step is detecting the PV within the accuracy satisfying the requirements. In the following three subsections, detection of a stationary PV at a fixed position, then, position, and attitude estimation of a stationary PV, and tracking of a moving PV are discussed. Each subsection corresponds to Sections 4, 5, and 6.

Even though it is an important technical challenge in OWPT to recognize PV stably and estimate its position and attitude under varying illuminating conditions, there are a small number of studies so far. However, in OWPTs, special attention must be paid from a safety

point of view. It must be avoided that an object that is not a solar cell is misidentified as a solar cell and transmit a power beam. For this purpose, it is desirable to adopt a recognition method that uses the essential features of solar cells (which must be fulfilled by solar cells and are very unlikely to be fulfilled by non-solar cell objects) rather than the conventional recognition method using general features. The recognition method using differential absorption proposed in this paper has this feature and is superior to other methods in terms of safety with an extremely low possibility of misrecognition.

This study proposes a method to address these challenges by introducing differential absorption imaging. The differential technique is widely used for contrast enhancement in signal and image processing. When the target shows different optical properties for two wavelengths, such a differential technique applied to the image is useful to enhance detection performance [7–9].

Many PVs are semiconductors, such as Si or GaAs, and their light absorption changes rapidly within a narrow wavelength range including their band gaps. On the other hand, compared with PV, the background illumination of the environment surrounding the PV is expected to be sufficiently flat in the above narrow wavelength range. By utilizing this essential feature of PV, a more robust detection would be realizable than other methods using much more general features such as shapes or colors. Images are captured in both wavelengths which are strongly absorbed by the PV (λ_{ON}) , and the one which is not (λ_{OFF}). Then the unnecessary common background in these images is canceled in the differential image of these two, and the PV image is extracted from it.

In Figure 2-3, (a) represents illumination and reflection of the background, and (d) shows the reflection from the front surface of PV. (b) is λ_{ON} light entering the PV and is absorbed in it. (c) shows λ_{OFF} light entering the PV and reflected by its rear surface. In the Figure 2-3 system, the λ_{ON} and λ_{OFF} images are captured by the camera, and a differential image is generated from the two.

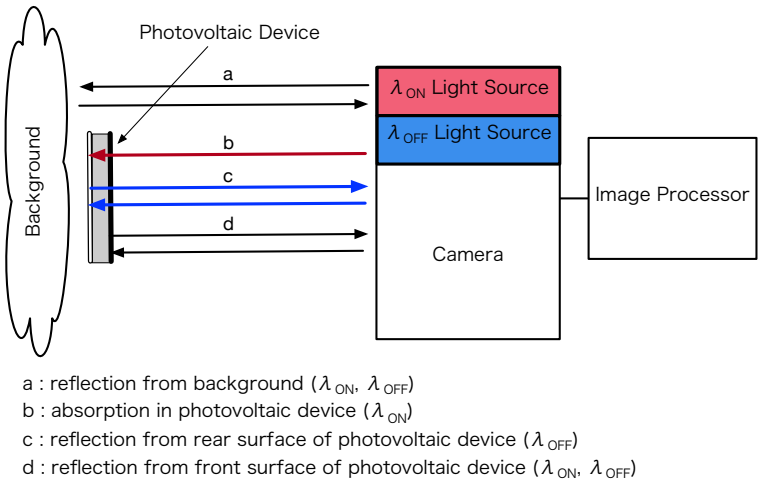


Figure 2-3 Principle of differential absorption image sensor.

The concept of generating a differential image is shown in Figure 2-4. In the figure, the center circle in the λ_{ON} and λ_{OFF} images represent the PV image, and the area between the circle and the surrounding rectangle is the background image. Since the λ_{ON} and λ_{OFF} are assumed to be close enough, the background images are similar for the two images on the right-hand side. The reflection from the rear surfaces of the PV is low for the λ_{ON} (black in the λ_{ON} image) and sufficiently high for the λ_{OFF} (blue in the λ_{OFF} image). The differential image generated from the λ_{ON} and λ_{OFF} images is the left-hand side image, and it shows that the PV image is captured without any disturbance from the background.

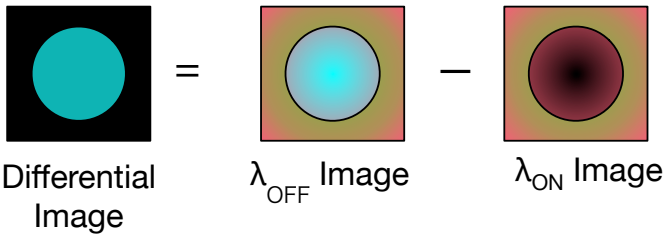


Figure 2-4 Generation of differential absorption image.

A proof-of-concept study utilized λ = 532 nm and an etched Si substrate as a diffuse target. Accuracy requirements for the X and Y center coordinate and the area size of the PV targets are derived from the system-level requirements. Then, the “detectability criteria” is defined as simultaneously fulfilling these three requirements. Similarly, “detectable range” is defined as the maximum range of the target satisfying the criteria and is determined basically by SNR.

When the range to the target in an OWPT system is scaled, SNR can be kept constant by scaling the other parameters appropriately. Throughout this thesis, such property as SNR is referred to as 'scale-invariant'. Detectability is determined in a scale-invariant way.

In differential absorption imaging, received λ_{OFF} power estimation from the rear surface of the target PV is important to estimate its center coordinates and the area size. The equation is derived to calculate the reflection from a diffuse target. Combining this with the threshold of the differential absorption imaging, the "threshold equation" is derived. Then, the equation is generalized to include a physical model of the non-diffuse reflection from the real PV. The generalized threshold equation is applied to estimate the attitude angle of the non-diffuse PV target. This is studied in the following section.

The SNR is calculated using the threshold equation. Then, the detectable range is estimated. Simulation shows that the detectable range can be largely enhanced by enlarging the receiver diameter, and beam size adjustment to the target.

Following the proof-of-concept study, the detection a GaAs substrate and a real GaAs PV and determination of their position, and area were investigated utilizing two infrared wavelengths 850 nm (λ_{ON}), and 940 nm (λ_{OFF}). Two options would be expected for the rear surface reflection characteristic of the target. One is diffuse, and the other is non-diffuse (specular). A GaAs substrate showed a diffuse reflection characteristic, like the reflection from the PV combined with the fly-eye module. On the other hand, a GaAs PV, whose rear surface is a copper electrode, showed a non-diffuse reflection.

Assume that the λ_{ON} image is brighter than that of λ_{OFF}. This is naturally realized in the infrared experiments due to the wavelength dependence of the camera's sensitivity. Assuming such a condition, the grayscale level of each pixel in the differential image is calculated by subtracting λ_{ON} image from λ_{OFF}, referred to as "over-subtraction". While this does not affect the target region where the brightness of λ_{ON} image is negligible, it eliminates unnecessary background where λ_{ON} image is expected to be brighter than λ_{OFF}. This technique reduces noise with longer exposure time even for a full-size image (640 × 480 px).

Like the visible experiments, the simulation predicts the detectable range for diffuse and non-diffuse targets. Especially, utilizing the strong directional reflection from the real PV, a much

longer detectable range than the diffuse target is achievable, whose range performance is limited only by the camera's resolution.

2.1.3. The Position and Attitude Estimation of the Photovoltaic Targets (Section 5)

A position estimation method is proposed to accommodate the detectability criteria in a scale-invariant (non-dimensional) way. Experiments are discussed in Sections 5 and 6 using scale-invariant parameters such as pixel coordinates, SNR (equivalent to Exp: exposure time), and other inherent lengths to make the discussion in such a way except discussion in the real 2D experiment space in which the scale is fixed at a certain value.

Position, and direction (azimuth angle) estimation of the PV target is studied on a real two-dimensional (2D) plane using differential absorption imaging. A GaAs substrate is used as a diffuse target and a GaAs thin-film PV as a non-diffuse one. The accuracy of the position and direction are studied from the viewpoint of reflection characteristics and the attitude angle of the target. Two methods are used for positioning. One is stereo imagery, and the other is a combination of direction and range estimation by the apparent size of the target.

Stereo imagery is a scalable technology widely used in small equipment to larger systems such as geographic information systems and satellite remote sensing systems [16–18]. This method can directly generate the coordinates of the targets on the 2D plane. On the other hand, ranging information can be obtained by measuring the apparent size of a target, assuming its size is known in advance. In this method, to determine its 2D coordinates, the direction of the target should be obtained from the differential image.

Images of the left/right sensors are generated by the camera assembly shown in Figure 2-5. It is composed of two cameras each of which corresponds to λ_{ON} and λ_{OFF}, respectively, and each camera has two (left and right) image sensors.

Since the rear surface of the PV used in the experiments is a copper electrode and its reflection characteristics were mainly specular accompanied by a small diffuse component, the differential absorption image generated in the experiments is incomplete and varies largely by the target's attitude angle (Figure 2-6).

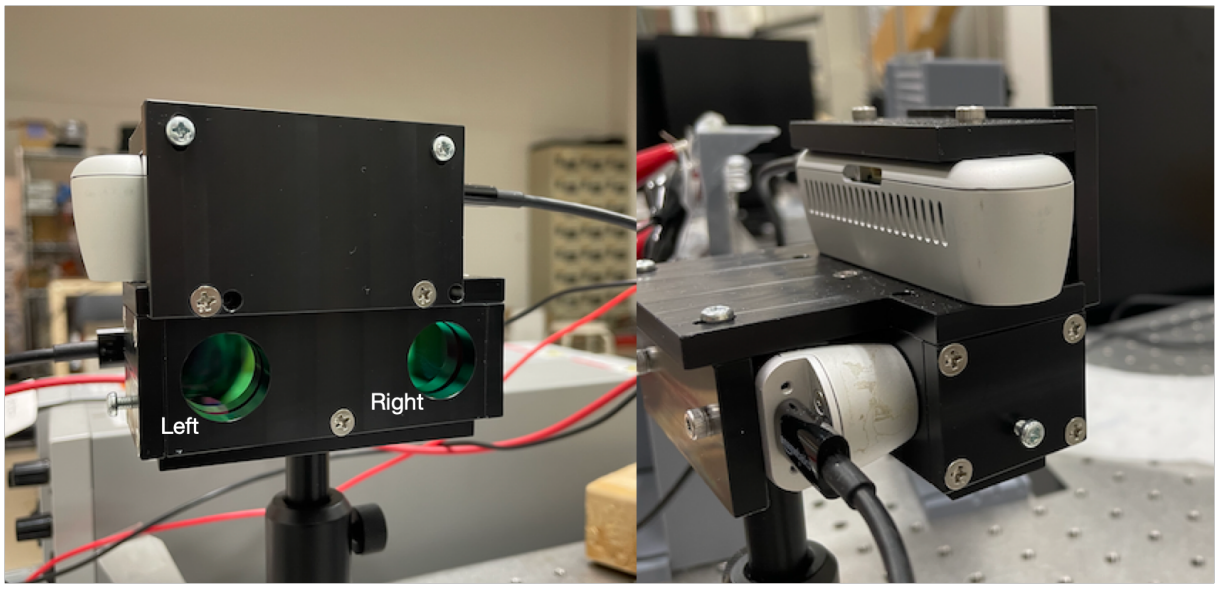


Figure 2-5 Camera Assembly

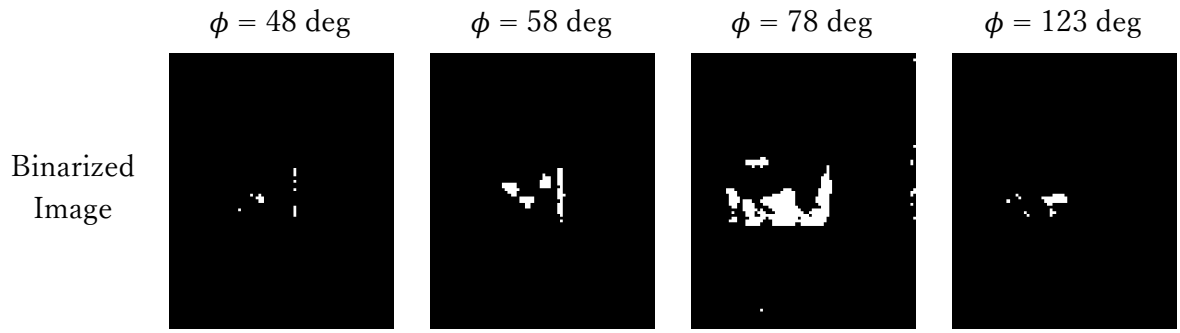


Figure 2-6 Differential binarized images of the PV.

In stereo imagery, the position and direction of the target are estimated as follows. First, target images are generated by differential absorption imaging for the left and right image sensors. Then, the center coordinates of the PV are estimated for the left and right images in the pixel coordinate system. Finally, the X and Y coordinates of the target's position are determined in real 2D space by stereo imagery. In the method using the apparent size of the target, the X and Y coordinates are calculated similarly.

In the case of estimation by stereo imagery, a condition referred to as the "integrity measure" can be defined to avoid inconsistencies between images captured by the two sensors. While a complete (entire target) image can be captured from a diffuse target, a non-diffuse target image is incomplete and varies with its attitude as shown in Figure 2-6. Even though the complete

image is necessary for the accurate positioning in stereo imagery for differential absorption imaging, the integrity measure can be used as the condition instead. By applying this condition used for screening of the data, the position of the PV is available with incomplete information of the target. The integrity measure behavior depends on the exposure time of the camera. While it fluctuates randomly when the exposure time is short, it converges rapidly above a certain threshold exposure time. Therefore, a minimum exposure time exists associated with the convergence of the integrity measure.

This minimum exposure time depends on the target's attitude angle. The generalized threshold equation is derived by combining with a physical reflectance model of the non-diffuse PV target instead of the diffuse one. Using this equation, the minimum exposure time can be determined for the attitude angle of the target. Thus, the target's attitude angle can be determined by this equation. The attitude angle estimation based on this model has a feature that the method shows no degradation in accuracy near the normal. On the other hand, the traditional method of estimating the target's attitude is measuring the change in the apparent size of the target with its attitude angle. Even though its accuracy deteriorates in the dead zone around its normal, the accuracy recovers apart from the zone. While the integrity measure method is suitable for the non-diffuse target, the traditional method is for the diffuse target. These two methods are complementary to each other.

2.1.4. Real-Time Tracking of the Photovoltaic Targets (Section 6)

Real-time position and attitude estimation for a moving non-diffuse PV target are much more challenging than for a diffuse target. For a target with non-diffuse reflection characteristics, the position estimation error increases when the target attitude deviates from the normal to the light source. This leads to outliers and data loss, particularly problematic in real-time consecutive position estimation. Thus, every (non-diffuse) PV tracking algorithm should include smoothing processes that appropriately handle outliers, interpolation processes that complement missing data, and position estimation and correction processes for the target (if necessary). In this thesis, the following three methods for the tracking algorithm are compared and their performance is evaluated.

1. An autoregressive (AR) model to correct the target position estimation when changes exceed the predetermined thresholds.

2. A uniform motion model estimated by a Kalman filter.

3. The AR model combined with a Kalman filter.

An accuracy improvement is proposed for the estimation employing the direction (azimuth) angle estimation results which can be estimated with precision.

There are requirements to be addressed for the camera to be used in real-time attitude estimation. These requirements must be considered when selecting or developing the appropriate hardware for the operational system.

2.1.5. Operational Concept of a Cooperative OWPT System (Section 7)

Unlike traditional solar power generation, OWPT requires the detection of the PV from the transmitter, tracking it if necessary, and then irradiating the power beam. Following the consolidation of requirements, a cooperative OWPT system and the beam alignment concept are proposed based on the discussions in the thesis. Finally, to summarize the whole discussion of this thesis, consistency between the system-level requirement study and the infrared differential absorption imaging regarding the tracking errors for a moving target and the detection range limit of the target is discussed. The consistency is scale-invariant. Utilizing this property and scalability OWPT system parameters, some examples of the OWPT system designs are presented for various scales.

References 2

1. Imai, H.; Watanabe, N.; Chujo, K.; Hayashi, H.; Yamauchi, A. Beam-Tracking Technology Developed for Free-Space Optical Communication and Its Application to Optical Wireless Power Transfer. In Proceedings of the 4th Optical Wireless and Fiber Power Transmission Conference (OWPT2022); Yokohama, Japan.
2. Tang, J.; Matsunaga, K.; Miyamoto, T. Numerical Analysis of Power Generation Characteristics in Beam Irradiation Control of Indoor OWPT System. *Opt Rev* **2020**, *27*, 170–176, doi:10.1007/s10043-020-00590-z.
3. Kakeya, H.; Sawada, S.; Ueda, Y.; Kurokawa, T. Integral Volumetric Imaging with Dual Layer Fly-Eye Lenses. *Opt. Express* **2012**, *20*, 1963, doi:10.1364/OE.20.001963.
4. Mori, N. Design of Projection System for Optical Wireless Power Transmission Using Multiple Laser Light Sources, Fly-Eye Lenses, and Zoom Lens. *OWPT2019* **2019**, OWPT-4-02.
5. Katsuta, Y.; Miyamoto, T. Design, Simulation and Characterization of Fly-Eye Lens System for Optical Wireless Power Transmission. *Jpn. J. Appl. Phys.* **2019**, *58*, SJJE02, doi:10.7567/1347-4065/ab238b.
6. Tai, Y.; Miyamoto, T. Experimental Characterization of High Tolerance to Beam Irradiation Conditions of Light Beam Power Receiving Module for Optical Wireless Power Transmission Equipped with a Fly-Eye Lens System. *Energies* **2022**, *15*, 7388, doi:10.3390/en15197388.
7. Differential Absorption Lidar | Elsevier Enhanced Reader Available online: https://reader.elsevier.com/reader/sd/pii/B9780123822253002048?token=ACBBE2F8761774F5628FC13C0F6B8E339140949E50BF9DE9F5063F95873CC081FB2353E862E10CA4576416252562C600&originRegion=us-east-1&originCreation=20220824035349 (accessed on 24 August 2022).
8. Dual-Wavelength Measurements Compensate for Optical Interference | May 7, 2004 Available online: https://www.biotek.com/resources/technical-notes/dual-wavelength-measurements-compensate-for-optical-interference/ (accessed on 24 August 2022).
9. Herrlin, K.; Tillman, C.; Grätz, M.; Olsson, C.; Pettersson, H.; Svahn, G.; Wahlström, C.G.; Svanberg, S. Contrast-Enhanced Radiography by Differential Absorption, Using a Laser-Produced x-Ray Source. *Invest Radiol* **1997**, *32*, 306–310, doi:10.1097/00004424-199705000-00009.
10. Lagendijk, R.; Franich, R.E.; Hendriks, E. Stereoscopic Image Processing. In *Video, Speech, and Audio Signal Processing and Associated Standards*; Electrical

Engineering Handbook; CRC Press, 2009; Vol. 20096073, pp. 1–11 ISBN 978-1-4200-4608-3.
11. Lu, Y.; Kubik, K. STEREO IMAGE MATCHING USING ROBUST ESTIMATION AND IMAGE ANALYSIS TECHNIQUES FOR DEM GENERATION. *Part B*.
12. IKONOS Stereo Satellite Imagery, Satellite Images | Satellite Imaging Corp Available online: https://www.satimagingcorp.com/satellite-sensors/ikonos/ikonos-stereo-satellite-images/ (accessed on 15 May 2023).
13. Xu, W.; Wang, X.; Li, W.; Li, S.; Lu, C. Research on Test and Evaluation Method of Laser Wireless Power Transmission System. *EURASIP Journal on Advances in Signal Processing* **2022**, *2022*, 1–18.

3. System-Level Requirements Analysis for Beam Alignment and Shaping

3.1. Definition of OWPT System Model for Requirement Analysis

Since power transmission is the essential function of OWPT, its efficiency is quite an important characteristic of every OWPT system. While the efficiency of OWPT (η_{system}) is a product of some factors, there is a factor evaluating system-level performance including optics such as beam alignment and shaping. Such a factor can be defined using "the power generation ratio" concept, which Tang, et al studied [1]. The new factor power generation ratio ($\eta_{Power\ Generation}$), coming into η_{system}, accounts for light beam power contributing to power generation in the PV, which is a portion of transferred power by the incident beam. According to their study, $\eta_{Power\ Generation}$ is expressed as the product of two factors ($\eta_A \times \eta_B$). η_A accounts for a portion of the light beam irradiating the PV. It is defined by the ratio of the irradiated area S_{irr} in the PV to the incident beam area S_{prj} onto the PV for a uniform beam as (3-1).

$$\eta_A = \frac{S_{irr}}{S_{prj}} \tag{3-1}$$

For non-uniform beams, the effect of non-uniformity should be additionally included as a correction. η_B accounts for the output characteristics of the PV. The example is a series-connected solar array module without any bypass diodes discussed by Tang, et al. They investigated empirically using a solar cell module of 10× 10 cm size. There are two columns of solar cell arrays on the module, and each column is composed of 6 series connected solar cell arrays. The two columns are connected to form a 12-series connected array. Any non-irradiated (shadowed) cell does not generate any power and such behavior results in a complex output characteristic of the solar cell array. In a more general case, η_B is extended to a correction factor that accounts for the general shadowing condition of the solar cell array module, and η_B will depend on the detailed internal configuration of the array such as the number, shape, and orientation of each solar cell element and additional components like bypass diodes. Thus, the power generation ratio describes the non-linear output nature of the shadowed array for the irradiated beam. It becomes 100% when there is no shadowing on the PV. The electrical output

power of the solar cell array can be obtained by multiplying this power generation ratio by the photoelectric conversion efficiency and the light source beam intensity at the PV.

Since the objective of this section is to derive requirements for beam alignment, etc. to maximize the power generation ratio, an assumption is adopted that η_B depends only on the ratio of the irradiated area S_{irr} of the PV to the total area S_{PV}. η_B is expressed by the nonlinear function that Tang, et al investigated. Their configuration and results are quoted in Figure 3-1 and Figure 3-2.

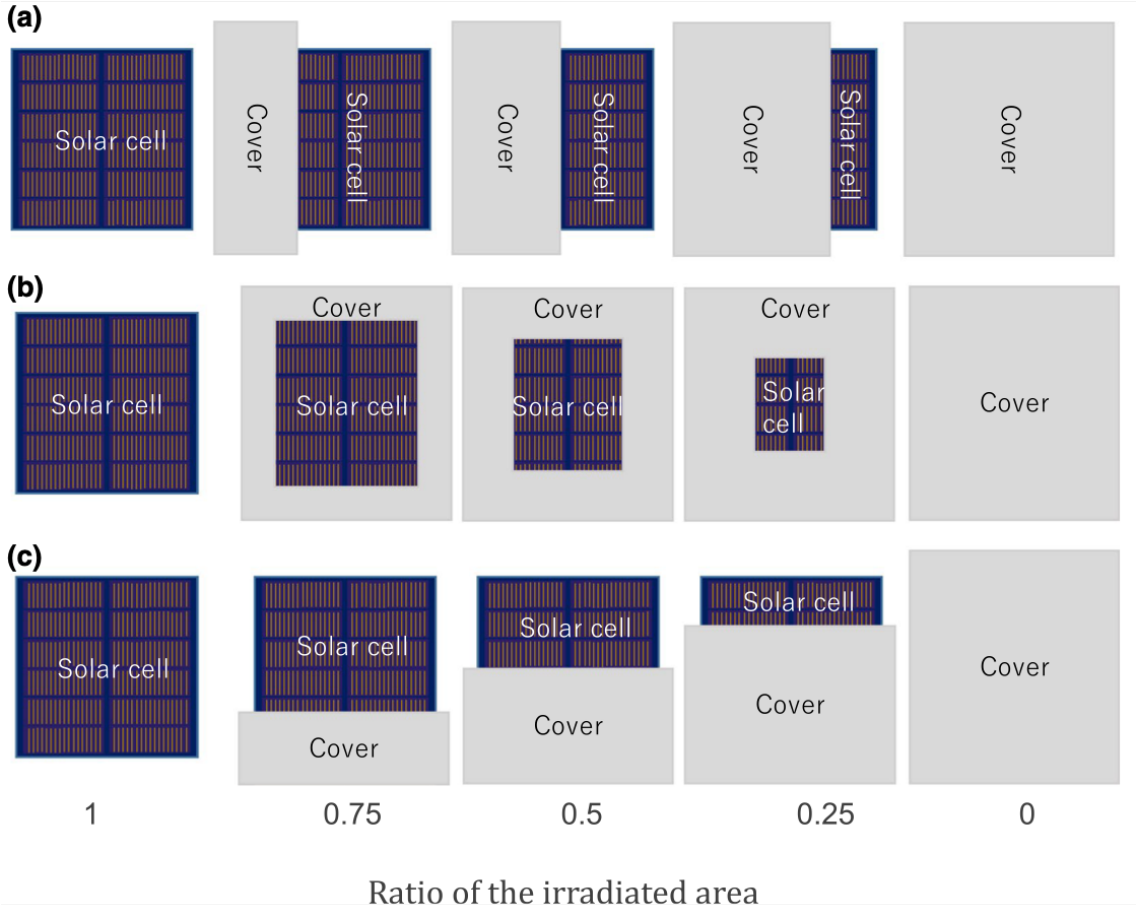


Figure 3-1 The experimental study of η_B by Tang , et.al. (configuration) [1]

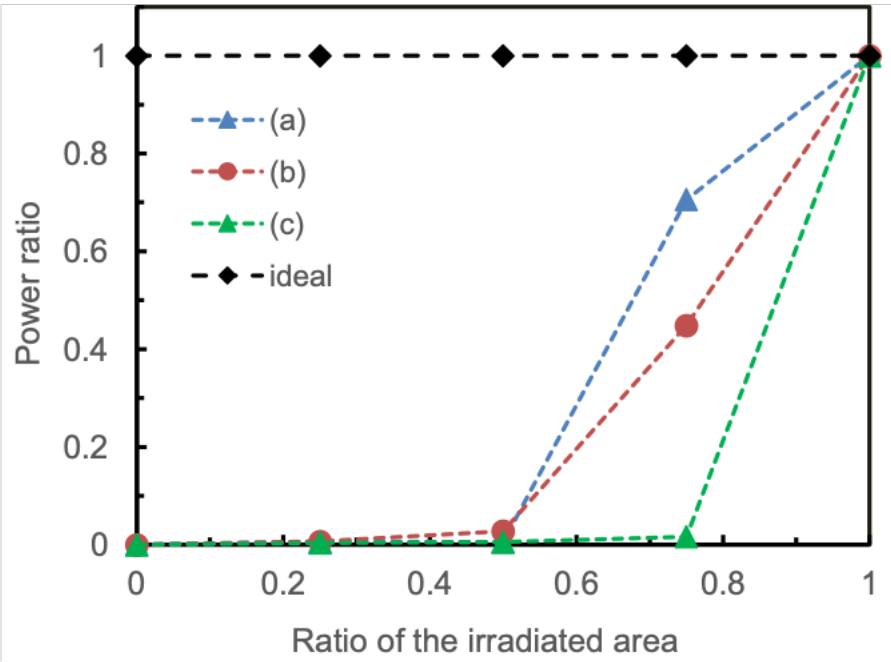


Figure 3-2 The experimental study of η_B by Tang , et.al. (results) [1]

This assumption is valid in the neighborhood of the point where focus and beam alignment are perfect. With this assumption, their power generation ratio concept can be extended to include errors of all DoF of beam alignment, shaping as perturbations. A functional form of η_B can be obtained by interpolating the data (b) in Figure 3-2 that Tang et al. reported.

$$\eta_B = 1.04x - 7.19x^2 + 13.76x^3 - 6.61x^4, \quad x = \frac{S_{irr}}{S_{PV}} \tag{3-2}$$

Other functional form will be obtained for other configurations of PV.

In many use cases of PV for solar power generation, one may naturally assume that the whole area of the solar cell array module is uniformly irradiated and both factors can achieve nearly 100 %. However, OWPT's situation is different in that the beam size is finite. One needs to adjust the incident beam shape with PV to avoid non-irradiated area and power loss due to shape mismatch between the beam and the PV. In other words, from the system efficiency point of view, one needs active control of beam alignment and its shape to maximize both factors of $\eta_{Power\ Generation}$ and to maintain high efficiency. If the beam size is large enough to cover the solar cell array, η_B becomes 100 %, and the requirement would be relaxed. However, light

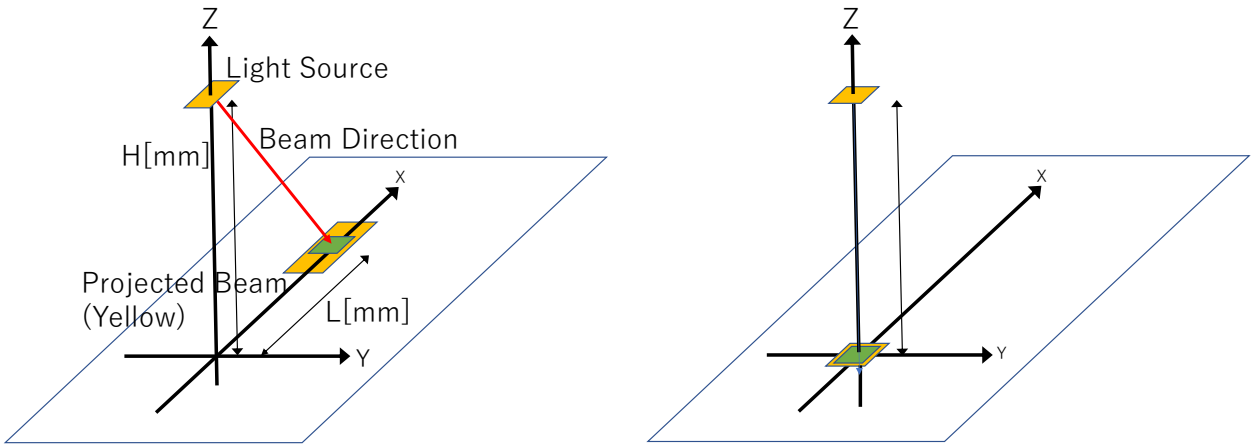
beam power spilled from the array deteriorates η_A. Since this degrades overall efficiency and spilled power may cause eye safety problems if such power is larger than the laser safety standard, the size of the irradiation beam should not be oversized.

3.2. Beam Shaping and Beam Alignment Requirement in Non-Cooperative OWPT

It is necessary to introduce appropriate simulation models to evaluate system-level requirements. These are the geometrical configuration and optics model [20].

3.2.1. Geometrical Configuration

Figure 3-3 is the geometrical configuration of the analysis. The shape of the solar cell array module is 100 mm × 100 mm square, which would generate power up to a few tens of watts, and it is placed at (L, 0, 0) in the coordinate system in Figure 3-3(a). L varies from 0 m in Figure 3-3 (b) to 10 m (or more). The size of this array is suitable for light beam propagation and many indoor, and outdoor applications of OWPT of this scale are expected. The shape of the array is assumed to be a rectangle, and its orientation is fixed along the X-axis. A typical realization of this configuration is the movements of an Automatic Guided Vehicle (AGV), which would move along a fixed axis during some period. There would be more than one transmitter in an area and one of the transmitters tracks AGV and adjusts beam shape and alignment within its limit, then hands it over to the other transmitter in the outside of it. The center of the beam is (0, 0, H) on the Z-axis, and H is fixed at 2500 mm (2.5 m), which is a suitable condition for indoor and outdoor environments. The beam shape is square and is tilted around the Y-axis to irradiate the array displaced in the X-direction on the XY plane, while the position of the emission center is fixed. The beam propagates with some beam divergence angle and its projected shape is deformed from square to generally trapezoid which is dependent on L.



(a) (b)

Figure 3-3 Geometrical configuration of non-cooperative OWPT study (a) General configuration of L≠0; (b) Configuration of L=0

3.2.2. Orthogonal Cylindrical Beam Expander Optics

To evaluate errors and to develop requirements for beam alignment and shaping, an appropriate optics model is necessary to simulate dealing with 3-dimensional errors. Even though beam shaping mechanisms are proposed for OWPT [2,3], they are static beam shaping or complex mechanisms for quite long-range utilizing adaptive optics. Here we propose a simple model that supports focus adjustment for moving targets with about 100 m range. The size of the light source at (0, 0, H) is 5 mm × 5 mm (square), its beam divergence is 0.8 deg (half angle), and the power profile is a top hat. A Gaussian beam with a homogenizer at the receiver side will provide the same result as this power profile. Since the projected beam size at the PV location on the XY plane is different along the X- and Y-direction, independent beam shape correction is necessary on each axis. Then, as shown in Figure 3-4, an optics system is proposed based on two independent beam expanders consisting of convex and concave lenses. To perform beam shape corrections independently for the X- and Y-axis direction, two identical cylindrical beam expanders are configured orthogonally and shifted 30 mm along the optical axis (beam direction). The lenses of each beam expander are cylindrical, their focal lengths are 150 mm (convex), and −30 mm (concave), and two lenses are separated by 120 mm nominally. Some geometric parameters in Figure 3-4 can be changed and adjusted depending on the actual operational system design. The optics with mathematical model was realized by Moriyama, et.al.[4,5]

Knowing the slant range from the light source to the PV and defocusing two convex lenses in X and Y directions independently, one can adjust the projected beam shape to the PV. Figure 3-5 shows the relation between the power generation ratio and position L from the foot of the Z-axis. Results of different beam control configurations are also displayed such as single-axis beam expander (Y-axis Adjustment) and without (no) beam expander configuration (Nominal Beam Expander w/o Adjustment). Using the orthogonal cylindrical beam expander optics, the power generation ratio can be maintained at 100 % even for L = 100 m and expects efficient power transfer from the light source to the panel (w/ X/Y Axis Adjustment). When a single-axis beam expander is applied or without beam expander optics, the power generation ratio is largely degraded and operation is restricted within a short L. This means OWPT efficiency would be quite low without appropriate optimization. Details of the simulation method for its range-dependent optimization of the power generation ratio are summarized in A.3.1 and A.3.2.

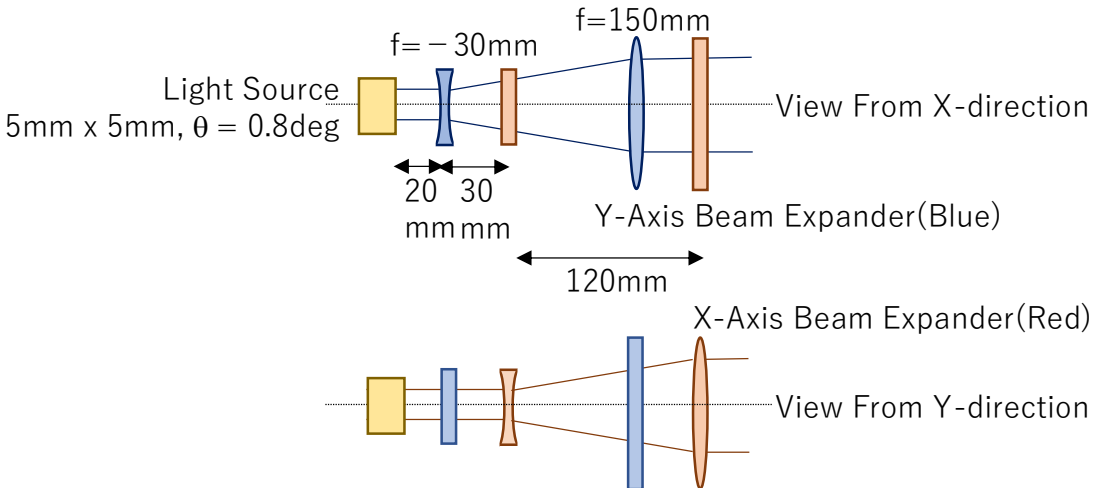


Figure 3-4 Orthogonal cylindrical beam expander optics.

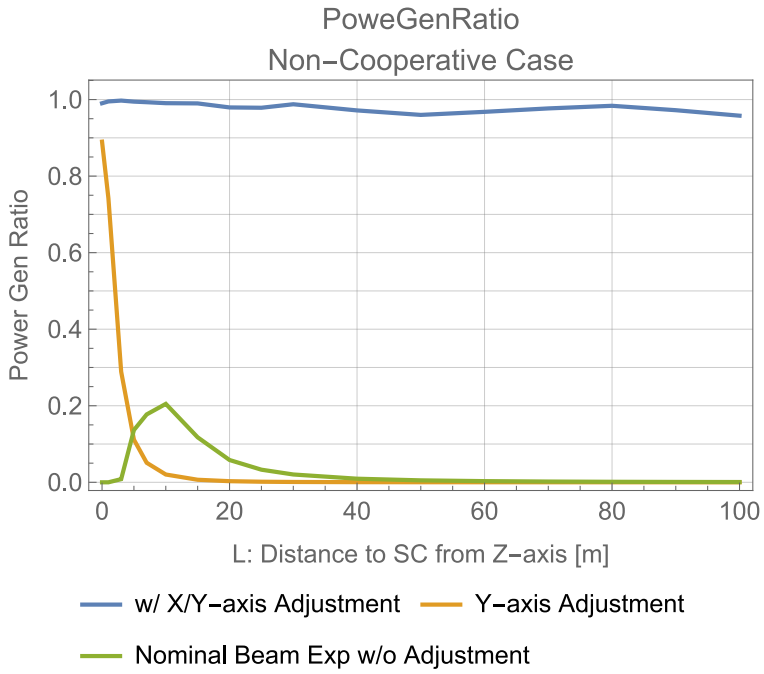


Figure 3-5 Power Generation Ratio (Non-Cooperative OWPT)

3.2.3. Requirement for Focus Adjustment (Beam Size Control)

To control beam size to accommodate the PV size, (de)focusing control of the beam expander is necessary. Its accuracy requirement would strongly affect the feasibility and cost of the system. In this section, the X and Y direction focus adjustment accuracy requirements are investigated based on the power generation ratio. Figure 3-6 shows the sensitivity analysis of the power generation ratio for focus adjustment error with various L of the array. Assume the power generation ratio to be more than 80%, requirement for focus adjustment error depends on L, e.g., less than 2.3 mm (L = 1 m), 76 μm (L = 10 m), 1.2 μm (L = 100 m). When the X-Focus Error is increased from zero in each plot, the size of the incident beam in the X-direction decreases until the beam becomes focused. The beam size increases again passing after the focus point with increments of the error, and the power generation ratio increases again and reaches its second peak. Such peaks are seen in each plot in Figure 3-6. Details of the power generation ratio simulation including focus perturbation is summarized in A.3.3.

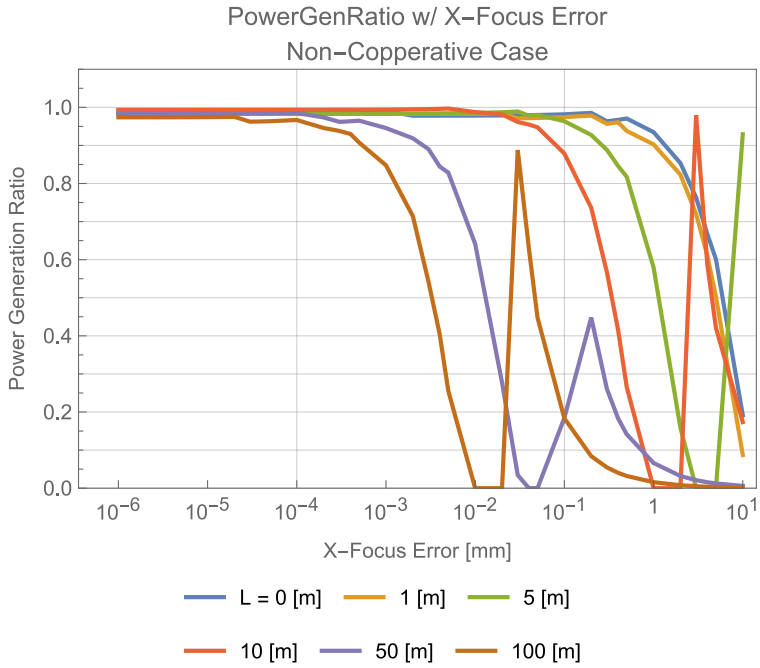


Figure 3-6 X direction focus adjustment dependence of power generation ratio

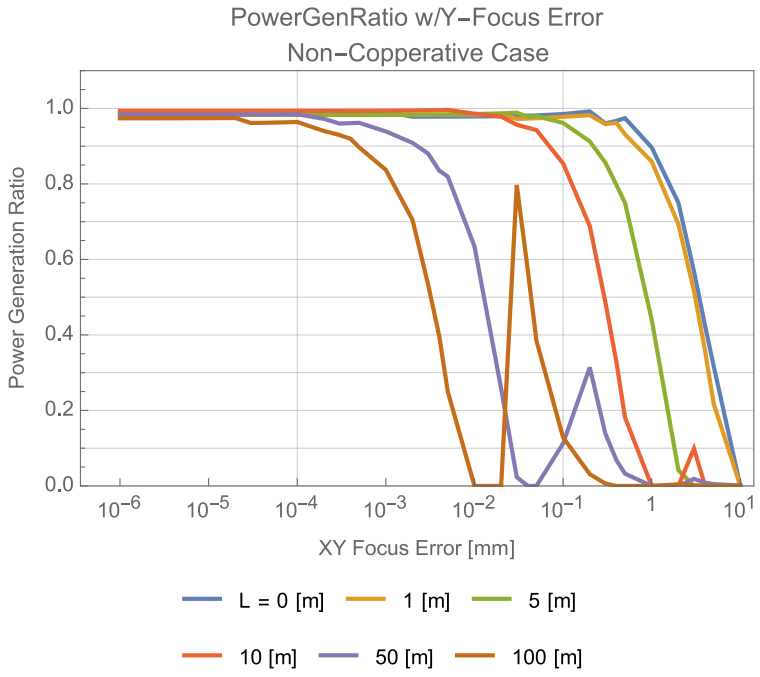


Figure 3-7 Y direction focus adjustment dependence of power generation ratio

Similar requirements are obtained for Y-direction (Figure 3-7). Similar peaks in power generation ratio are observed like in the X-direction. Determined at power 80 % generation ratio, requirements for focus adjustment are, e.g., less than 1.32 mm (L = 1 m), 132 μm (L = 10 m), 1.2 μm (L = 100 m).

Focus adjustment is necessary for each L to optimize the power generation ratio. This means real-time focus control is needed for a moving array. To relax focus control requirements, a simpler system is investigated. Assume focus is optimized not continuously for each target range (L) but adjusted at particular ranges such as 0 m, 1 m, 5 m, 10 m, 20 m, 50 m, 80 m, and 100 m. This leads to several power generation ratio plots for such ranges. Figure 3-8 shows each power generation ratio dependence on selected L. When the X and Y focus are adjusted at a particular L, the power generation ratio degrades much for the other L. This result strongly restricts the operation of this system. Assume one requires the power generation ratio to be greater than 80 %. From Figure 3-8, one can see the operation of this system is limited to the width of the range less than ±10 % × L, e.g., ±3m for the L = 50 m plot. It is recognized as necessary for the transmitter to track the distance (L) to the array and to adjust focus appropriately for each L.

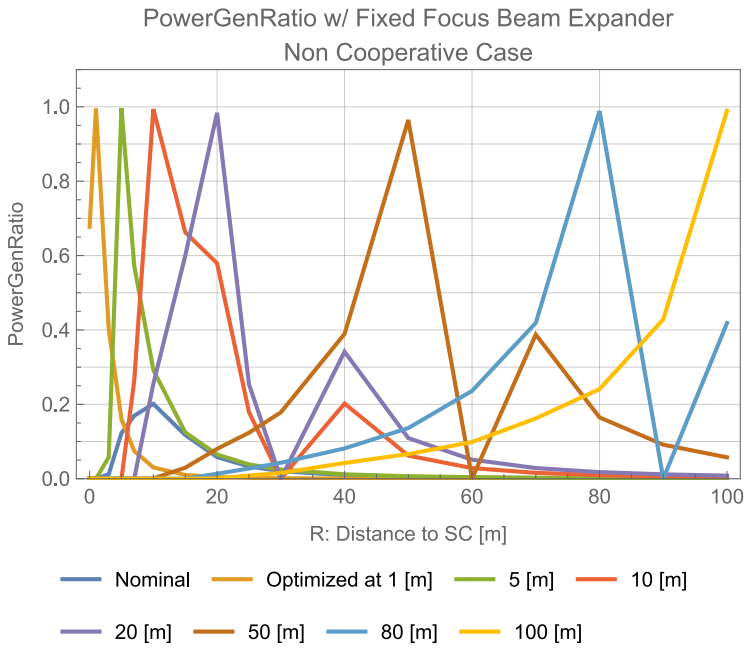


Figure 3-8 Range dependence of power generation ratio of fixed focus (Non-Cooperative OWPT)

3.2.4. Requirement for Beam Alignment

Since the solar cell array is fixed in a non-cooperative OWPT system, the necessary DoF for beam alignment is three, which is the relative attitude between the light source and the PV. To determine beam alignment allowance, the power generation ratio calculations were conducted for Figure 3-3 configuration with beam deviation along the X-direction, the Y-direction, and the rotation around the beam propagation direction (defined as “the optical axis”) (Figure 3-9). Details of the simulation method including the rotational perturbation are summarized in A.3.3.2.

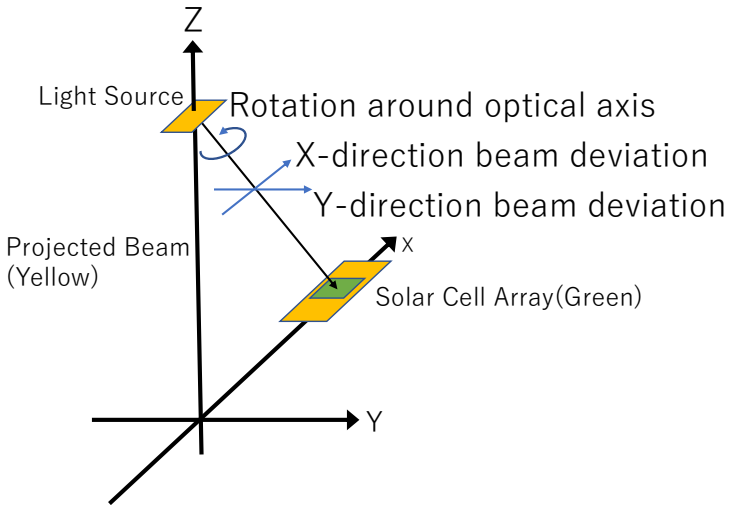


Figure 3-9 Beam alignment freedom in the analysis (Non-Cooperative OWPT)

The beam propagates towards the center of the PV, and the power generation ratio is calculated with beam deviation along the X-direction, which means rotation around the Y-axis (Figure 3-10). Determined at 80 % power generation ratio, requirements for beam deviation along the X-direction are, e.g., less than 2.21 mrad (L = 1 m), 149 μrad (L = 10 m), 11.7 μrad (L = 100 m).

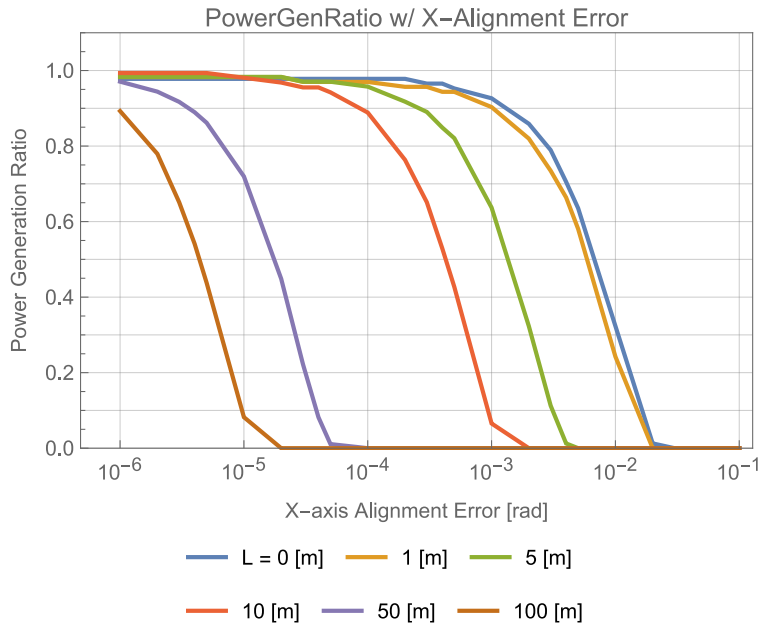


Figure 3-10 X direction beam deviation dependence of power generation ratio

Similarly, the power generation ratio for the Y-direction beam deviation, which is rotation around the X-axis, is calculated (Figure 3-11). Determined at 80 % power generation ratio, requirements for beam deviation along the Y-direction are, e.g., less than 2.51 mrad (L = 1 m), 631 μrad (L = 10 m), 57.5 μrad (L = 100 m).

The power generation ratio is calculated when the beam is rotated around its optical axis (Figure 3-12). When the beam shape is rotated around the optical axis, it produces multiple peaks of power generation ratio every 180-degree rotation angle because of the symmetry of the beam shape about the X-axis. For plots for small L, the projected beam shape is square-like. When such a beam is rotated, it produces additional sub-peaks at a 90-degree rotation angle because of its approximate 90-degree rotational symmetry around the optical axis. Those peaks of the power generation ratio are observed in Figure 3-12. Determined at an 80 % power generation ratio, requirements for beam rotation around the optical axis are, e.g., less than 182 mrad (L = 1 m), 74.1 mrad (L = 10 m), 6.7 mrad (L = 100 m).

The requirement for the X, Y-direction deviation is quite strong. There needs to be a complex mechanism to support such accuracies.

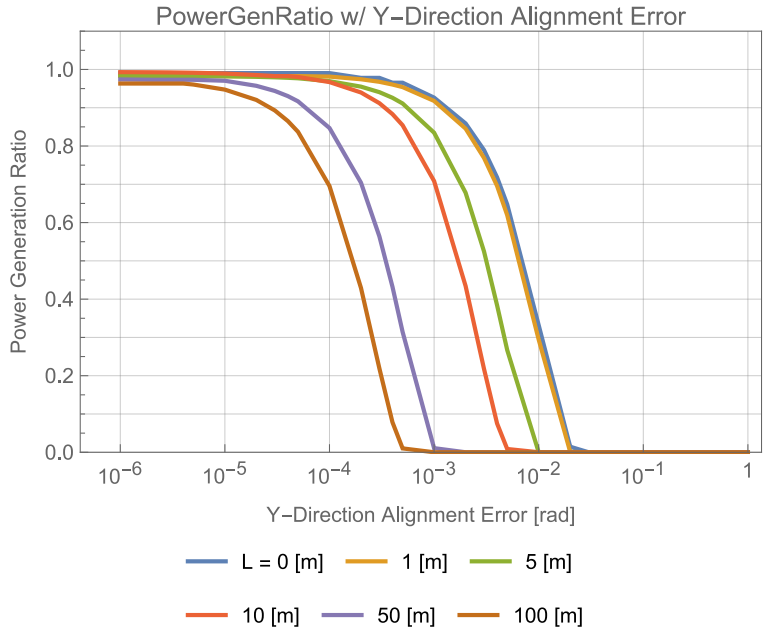


Figure 3-11 Y direction beam deviation dependence of power generation ratio

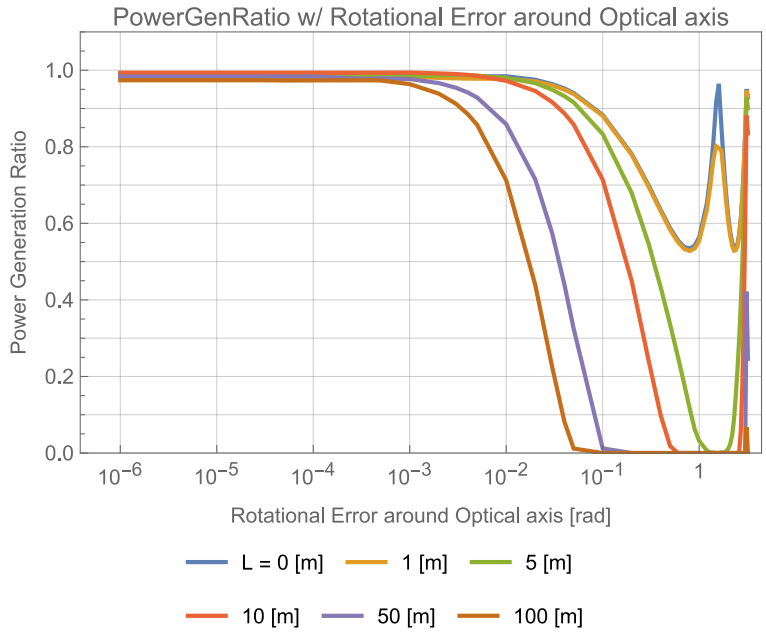


Figure 3-12 Rotation angle dependence of power generation ratio around optical axis

3.3. Beam Shaping and Beam Alignment Requirement in Cooperative OWPT

3.3.1. Geometrical Configuration and Optics

Assume the PV's attitude is dynamically controlled and the PV always faces the transmitter (cooperative OWPT) (Figure 3-13). In this case, the transmitter optics do not need to control the X and Y directions independently, thus, it is a single XY symmetrical beam expander. Its focus is adjusted using the relative range of the PV. Same as the condition in 3.2.2, the two lenses of the expander are 150 mm and −30 mm focal length, and their nominal separation is 120 mm. The simulation method for cooperative OWPT is the same as the non-cooperative one and the equations to calculate the power generation ratio including its range-dependent optimization for the cooperative OWPT model are given by setting $\phi = 0$ ($tan\phi = L/H$) in equations in A.3.1, A.3.2.

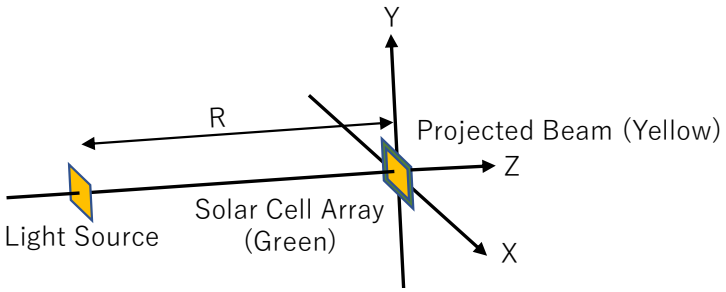
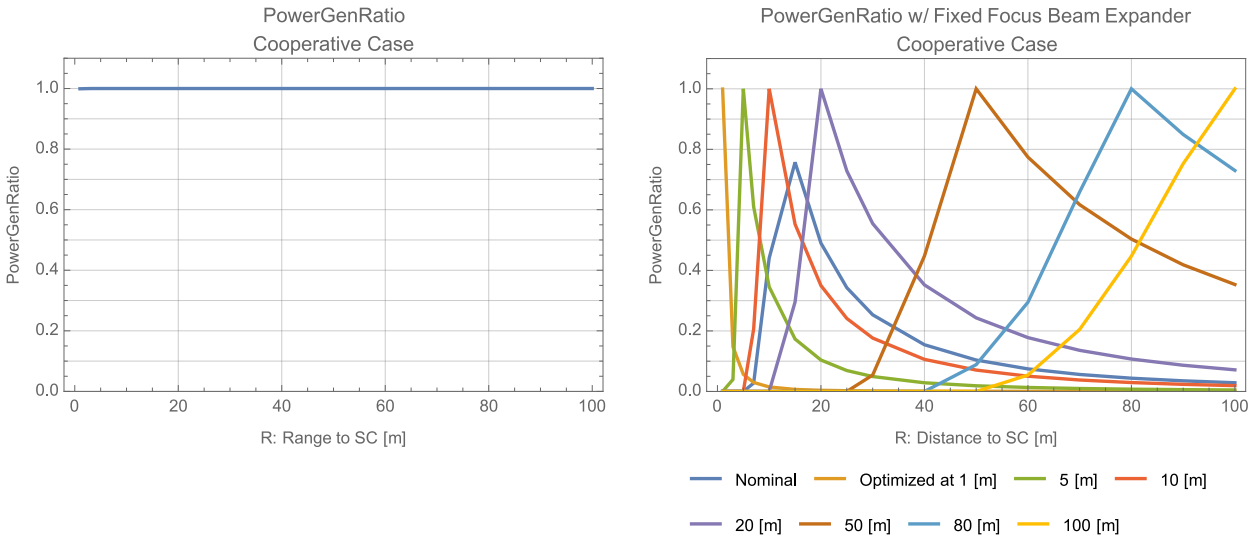


Figure 3-13 Configuration of Cooperative OWPT

If the focus is adjusted for each R, the power generation ratio is stable at 100 % (Figure 3-14 (a)). However, when the focus is adjusted at specific ranges, there is a large variation in power generation ratio for the range from 0 m to 100 m in case (Figure 3-14 (b)) like in non-cooperative OWPT. Thus, range-dependent focus adjustments are necessary to maintain a high power generation ratio. When the focus is adjusted at the specific range, comparing Figure 3-14(b) with Figure 3-8, the operatable range in the cooperative case is larger than the non-cooperative case in Figure 3-8. Assuming one requires the power generation ratio to be more than 80 %, one can see the operatable range is ±6.5 m for the "Optimized at 50 m" plot from Figure 3-14(b), and ±3 m from Figure 3-8.



(a) (b)

Figure 3-14 Range dependence of power generation ratio (Cooperative OWPT) (a) When focus is adjusted for each R, power generation ratio is stably maintained 100%.; (b) There is large variation in power generation ratio for range from 0m to 100m in case that focus is optimized and fixed at specific range.

3.3.2. Requirement for Focus Adjustment

The requirement for range-dependent focus control accuracy is investigated (Figure 3-15). Requirements for focus control accuracies are, e.g., less than 3.5 mm (R = 1 m), 350 μm (R = 10 m), 39 μm (R = 100 m).

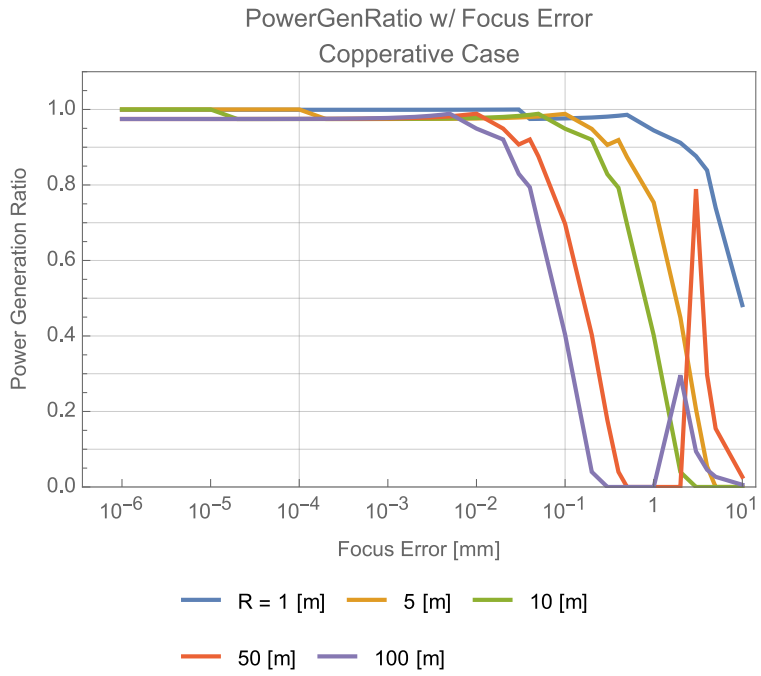


Figure 3-15 Focus dependence of power generation ratio (Cooperative OWPT)

3.3.3. Requirement for Beam Alignment

For beam alignment in cooperative OWPT, one needs to independently adjust the relative position and attitude of both the transmitter and solar cell array module. DoF of the beam alignment is 2 for beam deviation in the X and Y directions, 2 for solar array rotation around the X and Y axes, and 1 for rotation around the optical axis (beam direction). Since X, and Y directions are identical, the necessary number of relative DoF to be analyzed is reduced to 3. Those can be chosen as 1 for beam deviation in the X direction, 1 for beam rotation around the optical axis, and 1 for the tilt of the array in the X direction (Figure 3-16).

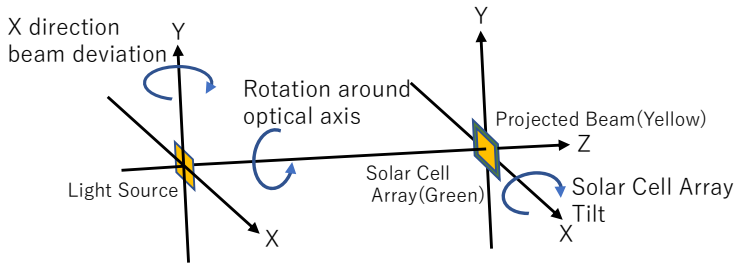


Figure 3-16 Beam alignment freedom in the analysis (Cooperative OWPT)

Figure 3-17 shows the power generation ratio calculation with an X-direction alignment error (beam deviation). Requirements for beam deviation in the X-direction are, e.g., less than 6.9 mrad (R = 1 m), 0.8 mrad (R = 10 m), 69 μrad (R = 100 m).

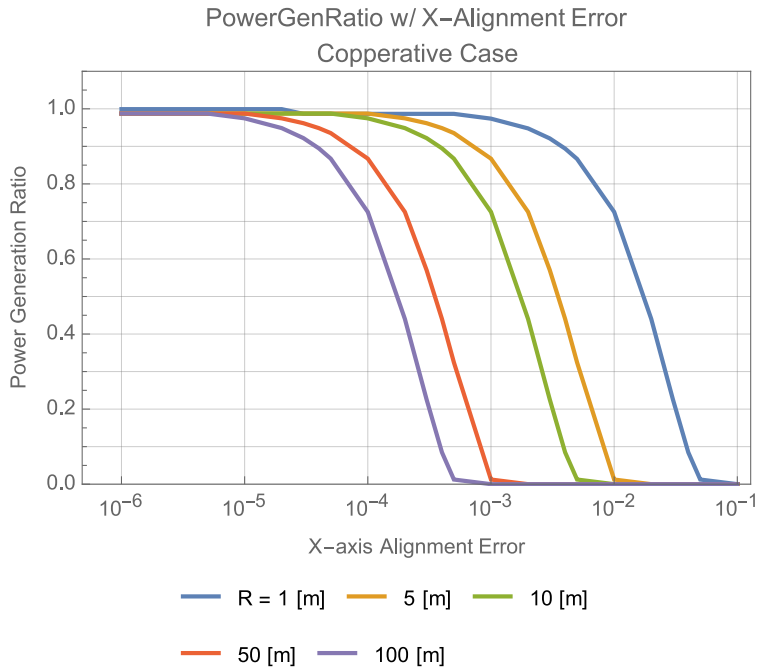


Figure 3-17 Beam deviation dependence of power generation ratio in X(Y) direction

Consider rotation around the optical axis and relative tilt between the incident beam and the array, and assume there are no misalignments for the X (Y) directions. In the cooperative case, both the size and shape of the incident beam at the entrance of the array coincide with those of the array (100 mm × 100 mm, square) at any R. When one rotates the beam around the optical axis, the square beam shape is rotated around the optical axis. There will be multiple peaks in the power generation ratio due to the rotational symmetry of the square shapes at every 90-degree rotation angle. This condition is the same for any R as shown in Figure 3-18.

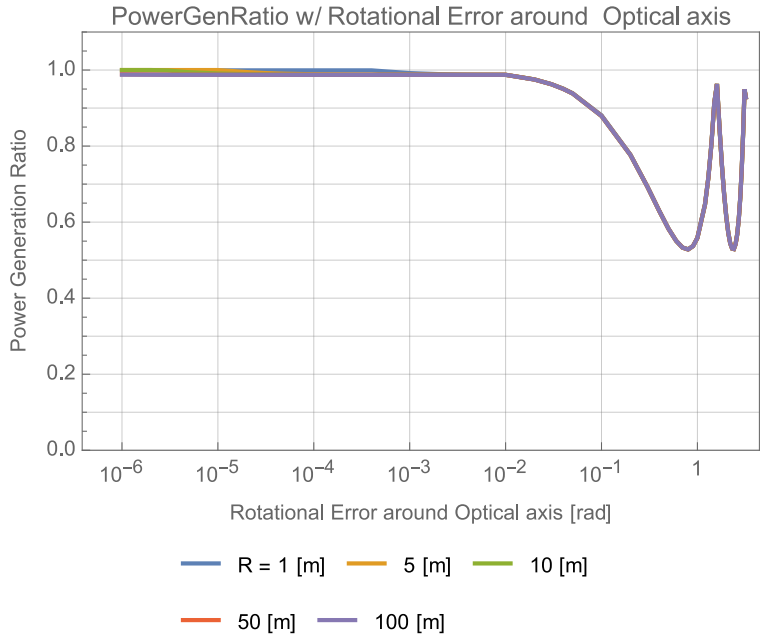


Figure 3-18 Power Generation Ratio Dependence on Beam Rotation around Optical Axis

Regarding relative tilt $\delta\theta$ from the normal, the apparent area size of the incident beam increases like $S_{prj}/cos\delta\theta$ where S_{prj} is calculated by the method in 1.1.1.1.1.1A.3.1 and 1.1.1.1.1.1A.3.2., and $\delta\theta$ is the relative tilt angle. When $S_{prj}/cos\delta\theta$ instead of S_{prj} is used for the calculation, this causes degradation of the power generation ratio. This relationship is independent of L. Setting $\delta\psi = \delta\phi = \delta\omega = 0$ and replacing the area of the array S_{prj} with $S_{prj}cos\delta\theta$, these result in Figure 3-19.

The above analysis suggests that the power generation ratio regarding rotation and tilt is independent of R. The following Figure 3-18 and Figure 3-19 calculations confirm above expectations including multiple peaks in Figure 3-18. Requirements for beam rotation around the optical axis are, e.g., less than 180 mrad (independent of R).

The requirement for solar cell array tilt angle is 645mrad independent of R.

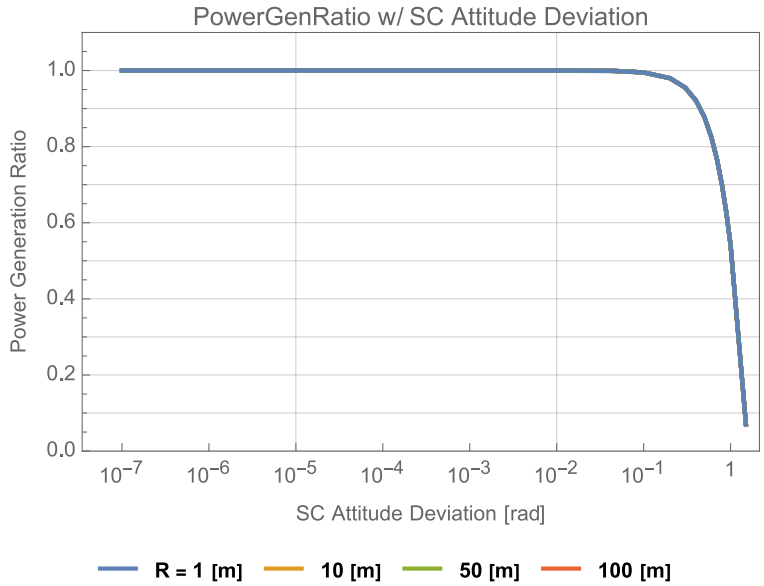


Figure 3-19 Power Generation Ratio Dependence on Solar Cell Array's Tilt Angle

3.4. Summary of the requirement for Focus Adjustment and Beam Alignment

The following table is excerpted from the requirement investigation using power generation ratio calculation. Each requirement is determined at an 80 % power generation ratio. The calculations are based on definitions in Figure 3-9 and Figure 3-16. The mathematical definitions of each symbol are described in A.3.1, A.3.2, and A.3.3. The definition of $\delta\theta$ is described in 3.3.3.

Table 3-1 Requirement for Focus Adjustment and Beam Alignment

Direction	Accuracy Requirement	
	Non-Cooperative	Cooperative
(de)Focus (X direction) (Δ'_x)	2.3 mm (L=1m) 76 μm (L=10m) 1.2 μm (L=100m)	3.5 mm (R=1m) 350 μm (R=10m) 39 μm (R=100m) * X, and Y directions are identical
(de)Focus (Y direction) (Δ'_y)	1.32 mm (L=1m) 132 μm (L=10m) 1.2 μm (L=100m)	
Beam Deviation (X direction) ($\delta\phi$)	2.21 mrad (L=1m) 149 μrad (L=10m) 11.7 μrad (L=100m)	6.9 mrad (R=1m) 0.8 mrad (R=10m) 69 μrad (R=100m) *X, and Y directions are identical
Beam Deviation (Y direction) ($\delta\psi$)	2.51 mrad (L=1m) 631 μrad (L=10m) 57.5 μrad (L=100m).	
Beam Rotation (Around Optical Axis) ($\delta\omega$)	182 mrad (L=1m) 74.1 mrad (L=10m) 6.7 mrad (L=100m)	180 mrad (R<100m)
Solar Cell Array Tilt (X(Y) direction) ($\delta\theta$)		645 mrad (R<100m) * X, and Y directions are identical

The requirement for cooperative OWPT is more relaxed than non-cooperative one. On the other hand, cooperative OWPT requires mutual alignment and interaction between the transmitter and solar cell array, which increases system complexity. This is a trade-off item in actual operational OWPT system design.

3.5. Relaxation of the System-Level Requirements using a Fly Eye Module

3.5.1. The Fly-Eye Module and Its Qualitative Characteristics

The factor, the "power generation ratio ($\eta_{Power\ Generation}$)" describes the effect of system-level efficiency, including optics such as beam alignment and shaping. It is calculated from the light beam power contributing to power generation in the PV, which is a portion of the power of the incident beam. The investigation in this section is to enhance this factor by utilizing a module with a fly-eye lens.-

Figure 3-20 shows a basic configuration of a PV with a fly-eye lens. As examples of lens parameters for assumed configuration, the focal length of each element lens is f= 20 mm, and its shape is square with d = 10 mm side length. The focal length of the condenser lens is F = 200 mm, and it is a square shape with D = 100 mm side length. 10 × 10 (100) element lenses compose a fly-eye lens. When the incident beam size is equal to or larger than the element lens, even if it is smaller than the size of the solar cell array, each image of the element lens is projected onto the focal plane of the condenser lens with Fd/f size. It should be noted that this is independent of incident beam size. Matching the size of the solar cell array in Figure 3-20 as Fd/f, the whole area is irradiated by the incident beam without any non-irradiated area.

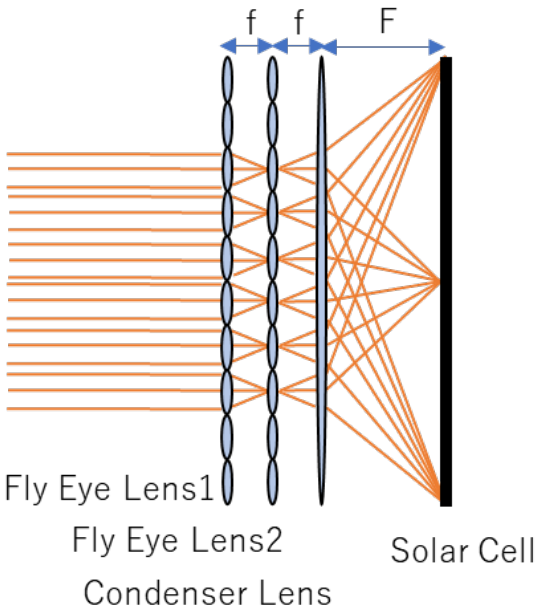


Figure 3-20 Solar Cell Array with Fly Eye Lens

To qualitatively confirm these effects, the power density of the incident beam on the fly-eye module of Figure 3-20 is plotted on the surface of the fly-eye lens and the PV surface. The incident beam is assumed to be 1 W top hat profile and the beam size is 50 mm × 50 mm. Horizontal and vertical axes represent 100 × 100 grid points defined in each fly-eye lens and PV. The calculation method is described in 3.5.3.

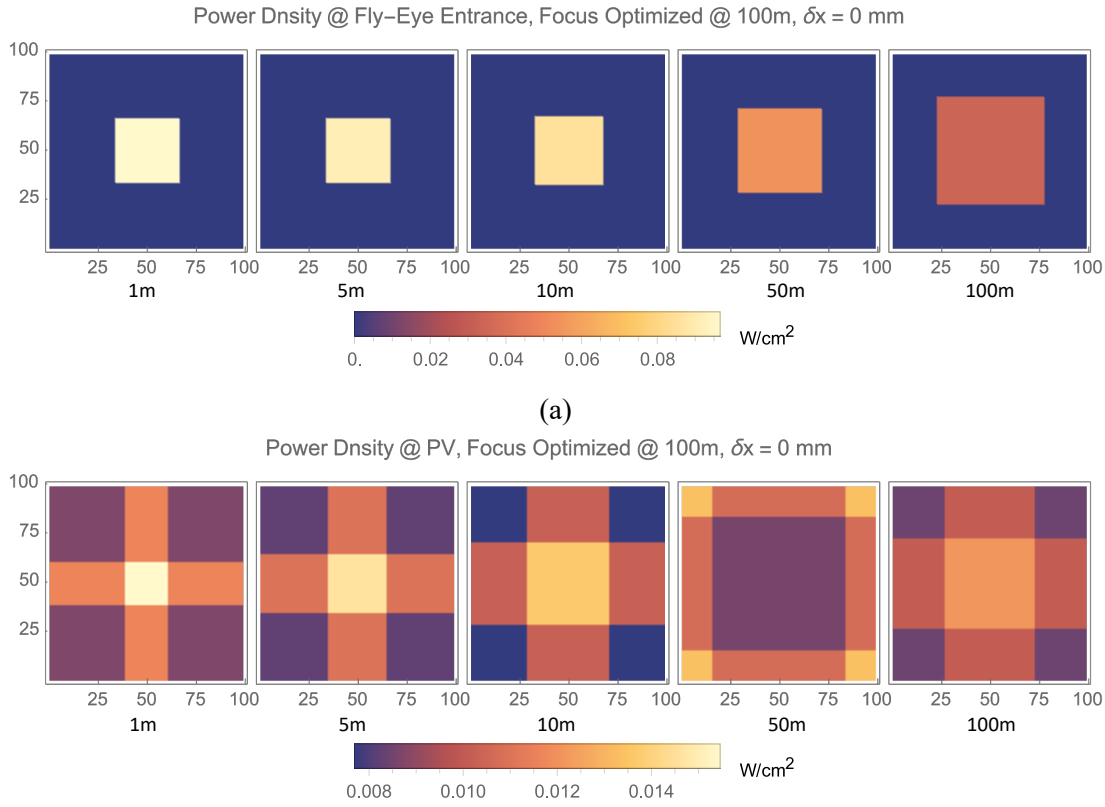


Figure 3-21 Power density in the fly-eye module. (a) at the fle-eye lens entrance; (b) at the PV surface

In Figure 3-21, the power density is plotted for distances of 1, 5, 10, 50, and 100 m when the incident beam is focused at 100 m to a beam size of 1/2 (50 mm × 50 mm) of the fly-eye lens and aligned to the center of the fly-eye lens. It can be seen that even though the beam size at the fly-eye lens surface changes by a factor of 2 as the distance changes from 1 m to 100 m, the beam at the PV surface always completely covers the PV and the power density changes by a factor of 2 at most.

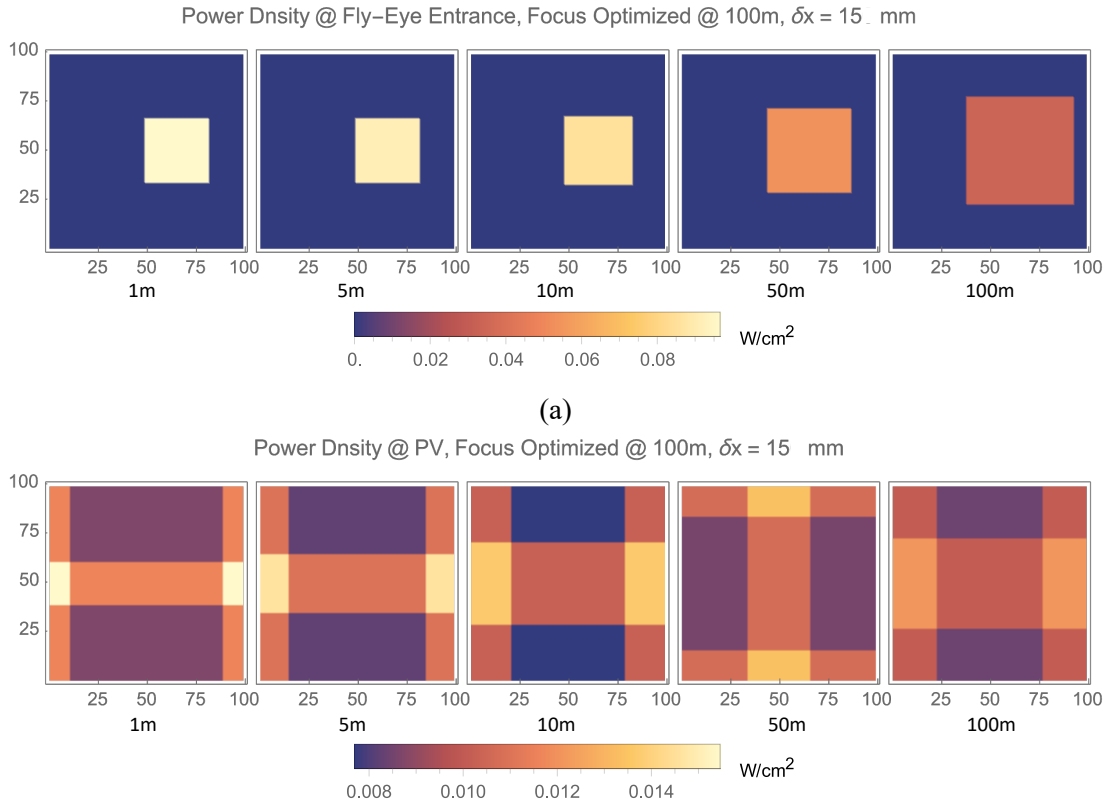


Figure 3-22 Power density in the fly-eye module(δx = 15 mm). (a) at the fly-eye lens entrance; (b) at the PV surface

Figure 3-22 plots the case of a 15 mm misaligned beam in the horizontal direction (δx = 15 mm) to Figure 3-21. It can be seen that if the incident beam is sufficiently small on the fly-eye lens and its power is not spilled from the fly-eye lens, then changes in distance and misalignment on the fly-eye lens have no impact on the uniformity of the power density, nor the property of the beam to cover the PV completely.

3.5.2. Geometrical, and Optical Configuration of the Analysis

The geometrical configuration of this analysis is the same as Figure 3-13, assuming the attitude of the solar cell array is always dynamically controlled to face the transmitter (cooperative OWPT). Other parameters of the transmitter optics are the same as in 3.2.2. The beam expander is defocused to adjust the beam size at the entrance of the fly eye module. The size of the PV is 100 mm × 100 mm, and the beam size is adjusted to a smaller size of the PV by controlling the focus of the beam expander. In the following investigation in this section, the beam size is

assumed to be 1/2 of the size of the array. Even though each size in the system in this calculation is fixed, the result is readily scalable to the other sizes.

3.5.3. Power Generation Ratio, Homogenization by Fly Eye Module

η_B of the power generation ratio will be a complex function of the internal configuration of the solar cell array. However, since the whole area of the PV is irradiated by the incident beam in the Figure 3-20 module, η_B always becomes 100 %. If the efficiency of a solar cell depends on η_B, the internal configuration of the solar cell array information is necessary for its efficiency calculation [6–8]. This fly-eye module does not need such information, and its efficiency calculation model becomes much simpler than the one without this module. When an operational OWPT is composed of solar cells that have different internal configurations from each other, there is a possibility that the efficiencies of different internal PV configurations are different. This module absorbs such internal configuration differences and would produce uniform efficiency.

The remaining issue is to maximize η_A, and needs to avoid beam spilling over from the module. Focus adjustment, beam alignment, and beam confinement for this module are studied in the following sections.

As the array always faces the transmitter in cooperative OWPT, the power generation ratio is 100 % if the beam expander is defocused appropriately. In the case of a moving array, this requires real-time focus adjustment based on range information to the array. To relax this strong requirement, defocusing at a fixed range is investigated. Figure 3-23 shows the range dependence of the size of the beams, and each beam size is adjusted to be 1/2 of the PV size at various distances from the transmitter. If the beam size is adjusted at a distance further than 30 m, e.g., 40 m, 80 m, 100 m, the size of the beam is always less than the size of the array (100 mm) within 100 m. Otherwise, the beam size becomes larger than the array (> 100 mm) at some range.

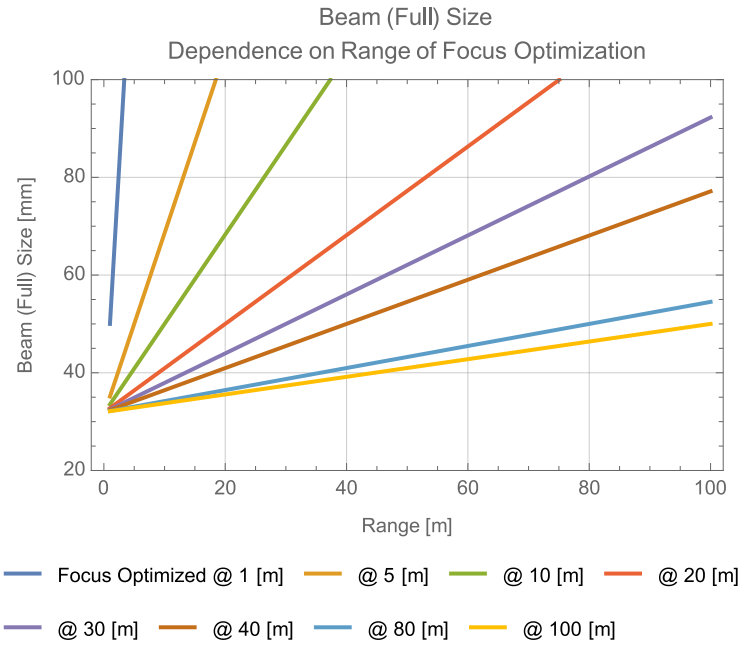


Figure 3-23 Beam size with focus adjustment at fixed range

From here, defocusing the beam expander is called “focus adjustment” or “focus optimization” and the distance from the transmitter to the solar cell array is denoted as “L”.

Assume each focus of beams is adjusted such that the size of the beams at 40 m, 80 m, and 100 m are to be 1/2 of the size of the array. Such beam sizes do not exceed that of the solar cell array within 100 m. To see the homogenization effect for these beams by the fly-eye module, the range dependence of power density of the incident beam is calculated at the fly-eye module entrance shown in Figure 3-24 and at the solar cell array (PV) in Figure 3-25, respectively.

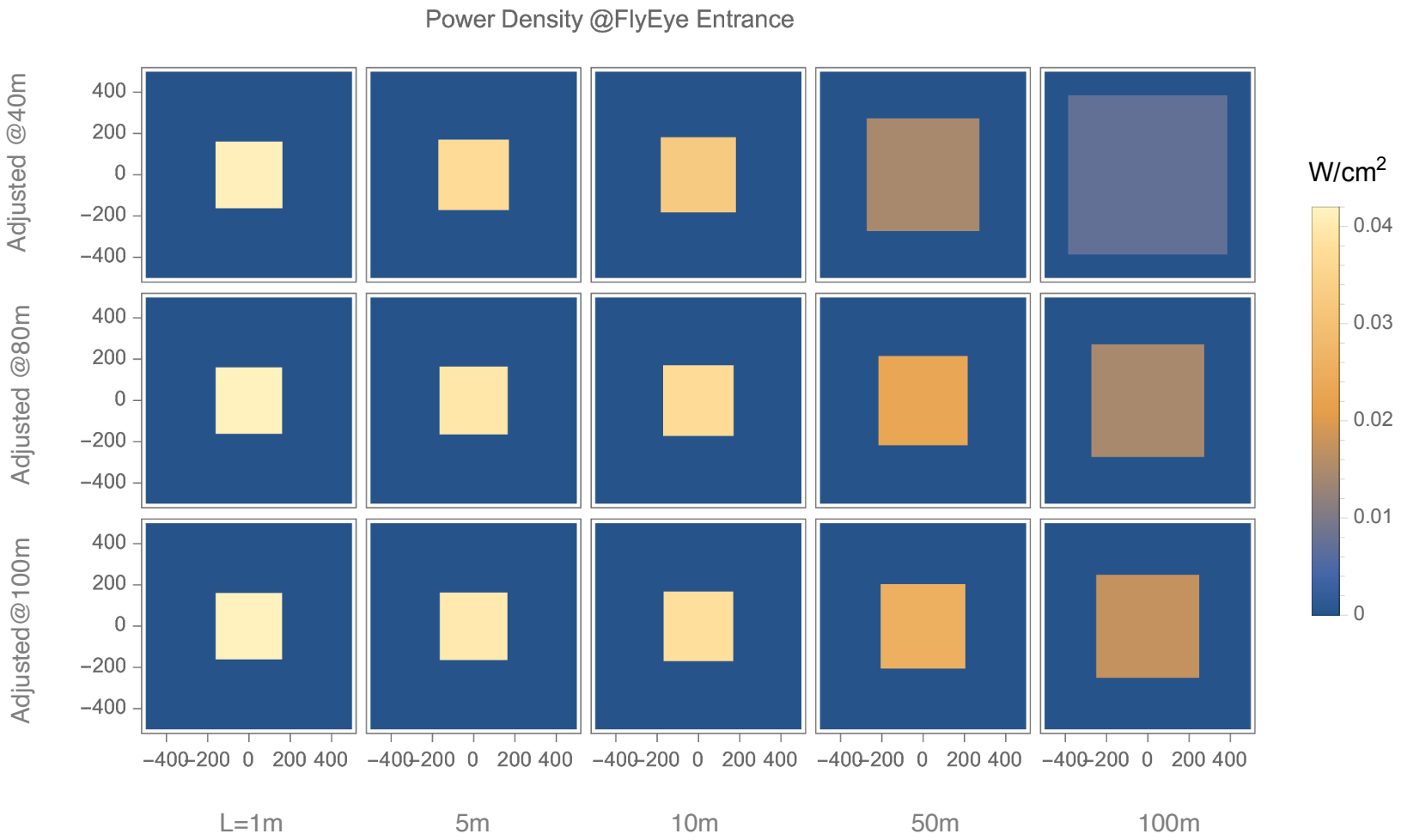


Figure 3-24 Power density of the incident beam at fly eye module's entrance

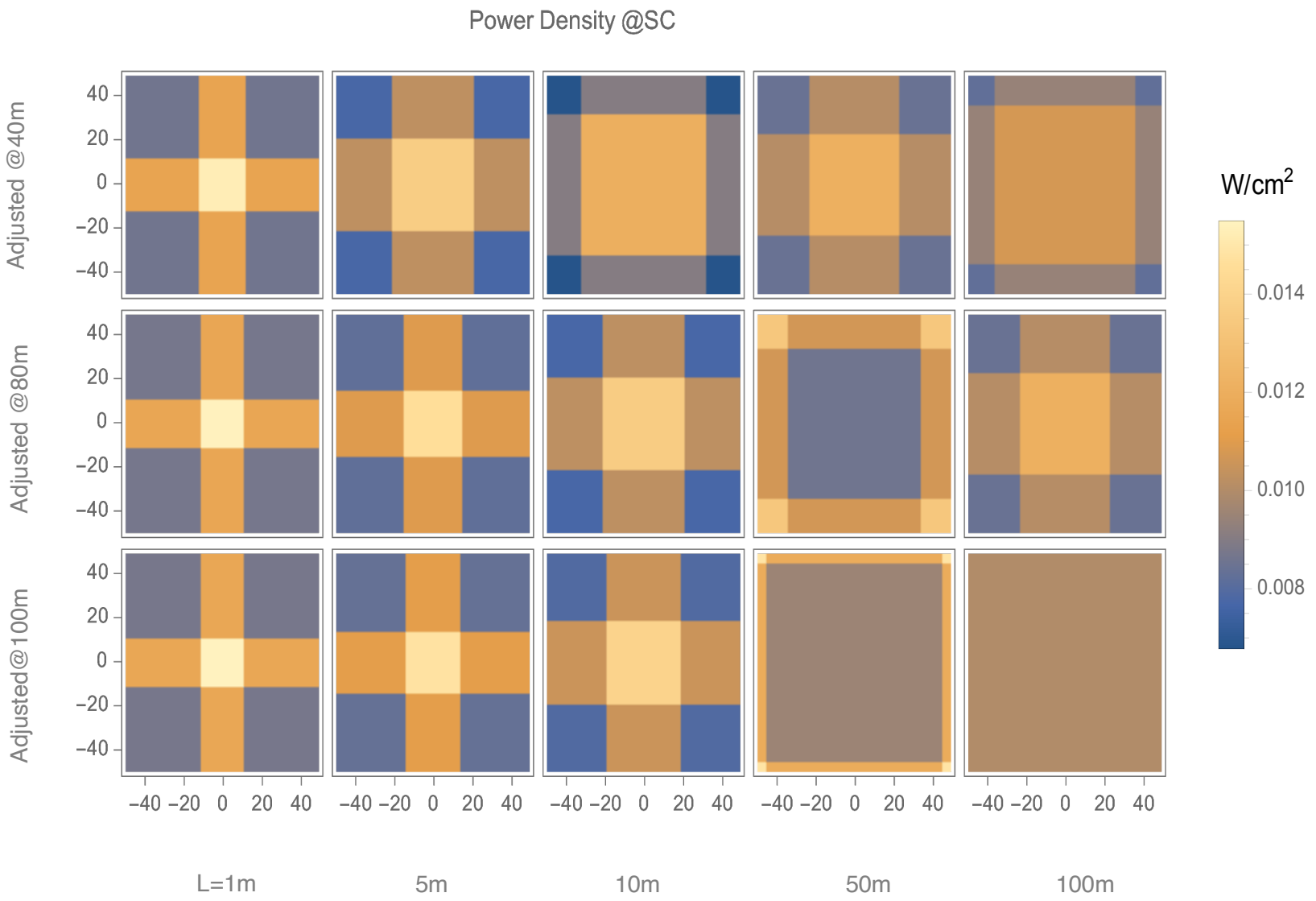


Figure 3-25 Power density of the incident beam at solar cell array (SC)

In the calculation, power of each beam is assumed 1 Watt and size of the fly-eye entrance and the solar cell array are both 100 mm × 100 mm like in Figure 3-21 and Figure 3-22. For the calculation, 100 × 100 grid points are defined in each fly-eye element lens. Power densities are calculated on each 100 × 100 grid points of each element lens at the module entrance and projected onto 100 × 100 grid points at the solar cell array.

Power density at (I,J) grid point (I,J : $1\ to\ 100$) of the solar cell array is given by

$$I_{PV}(I,J) = \sum_{a,b=1}^{10} I_{a,b}(I,J) \tag{3-3}$$

where $I_{PV}(I,J)$ is power density at (I,J) grid point of the solar cell array, $I_{a,b}(I,J)$ is power density at (I,J) grid point of (a,b) element lens. Since 10 × 10 element lens compose one fly-eye lens, indices a,b run from 1 to 10.

Power density varies with both focus adjustment range (40 m, 80 m, 100 m) and range to the array (1 m, 5 m, 10 m, 50 m, 100 m). Figure 3-26 and Figure 3-27 show homogeneity at the solar cell array. In these plots, homogeneities are defined as the ratio of minimum power density to mean power density over the array in Figure 3-26 and the ratio of minimum power density to maximum power density in Figure 3-27.

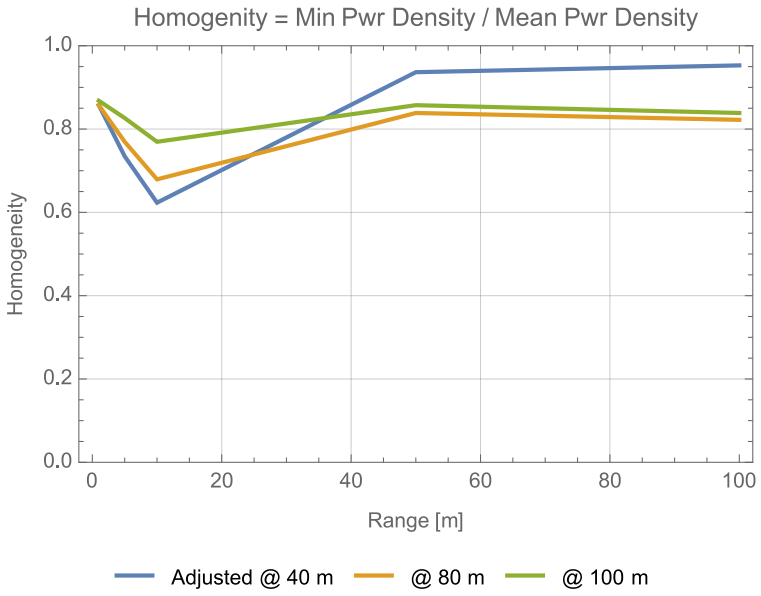


Figure 3-26 Homogeneity (Min Power Density/Mean Power Density)

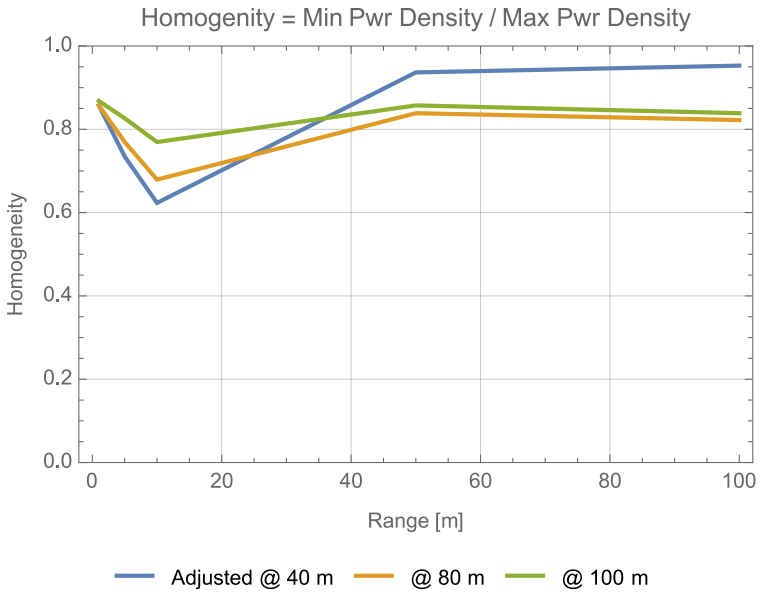


Figure 3-27 Homogeneity (Min Power Density/Max Power Density)

Even though there are some inhomogeneities of power density at the array in each plot, such inhomogeneities are less than factor of two in Figure 3-26 and Figure 3-27, and they are acceptable for practical purpose of OWPT.

Figure 3-28 shows power generation ratio for each adjustment. As shown in Figure 3-23, if the focus is adjusted at more than 30 m, the beam size is less than 100 mm within 100m. Thus power generation ratio is 100 % from 0 m to 100 m for adjustment at 40, 80, 100 m in Figure 3-28. This means that if the beam size is less than the array size (100 mm), power generation ratio is maintained at 100 %. When the focus of the beam expander is fixed (optimized) at an appropriatre distance, the power generation ratio can be stably efficient even if L varies. This example shows that one time focus adjustment at more than 30 m is enough for stabilizing power generation ratio from 0 m to 100 m.

The fly-eye module relaxes the focus adjustment at every distance from the transmitter to an one time adjustment at a fixed appropriate distance. Therefore, in the fly-eye module study, investigations were conduted adjustment at every distance and adjustment at a particular distance (100m).

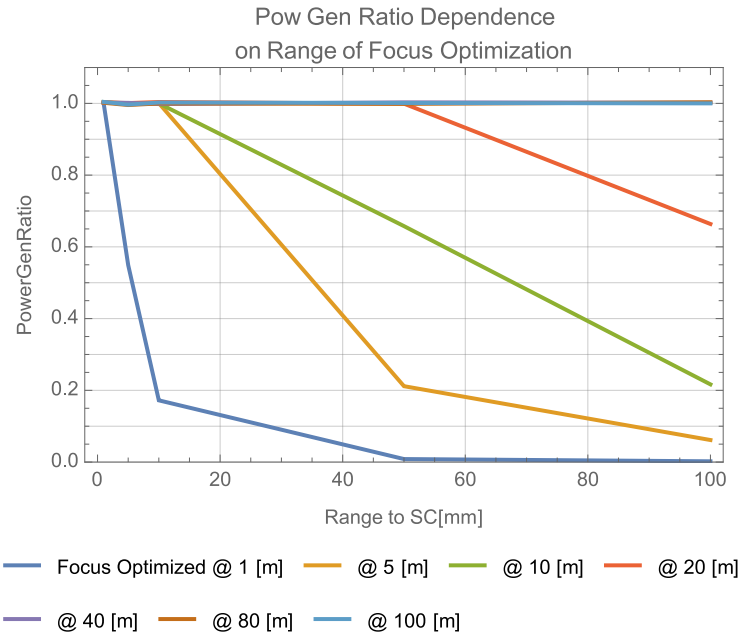
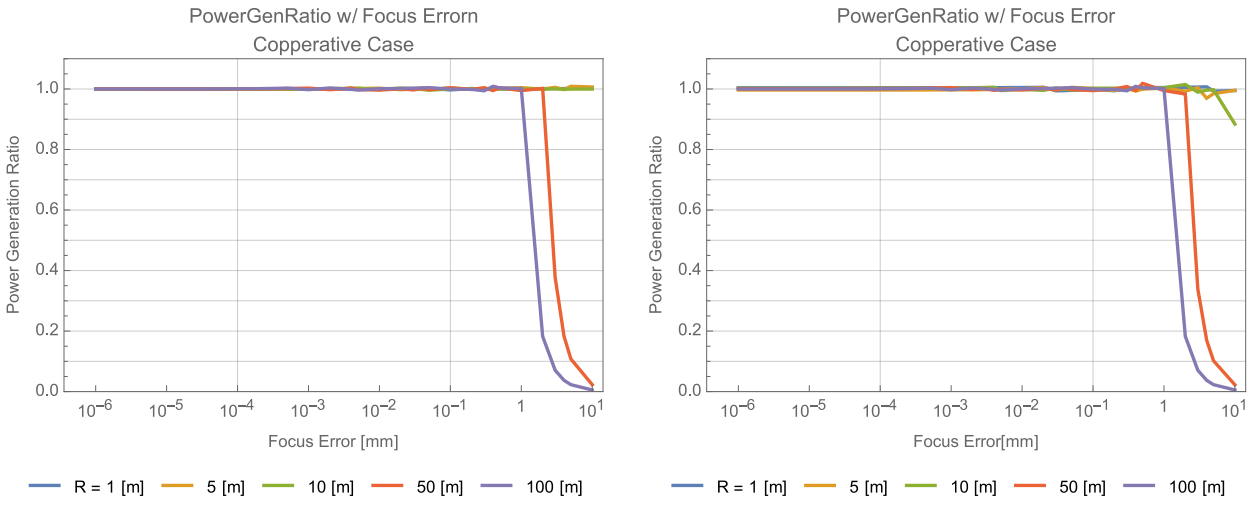


Figure 3-28 Range dependence of power generation ratio for various focus adjustment range

3.5.4. Requirement for Focus Adjustment of Transmitter Beam Expander

The requirement for focus adjustment is investigated. In case that focus is optimized for each L, about 1 mm focus error is allowable (Figure 3-29(a)). When focus is fixed at 100 m in Figure 3-29(b), similarly 1 mm focus error is allowed in this case. The requirements for this focus adjustment are relaxed compared to when the fly's eye is not used Figure 3-15.



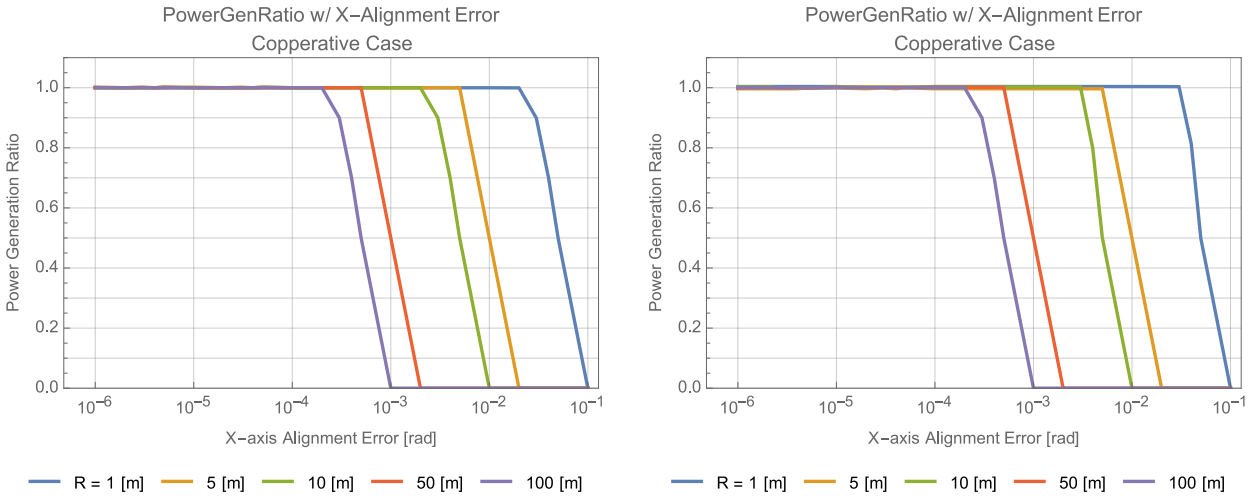
(a) (b)

Figure 3-29 Power Generation Ratio Dependence on Focus Adjustment (a) Focus Optimized at Each L; (b) Focus Optimized at 100 m

3.5.5. Requirement for Beam Alignment

3.5.5.1. X(Y) Direction Beam Alignment

The analysis is conducted the same way as in 3.2.4 and 3.3.3. In Figure 3-30(a), like Figure 3-29(a), focus is optimized for each L, and the effect of the X(Y) axis alignment error is calculated. In Figure 3-30 (b), like Figure 3-29(b), the focus is optimized at 100 m and fixed. Similar results are obtained from both cases. L-dependent requirements are, which is determined at 80 % of the power generation ratio, e.g., 34 mrad at L = 1 m, 3.4 mrad at L = 10 m, 0.32 mrad at L = 100 m. Since the X and Y directions are identical, requirements for both X and Y directions are the same. In this study, the beam size was set to 1/2 of the size of the fly eye lens array. Changing this size slightly changes the characteristics in Figure 3-30.

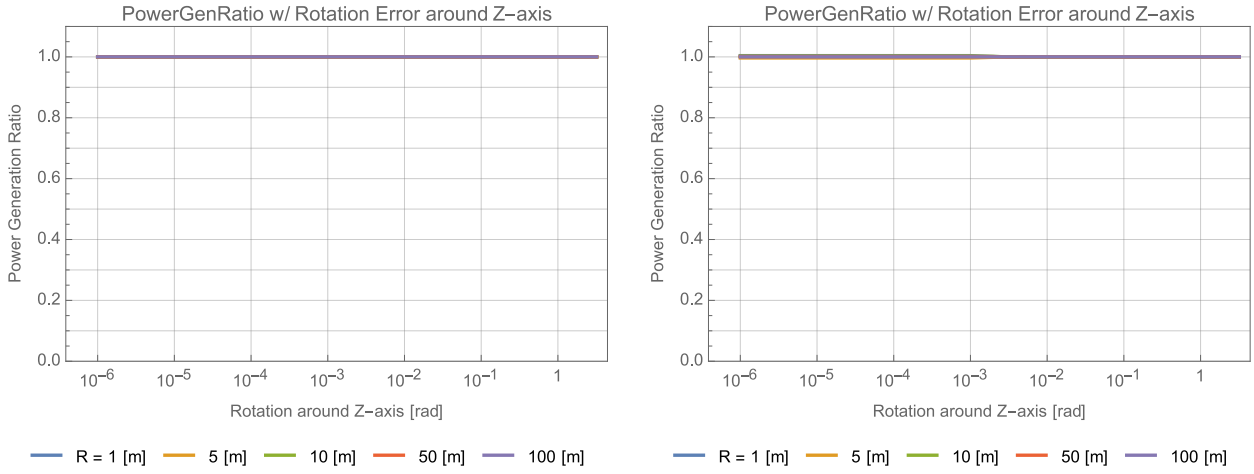


(a) (b)

Figure 3-30 Power Generation Ratio Dependence on X(Y) Direction Deviation. (a) Focus Optimized at Each L; (b) Focus Optimized at 100m

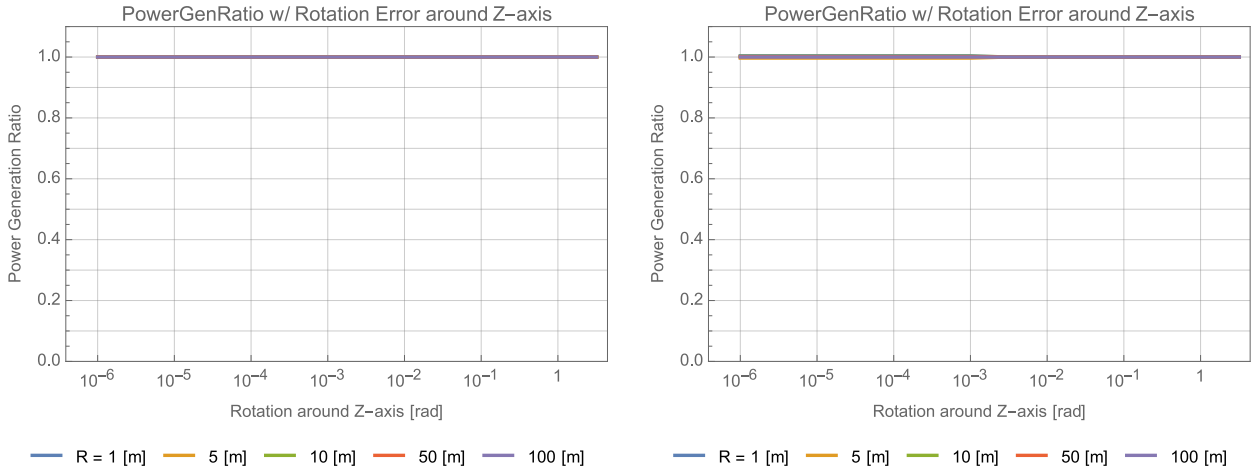
3.5.5.2. Rotational Alignment around Beam Direction

The requirement for rotational alignment around the optical axis is investigated. In



(a) (b)

Figure 3-31(a), the focus is optimized for each L, and the effect of the rotational alignment error is calculated. In (b), the focus is optimized at 100 m and fixed. Similar results are obtained from both cases. Since the beam size is less than the size of the array for every rotation angle and every L < 100m, the power generation ratio is stably 100% for any rotation angle and L. When this beam size approaches the array size, the efficiency degrades because part of the beam leaks out of the lens array, especially under a rotation angle of close to 45 degrees. This means that maintaining a sufficiently small beam size is advantageous for the proposed configuration.



(a) (b)

Figure 3-31 Power Generation Ratio Dependence on Rotation around Optical Axis. (a) Focus Optimized at Each L; (b) Focus Optimized at 100m

3.5.6. Requirement for Solar Cell Tilt and Beam Energy Confinement in the Fly Eye Module

3.5.6.1. Upper Wall Mirror and lower Wall Mirror configurations

When the solar cell array tilts, the beam's incident angle to the array changes. The beam is not only projected to the adjacent area but also is vignetted in some portion. To avoid these problems, Katsuta, et al. suggested surrounding reflective side panels between the fly eye lens and solar cell array [7] (Lower Wall Mirror in Figure 3-32).

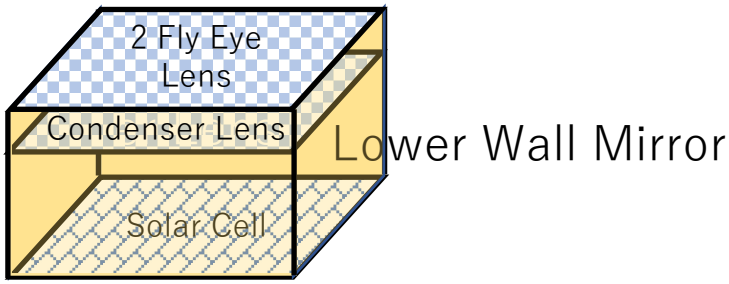


Figure 3-32 Fly Eye Module with Lower Wall Mirror

There will be another configuration with upper wall mirrors above the fly-eye lens (Upper Wall Mirror in Figure 3-33). A similar idea is found in literature [9].

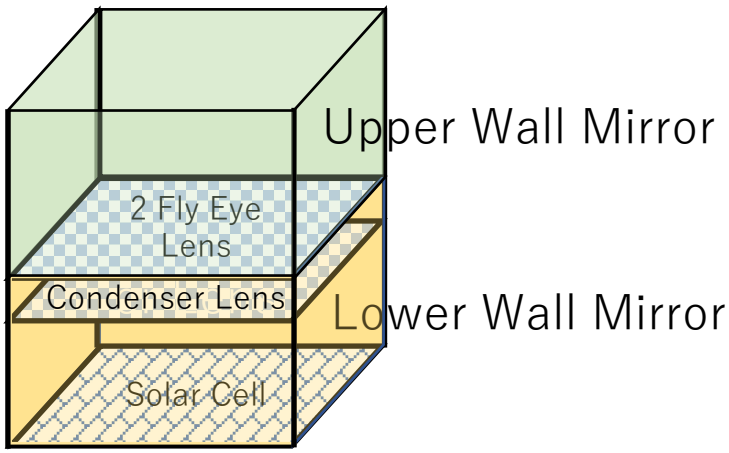


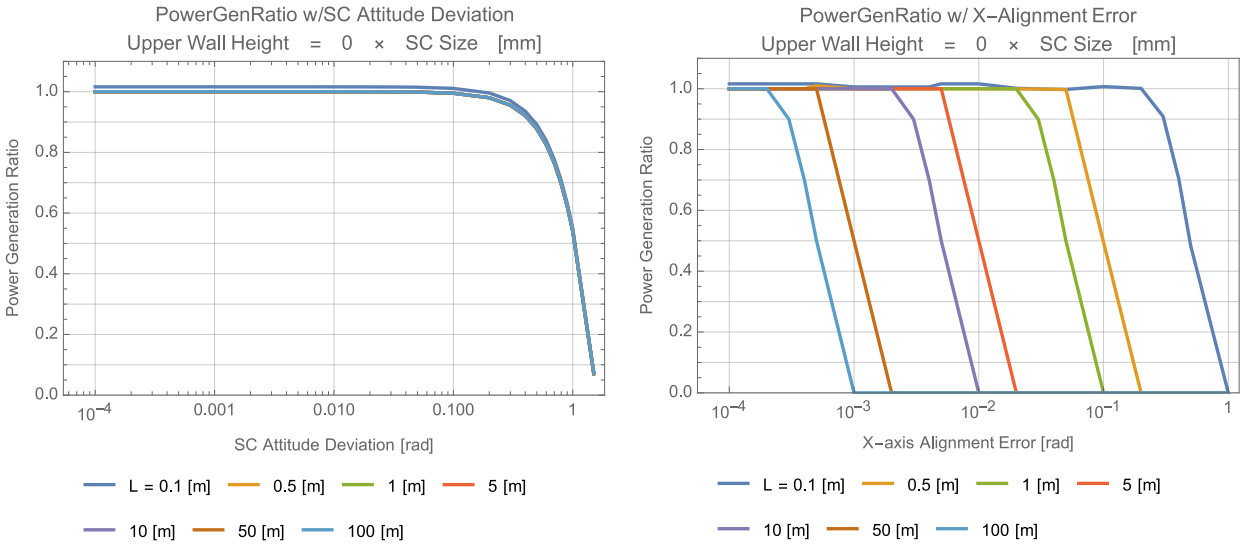
Figure 3-33 Fly Eye Module with Upper Wall Mirror and Lower Wall Mirror

Using such surrounding mirror configurations, spilled beam energy from the side of the module is reflected and beam energy is expected to be confined in the module as a result. There are some studies of solar cell device level light trapping structures to avoid beam energy loss [8,10]. These module-level beam confinement configurations avoid spilled energy from the module, thus, they relax the requirement for the X (Y) direction beam deviation. The beam energy is

efficiently transferred to the array by this configuration and trapped there. In this study, the beam confinement concept is numerically analyzed by power generation ratio and requirements are derived for beam alignment in Figure 3-32 and Figure 3-33 configurations. In the analysis, the reflectivity of the surrounding mirrors is assumed to be 100% for any reflection angle.

3.5.7. Beam Acceptance Angle and Beam Confinement Effect in Fly Eye Module with Uppwe/Lower Wall Mirror

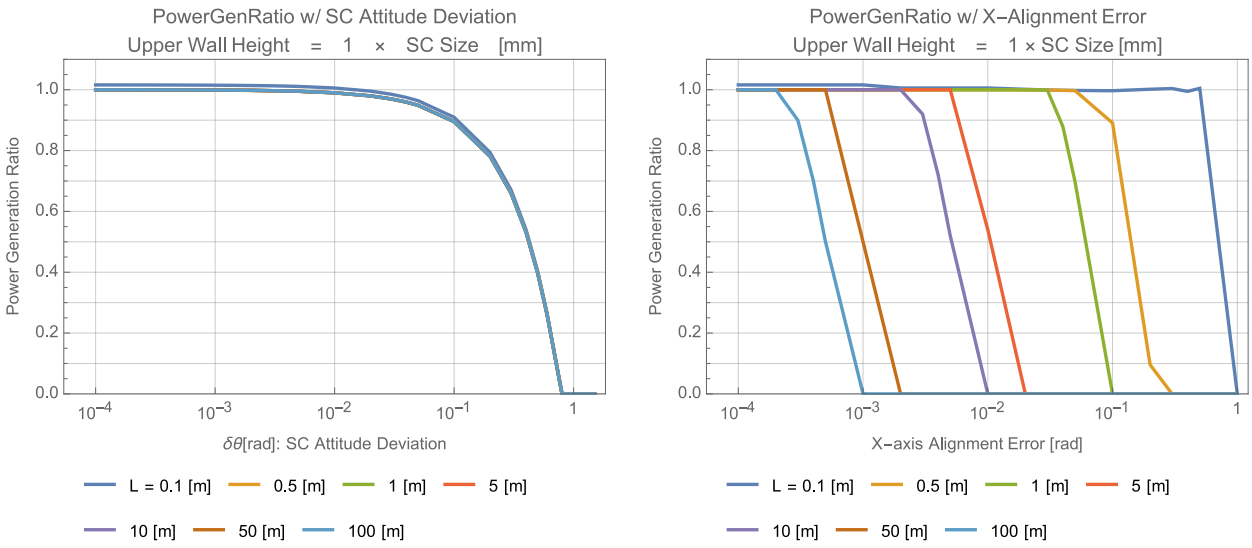
In Figure 3-32 configuration with lower wall mirror only, the power generation ratio is calculated for tilt angle relative to the beam (incident angle of the beam), and for the X (Y) deviation of the beam (Figure 3-34).



(a) (b)

Figure 3-34 Beam Energy Confinement by Lower Wall Mirror

In the configuration of Figure 3-33 with upper wall height = SC (solar cell array size). The power generation ratio is calculated for solar cell array attitude deviation and the X (Y) axis angle deviation (Figure 3-35).



(a) (b)

Figure 3-35 Beam Energy Confinement by Upper & Lower Wall Mirror (Upper Wall Height = SC)

Let H the height of the upper wall mirror, θ the X (Y) axis angle deviation limit, LS the size of the light source, and SC the size of the PV (solar cell array). When the beam is deviated in the X (Y) direction, the upper wall mirror reflects the deviated beam onto the fly-eye module. The beam deviation $\delta\theta$ is equivalent to extension of the size of the fly-eye module by $H\ tan(\theta + \delta\theta)$ as shown in Figure 3-36. While the upper wall intercepts the beam, it improves the power generation ratio.

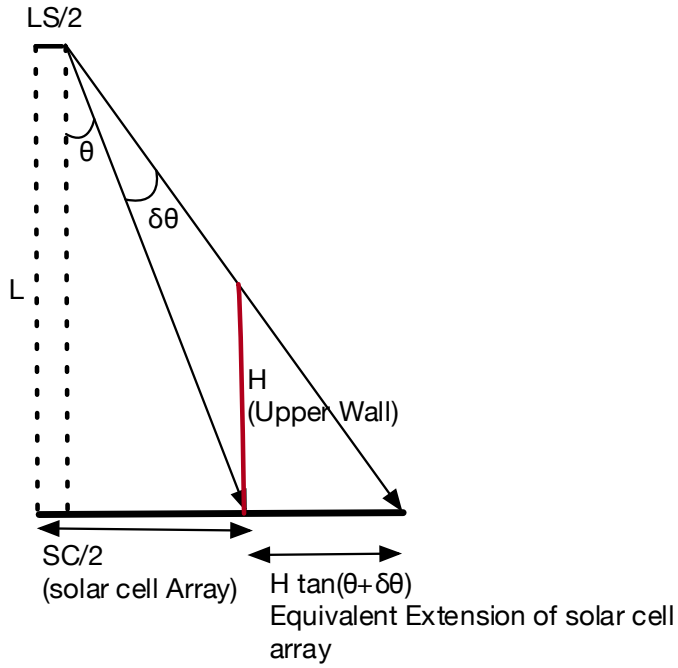


Figure 3-36 Equivalent extension of the fly eye module size

The order of θ and $\delta\theta$ is $\mathcal{O}(SC/2L)$. In the case $H = SC$ = 100 mm, L = 1000 mm, this is equivalent to extending the module size by about 10 %. The upper wall mirror's beam confinement effect becomes larger when L and SC are comparable and negligible when $L \gg SC$. This is observed in the right figures of Figure 3-34 and Figure 3-35.

Each requirement depends on L. Table. 1 shows excerpts from Figure 3-34 and Figure 3-35. Each requirement is defined at the point of power generation ratio equal to 80 %. SC means the size of the solar cell array (100 mm). These system-level requirements are relaxed from requirements without the fly eye module in 3.4.

Table 3-2 Requirement for Beam Incident Angle and Deviation in X (Y) Direction with Upper & Lower Wall Mirror Configuration

Configuration	Upper Wall Height	Requirement for Incident Angle	Requirement for X(Y) deviation
Wall-Less	0	245 mrad	340 mrad (L = 0.1m) 34 mrad (L = 1 m) 3.4 mrad (L = 10 m) 0.32 mrad (L = 100 m)
Lower-Wall Mirror	0	499 mrad	340mrad (L = 0.1m) 34 mrad (L = 1 m) 3.4 mrad (L = 10 m) 0.32 mrad (L = 100 m)
Upper and Lower-Wall Mirror	SC	180 mrad	606 mrad (L = 0.1 m) 117 mrad (L = 1 m) 4.2 mrad (L = 10 m) 0.36 mrad (L = 100 m)

When a beam enters the fly-eye lens with a larger angle than its critical angle, the projected beam image is transferred to the adjacent area. This critical angle is 245 mrad in Figure 3-20 configuration. Without the lower-wall mirror, this results in a zero power generation ratio.

- For a module with neither upper nor lower wall mirror (Wall-Less configuration), the power generation ratio changes like the lower wall mirror configuration for incident angle $\theta < \theta_c$ and becomes zero for $\theta \geq \theta_c$. This leads to the requirement of within 245 mrad incident angle. Regarding X (Y) direction beam deviation, requirements are the same as the Lower Wall Mirror configuration, since both configurations do not have an upper wall mirror.

- For a lower-wall reflective mirror (Lower-Wall Mirror configuration), the power generation ratio is maintained at high efficiency, and the incident angle of the beam critical angle is no longer restricted by θ_c. On the other hand, assuming the beam enters the solar cell array of cross-section $S\ (= SC \times SC)$ with incident angle θ, its apparent area of solar cell array become $Scos\theta$ when observed from the incident beam. The power generation will deteriorate when the beam size exceeds $Scos\theta$. This is the only restriction for beam incident angle in terms of power generation ratio in Lower-Wall Mirror configuration. Beam size control on the light source side will be effective for this.

- In the case of the Two-Wall Mirror configuration, the requirement for the incident angle is stronger than the lower-wall mirror case. This is due to vignetting of the incident beam by the upper wall in this configuration since the effective area of the solar cell array is reduced to $S(cos\theta - H/SC\ sin\theta)$. If the beam size is sufficiently large, such vignetting is compensated by an equivalent extension of the solar cell array's area by the upper-wall mirror of the opposite side like in the case of X (Y) direction (Figure 3-37). In this case, since the beam size at the solar cell is 1/2 (half) of its size, this does not occur.

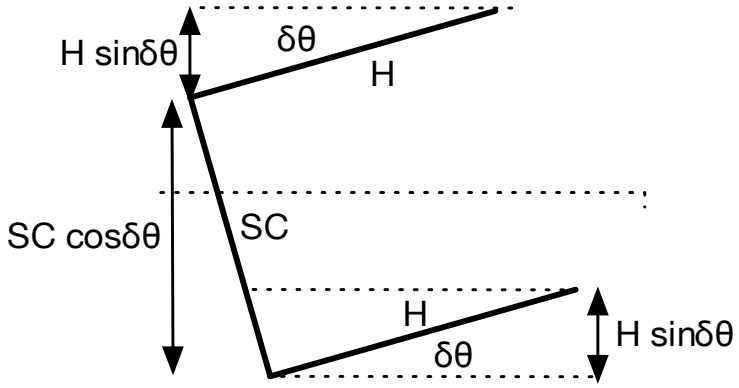


Figure 3-37 Beam tilt in two-wall mirror configuration

On the other hand, the X (Y) beam deviation requirement is more relaxed than the lower-wall mirror configuration. This is due to the beam confinement effect by the upper wall. In the case that L and SC are comparable, precise beam alignment for the tilt of the solar cell array (the fly eye module) is almost unnecessary.

3.5.8. Miniaturization of the Fly-Eye Module

The fly-eye module in Figure 3-20 with both upper and lower wall mirrors suffers increase in its size. In Figure 3-20, size of the fly eye lens is 100 mm × 100 mm, its element lens is 10 mm × 10 mm with a 20 mm focal length, and the size of the condenser lens is 100 mm × 100 mm with a 200 mm focal length. The size of the whole module is at least 100 mm × 100 mm × 200 mm. When the upper wall mirror is included, module size depends on the upper wall height. If upper wall height is the same as solar array, module size increases to 100 mm × 100 mm × 300 mm. For a module like Figure 3-20, problem would be size and focal length of each lens, and height of upper wall mirror. The size of the fly-eye module will increase or decrease in proportion to the size of the solar cell element. Even though such module like Figure 3-20 would be acceptable by some applications, miniaturization is always favorable. If miniaturized solar cell

array could be developed, miniaturization of fly eye module would be also feasible. Even though such miniature module can generate small amount of electrical current, necessary number of parallel connected such modules would both generate enough current and achieve compactification of the whole OWPT system. Development effort towards such miniaturization is proposed and expected.

Appendix 3

A.3.1. Ray transfer matrices of the optics used in this study

The optics in this study are simulated in the paraxial approximation using a ray transfer matrix (ABCD matrix). There are two such matrices for X and Y directions. Let l_x, θ_x the height of the ray and the angle that makes with the optical axis in the X direction at the exit of the optics. Similarly, l_y, θ_y are defined. The ray transfer matrices of these optics are written as follows.

$$\begin{pmatrix} l_y \\ \theta_y \end{pmatrix} = \begin{pmatrix} 1 & 0 \\ 0 & 1 \end{pmatrix}\begin{pmatrix} 1 & d_1 \\ 0 & 1 \end{pmatrix}\begin{pmatrix} 1 & 0 \\ -1/f_{cnv} & 1 \end{pmatrix}\begin{pmatrix} 1 & d_2 - d_1 \\ 0 & 1 \end{pmatrix} \times \begin{pmatrix} 1 & d_1 \\ 0 & 1 \end{pmatrix}\begin{pmatrix} 1 & 0 \\ 1/f_{ccv} & 1 \end{pmatrix}\begin{pmatrix} 1 & d_3 \\ 0 & 1 \end{pmatrix}\begin{pmatrix} l_{lc}/2 \\ \theta_{beam} \end{pmatrix} \quad (3\text{-}4)$$

$$\begin{pmatrix} l_x \\ \theta_x \end{pmatrix} = \begin{pmatrix} 1 & 0 \\ -1/f_{cnv} & 1 \end{pmatrix}\begin{pmatrix} 1 & d_1 \\ 0 & 1 \end{pmatrix}\begin{pmatrix} 1 & 0 \\ 0 & 1 \end{pmatrix}\begin{pmatrix} 1 & d_2 - d_1 \\ 0 & 1 \end{pmatrix} \times \begin{pmatrix} 1 & 0 \\ 1/f_{ccv} & 1 \end{pmatrix}\begin{pmatrix} 1 & d_1 \\ 0 & 1 \end{pmatrix}\begin{pmatrix} 1 & d_3 \\ 0 & 1 \end{pmatrix}\begin{pmatrix} l_{lc}/2 \\ \theta_{beam} \end{pmatrix} \quad (3\text{-}5)$$

where d_1 = 30 mm which is the default value. The rest are fixed parameters such as d_2 = 120 mm, d_3 = 20 mm, f_{cnv} = 150 mm, f_{ccv} = 30 mm, l_{sc} = 5 mm, θ_{beam} = 0.8 deg.

A.3.2. Beam propagation and power generation ratio calculation

The light source is at $(0\,,\ \ 0\,,\ \ H)$. The beam propagating from four apexes P_1, P_2, P_3, P_4 of the square beam are expressed by the following equations using a real parameter k. The beam is projected onto the XY plane, whose center is deviated length L from Z-axis. This projection is written in terms of a rotation matrix like $R(\phi)P_i, i = 1,2,3,4$. Since the origin of the rotation is $(0\,,\ \ 0\,,\ \ H)$ and angle of the rotation is $tan\phi = L/H$, rotation matrix $R(\phi)$ is written as,

$$R(\phi) = \begin{pmatrix} cos\phi - Hsin\phi & 0 & H - Hcos\phi - sin\phi \\ -Hsin\phi & 1 & H - Hcos\phi \\ sin\phi - Hsin\phi & 0 & H - Hcos\phi + cos\phi \end{pmatrix} \quad (3\text{-}6)$$

$$P_1 = (l_x\,,\ \ l_y\,,\ \ H) + k_1(tan\theta_x\,,\ \ tan\theta_y\,,\ \ -1) \quad (3\text{-}7)$$

$$P_2 = (l_x\,,\ \ -l_y\,,\ \ H) + k_2(tan\theta_x\,,\ \ -tan\theta_y\,,\ \ -1) \quad (3\text{-}8)$$

$$P_3 = (-l_x\,,\ \ l_y\,,\ \ H) + k_3(-tan\theta_x\,,\ \ tan\theta_y\,,\ \ -1) \quad (3\text{-}9)$$

$$P_4 = (-l_x\,,\quad -l_y\,,\quad H) + k_4(-tan\theta_x\,,\quad -tan\theta_y\,,\quad -1) \tag{3-10}$$

The value of k_i is determined by setting each Z-coordinate of each rotated beam to be zero. Inserting the determined value of k_i, the coordinates of the apexes projected on the XY-plane (C_1, C_2, C_3, C_4) are determined by (3-7)~(3-10). The area of the projected beam (S_{prj}) is determined by coordinates of C_1, C_2, C_3, C_4. Since the position coordinates of the solar cell array is known, the irradiated area of the PV (S_{irr}) can also be calculated. Thus the two factors of the power generation ratio can be calculated using (3-1) and (3-2).

The focus adjustment in X, Y direction (Δ_x, Δ_y) are introduced in ray transfer matrices as follows,

$$\begin{pmatrix} l_y \\ \theta_y \end{pmatrix} = \begin{pmatrix} 1 & 0 \\ 0 & 1 \end{pmatrix}\begin{pmatrix} 1 & d_1+\Delta_x \\ 0 & 1 \end{pmatrix}\begin{pmatrix} 1 & 0 \\ -1/f_{cnv} & 1 \end{pmatrix}\begin{pmatrix} 1 & d_2-d_1+\Delta_y \\ 0 & 1 \end{pmatrix} \times \begin{pmatrix} 1 & d_1 \\ 0 & 1 \end{pmatrix}\begin{pmatrix} 1 & 0 \\ 1/f_{ccv} & 1 \end{pmatrix}\begin{pmatrix} 1 & d_3 \\ 0 & 1 \end{pmatrix}\begin{pmatrix} l_{lc}/2 \\ \theta_{beam} \end{pmatrix} \tag{3-11}$$

$$\begin{pmatrix} l_x \\ \theta_x \end{pmatrix} = \begin{pmatrix} 1 & 0 \\ -1/f_{cnv} & 1 \end{pmatrix}\begin{pmatrix} 1 & d_1+\Delta_x \\ 0 & 1 \end{pmatrix}\begin{pmatrix} 1 & 0 \\ 0 & 1 \end{pmatrix}\begin{pmatrix} 1 & d_2-d_1+\Delta_y \\ 0 & 1 \end{pmatrix} \times \begin{pmatrix} 1 & 0 \\ 1/f_{ccv} & 1 \end{pmatrix}\begin{pmatrix} 1 & d_1 \\ 0 & 1 \end{pmatrix}\begin{pmatrix} 1 & d_3 \\ 0 & 1 \end{pmatrix}\begin{pmatrix} l_{lc}/2 \\ \theta_{beam} \end{pmatrix} \tag{3-12}$$

These matrices including Δ_x, Δ_y are used for calculation and optimization of power generation ratio. Setting $l_x = (size\ of\ solar\ array)/2$ gives the optimum value of Δ_x which depends on L. Similarly setting $l_y = (size\ of\ solar\ array)/2$ gives the optimum value of Δ_y.

A.3.3. Power generation ratio calculation including perturbations

A.3.3.1.Focus perturbation

Assume $\Delta_{x\,opt}$ and $\Delta_{y\,opt}$ give optimum of power generation ratio in X, Y direction focus. Additional focus perturbation Δ'_x, Δ'_y are introduced to estimate requirement for focus adjustment with replacements $\Delta_x \rightarrow \Delta_{x\,opt} + \Delta'_x$ and $\Delta_y \rightarrow +\Delta_{y\,opt} + \Delta'_y$.

$$\begin{pmatrix} l_y \\ \theta_y \end{pmatrix} \tag{3-13}$$
$$= \begin{pmatrix} 1 & 0 \\ 0 & 1 \end{pmatrix}\begin{pmatrix} 1 & d_1+\Delta_{x\,opt}+\Delta'_x \\ 0 & 1 \end{pmatrix}\begin{pmatrix} 1 & 0 \\ -1/f_{cnv} & 1 \end{pmatrix}$$
$$\times \begin{pmatrix} 1 & d_2-d_1+\Delta_{y\,opt}+\Delta'_y \\ 0 & 1 \end{pmatrix}\begin{pmatrix} 1 & d_1 \\ 0 & 1 \end{pmatrix}\begin{pmatrix} 1 & 0 \\ 1/f_{ccv} & 1 \end{pmatrix}\begin{pmatrix} 1 & d_3 \\ 0 & 1 \end{pmatrix}\begin{pmatrix} l_{lc}/2 \\ \theta_{beam} \end{pmatrix}$$

$$\begin{pmatrix} l_x \\ \theta_x \end{pmatrix} \quad \text{(3-14)}$$
$$= \begin{pmatrix} 1 & 0 \\ -1/f_{cnv} & 1 \end{pmatrix} \begin{pmatrix} 1 & d_1 + \Delta_{x\,opt} + \Delta'_x \\ 0 & 1 \end{pmatrix} \begin{pmatrix} 1 & 0 \\ 0 & 1 \end{pmatrix}$$
$$\times \begin{pmatrix} 1 & d_2 - d_1 + \Delta_{y\,opt} + \Delta'_y \\ 0 & 1 \end{pmatrix} \begin{pmatrix} 1 & 0 \\ 1/f_{ccv} & 1 \end{pmatrix} \begin{pmatrix} 1 & d_1 \\ 0 & 1 \end{pmatrix} \begin{pmatrix} 1 & d_3 \\ 0 & 1 \end{pmatrix} \begin{pmatrix} l_{lc}/2 \\ \theta_{beam} \end{pmatrix}$$

These matrices including perturbations Δ'_x, Δ'_y are used in calculation for power generation ratio.

A.3.3.2.Rotational perturbations

To include perturbation $(\delta\psi,\ \delta\phi,\ \delta\omega)$ in rotation angle for X, Y, Z axis respectively, the rotation matrix is extended as follows.

$$R(\phi, \delta\psi, \delta\phi, \delta\omega) \quad \text{(3-15)}$$
$$= \begin{pmatrix} \cos(\phi+\delta\phi) - Hsin(\phi+\delta\phi) & 0 & H - Hcos(\phi+\delta\phi) - \sin(\phi+\delta\phi) \\ -Hsin(\phi+\delta\phi) & 1 & H - Hcos(\phi+\delta\phi) \\ \sin(\phi+\delta\phi) - Hsin(\phi+\delta\phi) & 0 & H - Hcos(\phi+\delta\phi) + \cos(\phi+\delta\phi) \end{pmatrix}$$
$$\times \begin{pmatrix} cos\delta\omega & sin\delta\omega & 0 \\ -sin\delta\omega & cos\delta\omega & 0 \\ 0 & 0 & 1 \end{pmatrix} \begin{pmatrix} 1 & -Hsin\delta\psi & H - Hcos\delta\psi \\ 0 & cos\delta\psi - Hsin\delta\psi & H - Hcos\delta\psi - sin\delta\psi \\ 0 & sin\delta\psi - Hsin\delta\psi & H - Hcos\delta\psi + cos\delta\psi \end{pmatrix}$$

1. X-direction deviation error is caused by alignment error around the Y-axis. To calculate the power generation ratio, $\delta\omega$ and $\delta\psi$ are set to be zero.
2. Y-direction deviation error is caused by alignment error around the X-axis. To calculate the power generation ratio, $\delta\omega$ and $\delta\phi$ are set to be zero.
3. To calculate the power generation ratio with the Z-axis rotational alignment error, $\delta\psi$ and $\delta\phi$ are set to be zero.

References 3

1. Tang, J.; Matsunaga, K.; Miyamoto, T. Numerical Analysis of Power Generation Characteristics in Beam Irradiation Control of Indoor OWPT System. *Opt Rev* **2020**, *27*, 170–176, doi:10.1007/s10043-020-00590-z.
2. Feng, H.; Hui, H.; Hui, D.; Yang, T.; Zhang, X. Beam Collimation Scheme of Laser Wireless Power Supply System for High Potential Monitoring Node of Power Transmission and Transformation. *J. Phys.: Conf. Ser.* **2021**, *1885*, 042031, doi:10.1088/1742-6596/1885/4/042031.
3. Bennett, H.E. DOD and Navy Applications for Laser Power Beaming.; Bennett, H.E., Doolittle, R.D., Eds.; San Jose, CA, April 26 1995; pp. 21–30.
4. Moriyama, K.; Asaba, K.; Miyamoto, T. Beam Shaping by Cylindrical Lens Systems in OWPT. In Proceedings of the IEICE Society Conference 2023 C-3/4-11; 7-10 March, Nagoya, Japan.
5. Moriyama, K.; Asaba, K.; Miyamoto, T. Beam Shape Control System Based on Lens System Numerical Modeling for OWPT. The 70th JSAP Spring Meeting 2023 22a-12A-9; 22-25 March 2024 Tokyo, Japan
6. Asaba, K.; Miyamoto, T. System Level Requirement Analysis of Beam Alignment and Shaping for Optical Wireless Power Transmission System by Semi–Empirical Simulation. *Photonics* **2022**, *9*, 452.
7. Katsuta, Y.; Miyamoto, T. Design, Simulation and Characterization of Fly-Eye Lens System for Optical Wireless Power Transmission. *Jpn. J. Appl. Phys.* **2019**, *58*, SJJE02, doi:10.7567/1347-4065/ab238b.
8. Takeda, Y.; Iizuka, H.; Mizuno, S.; Hasegawa, K.; Ichikawa, T.; Ito, H.; Kajino, T.; Ichiki, A.; Motohiro, T. Silicon Photovoltaic Cells Coupled with Solar-Pumped Fiber Lasers Emitting at 1064 Nm. *Journal of Applied Physics* **2014**, *116*, 014501, doi:10.1063/1.4885758.
9. Wagner, L.; Bett, A.W.; Helmers, H. On the Alignment Tolerance of Photovoltaic Laser Power Converters | Elsevier Enhanced Reader. *Optik* **2017**, *131*, 5, doi:10.1016/j.ijleo.2016.11.072.
10. Alsaigh, R.E.; Bauer, R.; Lavery, M.P.J. Multi-Element Lenslet Array for Efficient Solar Collection at Extreme Angles of Incidence. *Sci Rep* **2020**, *10*, 8741, doi:10.1038/s41598-020-65437-8.

4. Detection of Photovoltaics by Differential Absorption Imaging

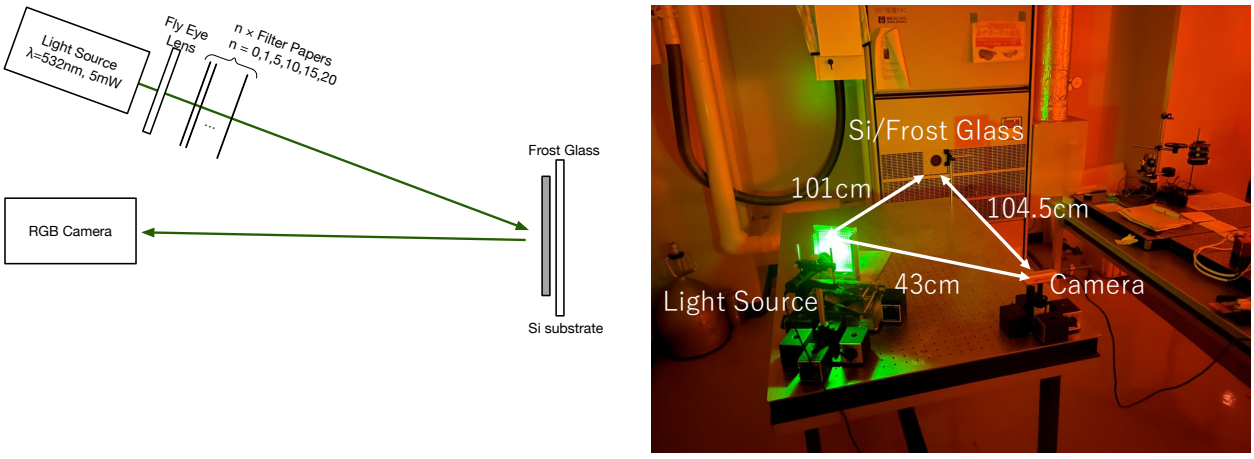
4.1. The Proof-of-Concept Experiments using $\lambda = 532$ nm and Si substrate

4.1.1. The Design of the Experiments

Proof-of-concept experiments were conducted for the PV detection by differential absorption imaging. Figure 4-1 shows the experiment configuration. A Si substrate (two-inch diameter) was utilized to simulate a PV. Its front surface is polished, and its rear surface is diffuse (etched). For experiments, two kinds of samples were prepared, the Si substrate attached to a 10 cm × 10 cm frost glass plate (Si target), and a frost glass of the same size without the Si substrate (frost glass target). The frost glass simulates a reflection from the rear surface of the PV and the background. In this experiment, λ = 532 nm, absorbable by Si, was used. Instead of switching two wavelengths of λ_{ON} and λ_{OFF}, two images were alternately captured by changing the two samples. For λ =532 nm, the Si target behaves like PV illuminated by λ_{ON}, and the frost glass target does like PV by λ_{OFF}. This configuration is equivalent to a two-wavelength one. This makes the experiment easier to execute than handling two invisible wavelengths of infrared, and an ordinary visible light camera can be used. A differential image is generated from the data of these samples.

The image-capturing camera was a small, off-the-shelf product without any zooming capability. With these simple experiment configurations, the essence of concept validation was focused on. With such a simple but equivalent experiment configuration, performance assessment results were obtained, the performance improvement was predicted to be verified in the future experiments, and issues were identified.

In the actual operation of OWPT, illumination by two beams of λ_{ON}, λ_{OFF} is necessary for target detection. Since the two wavelengths are close enough to each other, the optics of the main power transmission beam of OWPT are commonly usable for λ_{ON}, λ_{OFF} beams.



(a) (b)

Figure 4-1 Configurations of experiments: (a) Experiment apparatus; (b) Setup of experiments.

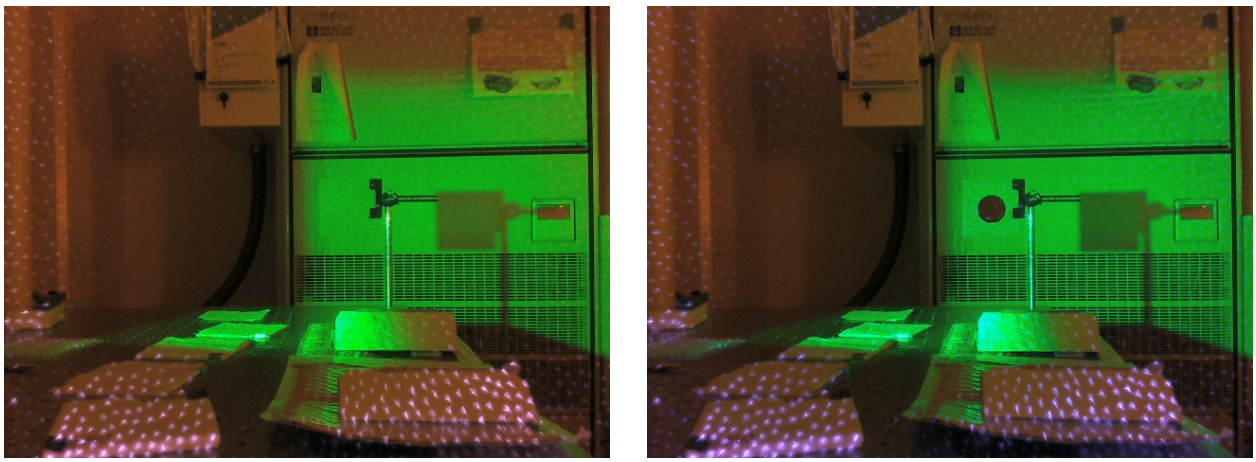
The light source was λ = 532 nm and CW 5 mW, with a Gaussian beam pattern. The distance between the RGB camera and Si/frost glass target was 104.5 cm. The beam diameter was 7.4 cm when it irradiated the target directly. To irradiate the target uniformly over the FOV of the camera, the fly-eye lens was set in front of the light source during data acquisition. To change the intensity on the Si/frost glass target, white filter papers were placed in front of the light source, and the number of filter papers was changed. Intensity reduction on the Si/frost glass target is equivalent to scattered light around the surrounding environment. Such background intensity is subtracted in the data processing. Regarding the image capturing camera, 640 × 480 pixel (px), RGB images were captured by Intel's Realsense D435™ [4]. Even though this camera supports the depth information output, these experiments did not use it.

4.1.1.1. The Captured Raw Data in the Experiments

The γ parameter of the D435, which indicates the intensity response characteristics of the camera, was externally set by its internal parameter GAMMA, and its value was 450. For parameter setting and control software for the camera, Realsense™ SDK [5], Open CV™ [6] and Python™ [7] were employed. The correspondence between γ and GAMMA is investigated in a later section. Every time of data acquisition, the exposure time of the camera (39, 78, 156, 412, 625, 1250, 2500, 5000, 10,000 μs) was set and reconfirmed by the PC. Other internal parameters of the D435 were not changed from their default values. To control the intensity on the Si/frost glass target, the number of sheets of filter paper was changed between 0, 1, 5, 10, 15, and 20 (P0, P1, P5, P10, P15, P20). 100 images were consecutively taken for both the Si target and for the frost glass target, with every combination of the parameter set of exposure time and the filter papers.

The frost glass intensity of the diffuse reflection was also measured with and without the fly-eye lens to evaluate the intensity reduction by the fly-eye lens. Similar data were obtained while varying the number of sheets of the filter paper.

An example of raw data acquired in the experiments is shown in Figure 4-2. Figure 4-2 (a) is the frost glass target data captured with $\lambda = 532$ nm light source illumination. Figure 4-2 (b) is the image with the Si target. A black circular object centered in Figure 4-2 (b) is the Si substrate, and the white diffusing rectangular image surrounding the Si substrate is the frost glass. The frost glass also can be observed in Figure 4-2 (a).



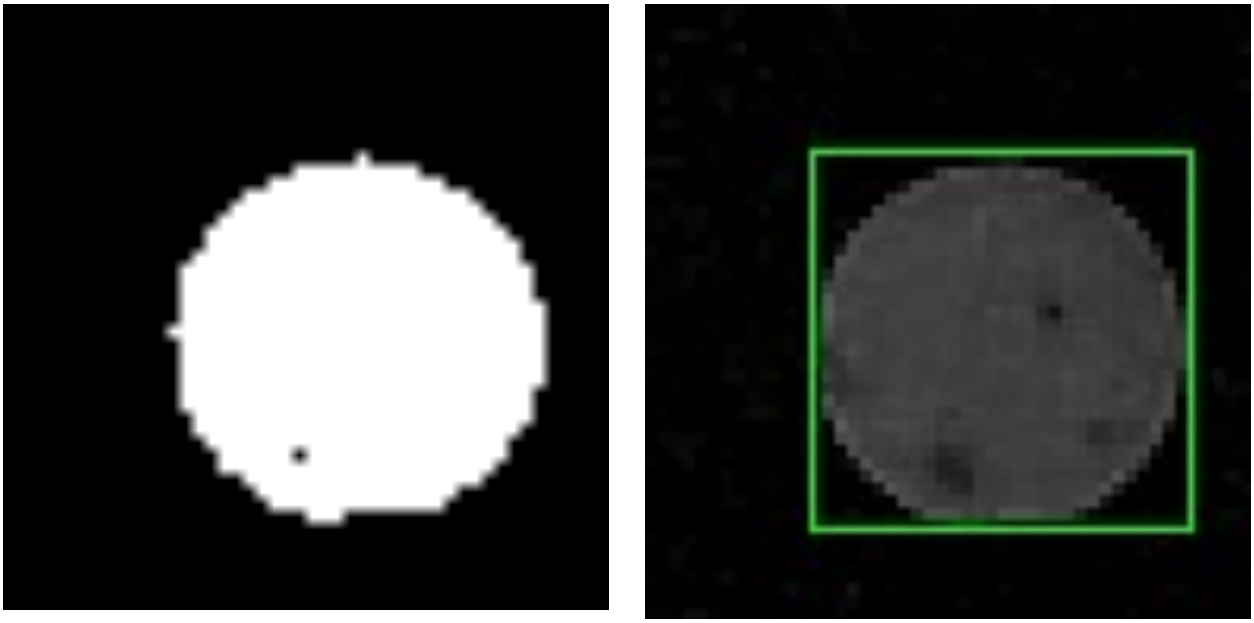
(a) (b)

Figure 4-2 Examples of acquired raw data (P0, Acc = 1, Exp: 10,000 µs, image size 640 × 480 px). (a) Raw data with frost glass sample; (b) Raw data with Si sample.

4.1.1.2. The Data Processing and Software Tools

Acquired image data were processed after trimming. The following several trimming sizes were investigated in this study: 48 × 49, 72 × 71, 95 × 95, 143 × 143, 237 × 237, 331 × 331, 384 × 448, 384 × 480 and 640 × 480 px. The default size used for image processing in this study was 48 × 49 px, except in investigation regarding trimming size effect.

Differential image was generated and binarized with the trimmed images, then, the Si image was extracted. The position of the Si image was determined in pixel coordinates. Figure 4-3(a) is a binarized image including Si, and Figure 4-3(b) is a boundary rectangle of the extracted Si image superimposed on the original differential image before binarization. The data analysis process is described in a later section.

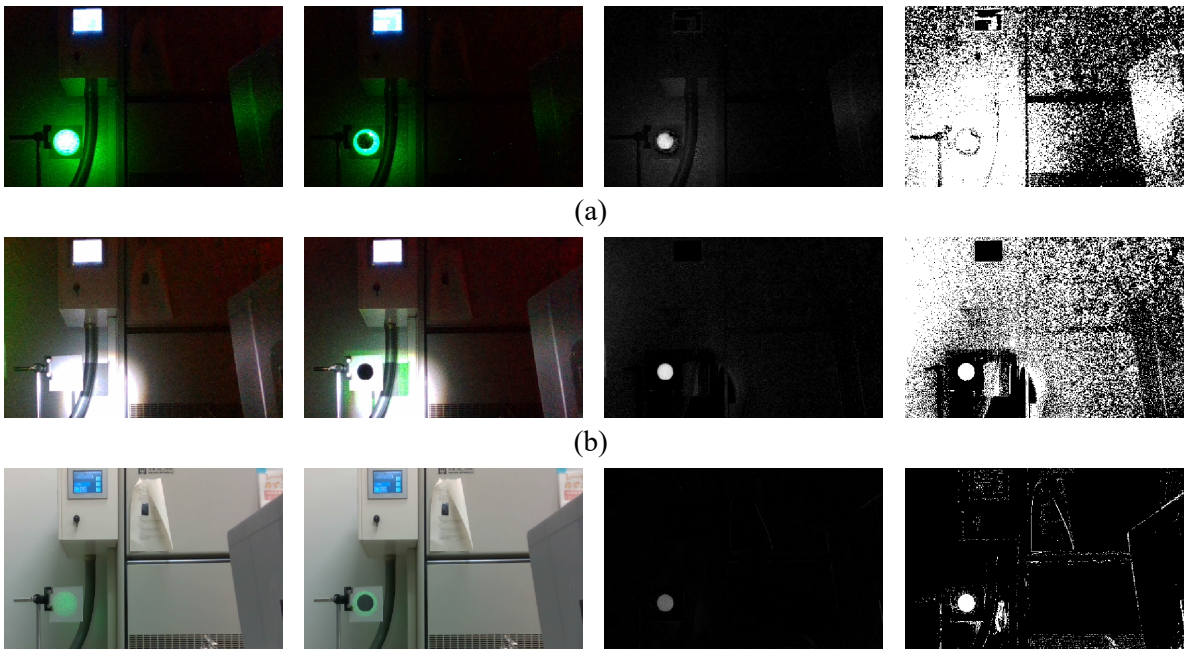


(a) (b)

Figure 4-3 Generation of the Si image by binarization (P0, Acc = 1, Exp: 10,000 μs, image size 48 × 49 px). (a) Binarized image of differential absorption image; (b) Boundary rectangle of the extracted Si image superimposed on the original differential image.

4.1.2. Robustness of the Method

To evaluate the method's robustness, target detection by differential absorption images was assessed in an environment without illumination, with strong target illumination and room light (Figure 4-4). Figure 4-4(a) shows, from left to right, the frost glass image under no illumination (λ_{OFF} image), the image of the Si substrate (λ_{ON} image), the differential image and the binarized image. Note that the filter paper is excluded (P0). The images in (b) and (c) were taken under conditions where the target was illuminated by white LED lights, and under conditions where the room light was switched on. Even though the exposure time was set to automatic, it was estimated to be 78 µs. In the frost glass image in (a), the $\lambda = 532$ nm beam penetrated the frost glass and illuminated the background. This made the image brighter overall than the Si substrate image and the background is not completely cancelled in the differential image. In (b) and (c), the image of the Si substrate was bright enough to extract the image of the Si substrate.



(a)

(b)

(c)

Figure 4-4 Target detection in various illumination environments (exposure time: automatic). From left to right, the frost glass image under no illumination (λ_{OFF} image), the image of the Si substrate (λ_{ON} image), the differential image and the binarised image; (a) Dark Room Environment, (b) LED illumination, (c) Room Light

Even though Si image could be detected in every environment above, it is inferred that making the λ_{ON} image brighter than the λ_{OFF} image has a positive influence on target detection. For this reason,

in Figure 4-5 the P0 λ_{ON} image was replaced by the P1 λ_{OFF} image, while the same P0 λ_{OFF} image was kept.

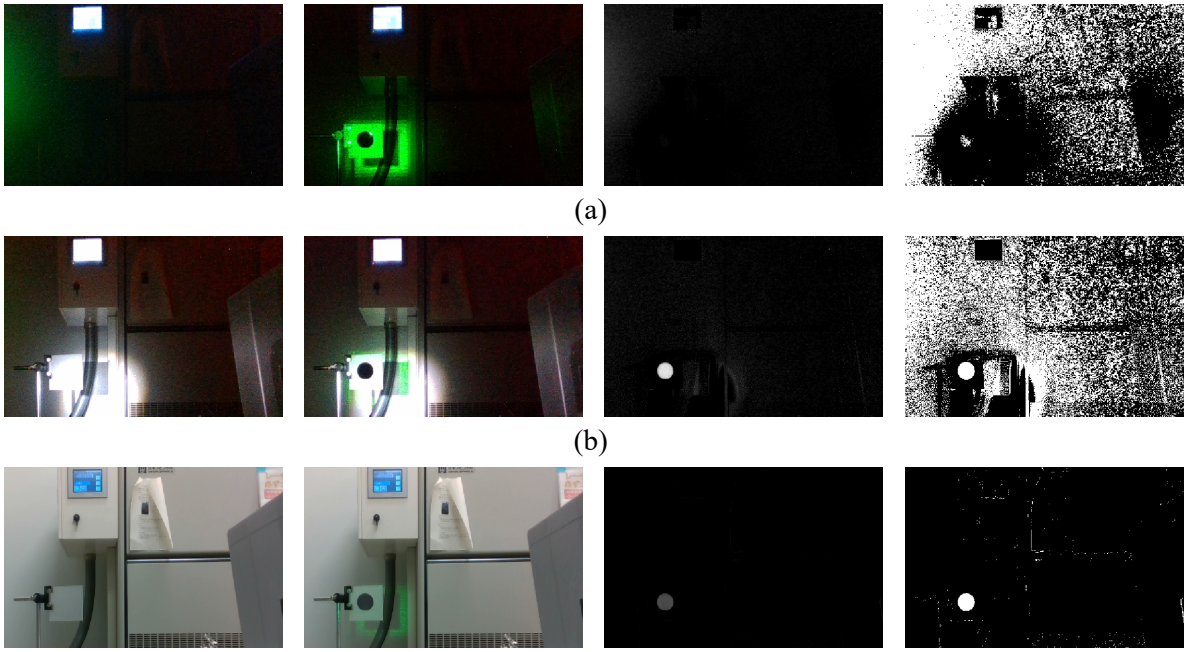


Figure 4-5 Target detection in various illumination environments P0 λ_{ON} image combined with P1 λ_{OFF} image (exposure time: automatic) From left to right, the frost glass image under no illumination (λ_{OFF} image), the image of the Si substrate (λ_{ON} image), the differential image and the binarised image; (a) Dark Room Environment, (b) LED illumination, (c) Room Light

The Si image is detected against the background in bright regions, while random noise dominates in dark regions. The following issues were obtained as lessons-learned from the evaluation of this naive differential absorption images.

1. The λ_{ON} image should have a higher image luminance than the image over the entire image except for the PV region

2. Random noise in regions of low luminance should be reduced

Random noise can be reduced by trimming the image according to the target size, so the discussion will proceed with trimming for the time being. The complete solution to these issues will be provided in 4.3.2 and 4.3.3.

4.1.3. Calibration of the Experiment System

First, as calibration of the experiment system, setting the D435 internal parameter GAMMA = 450, then, the corresponding γ value was estimated in 4.1.3.1.1. Since the estimated γ value was close to 1, γ parameter correction is not applied in the following data analysis. Next, the intensity reduction factor on Si/frost glass targets was estimated. The fly-eye lens and the filter papers set in front of the camera reduce the intensity of λ=532 nm on the Si/frost glass targets. Intensity reduction on the samples is represented by intensity reduction factor T, defined as below:

$$T = E_{w/FE,P}/E_{w/o\ FE,P} = T_{FE} \times T_p(n) \quad (4\text{-}1)$$

$E_{w/FE,P}$ represents intensity on the Si/frost glass targets through both the fly-eye lens and the filter papers. To make it background-free, if there is non-negligible background intensity, such background was subtracted. $E_{w/o\ FE,P}$ represents intensity with neither the fly-eye lens nor the filter papers. This should also be background-free. Since the fly-eye lens and the filter papers contribute independently to intensity reduction, T is factorized as $T_{FE} \times T_p(n)$. T_{FE} represents the contribution from the fly-eye, and $T_p(n)$ represents the contribution from the filter papers, which depends on the number of papers n. Details of estimations are summarized in 4.1.3.1.2.

Estimation of $T_p(n)$ shows $T_p(n) = (0.13)^n$ and $T_{FE} = 0.06 \pm 0.03$. These parameters are used in a later section. From the estimation of $T_p(n)$ and T_{FE}, intensity on the Si/frost glass targets for the number of filter papers is calculated in Figure 4-6. In the calculation, the light source power is 5 mW, and the beam diameter on the Si/frost glass is 7.4 cm when any filters and the fly-eye lens were not introduced.

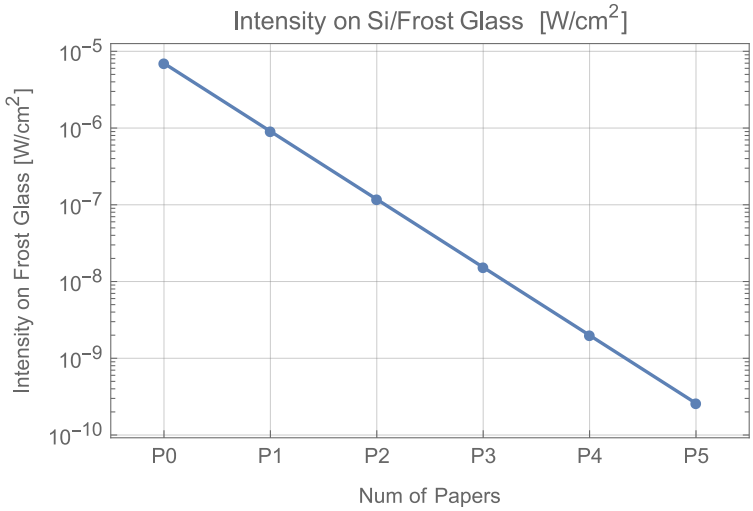


Figure 4-6 Intensity on Si/frost glass.

4.1.3.1.1. Estimation of the γ Parameter

Light source beam power is 5 mW (CW) and the accumulated intensity is proportional to exposure time. Since the γ parameter of the camera was not disclosed, the γ parameter was estimated from the proportional relationship between exposure time and intensity recorded on pixels in image data. Figure 4-7 shows the exposure time dependence of the grayscale level of a frost glass target illuminated by the light source with the number of filter papers as a parameter.

Each data point is the grayscale level of a pixel, which is the average of 100 images of mean intensity of a 48 × 49−pixel image. Figure 4-7 plot is a log scale for both the vertical and horizontal axis, and the slope of each plot represents the γ parameter. Slopes are unstable for a small grayscale level, and the saturation effect is visible for a large level, especially in the P0 plot.

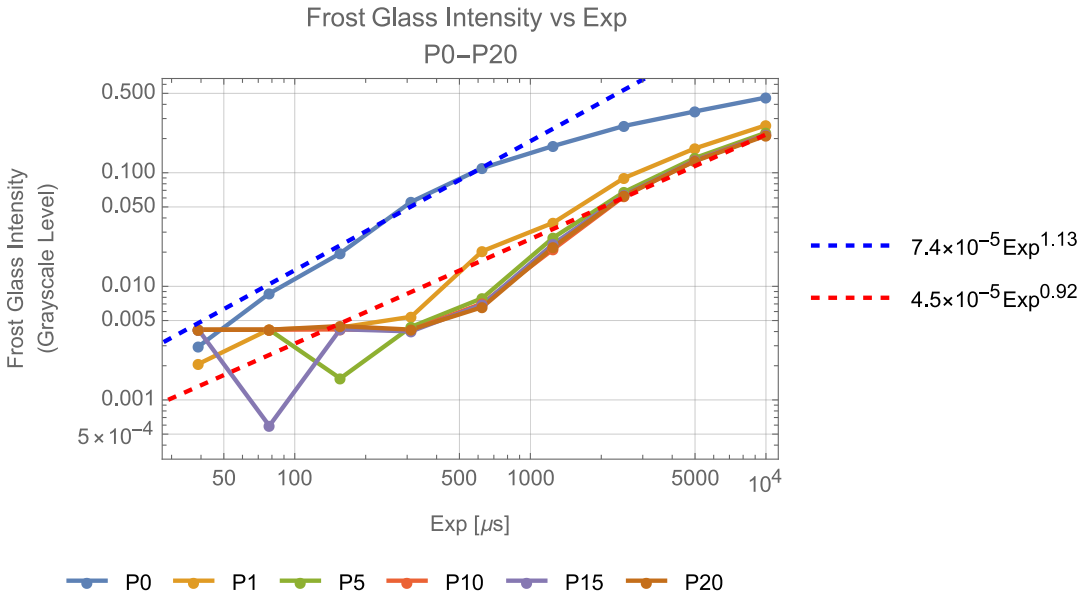


Figure 4-7 Grayscale level dependence on exposure time.

Even though the grayscale level differs nearly 10 times between P0 and P1, P5, P10, P15, and P20, by looking at the power of Exp, each estimation of the γ parameter using data from each plot's linear region is close to one. Therefore, γ parameter correction is not applied in the following data analysis.

4.1.3.1.2. Estimation of the intensity reduction factor

The fly-eye lens and the filter papers in front of the camera reduce the intensity of $\lambda = 532$ nm on the Si/frost glass targets. Intensity reduction on the samples is represented by intensity reduction factor T, defined as in (4-1) $T = T_{FE} \times T_p(n)$.

- Estimation of $T_p(n)$

Setting the fly-eye lens and changing the number of filter papers, the mean intensity of each acquired image is measured as grayscale intensity for exposure time (Exp) as a parameter (Figure 4-8).

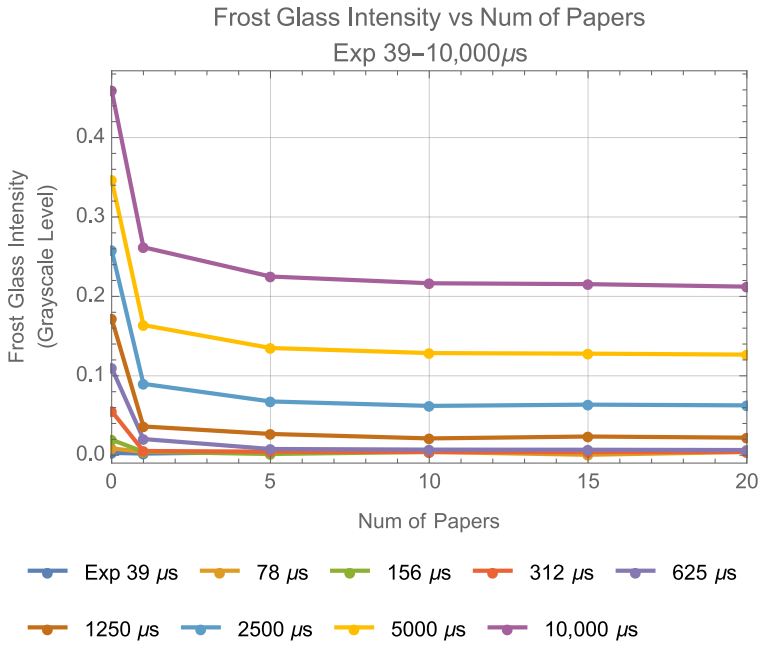


Figure 4-8 Frost glass intensity.

As the number of the filter papers increases, each grayscale level approaches a constant value. From Figure 4-8, this value is confirmed to be monotonically increasing with exposure time, and this is regarded as the background. Let n the number of filter papers and $E(n)$ be intensity. $E(n)$ can be expressed using attenuation factor $T_p(n)$ and by the flowing equation:

$$E(n) = [E(0) - E(\infty)]T_p(n) + E(\infty) \tag{4-2}$$

Since each intensity value at the number of papers = 20 looks stably constant for each exposure time, these data are regarded as constant offsets and set as follows:

$$E(\infty) = E(20) \tag{4-3}$$

Then, (4-2) is modified as:

$$T_p(n) = [E(n) - E(20)]/[E(0) - E(20)] \tag{4-4}$$

$T_p(n)$ is plotted for each exposure time in Figure 4-9.

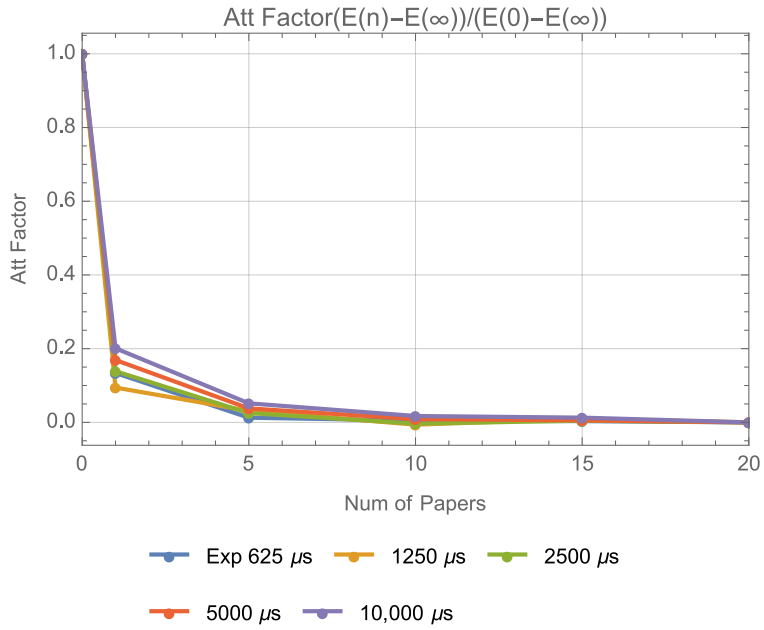


Figure 4-9 Attenuation factor $T_p(n)$.

Figure 4-9 is fitted by $T_p(n) = e^{-\beta n}$ with a constant parameter β. Let $T_p \equiv e^{-\beta}$, and $T_p(n) = T_p^n$. Figure 4-10 Estimation of $\mathbf{T_p}$. shows an estimation of T_p; it appears constant for exposure time, and its value is $T_p = 0.13 \pm 0.04$.

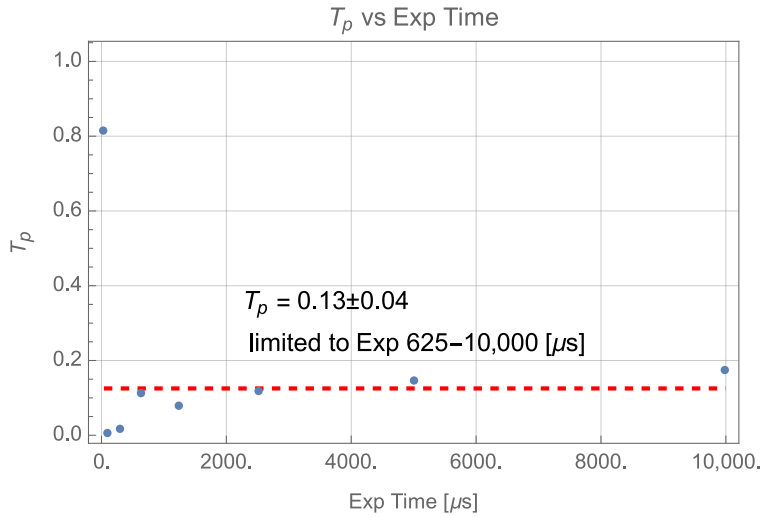


Figure 4-10 Estimation of T_p.

Therefore, $T_p(n)$ becomes $T_p(n) = (0.13)^n$.

- Estimation of T_{FE}

T_{FE} is expressed by the following equation:

$$T_{FE} = [E_{w/FE} - E_{Bg}]/[E_{w/oFE} - E_{Bg}] \quad (4\text{-}5)$$

$E_{w/FE} - E_{Bg}$ represents the background free intensity on an Si/frost glass target with the fly eye lens and filter papers. $E_{w/o\ FE} - E_{Bg}$ represents the background free intensity on an Si/frost glass target with neither the fly eye lens nor the filter papers. E_{Bg} is the 100 image average of mean intensity of a 48 × 49 pixel image with the light source OFF. Figure 4-11 shows the $E_{w/FE}/E_{Bg}$ and $E_{w/o\ FE}/E_{Bg}$ plot for exposure time.

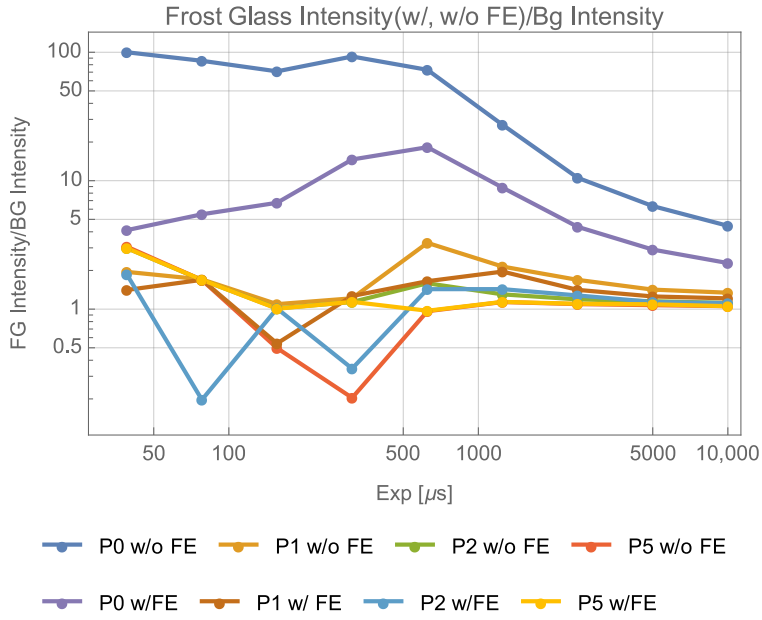


Figure 4-11 Frost glass intensity/background intensity.

Looking into exposure time greater than or equal to 625 μs, whose intensity data are stable in Figure 4-7, Figure 4-11 shows that the intensity ratio between frost glass and background approaches constant value 1 due to saturation regardless of w/ or w/o the fly-eye lens. Since usable data are limited whose frost glass intensity to background is larger, only P0 and P0 w/FE data are used to estimate T_{FE}. In Figure 4-11, P0 data look affected by saturation for exposure time ≥ 312 μs. To avoid this saturation, T_{FE} is estimated by limiting data for exposure time $= 39, 78, 156$ μs. The result is shown in Figure 4-12, and the estimation is $T_{FE} = 0.06 \pm 0.03$.

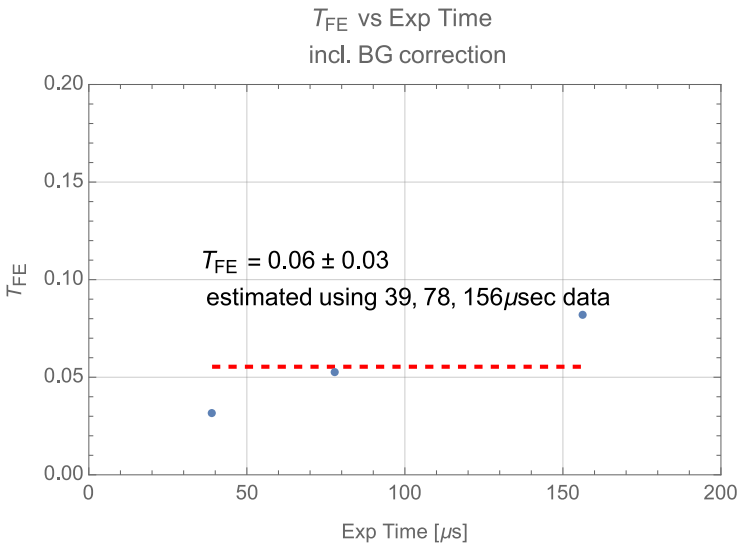


Figure 4-12 Estimated T_{FE}.

4.1.4. The Data Processing of Captured Image

The 640 × 480 px size images, taken from Si/ frost glass targets with λ =532 nm light source illumination, are trimmed down to images of 9 trimming sizes. To extract Si images, data processing generates differential and binarized images. Regarding the binarization scheme, the Otsu algorithm [8], implemented in Mathematica [9], is exploited, in which the binarization threshold separates pixels into two classes and is determined by minimizing the intensity variance of the two classes. The generation of differential images and their binarizations is conducted in the following way:

1. First, 100 raw 640 × 480 px image data of the frost glass target (λ_{OFF} image: $\mathrm{Img}_{OFF}(\mathrm{Exp}, \mathrm{P}, \mathrm{i})_{raw}$) and 100 same-size images of the Si target (λ_{ON} image: $\mathrm{Img}_{ON}(\mathrm{Exp}, \mathrm{P}, \mathrm{i})_{raw}$) are taken for each combination of parameter set (Exp = 39, 78, …, 10,000 μsec and P = 0, 1, … 20, i = 1,2, …, 100).

2. These images are trimmed down to each image size (48 × 49, 72 × 71, 95 × 95, 143 × 143, 237 × 237, 331 × 331, 384 × 448, 384 × 480, 640 × 480 px) and grayscaled.

3. For each λ_{ON}, λ_{OFF} image data point, P20 data is regarded as background data and subtracted from $\mathrm{Img}_{ON}(\mathrm{Exp}, \mathrm{P}, \mathrm{i})_{raw,gray}$ and $\mathrm{Img}_{OFF}(\mathrm{Exp}, \mathrm{P}, \mathrm{i})_{raw,gray}$. Then, background-free 100 λ_{ON} and 100 λ_{OFF} grayscale images are obtained, respectively.

$$\mathrm{Img}_{OFF}(\mathrm{Exp}, \mathrm{P}, \mathrm{i}) = \mathrm{Img}_{OFF}(\mathrm{Exp}, \mathrm{P}, \mathrm{i})_{raw,gray} - \mathrm{Img}_{OFF}(\mathrm{Exp}, 20, \mathrm{i})_{raw,gray} \quad (4\text{-}6)$$

$$\mathrm{Img_{ON}}(\mathrm{Exp,P,i}) = \mathrm{Img_{ON}}(\mathrm{Exp,P,i})_{\mathrm{raw,gray}} - \mathrm{Img_{ON}}(\mathrm{Exp,20,i})_{\mathrm{raw,gray}} \quad (4\text{-}7)$$

4. 100 differential images are generated for each combination of the parameter set of exposure time and the number of filter papers by subtracting the grayscale level of the λ_{ON} image from the λ_{OFF} image.

$$\mathrm{Img_{Diff}}(\mathrm{Exp,P,i}) = \mathrm{Img_{OFF}}(\mathrm{Exp,P,i}) - \mathrm{Img_{ON}}(\mathrm{Exp,P,i}) \quad (4\text{-}8)$$

5. Differential images are accumulated n times n=1, 2, … ,100.

$$\mathrm{Img_{Acc}}(\mathrm{Exp,P,n}) = \sum_{\mathrm{i=1}}^{\mathrm{n}} \mathrm{Img_{Diff}}(\mathrm{Exp,P,i}) \quad (4\text{-}9)$$

6. The differential images are binarized by the Otsu algorithm.

$$\mathrm{Img_{Bin}}(\mathrm{Exp,P,n}) = \mathrm{Binarize}[\mathrm{Img_{Acc}}(\mathrm{Exp,P,n})] \quad (4\text{-}10)$$

As an example of 5 and 6 above, differential images and binarized images of trimming size 48 × 49 px and exposure time 10,000 μs are attached in Figure 4-13.

Differential images and binarized images as in Figure 4-41 vary with the number of filter papers and the number of accumulations. They also vary with exposure time (39, 78, 156, 412, 625, 1250, 2500, 5000, 10,000 μs) and trimming size (48 × 49, 72 × 71, 95 × 95, 143 × 143, 237 × 237, 331 × 331, 384 × 448, 384 × 480, 640 × 480 px). Both differential images and binarized images are generated for all combinations of these parameter sets, and Si images are extracted from each binarized image. By the following procedures, the center coordinates, the area, and the SNR are calculated from the extracted Si images:

7. From the binarized image by (4-9), the connected component of the maximum area size is extracted and is regarded as the Si image.

8. The center coordinates are calculated as the center of the boundary rectangle of the extracted Si image.

9. The area is calculated as the area of the extracted Si image.

The Si portion is extracted from the λ_{OFF} image by multiplication of the binarized Si image. Then, signal intensity is calculated as the mean intensity of the extracted Si portion of the λ_{OFF} image. Noise

intensity is calculated as the P20 mean intensity of the frost glass target without the light source. SNR is calculated as the ratio of signal intensity to the noise intensity.

$$\mathrm{SNR}(\mathrm{Exp},\mathrm{P},\mathrm{n}) \equiv \frac{\text{mean intensity of } [\mathrm{Img}_{\mathrm{OFF}}(\mathrm{Exp},\mathrm{P},\mathrm{n})_{\mathrm{raw}} \times \mathrm{Img}_{\mathrm{Bin}}(\mathrm{Exp},\mathrm{P},\mathrm{n})]}{\text{mean intensity of } [\mathrm{Img}_{\mathrm{OFF}}(\mathrm{Exp},20,\mathrm{n})_{\mathrm{raw}}]} \quad (4\text{-}11)$$

To assess the performances of the image sensor, the center coordinates and the area size of the Si image were compared with true values measured from differential images before binarization. When estimating the true values, images with high SNR were used, such as P0 and Exp = 10,000 μs. The measured true area size is the same for all combinations of parameter sets, and the true center coordinates depends on the trimming size. In the case of a 48 × 49 px trimming size, the true center coordinates of the Si image that directly read out from the differential image are (X: 27.68, Y: 21.67), and the true value of the area is 706.85 px (circle image of 15 px radius).

The estimation error of the X, and Y center coordinates and the area size is plotted against exposure time for a 48 × 49 px trimming size. Figures are attached in Figure 4-14 and Figure 4-15. Similar plots were generated for other trimming sizes and analyzed similarly.

4.1.5. Supplemental Information and Data

4.1.5.1. Differential Images and Binarized Images of Trimming Size 48 × 49 px, Exposure Time 10,000 μs

The upper row of Figure 4-13 represents the accumulated differential images $\mathrm{Img}_{\mathrm{Acc}}(\mathrm{Exp},\mathrm{P},\mathrm{n})$, and the lower row is binarized image $\mathrm{Img}_{\mathrm{Bin}}(\mathrm{Exp},\mathrm{P},\mathrm{n})$. Horizontally, the changes in differential and binarized data are shown by variation in the number of accumulation (n: 1, 3, 5, 7, 10, 20, 30, 40, 50, 60, 70, 80, 90, 100). Vertically, the changes by variation in the number of the filter papers (P: P0, P1, P5, P10, P15, P20). In the case of n = 1, images are not accumulated.

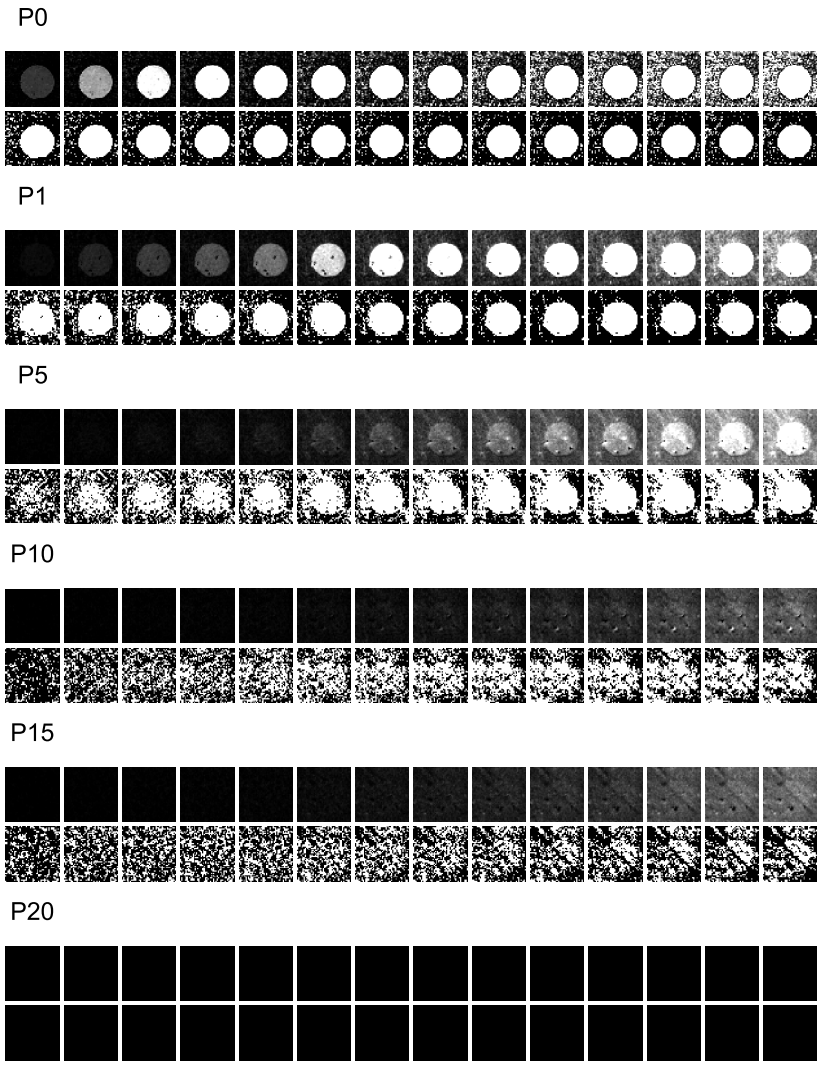


Figure 4-13 Si image of 48 × 49 px, Exp 10,000 μs.

4.1.5.2. Determination Error of the X, Y Center Coordinates, and the Area Size of the target

The determination error of the X, and Y center coordinates and the area size are plotted (48 × 49 px trimming size) in Figure 4-14 and Figure 4-15. The SNR plot is also included. In both figures, the numbers of the filter papers are the parameters. Due to the saturation effect, the SNR approaches one as the exposure time increases. In Figure 4-14, the X, and Y center coordinates, the area size, and the SNR are calculated without accumulation and averaging. In Figure 4-15, each point is the mean error of 100 data with 1σ error bar. The SNR is also mean in Figure 4-15. Comparing Figure 4-14 and Figure 4-15, the averaging in Figure 4-15 appears more stable than in Figure 4-14. Similar plots were

generated for other trimming sizes (72 × 71, 95 × 95, 143 × 143, 237 × 237, 331 × 331, 384 × 448, 384 × 480, 640 × 480 px, and analyzed similarly.

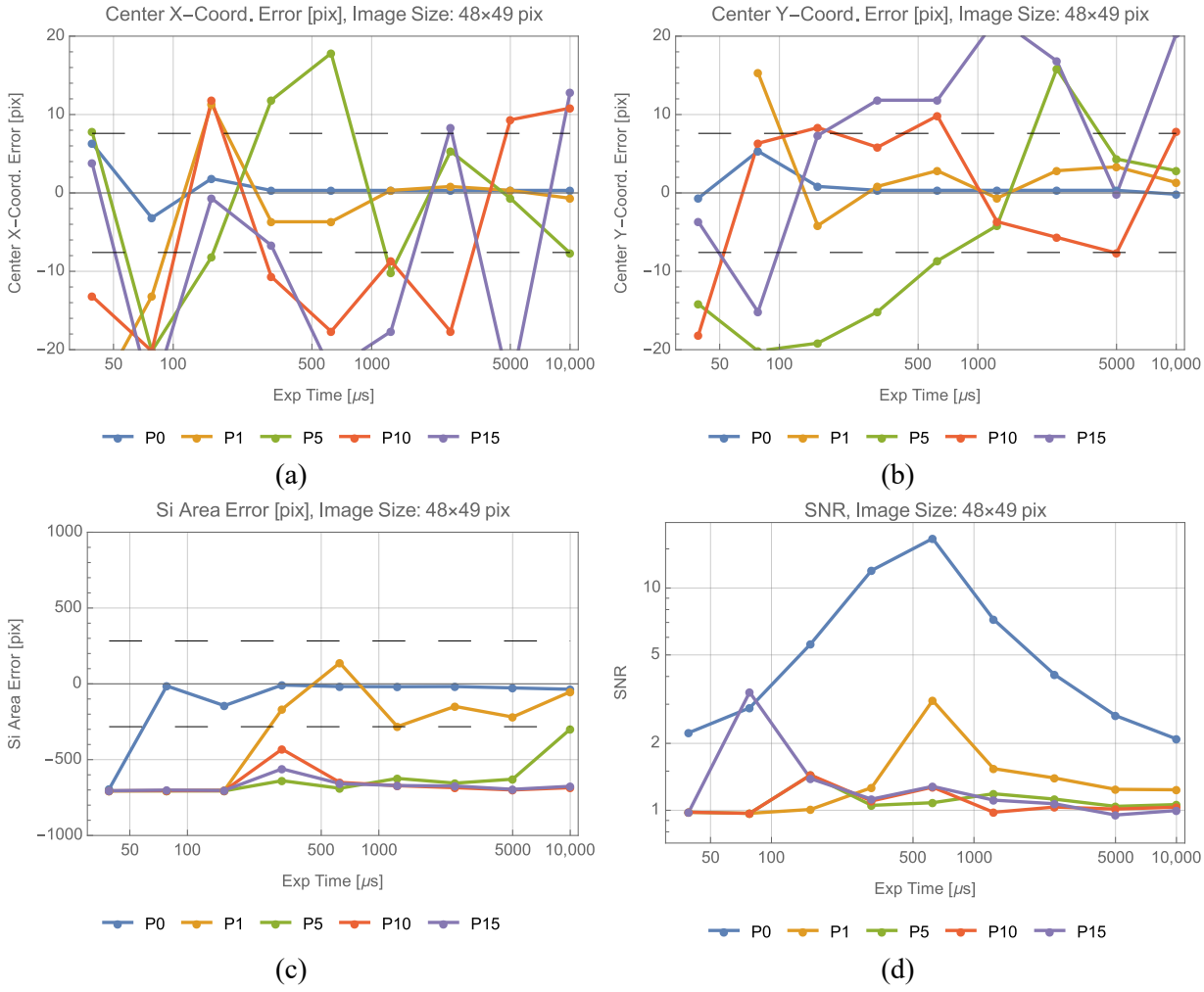


Figure 4-14 48 × 49 px trimming size, the determination error of X, Y center coordinates and area is plotted for exposure time, No Averaging

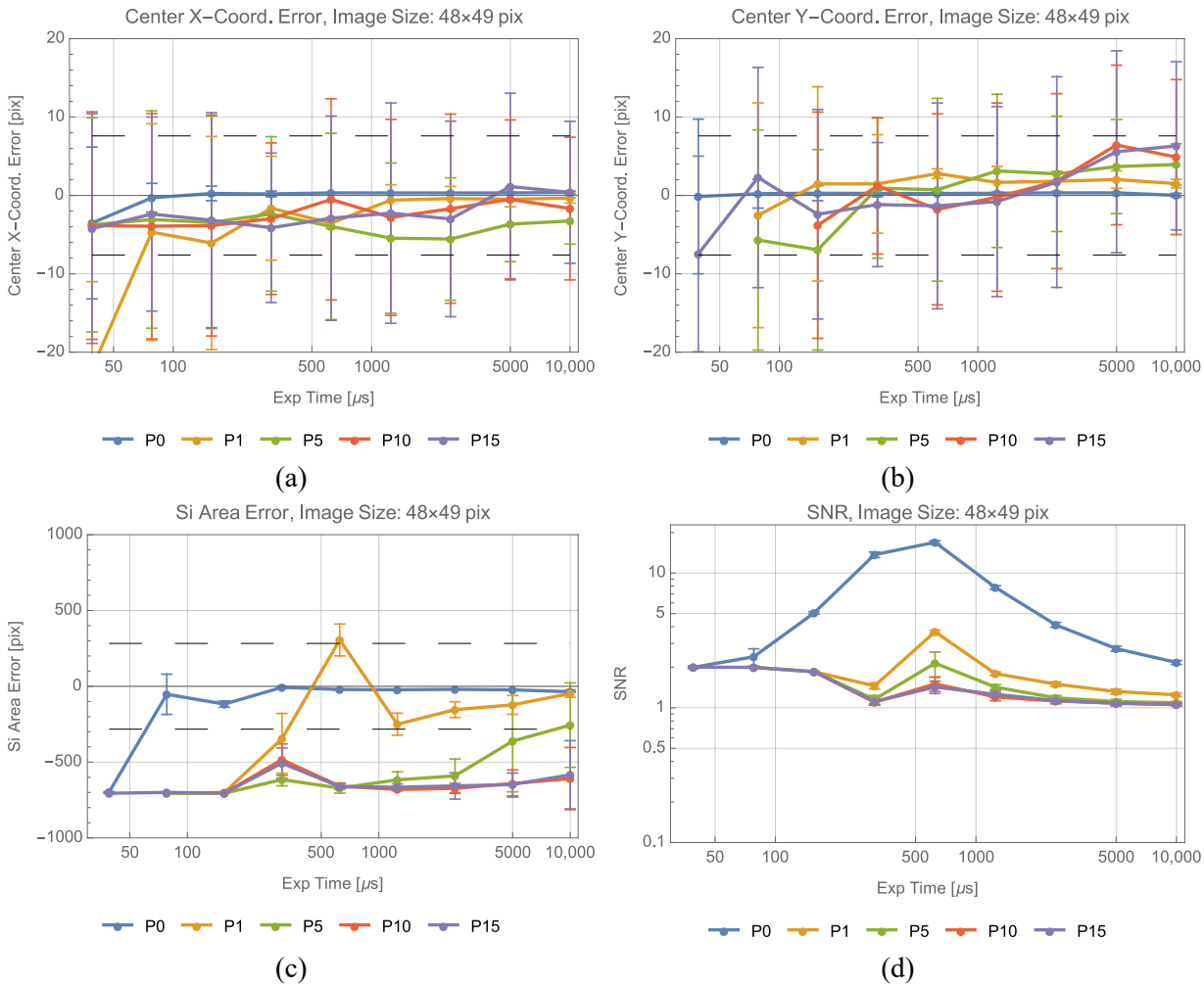


Figure 4-15 48 × 49 px trimming size, the determination error of X, Y center coordinates and area is plotted for exposure time, Averaged 100 data

4.2. Detectability Criteria

4.2.1. Definition of the Detectability

Even though all the data in the experiments were taken at 104.5 cm from the Si/frost glass targets, the real target will be at some different distance in actual operation. Regarding the center coordinates and the area of the target, it should be required that the estimation error be within some limits. The maximum distance to the target that accommodates the requirements for error will depend on exposure time, averaging, and trimming sizes. The performance of this image sensor is defined as the maximum distance that accommodates the determination of the center coordinates and the area of PV, which is the Si substrate in this experiment, within the required error limits. To assess this performance,

system-level requirements for errors are necessary. These requirements are derived from a discussion based on the power generation ratio in Section 3. Then, an equation that determines the maximum distance is derived. In this thesis, “target is detectable” means that the differential absorption image sensor accommodates the requirement, and the maximum distance that accommodates the requirements is “detectable range”.

Since errors are expressed in the pixel coordinate system in the later sections, representing requirements for errors in pixel units is 4.2.14.2.1. Let R the distance to the target, $\Delta\theta$ the angle resolution of the camera per pixel. Then, $R\Delta\theta\Delta px$ is an error and should be constant over ranges, where Δpx is the error corresponding in the pixel coordinate system. If $\Delta\theta$ varies as $1/R$, then $R\Delta\theta$ is constant and Δpx is a scale-invariant (non-dimension) error in the pixel coordinate system.

4.2.1.1. Cooperative System with the Fly Eye Module

The two kinds of OWPT systems were investigated in Section 3. One was cooperative OWPT, the other was non-cooperative. In cooperative OWPT, the fly-eye module relaxes the system-level requirement regarding beam alignment and shaping. When the fly-eye module is utilized, the power generation ratio is determined only by the overlapping ratio η_A of the incident beam area to the area of the module. Especially, when the incident beam size is smaller than the fly-eye module size and no portion of the incident beam spills from the fly-eye lens, the power generation ratio becomes 100%. A decrease in the overlapping ratio due to large center coordinate errors causes a reduction in the power generation ratio.

In the following discussion, the fly-eye module and the incident beam are assumed to be circles, and their radii are R (=15 px), and R/2, respectively. The radius of the PV is assumed 15 px, whereas the radius of the incident beam was not 15/2 px in the experiment. Let $(\Delta x,\ \Delta y)$ errors in the x direction and y direction, respectively. The overlapping region (x, y) satisfies the following relationship: $\{(x, y) \in x^2 + y^2 \leq R^2\} \cap \{(x, y) \in (x - \Delta x)^2 + (y - \Delta y)^2 \leq R^2/4\}$. Like in Section 3, assume the usable lower limit of the power generation ratio from the system point of view is 80%. Then, $(\Delta x, \Delta y)$ is determined such that the area of this overlapping region is greater than 80% of the area of the beam ($\geq 0.8 \times \pi R^2/4$). Since it is sufficient to consider only the X direction, Δx is determined to be $\Delta x \leq 0.718 \times 15$ px $= 10.77$ px. The requirements are allocated for each X, Y direction as $\pm 10.77/\sqrt{2} = \pm 7.6$ px. During an OWPT operation, information on the area size of the incident

beam is necessary. Since $\Delta S/S = 2\,\Delta r/r = 4\Delta r/R$, and error allocation is set as $|\Delta r/R| \leq 0.1$, then the requirement for the area determination is $\left|\Delta S\right| \leq 0.4S = 282.74$

These requirements are already included in Figure 4-14 and Figure 4-15 as dashed horizontal lines. Hereafter, that a differential absorption image sensor accommodates all three requirements is referred to as "it accommodates detectability criteria".

4.2.1.2. Cooperative/Non-Cooperative System without the Fly Eye Module

When the fly-eye module is not utilized, it is necessary to assess both η_A (overlapping ratio of incident beam area to PV area) and η_B (nonlinear output characteristics of PV based on power distribution inside it) of the power generation ratio. Misalignment requirements for such systems were already discussed in Section 3. Assume again that the usable lower limit of the power generation ratio is 80%, and looking at Table 3-1 in Section 3, when the target distance is 1 m, requirements are 2.21 mrad (X direction) and 2.51 mrad (Y direction) for non-cooperative OWPT and 6.9 mrad for cooperative OWPT. Since the angle resolution of the D435 is $\Delta\theta$ = 2.6 mrad/px in the case of a 640 × 480 px image size, these requirements are equivalent to 0.85 px (X), 0.97 px (Y) for non-cooperative OWPT and 2.7 px for cooperative OWPT. The value of $\Delta\theta$ is estimated in the appendix of Section 5. For both cases, the requirement for the area determination can be allocated $\left|\Delta S\right| \leq 0.2S$

A cooperative OWPT with the fly eye module is investigated in the following sections.

4.2.2. Assessment of the Detectable Range

Detectability criteria, at a 104.5 cm target distance in case of 48 × 49 px trimming size, are read from Figure 4-14 and Figure 4-15. Then, for a value of exposure time, comparing these errors with requirements, the number of filter papers n such as P0, P1 accommodating detectability criteria are determined.

In the case of single data, detectability criteria are not accommodated by any number of filter papers for $\text{exposure time} = 39\ \mu s$. For $78 \sim 156\ \mu s$, they are accommodated by P0. For $312 \sim 10{,}000\ \mu s$, they are accommodated by P0 and P1. In the case that 100 data points are averaged, detectability criteria are not accommodated for $\text{exposure time} = 39\ \mu s$. For $78 \sim 312\ \mu s$, they are accommodated by P0. For $625 \sim 5000\ \mu s$, they are accommodated by P0 and P1. For $10{,}000\ \mu s$, they are accommodated by P0, P1, and P5. The number of filter papers (such as P0, P1, ⋯) that

accommodate detectability criteria changes by the trimming sizes. Plots like Figure 4-14 and Figure 4-15, were generated for each trimming size, and the relationship with exposure time and number of papers was read from the figures similarly. Thus, for each trimming size, the threshold (minimum) value of n corresponding to satisfying the detectability criteria is determined as a monotonical function of Exp. In Figure 4-14 and Figure 4-15, even though SNR approaches 1 for exposure time longer than 500 μs due to the saturation effect, the SNR increases with exposure time in the region of less than 500 μs. Ignoring the saturation effect due to constraints of the hardware used in the experiments, SNR would increase monotonically with exposure time, which means a one-to-one relationship between SNR and exposure time. SNR is a function of the number of signal electrons N_s whose explicit functional form will be derived in 1.1.1.1.1.1.A.4.1. Then, N_s can be written as below.

$$N_s = f(SNR) \tag{4-12}$$

In case that shot noise is negligible, N_s can be written as $N_s = SNR \times N_t$, where N_t is the number of thermal noise electrons. Since the threshold number of filter papers n is included in (4-36 as $\eta_t \propto T_p^n$,

$$T_p^n = \frac{N_s}{N_{s0}} = \frac{f(SNR)}{f(SNR_0)} \tag{4-13}$$

, where the subscript 0 denotes the values for $n = 0$. Thus,

$$n = \frac{1}{lnT_p} ln \frac{f(SNR)}{f(SNR_0)} \tag{4-14}$$

Thus, the threshold n can be expressed as a function of SNR in other words, SNR determines detectability threshold.

Generally, SNR would be a function of range, etc. Thus, for a given trimming size, the detectable range can be determined by an SNR expression containing Exp and n to be derived in a later section.

Thus we reached an important conclusion that, as long as we use scale-invariant detectability expression SNR, we can formulate detectability discussion in a scale-invariant way. Then, we will obtain scale-invariant (non-dimensional) detectability criteria, and come back to this point in Section 7.

Since SNR is a function of range, etc., the detectable range can be determined as a function of Exp and n at the detectability threshold for a given trimming size. The detectable range R′ for a fixed trimming

size with the receiver diameter D' is estimated as in the following equation, using the range R and the receiver diameter D in the experiment and calibration parameter T_{FE} and T_p^n.

$$R'^4 = R^4(D'/D)^2/\left(T_{FE}T_p^n\right) \tag{4-15}$$

The derivation of the equation is summarized in A.4.1. According to the D435 data sheet [4], the F-number of its color sensor optics is 2.0, and its focal length is 1.88 mm. Thus, the diameter D of the camera used in the experiment is 0.94 mm. *R* (= 104.5 cm) is the distance to the target in the experiments. Figure 4-16 shows simulation results of the detectable range (R') based on (4-15) for trimming size and exposure time, in the case that $D' = D$. These plots essentially show an SNR-based performance limit of a system with a 5 mW light source and D435 RGB camera. Plots are shown for two different image processing schemes, single data (Figure 4-16 (a)) and averaging 100 data points (Figure 4-16 (b)).

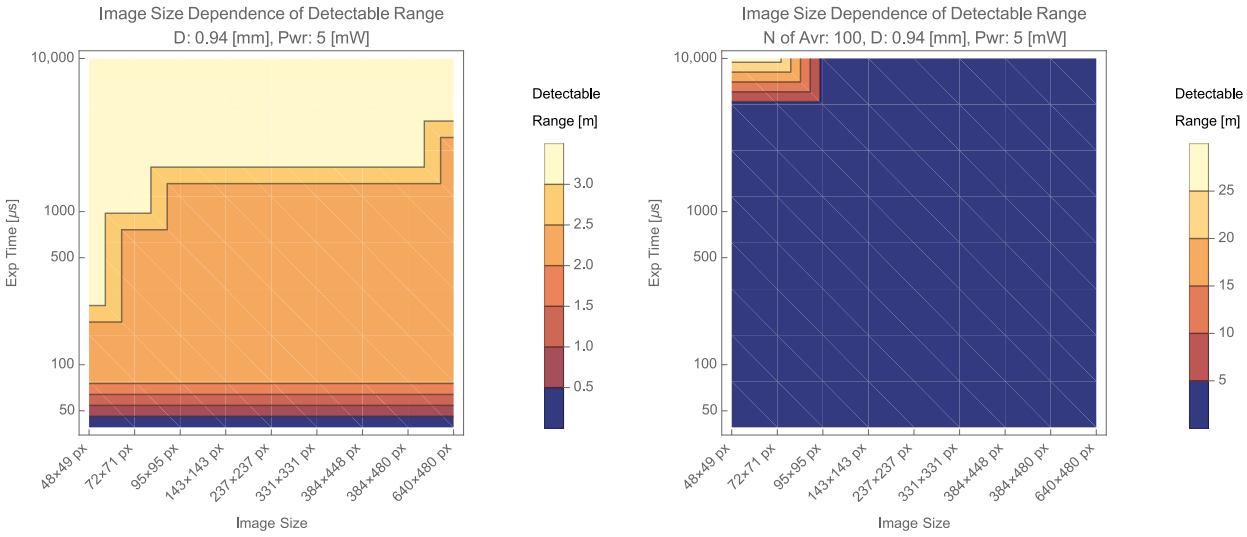


Figure 4-16 Detectable range plot for a 0.94 mm receiver diameter with beam size control: (a) Single data; (b) 100 averaging.

In Figure 4-16, generally, the detectable range tends to increase as the exposure time increases and image size decreases (the upper left corner). Comparing two image processing schemes, the

detectable range is quite enhanced by averaging. The maximum value of the detectable range is about 3.5 m in an accumulation scheme with a 10,000 μs exposure time. It reaches around 30 m in an averaging scheme in case of a 10,000 μs exposure time and 48 × 49 image size. This figure indicates that the performance limit of this image sensor is largely boosted when an averaging scheme and trimming down to an appropriate image size are applied. In image processing in this subsection, binarization is based on the unique threshold determined by the Otsu algorithm in the entire image. As trimming size increases, such a binarizing threshold tends to increase due to effects from objects other than the target and noise. On the other hand, in the case of the small trimming size, the area of the Si image is relatively large and dominant in the trimmed image. In such cases, the binarizing threshold tends to decrease, and the Si image is detectable even for a larger number of filter papers, such as P5 with Exp $= 10{,}000$ μs. When trimming size is small, averaging provides a longer detectable range than accumulation (e.g., upper left corner of Figure 4-16 (b)). This is because, in addition to the decrease in the binarizing threshold, scattered data tend to converge close to the true value by averaging. This is observed in 48 × 49 px and 72 × 71 px cases. Even for the same trimming size, the accumulation in Figure 4-16 (a) does not show such a performance improvement.

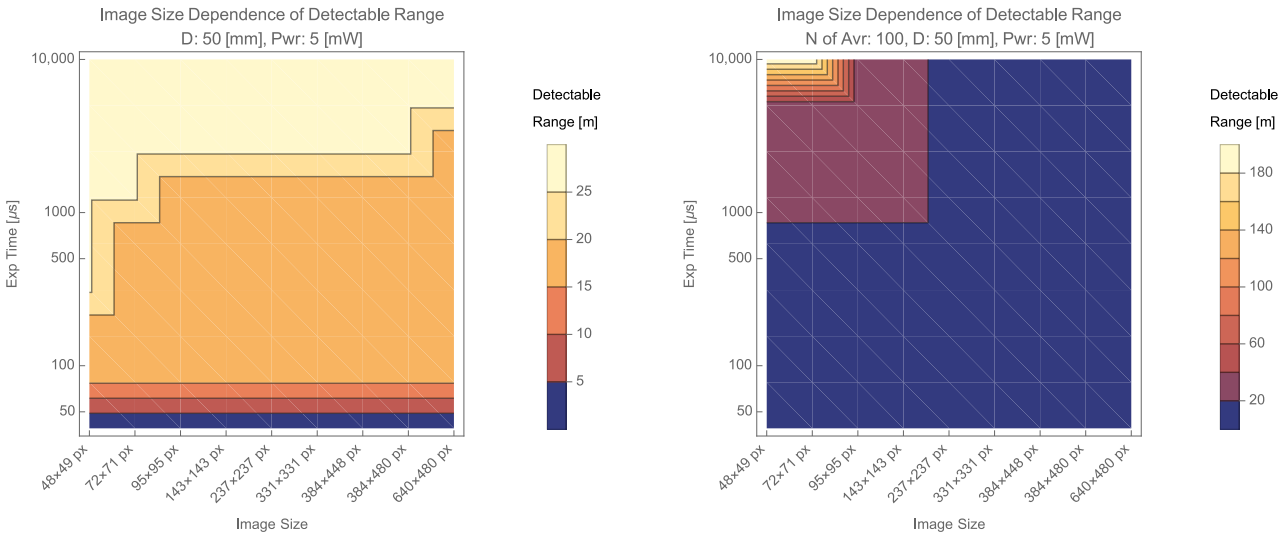
4.2.2.1. Improvement by Increase of the Effective Diameter of the Camera Optics

With the increase in the effective diameter of camera optics, the detectable range would be expanded. If the diameter is changed from D to D′ (D′ > D), the detectable range increases, with the following factor:

$$\sqrt{D'/D} \tag{4-16}$$

Figure 4-17 shows the simulation plot when the camera optics' diameter D' is 50 mm.

With the increase in the camera's optics diameter from 0.94 mm to 50 mm and accumulating 100 images, this image sensor potentially supports a 30 m detectable range in case of a 10,000 μs exposure time (Figure 4-17 (a)). Such performance would be realized with, e.g., a 10 cm size target and 15× zoom lens. When trimming down to the appropriate image size, Figure 4-17 (b) shows this image sensor would support about a 200 m detectable range, based on the SNR discussion. Such performance would be realized with, e.g., a 1 m size target and 10× zoom lens.



(a) (b)

Figure 4-17 Detectable range plot for 50 mm camera optics' diameter: (a) Single data; (b) 100 averaging.

4.2.2.2. Improvement by the Beam Size (Beam Divergence) Control

When $A_{SC} < A_{tr}$, (4-33) becomes $F(R) = A_{SC}/A_{tr}$. If the distance to the target is long enough, A_{tr} is approximated by (4-39). However, knowing the distance to the target by ranging or information from a positioning system before operation (transmission) and controlling θ_t so that $F(R)$ is kept constant for the distance, the determination equation of R' ((4-15)) is replaced by the following equation:

$$R'^2 = R^2(D'/D)^2/\left(T_{FE}T_p^n\right) \tag{4-17}$$

Figure 4-18 and Figure 4-19 show a simulation plot based on (4-17). Figure 4-18 shows D' = 0.94 mm case. In this case, the accumulation and averaging scheme support about a 10 m and 600 m maximum detectable range, respectively. Comparing this 10 m detectable range of accumulation scheme with Figure 4-16 (a) and Figure 4-17 (a), the maximum detectable range in each figure is not so different. Considering the beam adjusting mechanism in the image sensor is necessary for beam size control, Figure 4-18 (a) does not show enough advantage to allow for introducing such complexity to the image sensor. To achieve around a 10 m detectable range, increasing the diameter of the camera optics would be a simpler and better strategy.

This situation becomes quite different in the long-range case. Both Figure 4-18 (b) and Figure 4-19 (a) support about a 600 m maximum detectable range. Figure 4-19 (b), especially, supports

about a 35 km with 50 mm diameter of camera lens and trimming down to the appropriate image size. Neither Figure 4-17 nor Figure 4-18 (a) support such a long detectable range. For OWPT that supports a long-range, such as several hundred meters or more, the detection of PV in various illuminating conditions would be a serious problem. These three figures (Figure 4-18 (b) and Figure 4-19 (a) and (b)) indicate that utilizing this image sensor with trimming down to an appropriate image size or controlling beam size would be solutions for such a problem.

If rough information on the target position is provided before and during operation from a similar positioning system [13,14], the image size would be adjusted with the target size by zooming, and the detectable range would increase. There would be “assisted acquisition mode” and “stand-alone acquisition mode” for the actual operation mode of this differential absorption image sensor. Assisted acquisition mode expects assistance information of the target from an outside source, zooms target image using such information and achieves better performance than a stand-alone acquisition mode. ’Stand-alone acquisition mode’ supports a wider image size than the assisted acquisition mode and performs image processing with a default image size and target acquisition. A stand-alone acquisition with reasonable performance is necessary for self-contained target detection. This is related to the issues raised in 4.1.2 and will be realized by the over-subtraction technique combined with a longer exposure time in a later section.

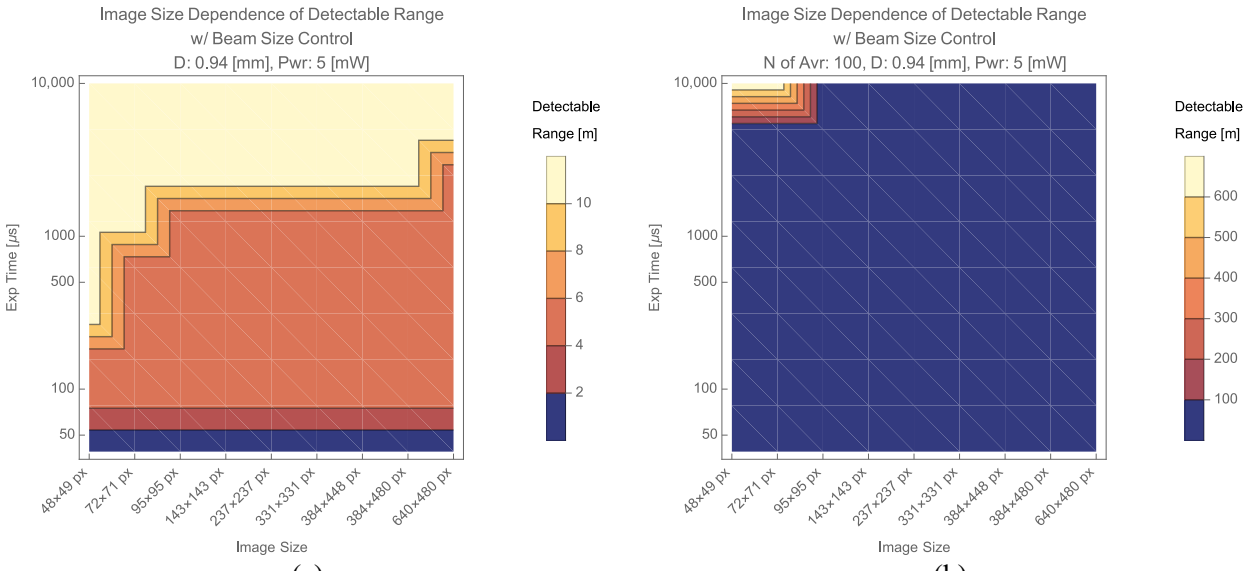
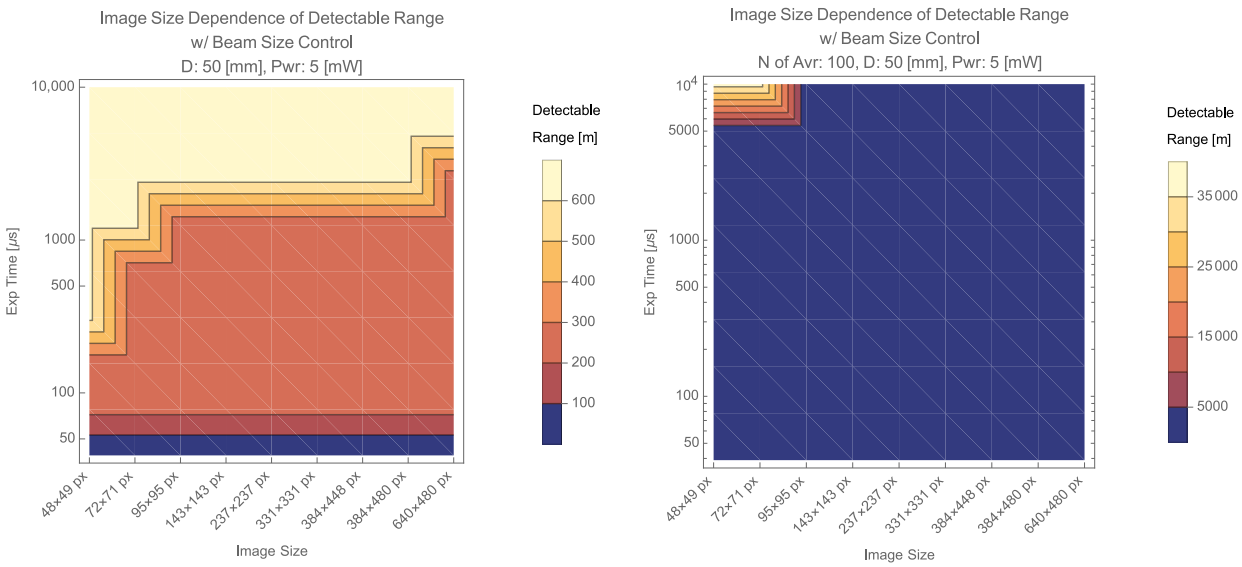


Figure 4-18 Detectable range plot for a 0.94 mm receiver diameter with beam size control: (a) Single data; (b) 100 averaging.



(a) (b)

Figure 4-19 Detectable range plot for a 50 mm receiver diameter with beam size control: (a) Single data; (b) 100 averaging.

4.2.3. Effect of the Background

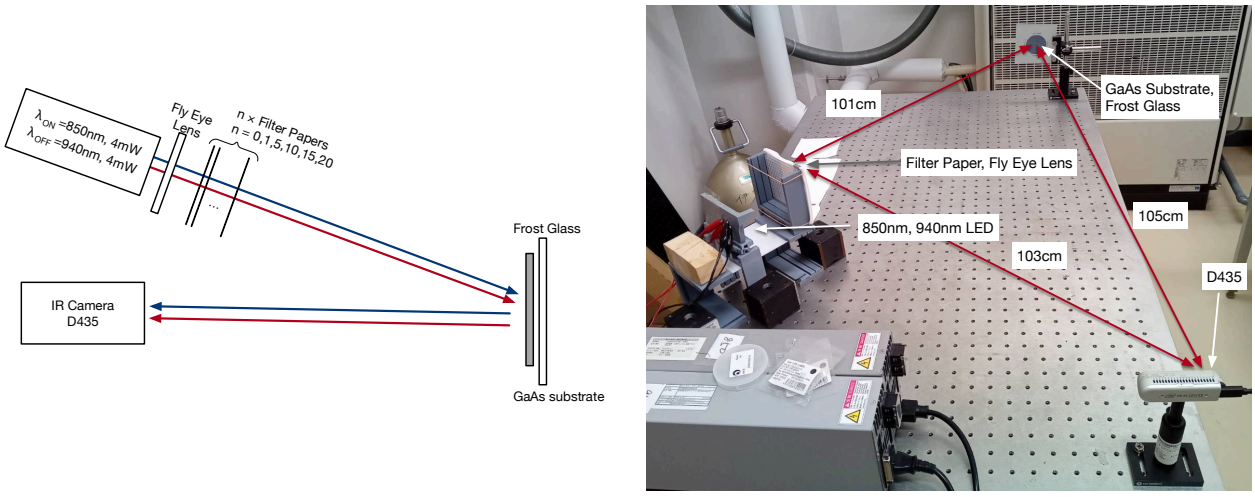
Figure 4-6 shows that intensity on the Si/frost glass target is less than $1\mu W/cm^2$ for P1 and less than $1nW/cm^2$ for P5. Therefore, if enough λ_{OFF} intensity is contained in the background, this differential absorption image sensor does not need any active λ_{OFF} illumination. In fact, during the experiments shown in Figure 4-1, the Si image was extracted and generated a differential image with enough SNR using only the room light of the laboratory or much stronger illumination from a white LED light as shown in 4.1.2. External illumination was an unnecessary disturbance in former studies; however, it provides additional λ_{OFF} illumination which helps it to detect the target in this sensor. These aspects show the robustness of this differential absorption image sensor. On the other hand, leakage of λ_{OFF} to the measurement of λ_{ON} (λ_{OFF} leakage) degrades SNR. In the actual operation scene, the background spectrum would be wide enough to cover both λ_{ON} and λ_{OFF}, and there would be λ_{OFF} leakage to the λ_{ON} image. Such leakage should be subtracted as a background in the differential image generation process (software measure), or λ_{OFF} leakage should be suppressed by inserting the λ_{OFF} cut filter (hardware measure) in front of an image sensor device in the case that λ_{OFF} leakage is near saturation level.

4.3. Reflectivity Characterization of the GaAs Targets

4.3.1. Configuration of the Experiments

The proof-of-concept experiments were conducted with λ = 532 nm, and differential images were generated from Si substrate and frost glass images. The detection experiments using Si substrate is followed by the experiments utilizing GaAs target, and λ_{ON}, λ_{OFF} were selected as 850 nm and 940 nm, respectively.

Figure 4-20 shows the configuration and layout of this experiment. The transmitter assembly consists of series-connected two LEDs for both 850 nm and 940 nm. The emitting power of individual LED is calculated as 2 mW from the data sheets[15,16]. For the infrared camera, Intel D435™ [5] depth camera was used, and one of its two infrared output streams (left channel) was inputted to the image processor (PC). As for software running on the image processor, D435 SDK [4], Python™ [7], and Open CV™ [6] were used to control the camera. Irradiated power onto the target is controlled by changing the number of filter papers like in the proof-of-concept experiments. Regarding the parameters setting of D435, the gain was set to 240, and the image size of raw data was set to 640 × 480 px throughout this study. Other internal parameters were not changed from their default values.



(a) (b)

Figure 4-20 The configuration and layout of the experiment (a) Configuration; (b) Layout of the experiment.

Images were captured by changing exposure times as 25, 50, 100, 250, 500, 1000, 2500, 5000, 10,000, 25,000, 50,000, 100,000, 200,000 μs, and power control status as P0, P1, P5, P10, P15. Captured 640 × 480 px images were trimmed down to 34 × 33, 51 × 49, 68 × 66, 102 × 99, 170 × 165, 238 × 231, 324 × 330, 324 × 480, 640 × 480 px. Differential images were generated for all combinations of the parameter sets, and GaAs substrate images were extracted from the binarized differential data.

4.3.2. GaAs Substrate Detection by the Differential Absorption Imaging

Infrared GaAs images captured by the measurement system are shown in Figure 4-21 (Exposure time 200,000 μs, P0). Comparing λ_{OFF} image (Figure 4-21(a)) with that of λ_{ON} (Figure 4-21(b)), the latter is brighter except for the PV area than the former due to the wavelength dependence of the camera's sensitivity. Instead of applying brightness correction, the grayscale level of each pixel in the differential image (gs_{diff}) is calculated by (4-18), which can be referred to as 'the over-subtraction'. This formula does not affect the target region in which λ_{OFF} image is expected to be brighter than λ_{ON}. On the other hand, it eliminates unnecessary background in which λ_{ON} image is expected to be brighter than λ_{OFF}.

$$gs_{diff} = \begin{cases} gs_{OFF} - gs_{ON}, & gs_{OFF} \geq gs_{ON} \\ 0 \quad , & gs_{OFF} < gs_{ON} \end{cases} \tag{4-18}$$

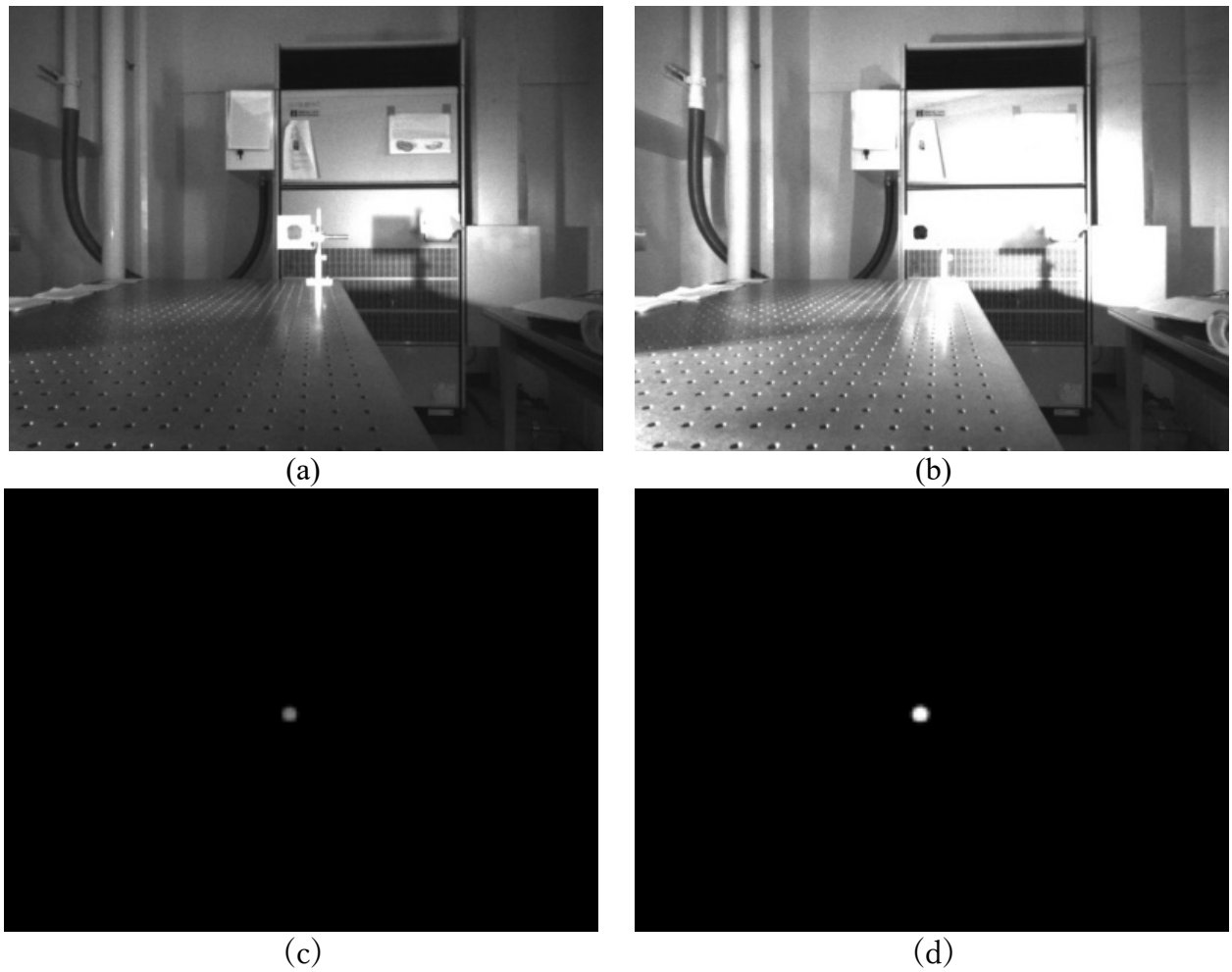


Figure 4-21 Infrared GaAs substrate image (a) λ_{OFF} image; (b) λ_{ON} image; (c) Differential image; (d) Binarized image.

The binarization threshold is determined using the Otsu algorithm. Specification of target GaAs substrate is that manufacturer AXT Inc. Fremont, CA, USA [18], n-type, carrier concentration $2\sim3\times10^{18}$ cm^{-3}, diameter 2", thickness 350 μm, surface orientation (001). Its front surface is polished, and its rear surface is diffuse (etched). Detection of the target by differentiation and binarization is demonstrated in A.4.3.

Figure 4-22 is an excerpt from data reduction products, whose image size is 34 × 33 px. After estimating the center coordinates and the area size, their mean values with 1σ error is plotted in the figure. System requirements for them can be calculated by the method described in 4.2.1.1, and the requirement for the center coordinate is given by $0.718\times\text{GaAs radius}/\sqrt{2}$. The radius

of the GaAs substrate was directly read from the captured images, and its mean value was 7.6 px. Then, the requirement for the center coordinates is 3.86 px. The requirement for the area is ±0.4S, where S is the area of the substrate, and its mean value was 181.94 px. The requirement for the area becomes ±72.78 px. These requirements are included in Figure 4-22 as horizontal dashed lines.

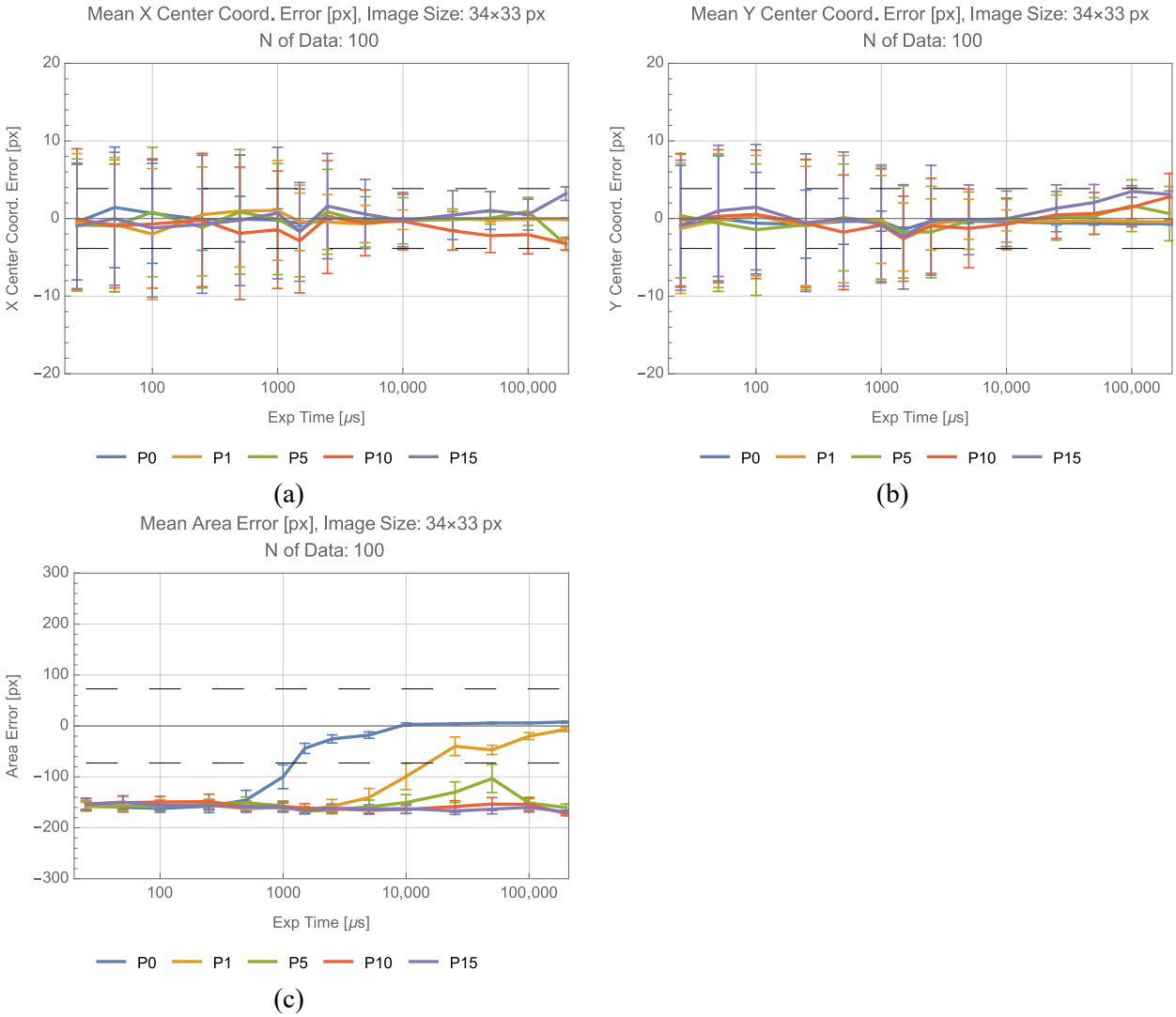


Figure 4-22 An example of estimation of the center coordinates and the area of GaAs substrate (a) X center coordinate; (b) Y center coordinate; (c) Area

4.3.3. Comparison of the GaAs Substrate Detection using Infrared with the Si Substrate Detection using Visible Light

From the data of visible and infrared experiments, a simple relationship can be verified regarding the signal electron number for the threshold of detectability. Then, a solution for issues raised in 4.1.2 is provided.

From the data in Figure 4-22, both X and Y center coordinates are within the requirements limit for every exposure time of P0 and P1. The areas are within them for exposure time longer than 1000 μs for P0, and 15,000 μs for P1. Data using visible light are included in Figure 4-15. Comparing these threshold exposure times of detectability, the ratio of infrared to visible is constant regardless of power control status, as shown in Table 4-1.

Table 4-1 The threshold exposure time of visible and infrared experiments.

Power Control status	Threshold Exposure Time in Visible Experiments	Threshold Exposure Time in Infrared Experiments	Ratio (Infrared/Visible)
P0	78 μs	1000 μs	12.8
P1	1250 μs	15,000 μs	12.0
P5	10,000 μs	—	—

The number of signal electrons generated in image capturing camera is calculated by (4-36).

$$N_s = (\lambda/hc)\eta_r\eta_t\eta_Q P_t F(R)\,\rho A_r Exp/\pi R^2 \quad (4\text{-}36)$$

here η_Q: quantum efficiency of the camera sensor, η_r: efficiency of camera optics, ρ: diffuse reflectivity of the target, hc/λ: photon energy of the incident beam, Exp: exposure time, P_t: incident beam power, A_{tr}: area of irradiated beam at the target point, η_t: efficiency of transmitter optics (including intensity reduction due to fly eye lens and filter papers), R: distance to the target, A_{SC}: Area of the target, and $F(R)$ is defined in (4-33).

$$F(R) \equiv \begin{cases} 1 & for\ A_{SC} \geq A_{TR} \\ A_{SC}/A_{tr} & for\ A_{SC} < A_{tr} \end{cases} \quad (4\text{-}33)$$

The ratio of the threshold exposure time of visible to the one of infrared is evaluated using (4-36). Regarding the signal electron number of infrared, one for λ = 940 nm is necessary for evaluation. The parameters, $F(R)$, η_r, η_t, A_{tr}, A_r, R can be regarded as the same between the two experiments. The other parameters are distinguished by adding subscripts ”532” for parameters included in λ = 532 nm experiment and “940” for λ = 940 nm. Then each parameter is evaluated as follows.

$$\frac{N_{s\,532}}{N_{s\,940}} = \frac{532\,\eta_{Q\,532}\,P_{t\,532}\,\rho_{532}Exp_{532}}{940\,\eta_{Q\,940}\,P_{t\,940}\,\rho_{940}Exp_{940}} \tag{4-19}$$

1. Exposure time

   From the data of the two experiments shown in Table 4-1,

$$\frac{Exp_{532}}{Exp_{940}} = 12\sim13 \tag{4-20}$$

2. Quantum efficiency

   Since the quantum efficiency data of the Si sensor used in D435 is not disclosed, this parameter should be evaluated by other available CMOS sensor data. Several commercial CMOS sensor data are compiled in the datasheets [14]. The ratio of quantum efficiency of CMOS sensor at λ = 532 nm to λ = 940 nm looks roughly varying from 4:1 to 10:1, and

$$\frac{\eta_{Q\,532}}{\eta_{Q\,940}} = 7 \tag{4-21}$$

   is adopted as the mean value.

3. Power

   Since λ = 532 nm experiments, its power was 5mW, power can be evaluated as

$$\frac{N_{s\,532}}{N_{s\,940}} = \frac{5mW}{4mW} = 1.25 \tag{4-22}$$

4. Diffuse reflectivity

   It is evaluated as

$$\frac{\rho_{532}}{\rho_{940}} = 1.7\sim2.75 \tag{4-23}$$

   Details are described in A.4.2.

From the series of evaluations above,

$$\frac{N_{s\,532}}{N_{s\,940}} = 0.65\sim1.13 \tag{4-24}$$

Since this ratio is close to 1, the threshold signal electron number for detectability is conjectured to be constant regardless of wavelength ($N_s|_{threshold} \equiv N_{s\,532} = N_{s\,940}$).

On the other hand, $N_s|_{threshold}$ would be proportional to the grayscale threshold level, identified as the binarization threshold. Differential intensity (I_{diff}) is defined as follows.

$$I_{diff} = \bar{I}_{TGT} - \bar{I}_{BG} \tag{4-25}$$

where $\bar{I}_{TGT}$ is mean level inside the target region in Figure 4-23, and $\bar{I}_{BG}$ is mean background level. As a result, I_{diff} is the mean signal level inside the target region.

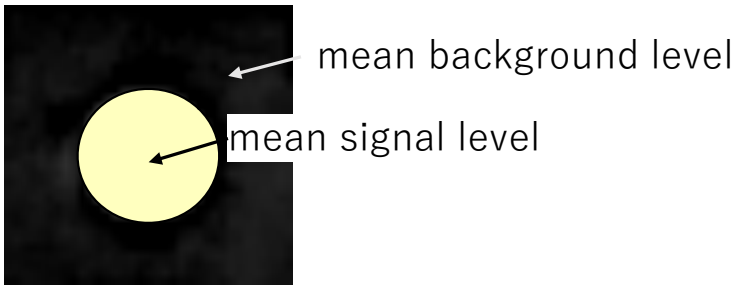
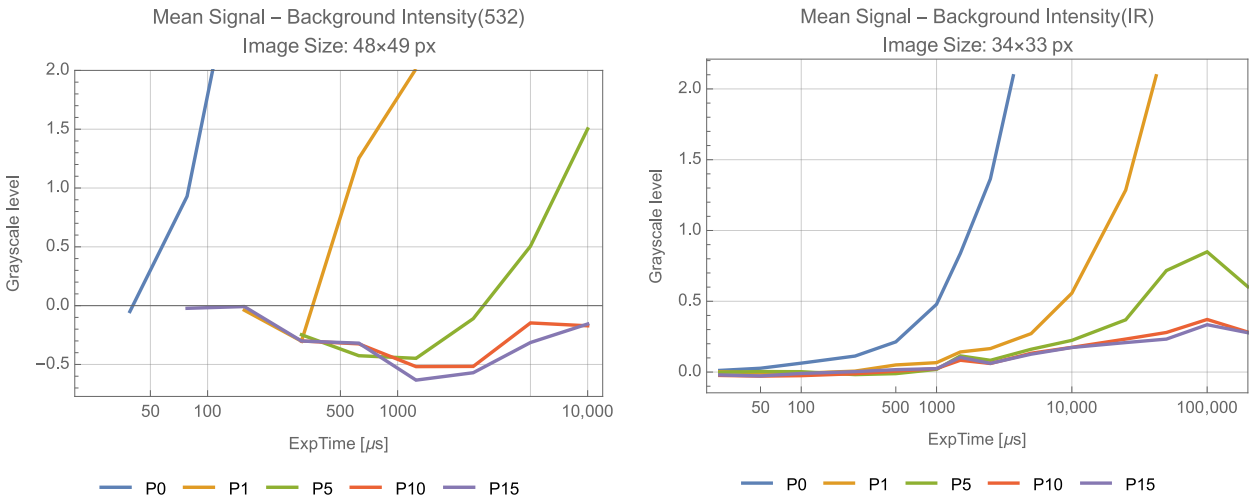


Figure 4-23 Mean signal level ($\bar{I}_{TGT}$) and mean background level ($\bar{I}_{BG}$).

Considering the sensor output is 8-bit grayscale, I_{diff} is normalized by 1/255, which is the minimum resolution of 8-bit. Figure 4-23 Mean signal level ($\bar{\boldsymbol{I}}_{\boldsymbol{TGT}}$) and mean background level ($\bar{\boldsymbol{I}}_{\boldsymbol{BG}}$). shows the normalized I_{diff} plot against exposure time.



(a) (b)

Figure 4-24 The normalized I_{diff} against exposure time (a) data from visible experiments; (b) data from infrared experiments.

These plots show that the threshold exposure time of both visible and infrared experiments included in Table 4-1 corresponds to the unit value 1 in the longitudinal axis. The above discussions show that threshold signal electron number and threshold differential intensity are constants between the two experiments. This suggests that the following "threshold equation" holds at the target detection threshold regardless of wavelength used in the two differential absorption imaging experiments.

$$\left[K(\lambda/hc)\eta_r\eta_t\eta_Q P_t F(R)\,\rho A_r Exp/\pi R^2\right]_{threshold} = \Delta I_{diff} \tag{4-26}$$

Here, ΔI_{diff} represents threshold differential intensity which is identified as binarization threshold and whose minimum value is 1 bit of grayscale level (1/255 for 8 bit), and K represents a coefficient to transform signal electron number to a grayscale level which also depends on the configuration of the measurement system and, especially, detectability criteria. All parameters on the left-hand side of (4-26) are for λ_{OFF}. The generalized form of the equation is obtained by including a term for λ_{ON} which is negligible in these experiments.

$$\begin{aligned}\Big[\Big(K(\lambda/hc)\eta_r\eta_t\eta_Q P_t\rho A_r\big|_{\lambda_{OFF}} \\ - K(\lambda/hc)\eta_r\eta_t\eta_Q P_t\rho A_r\big|_{\lambda_{ON}}\Big) F(R)\,Exp/\pi R^2\Big]_{threshold} \\ = \Delta I_{diff}\end{aligned} \tag{4-27}$$

The first term of (4-27) in the left-hand side parenthesis represents the parameters for λ_{OFF} and the second one represents λ_{ON}. A set of parameters on the left-hand side of (4-26) or (4-27) determines the threshold differential intensity (maximally settable binarization threshold) on the right-hand side. The right-hand side of the threshold requires the necessary parameters in the left-hand side to support the binarization threshold to be set. It should be noted that (4-26) and (4-27) are defined by mean noise value in a certain region and noise is generated randomly within such regions. Consider that noise covers uniformly over the entire image of λ_{OFF} and λ_{ON}. This case would occur with a long exposure time. Differentiating λ_{OFF} and λ_{ON} images by (4-18) would cause noise reduction in the resultant differential image. This is observed in Figure 4-25. It shows images of various exposure times with the constant binarizing threshold of 1/255. It is seen that increments of exposure time cause noise reduction. In Figure 4-25(a), whose exposure time is 500 μs, a tiny white dot of noise is spread over the entire image, and the GaAs image cannot be seen. As exposure time increases in Figure 4-25(b), (c), such noise

decreases gradually, and the GaAs image appears at the center. Finally, in Figure 4-25(d), only GaAs image can be seen. In this case, a globally clear noiseless image can be generated even for differential intensity ΔI_{diff} = 1/255. Thus, long exposure time combined with the over-subtraction causes global noise reduction even for non-trimming images.

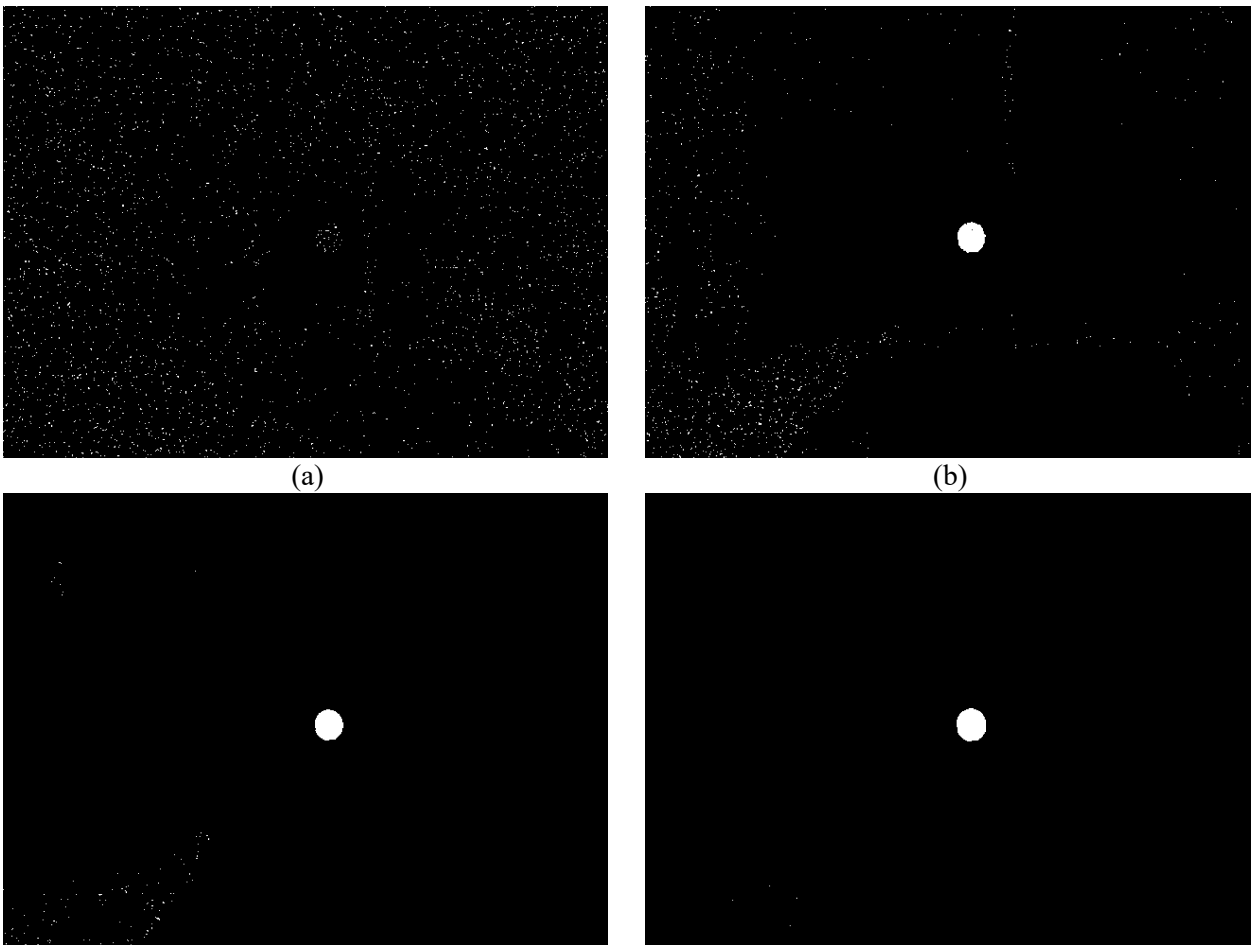
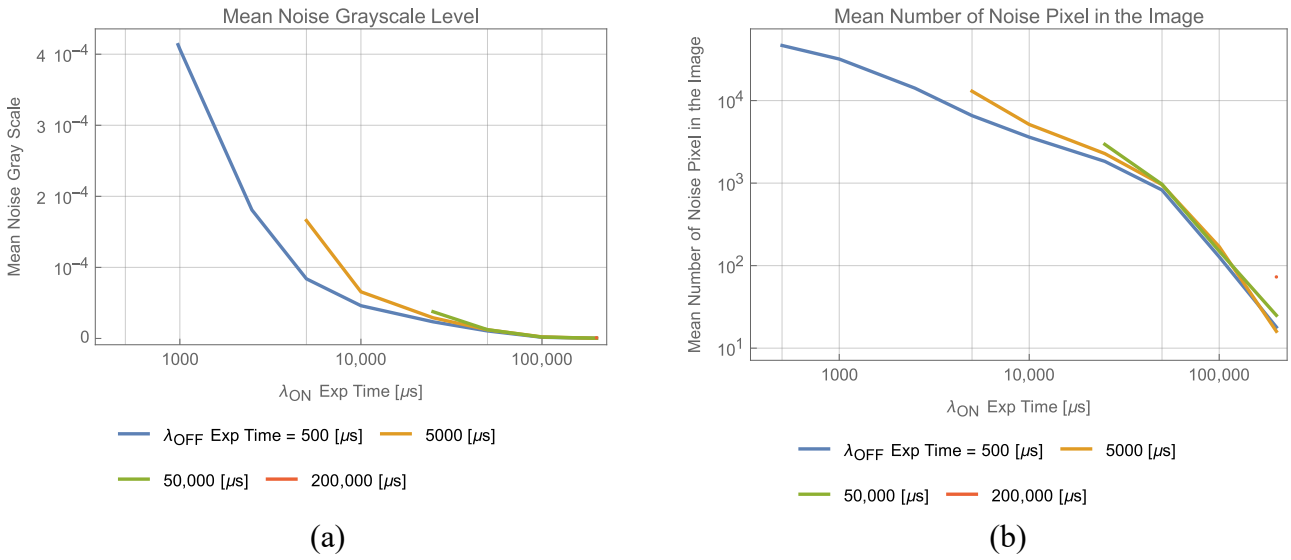


Figure 4-25 Noise reduction in Binarized Images by Increment of Exposure Time (a) Exposure Time 500 µs; (b) Exposure Time 5000 µs; (c) Exposure Time 50,000 µs; (d) Exposure Time 200,000 µs.

The above discussions can be quantitatively seen in Figure 4-26, where the same data are plotted as log-linear (Figure 4-26(a)) and log-log scale (Figure 4-26(b)), respectively. The horizontal axes represent the exposure time of λ_{ON} image to be subtracted from the λ_{OFF}. The vertical axes represent the mean differential noise over the image defined below. The bar above the right-hand side represents the mean over the entire image excluding the PV.

$$Mean\ Differential\ Noise_{\lambda_{OFF}\ Exp\ Time}(\lambda_{ON}\ Exp\ Time) = \overline{gs_{\lambda_{OFF}\ Exp\ Time} - gs_{\lambda_{ON}\ Exp\ Time}} \quad (4\text{-}28)$$

When one takes a λ_{OFF} image of an exposure time, its mean differential noise depends on the exposure time of λ_{ON} image to be subtracted, and it becomes sufficiently stable beyond 50 ms in the horizontal axes in Figure 4-26(a). The mean number of noised pixels in the 640×480 image in Figure 4-26(b), calculated as $Mean\ Differential\ Noise_{\lambda_{OFF}\ Exp\ Time}(\lambda_{ON}\ Exp\ Time) \times 640 \times 480 \times 1/255$. Thus, the effect of the over-subtraction combined with long exposure time reduces the noise globally about $\mathcal{O}(10^{-1})$~$\mathcal{O}(10^{-3})$, and essentially saturates. In this scheme, the noisier the λ_{ON} image, the better the noise reduction. Thus, the over-subtraction combined with long exposure time solves the issues raised in 4.1.2. These two methods enable to lower the binarization threshold to the minimum (= 1/255).



(a) (b)

Figure 4-26 Mean noise level over the image in the over-subtraction scheme combined with long exposure time

In case that noise does not cover the entire image, such noise would remain in some regions in the differential image after differentiation. This case would occur in a short exposure time. In such a case, there would be two strategies to avoid the noise effect. One is to increase ΔI_{diff} from 1/255 to an appropriate value. This causes an impact on the system parameters on the left-hand side of (4-27), such as an increment of irradiation power. The other option would be trimming images to an appropriate size in which the target size dominates the entire image. For example, in Figure 4-24, images were trimmed to 48 × 49 px for visible and 34 × 33 px for infrared. For short exposure time data, this trimming looks helpful to reduce noise and make ΔI_{diff} minimum. However, the larger the size of the images, the noisier the resultant images become. This phenomenon was observed in the experiments in Section 4.2.

The exposure time should be determined by system requirements, especially by its real-time requirement. It would be necessary to estimate the noise remaining in the differential images according to the determined exposure time and to develop plans of ΔI_{diff} setting. (4-26) and (4-27) provide logic for such system design strategies. In the following section of this thesis, the long exposure time and the over-subtraction strategy are utilized, and non-trimmed 640 × 480 px images are processed except where specifically noted.

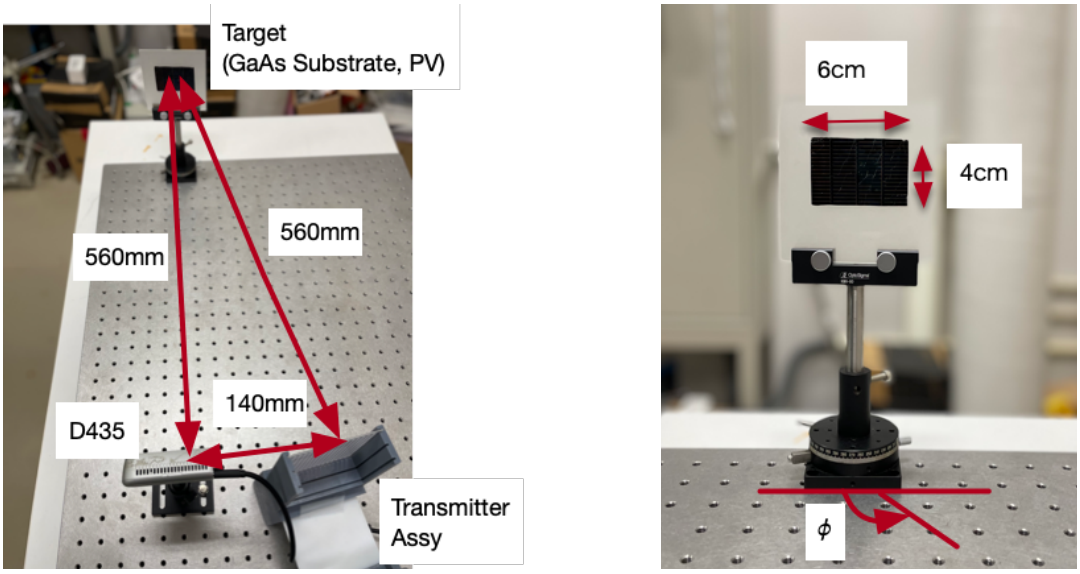
4.3.4. GaAs PV Detection by Infrared Differential Absorption Imaging

A real thin-film GaAs PV detection experiment was conducted (Manufacturer Advanced Technology Institute, Tokyo, Japan [29], five-cell series connected). The GaAs solar cell size is 6 cm × 4 cm. Its front surface is GaAs solar cell, and its rear surface is a copper electrode. The PV is fixed on a rotatable stage, and its rotation angle ϕ is set to 90 degrees when it faces normal to the camera.

During the initial trial test, strong non-diffuse reflection was observed near the PV normal and weak diffuse reflection from large angles. From an exposure time point of view, a short exposure time would be enough to detect vital components near the normal, and a long one would be necessary to detect weak components in large angles. Considering the noise reduction effect described in the last section, large angle components are expected to be detected by setting long exposure time and global binarization threshold of ΔI_{diff} = 1/255. Regarding the detection of strong components near the normal, there are two options. One is to increase the binarization threshold, since such reflection is due to high reflectivity in the left-hand side of (4-27), ΔI_{diff} can be increased accordingly. Another option is that ΔI_{diff} is kept globally at its minimum 1/255. Since the solar cell detection algorithm in these experiments is that the connected component with the maximum area in the binarized image is regarded as the PV, the area of the connected solar cell image generated by strong reflection would become dominant even in the noisy image of short exposure time. In such a case, the PV image would be detected even with short exposure time and minimum ΔI_{diff}. The second option looked simpler and was tried. ΔI_{diff} was kept globally 1/255 for every exposure time, and the solar cell was successfully detected.

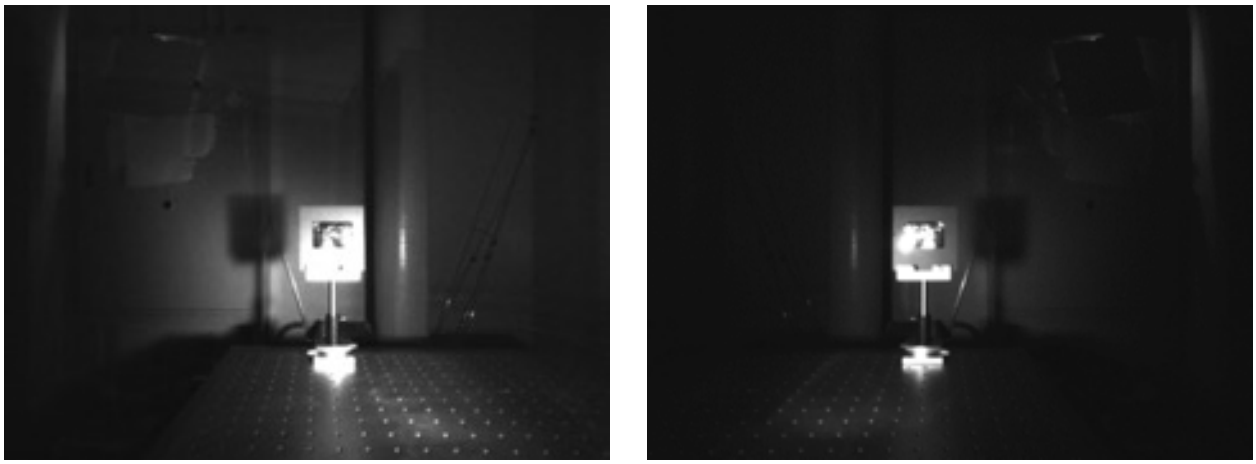
Experiments were conducted for various angles of the rotatable stage shown in Figure 4-27. From CCW to CW, they are 50, 60, 70, 75, 80, 85, 90, 95, 100, 105, 110, 115, 120, 130, and

140 degrees. An excerpt of λ_{ON} image (a) and λ_{OFF} (b) are shown in Figure 4-28(Exposure time 25,000 μs, P0, ϕ = 95 degrees).



(a) (b)

Figure 4-27 Layouts and target of the experiments (a) Layout of the Experiments; (b) GaAs Solar Cell.



(a) (b)

Figure 4-28 Example of captured images (a) λ_{ON} image; (b) λ_{OFF}.

The PV was detected in two image sizes. One is 82 × 83 px, the same size as the background frost glass. The other is non-trimmed 640 × 480 px. The solar cell was detected successfully in both image sizes. An excerpt from the data reduction products is shown in Figure 4-42. The center coordinates and the area size were determined using 82 × 83 px images

In Figure 4-29, the requirements are shown as horizontal dashed lines. Note that, the requirements plotted in Figure 4-22 were based on the cooperative OWPT with the fly-eye

module discussed in 4.2.1.1, however, the requirements in Figure 4-29 are based on the one without the fly-eye module discussed in 4.2.1.2. While the homogenized irradiation by the fly-eye lens will generate a substrate-like reflection from the PV, a non-diffuse reflection from the PV like Figure 4-30 is expressed by the cooperative OWPT without the fly-eye module. All the requirements are stably accommodated from exposure time = 25 μs. In case of prolonged exposure time, accommodation fails. This reflects the situation that both λ_{ON} and λ_{OFF} images are saturated, and solar cell images cannot be detected by differentiating the two images. Appropriate exposure time should be set to avoid such saturation. Generally, the minimum exposure time that accommodates the requirements depends on the rotation angle (the attitude angle) ϕ.

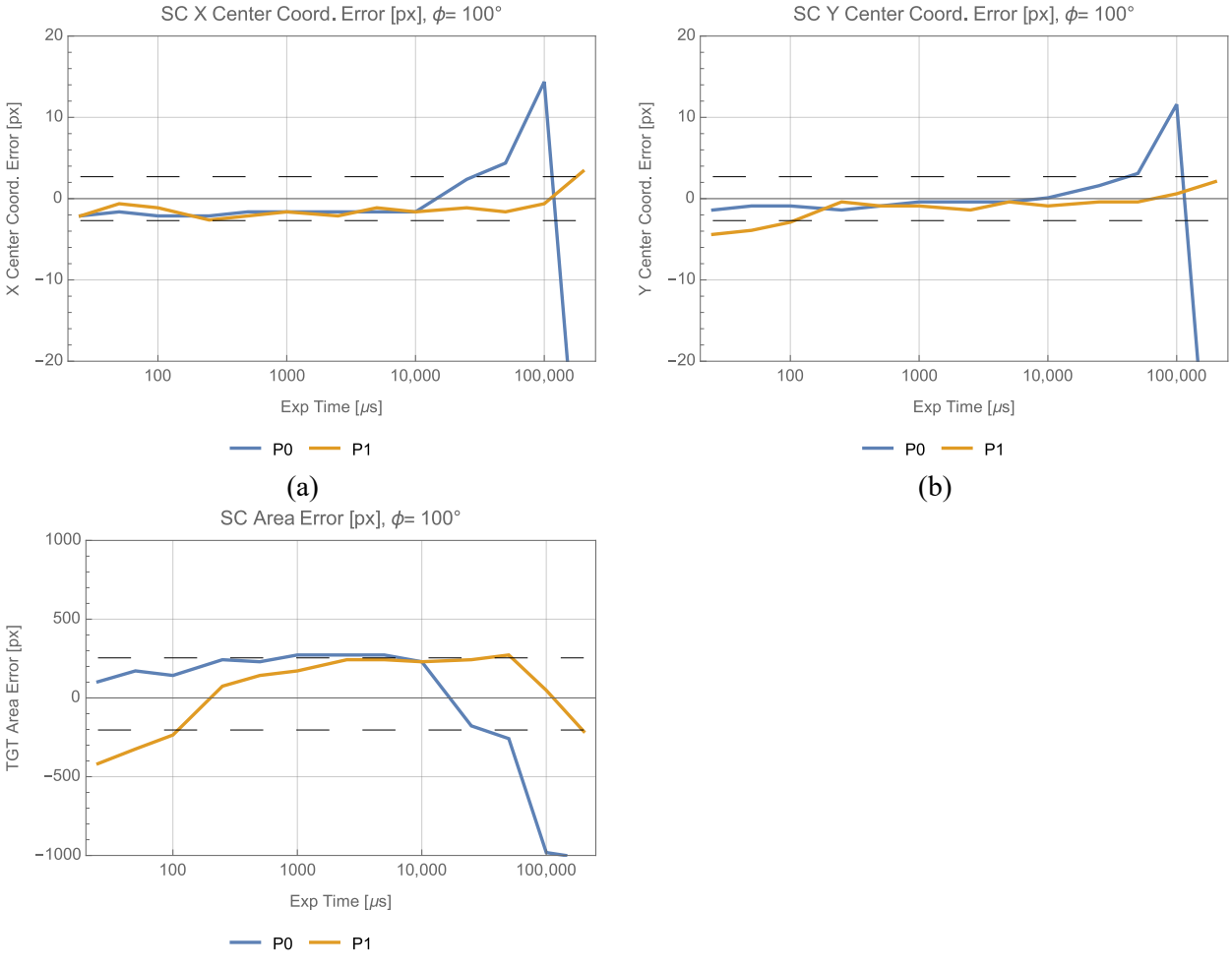


Figure 4-29 Determination example of the center coordinates and the area of GaAs solar cell (a) X center coordinate; (b) Y center coordinate; (c) Area.

Figure 4-30 shows the angular dependence of the minimum exposure time, accommodating the requirements.

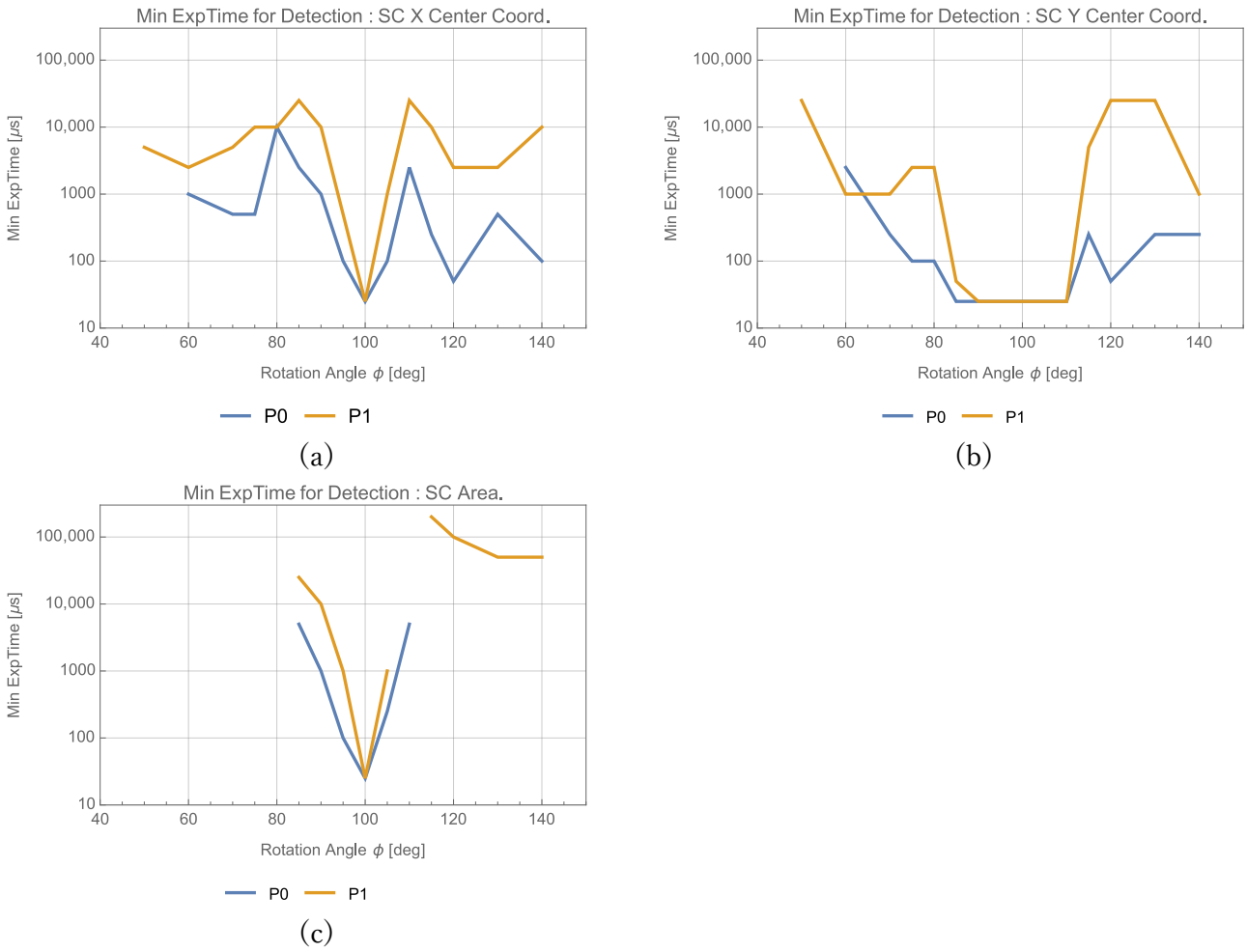


Figure 4-30 Angular dependence of the minimum exposure time for real GaAs solar cell detection, which accommodates the requirements (a) X center coordinate; (b) Y center coordinate; (c) Area.

The GaAs substrate could be stably detected within the range of 50~140 degrees. Like Figure 4-30, the angular dependence of minimum exposure time, which accommodates the requirements, is plotted in Figure 4-31. The difference between Figure 4-30 and Figure 4-31 shows the difference in angular reflectivity characteristics between the GaAs PV and the GaAs substrate. Such angular characteristics affect the detectability range.

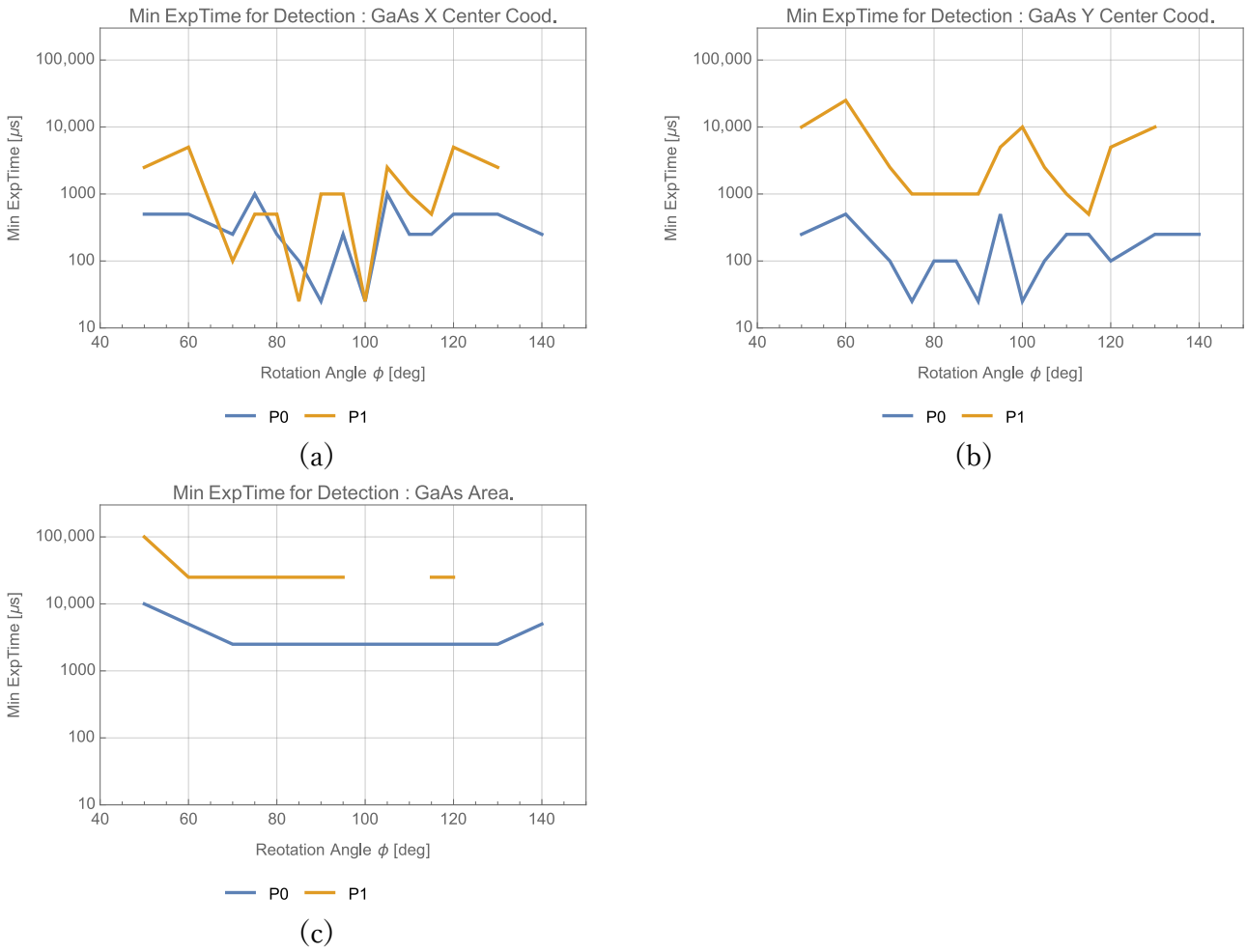


Figure 4-31 Angular dependence of the minimum exposure time for GaAs substrate detection, which accommodates the requirements (a) X center coordinate; (b) Y center coordinate; (c) Area.

It is worth discussing angular characteristics of the detectability range of GaAs PV and substrate. The minimum exposure time (Exp) to accommodate the detectability criteria at R = 56cm for the PV and 104cm for the substrate are plotted in Figure 4-30 and Figure 4-31 for a receiver diameter (D=0.94 mm), the fly-eye lens, and the number of the filter papers (n). Then, from (4-37) the range R' for different parameters such as the receiver diameter D', exposure time(Exp') without the fly-eye lens and the filter papers is expressed as follows.

$$\mathrm{R'^4} = \mathrm{R^4} Exp'/Exp(\mathrm{D'/D})^2/\mathrm{T_{FE}T_p^n} \tag{4-29}$$

For the case of the beam divergence control,

$$\mathrm{R'^2} = \mathrm{R^2} Exp'/Exp(\mathrm{D'/D})^2/\mathrm{T_{FE}T_p^n} \tag{4-30}$$

(4-29) and (4-30) for D′ = 0.94 and 50 mm are plotted in Figure 4-32 and Figure 4-33 for GaAs PV and substrate, respectively.

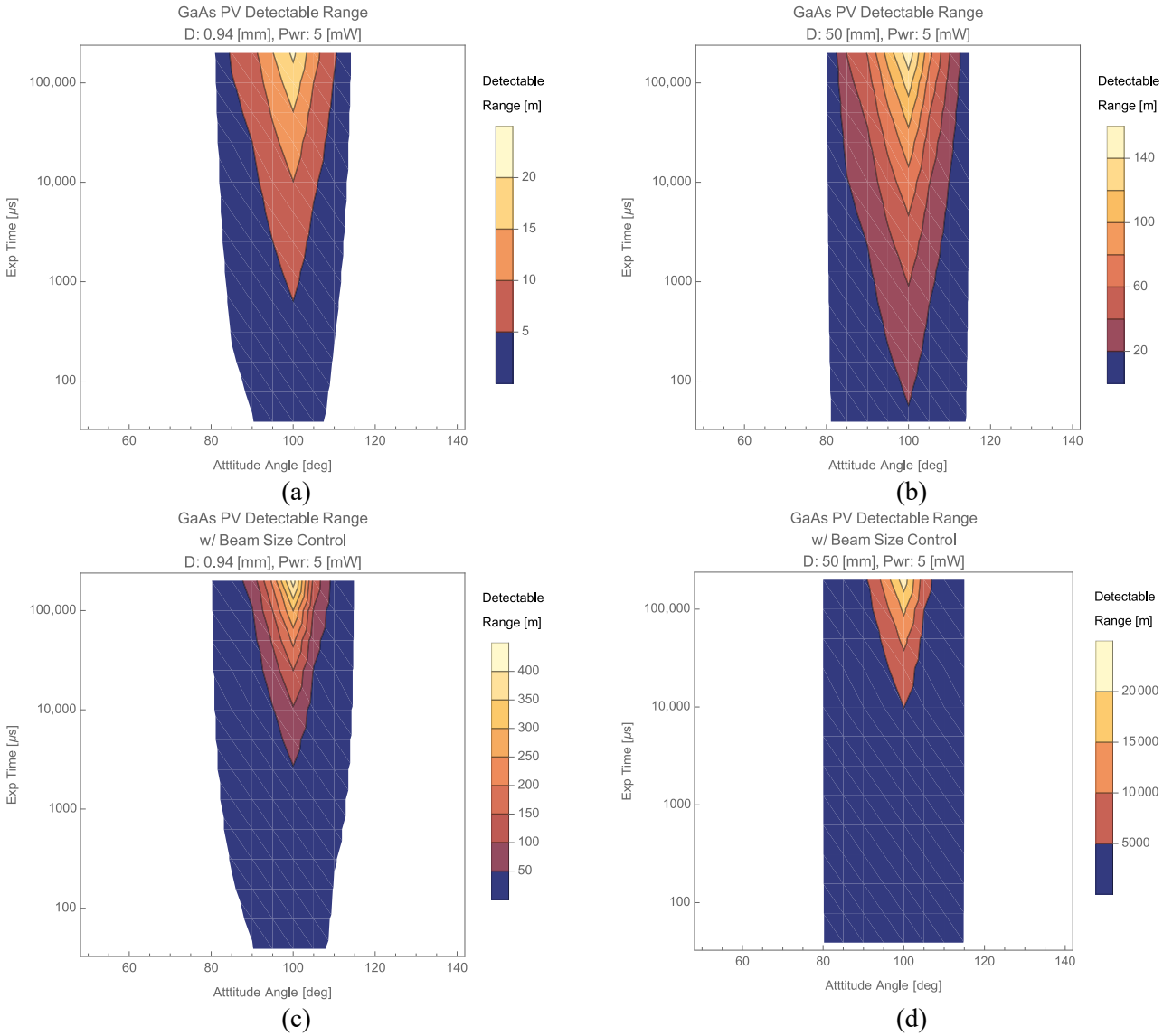


Figure 4-32 Detectable range plot for GaAs PV(Single data) (a)D=0.94mm; (b) D=50mm; (c)D=0.94mm w/Beam Size Control; (c)D=50 mm w/Beam Size Control

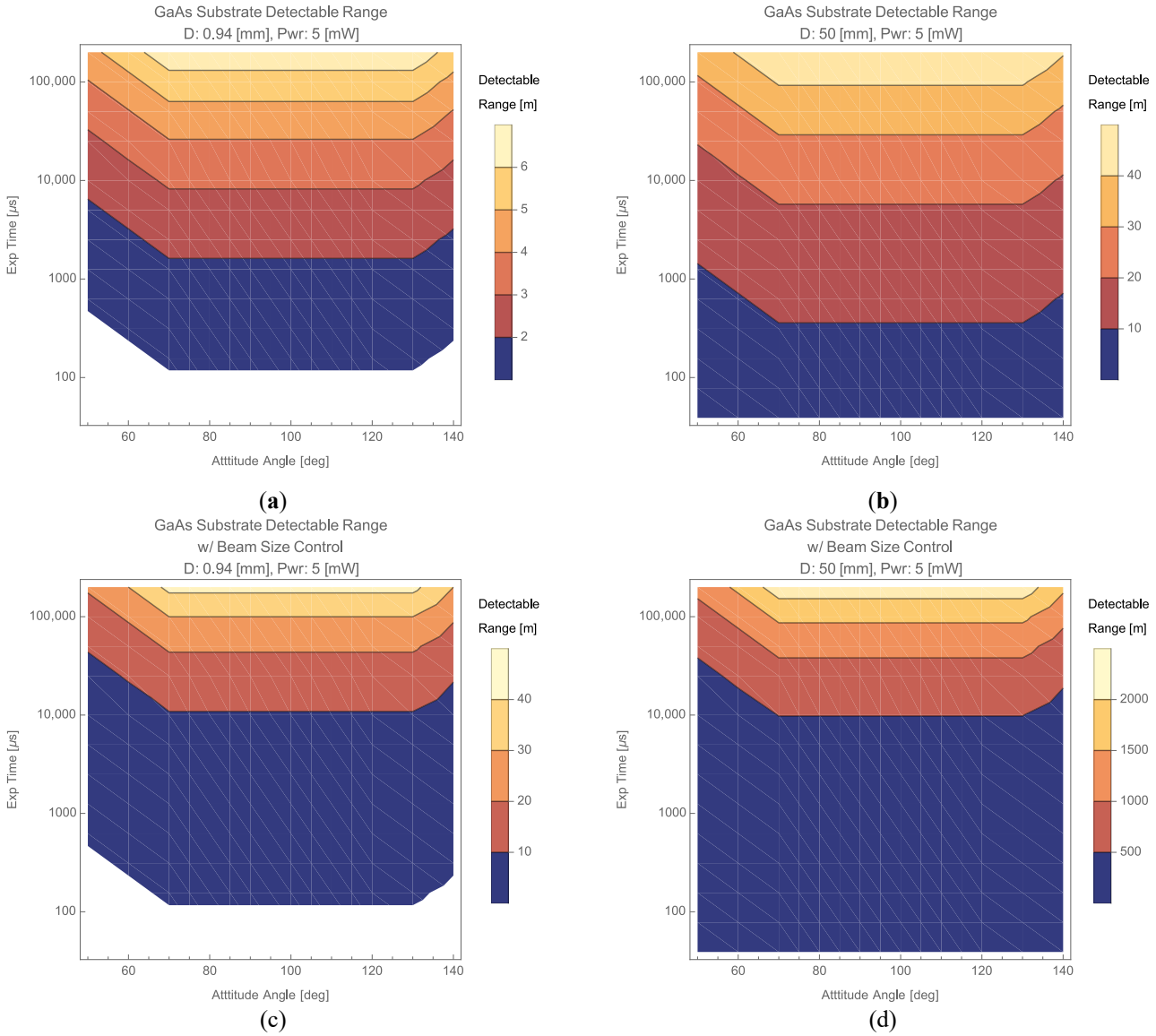


Figure 4-33 Detectable range plot for GaAs Substrate(Single data) (a)D=0.94mm; (b) D=50mm; (c)D=0.94mm w/Beam Size Control; (c)D=50 mm w/Beam Size Control

Compared with Figure 4-19(a), as long as the position and the attitude of the PV are well estimated, the strong directional reflective characteristics of the PV support a much longer detectable range, whose range performance is limited by the camera's resolution, etc. Since the reflection from the PV is limited within the neighborhood of its normal, detectability is limited within 80 ～110 deg, and outside of this region is colored white. There are similar regions in Figure 4-33(a), and (c), where detectability is limited to the exposure time larger than a certain value. Even though it is a single data, its performance is comparable with the one with the 100 data average (Figure 4-19(b)). It can be said that the effect of the over-subtraction combined with the long exposure time is comparable with the 100 data averaging.

For these two reflectivity options, the next issue is estimating the PV's position and attitude by infrared differential absorption. We propose a method to estimate position, attitude, and tracking, and we discuss consistency between the detectability criteria and the proposed position estimation method.

Appendix 4

A.4.1. Derivation of the received power model equation

Let the number of signal electrons and noise electrons be N_s, N_n, respectively. SNR is expressed by N_s, N_n.

$$\mathrm{SNR} = N_s/N_n \tag{4-31}$$

Since N_n is a function of exposure time, the number of accumulations, the internal noise parameter of the camera, and N_s, SNR is determined by N_s when the internal camera parameters, exposure time ,and the number of accumulations is a fixed constant. Assume the target is a Lambertian object. Let η_Q: quantum efficiency of a sensor inside the camera, $\Delta\sigma/\Delta\Omega$: differential cross-section of the target, $\Delta\omega$: field of view of the camera (solid angle), I_t: incident beam power density, η_r: efficiency of camera optics, ρ: diffuse reflectivity of the target, hc/λ: photon energy of the incident beam, Exp: exposure time.

Let P_t: incident beam power, A_{tr}: beam area at the target point, η_t: efficiency of transmitter optics (including intensity reduction factor). From the definition of a differential cross section in the scattering process:

$$I_t\Delta\sigma = \Delta\sigma\,\eta_t P_t/A_{tr} \tag{4-32}$$

$\Delta\sigma$ is written as $\Delta\sigma = A_{SC}$ when the area of target A_{SC} is smaller than the area of beam A_{tr}, $\Delta\sigma = A_{tr}$ when $A_{tr} > A_{SC}$. Then,

$$I_t\Delta\sigma = P_t F(R)$$

$$F(R) \equiv \begin{cases} 1 & (\text{if } A_{SC} \geq A_{TR}) \\ A_{SC}/A_{tr} & (\text{if } A_{SC} < A_{tr}) \end{cases} \tag{4-33}$$

When the target is Lambertian, $\Delta\Omega$ is evaluated as follows:

$$\Delta\Omega = \int_0^{\pi/2} 2\pi\sin\theta\cos\theta d\theta = \pi \tag{4-34}$$

Let range to target: R and the effective area of the receiver optics of the camera: A_r.

$$\Delta\omega = A_r/R^2 \tag{4-35}$$

Therefore, N_s is written as follows:

$$N_s = (\lambda/hc)\eta_r\eta_t\eta_Q P_t F(R)\, \rho A_r Exp/\pi R^2 \tag{4-36}$$

Note that the intensity reduction factor $T_{FE}T_p^n$ is included in η_t.

Assume two systems with different A_r, R, η_t provide the same SNR. Additionally, assume one system includes a fly-eye lens and n filter papers, and the other does not. The two systems are distinguished by adding a prime symbol to A_r, R, η_t, Exp. Then, equating N_s of the two systems,

$$\eta_r\eta'_t\eta_Q P_t F(R')\, \rho A'_r Exp'/\pi R'^2\, (\lambda/hc) = \eta_t\eta_t\eta_Q P_t F(R)\, \rho A_r Exp/\pi R^2\, (\lambda/hc) \tag{4-37}$$

Assume $A_{SC} < A_{tr}$ and let θ_t: transmitter beam divergence (half) angle. A_{tr} is represented as follows:

$$A_{tr} = \pi[(\theta_t R)^2 + D_0^2]/4 \tag{4-38}$$

where D_0 represents the incident beam diameter at the transmitter. In many cases, it would be reasonable to assume $(\theta_t R)^2 \gg D_0^2$ and A_{tr} is approximated as follows:

$$A_{tr} \approx \pi(\theta_t R)^2/4 \tag{4-39}$$

Regarding A_r, it is expressed using the effective diameter of the receiver optics of the camera.

$$A_r = \pi D^2/4 \tag{4-40}$$

Therefore, assuming $Exp' = Exp$, R′ is expressed by the following equation, which is (4-15), and this determines the detectable range with neither fly-eye lens nor filter papers.

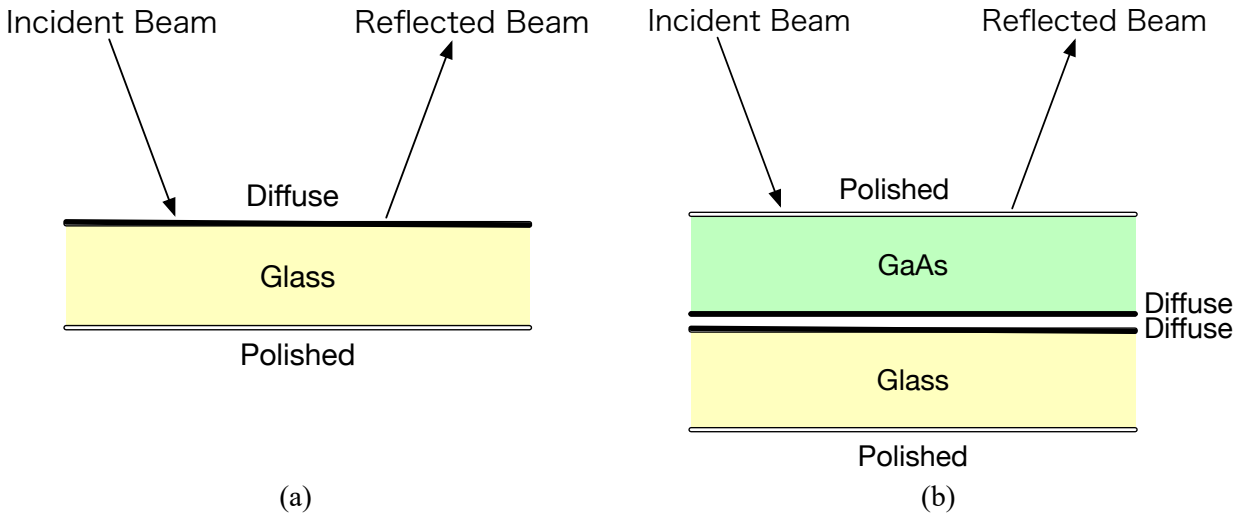
$$R'^4 = R^4(D'/D)^2/T_{FE}T_p^n \tag{4-41}$$

This expression does not include any unknown parameters, such as η_Q. All such unknowns are confined in parameters R, T_{FE}, T_p and n. Note that all of them are measured and estimated by the experiments.

A.4.2. Estimation of Diffuse Reflectivity of Si, GaAs Substrate

In the experiments of differential absorption imaging using visible light, λ_{ON} image was generated by irradiating λ = 532 nm to a Si substrate attached to a frost glass. Similarly, simulated λ_{OFF} image was generated by irradiating the same beam to the frost glass. Si image was generated from a differential image of these two. On the other hand, in infrared experiments, λ_{ON} image was generated by irradiating λ = 850 nm to a GaAs substrate attached to a frost glass. λ_{OFF} image was generated by irradiating λ = 940 nm beam to the same target. In both visible and infrared images, the brightness of λ_{ON} image of Si or GaAs is negligibly low because λ_{ON} would be strongly absorbed by these substrates.

Brightness at the position of these substrates in λ_{OFF} image affects contrast in differential data. It is affected by the frost glass diffuse reflectivity in the visible light experiments, shown in Figure 4-34(a). In infrared experiments, it is affected by the reflectivity of the composite target of a GaAs and a frost glass shown in Figure 4-34(b), each material consists of diffuse and polished surfaces. This appendix estimates the reflectivity of such targets for λ = 532 nm and λ = 940 nm based on the Fresnel reflection formula and assumption of Lambertian diffuse surface. The following notation is used throughout this section. When the entrance surface of the ray is polished (P) and the exit surface is diffuse (D), such medium is denoted as "PD". Using such notation, the medium in Figure 4-34(a) is denoted as DP, and composite media in Figure 4-34(b) is denoted as "PDDP".



(a) (b)

Figure 4-34 Samples used in the experiments (a) Frost glass sample used in visible experiments; (b) GaAs/Frost glass sample used in infrared experiments.

A.4.2.1.Reflectivity model (R_{DP}) of material of DP surfaces

Assume that light enters the medium of index n_t whose front surface is diffuse and rear surface is polished from the medium of the index n_i with incident angle θ_i, and that absorption in each medium is negligible. A light ray entering the front surface is randomly reflected and transmitted (diffused) in various directions. Each diffused ray is Fresnel reflected at the rear surface. Instead of tracing each ray, the reflectivity model is constructed such that the diffuse reflection of the front surface and the Fresnel reflection of the diffused ray at the rear surface are replaced by mean values of each ray's reflectivity over the whole beam.

In Figure 4-35, the ray entering the front surface is divided by a component diffusely reflected at the front surface ① and a component that transmits to the inside of the medium ②. Then, ② is divided into that is Fresnel reflected at the rear surface ③ and that escapes to the outside of the medium ④. Similarly, ③ is divided into that escapes to the outside ⑤ and that is diffusely reflected inside the medium.

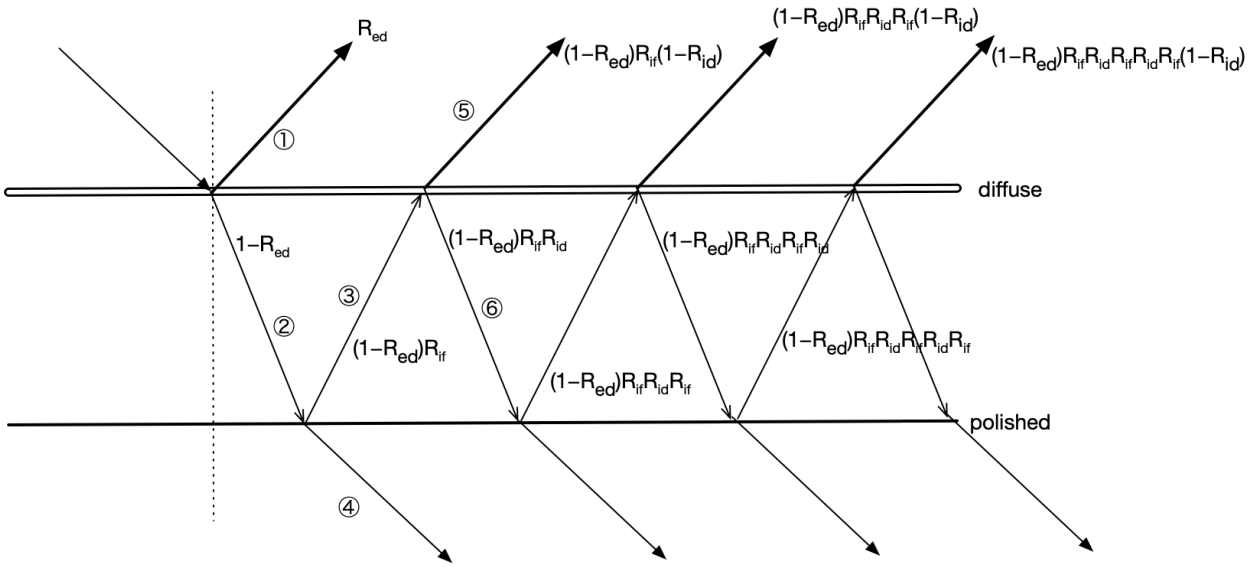


Figure 4-35 Reflectivity model of DP surface.

A.4.2.1.1. Diffuse reflectivity model (R_{ed}, R_{id})

The diffuse surface is modeled as a set of many micro facets, and each facet reflects rays following the Fresnel formula. Each facet has its tilt angle to the surface normal, and the tilt angle is distributed as Gaussian like models in[20,21]. Diffuse reflectivity is calculated by averaging resnel reflectivity of each facet. Fresnel (power) reflectivity averaged over p, s

polarization is denoted as $R(n_i, n_t, \theta_i)$. Then, $R_{ed}(n_i, n_t)$, $R_{id}(n_t, n_i)$ in Figure 4-35 can be written as

$$R_{ed}(n_i, n_t) = \int_0^{\frac{\pi}{2}} R(n_i, n_t, \theta)\, exp\left(-\frac{\theta^2}{2\sigma^2}\right) d\theta \Big/ \int_0^{\frac{\pi}{2}} exp\left(-\frac{\theta^2}{2\sigma^2}\right) d\theta \quad (4\text{-}42)$$

$$R_{id}(n_t, n_i) = \int_0^{\frac{\pi}{2}} R(n_t, n_i, \theta)\, exp\left(-\frac{\theta^2}{2\sigma^2}\right) d\theta \Big/ \int_0^{\frac{\pi}{2}} exp\left(-\frac{\theta^2}{2\sigma^2}\right) d\theta \quad (4\text{-}43)$$

A.4.2.1.2. Reflectivity model of diffused rays (R_{if})

Assume the radiance of diffusely transmitted ray is Lambertian. The model is constructed such that diffused ray with random incident angle is Fresnel reflected.

$$R_{if}(n_t, n_i) = \int_0^{\frac{\pi}{2}} R(n_t, n_i, \theta) cos\theta sin\theta\, d\theta \Big/ \int_0^{\frac{\pi}{2}} cos\theta sin\theta\, d\theta \quad (4\text{-}44)$$

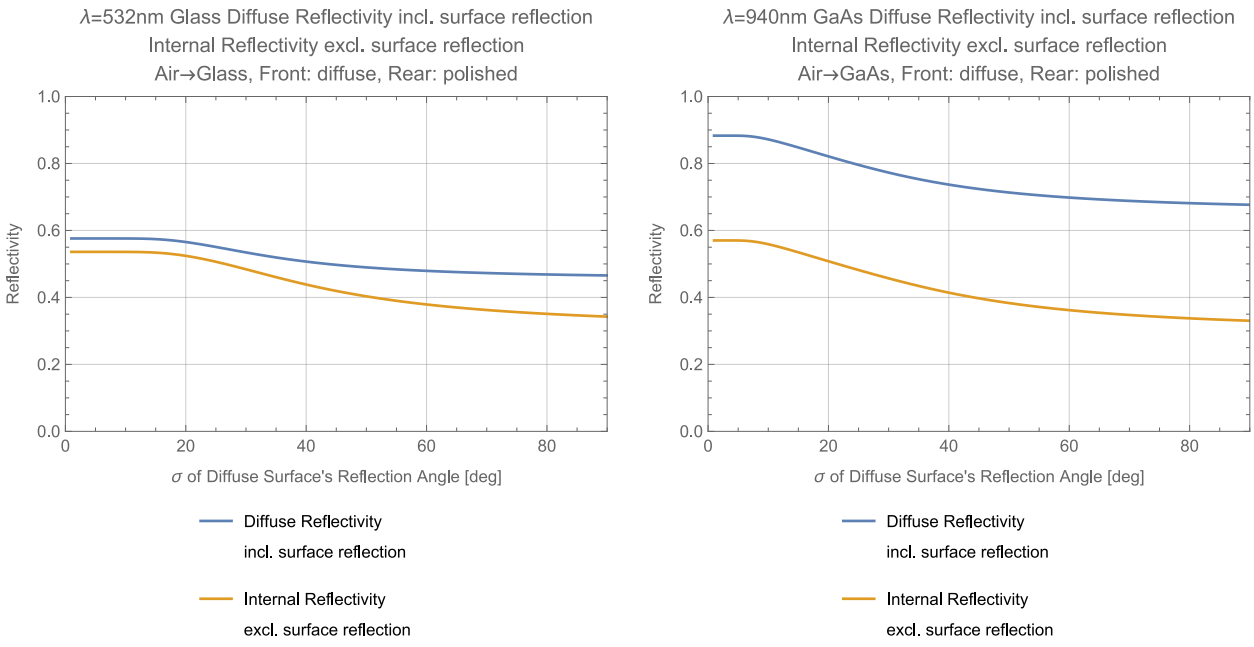
A.4.2.1.3. Calculation of reflectivity model (R_{DP})

R_{DP} can be calculated by summing all components escaping from the front surface in Figure 4-35.

$$\begin{aligned} R_{DP}(n_i, n_t) = {} & R_{ed} + (1 - R_{ed})R_{if}(1 - R_{id}) + (1 - R_{ed})R_{if}R_{id}R_{if}(1 - R_{id}) \\ & + (1 - R_{ed})R_{if}R_{id}R_{if}R_{id}R_{if}(1 - R_{id}) + \cdots \end{aligned} \quad (4\text{-}45)$$

$$= R_{ed} + (1 - R_{ed})R_{if}(1 - R_{id})/\left(1 - R_{id}R_{if}\right)$$

Figure 4-36 shows calculation for glass ($\lambda = 532$ nm, n_i=1, n_t=1.5), for GaAs ($\lambda = 940$ nm, n_i=1, n_t=3.54) with σ as the parameter. In Figure 4-36, "Diffuse Reflectivity" refers to the calculation of R_{DP}, and "Internal Reflectivity" refers to the second term of R_{DP}. The difference between "Diffuse Reflectivity" and "Internal Reflectivity" in GaAs is larger than glass. This reflects a difference in the index between glass and GaAs.



(**a**) (**b**)

Figure 4-36 Reflectivity model of DP surface R_{DP} (a) Glass; (b) GaAs.

A.4.2.2. The reflectivity model (R_{PD}) of the material consists of PD surfaces

The model can be constructed similarly. Reflectivity model R_{PD} of PD surface is obtained by summing over components escaping from the front surface in Figure A5.

$$R_{PD}(n_t, n_i, \theta) = R_{ef} + (1 - R_{ef})R_{id}(1 - R_{if}) + (1 - R_{ef})R_{id}R_{if}R_{id}(1 - R_{if}) + (1 - R_{ef})R_{id}R_{if}R_{id}R_{if}R_{id}(1 - R_{if}) + \cdots$$
$$= R_{ef} + (1 - R_{ef})R_{id}(1 - R_{if})/(1 - R_{if}R_{id}) \quad (4\text{-}46)$$

R_{ef} is Fresnel reflectivity at the polished front surface, R_{if} is the internal Fresnel reflection of diffused rays at the polished front surface described in (4-44).

$$R_{ef} = R(n_i, n_t, \theta) \quad (4\text{-}47)$$

Figure 4-38 Reflectivity model of PD surface $\boldsymbol{R_{PD}}$ (a) Glass; (b) GaAs. shows the calculation for glass and GaAs. Since the entrance surface is polished, reflectivity depends on the incident angle—the incident angle θ=36.5 degrees following the infrared experiments.

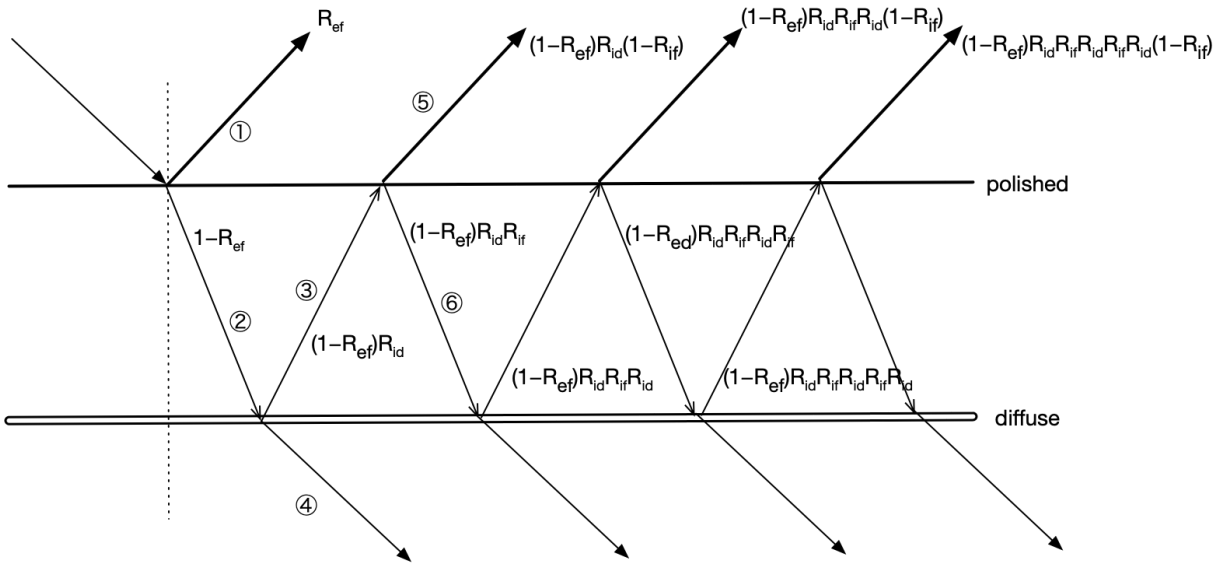
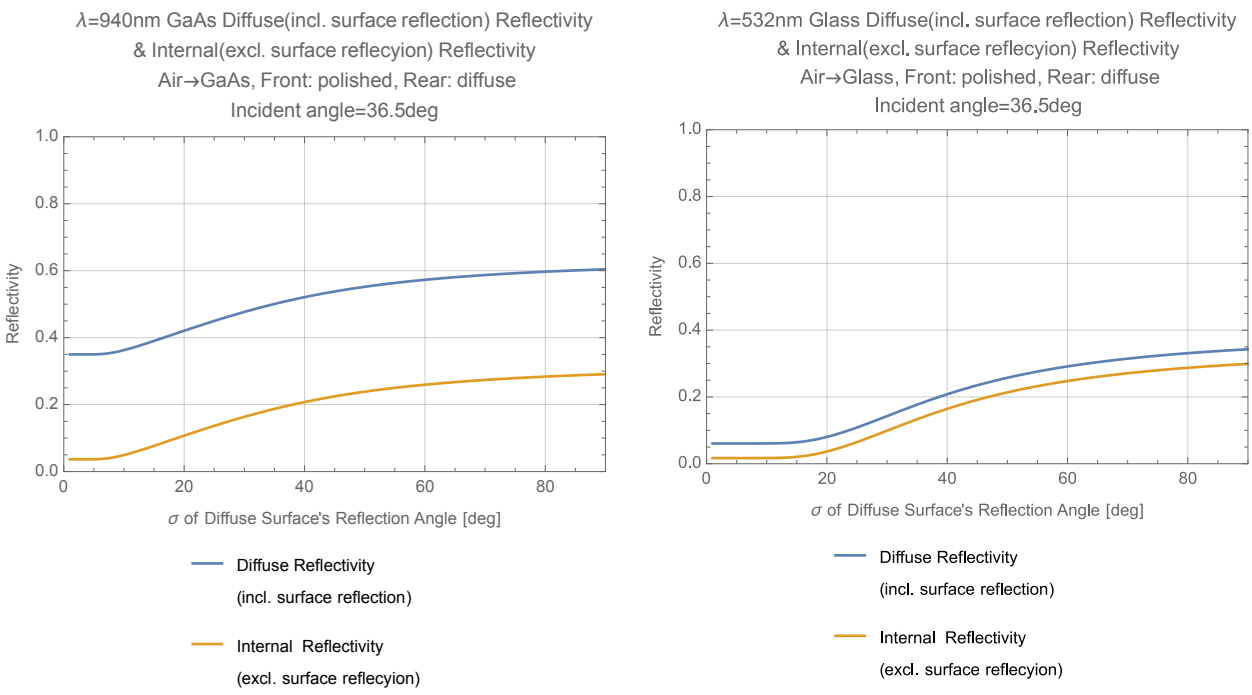


Figure 4-37 Reflectivity model of PD surface.



(**a**) (**b**)

Figure 4-38 Reflectivity model of PD surface R_{PD} (a) Glass; (b) GaAs.

Like R_{DP}, the difference between "Diffuse Reflectivity" and "Internal Reflectivity" in GaAs is larger than in glass. Especially in GaAs, it should be noted that the main part of "Diffuse

Reflectivity" comes from surface reflection and the internal reflection part is within the 10~20% range for σ = 20~40 degrees.

A.4.2.3.Reflectivity model (R_{PDDP}) of PDDP composite surface

To simulate infrared experiments, assume the ray enters a composite medium from the air of index n_i=1. The medium consists of medium1 and medium2. The medium1 (index n_t) has a PD surface, and the medium2 (index n_t') has a DP surface.

The reflectivity of medium1 is denoted as R_{PD}. Similarly, the reflectivity of medium2 is denoted as R'_{DP} in case that ray enters from a diffuse surface. There would be rays that escaped from the polished surface of medium2 and reenters. Such rays' contributions are ignored.

Considering Figure 4-35 and

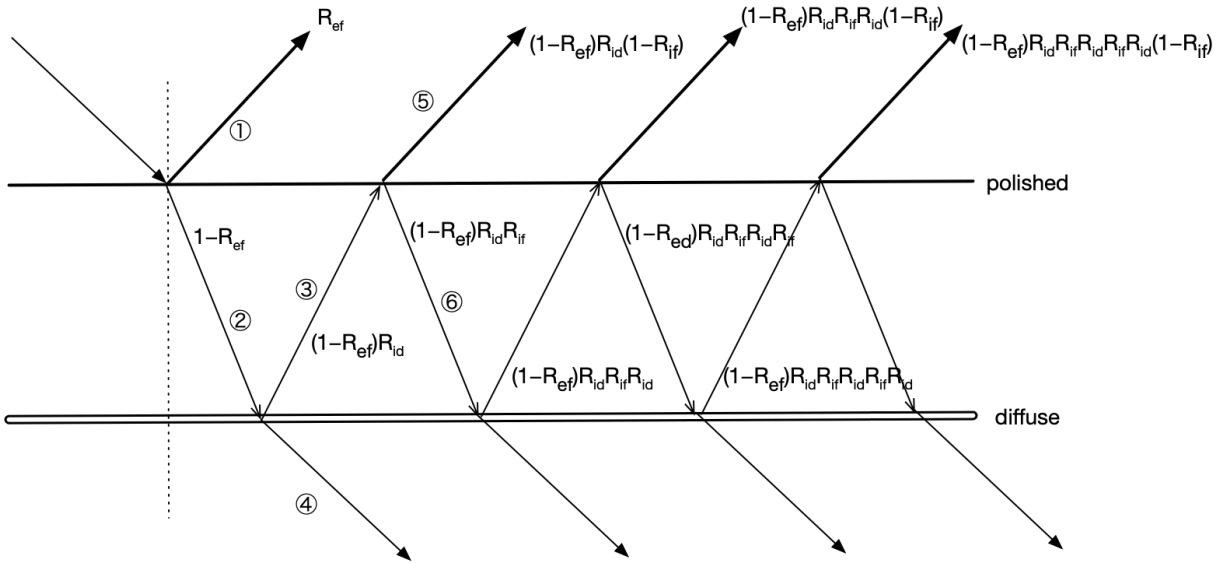


Figure 4-37, the reflectivity of composite media R_{PDDP} can be calculated from Figure 4-39 and expressed as,

$$R_{PDDP}(n_i, n_t, \theta) = R_{PD}(n_i, n_t, \theta) + \big(1 - R_{PD}(n_i, n_t, \theta)\big)R'_{DP}(n_i, n'_t)\big(1 - R_{DP}(n_i, n_t)\big)/\Big(1 - R_{DP}(n_i, n_t)R'_{DP}(n_i, n'_t)\Big) \quad (4\text{-}48)$$

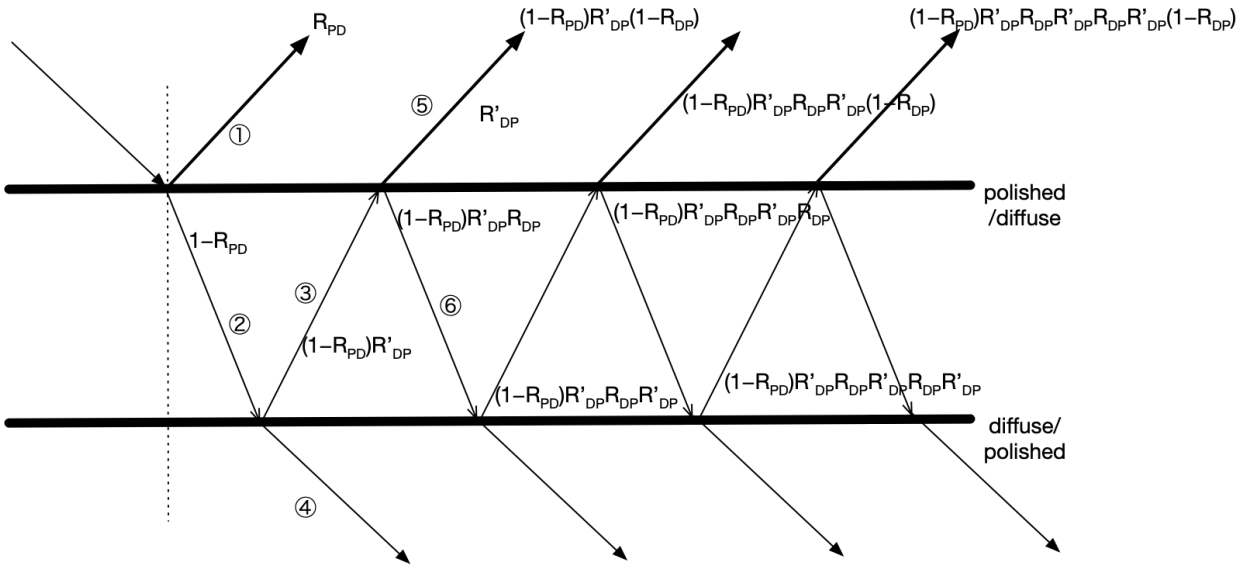


Figure 4-39 Reflectivity model of composite PDDP surfaces.

Figure 4-39 shows the reflectivity calculation of composite media consisting of GaAs PD and glass DP surface. Calculations are for both cases of including Fresnel reflection from the front surface and excluding such Fresnel components.

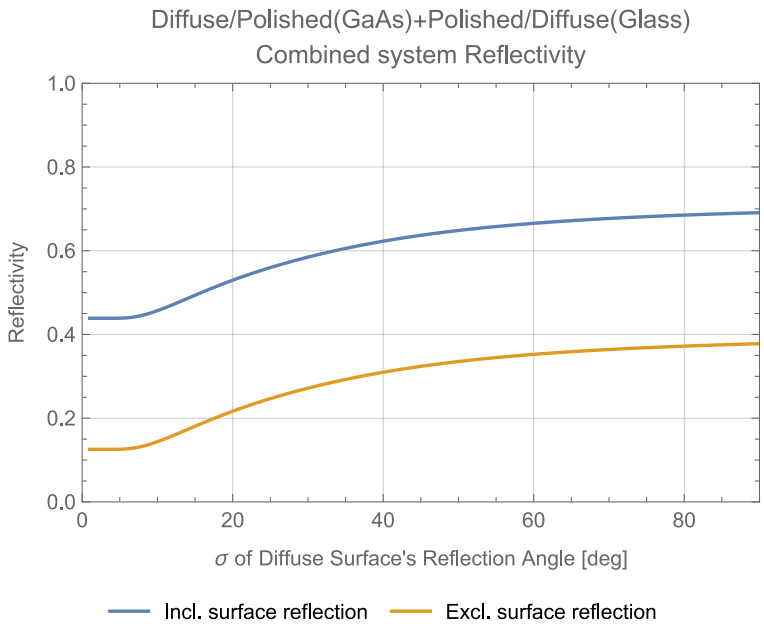


Figure 4-40 The reflectivity of composite media consisting of GaAs PD and glass DP surfaces.

A.4.2.4.The ratio of diffuse reflectivity of visible experiments to infrared

ρ_{532} in (4-23) is identified as $R_{DP}(Glass)$ and ρ_{940} as $R_{PDDP}\left(\frac{GaAs}{Glass}\right)$. From Figure 4-40, $R_{PDDP}\left(\frac{GaAs}{Glass}\right)$ = 0.2~0.3 within σ = 20~30degrees range [20]. Since $R_{DP}(Glass)$ = 0.5~0.55, therefore, their ratio is estimated to be

$$\frac{\rho_{532}}{\rho_{940}} = \frac{R_{DP}(Glass)}{R_{PDDP}\left(\frac{GaAs}{Glass}\right)} \cong 1.7\sim2.75 \quad (4\text{-}49)$$

A.4.3. Excerpt from Data Reduction Products (Example of Differential Image, Binarized Image of GaAs Substrate)

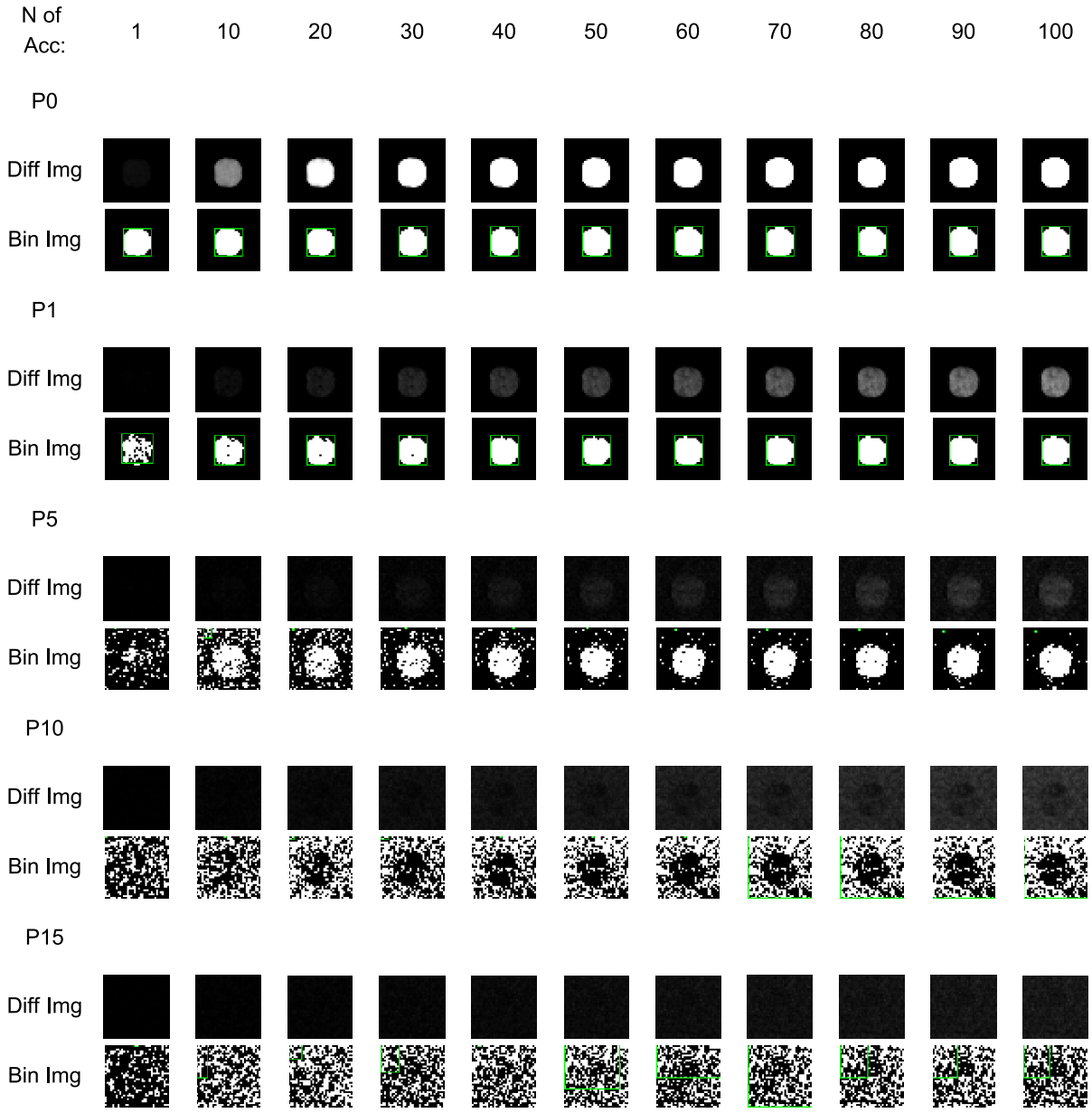


Figure 4-41 Example of differential, binarized image of GaAs substrate. Upper row: Differential image, Lower row: Binarized image, trimming size: 34 × 33 px, Exposure time: 25,000 μs, Horizontal: Number of accumulation (from left to right: 1, 10, 20, 30, 40, 50, 60, 70, 80, 90, 100 times) Highlight in the binarized image represents boundary rectangle of connected components which has the largest area.

A.4.4. Excerpt from Data Reduction Products (Example of Differential Image, Binarized Image of GaAs Solar of Cell)

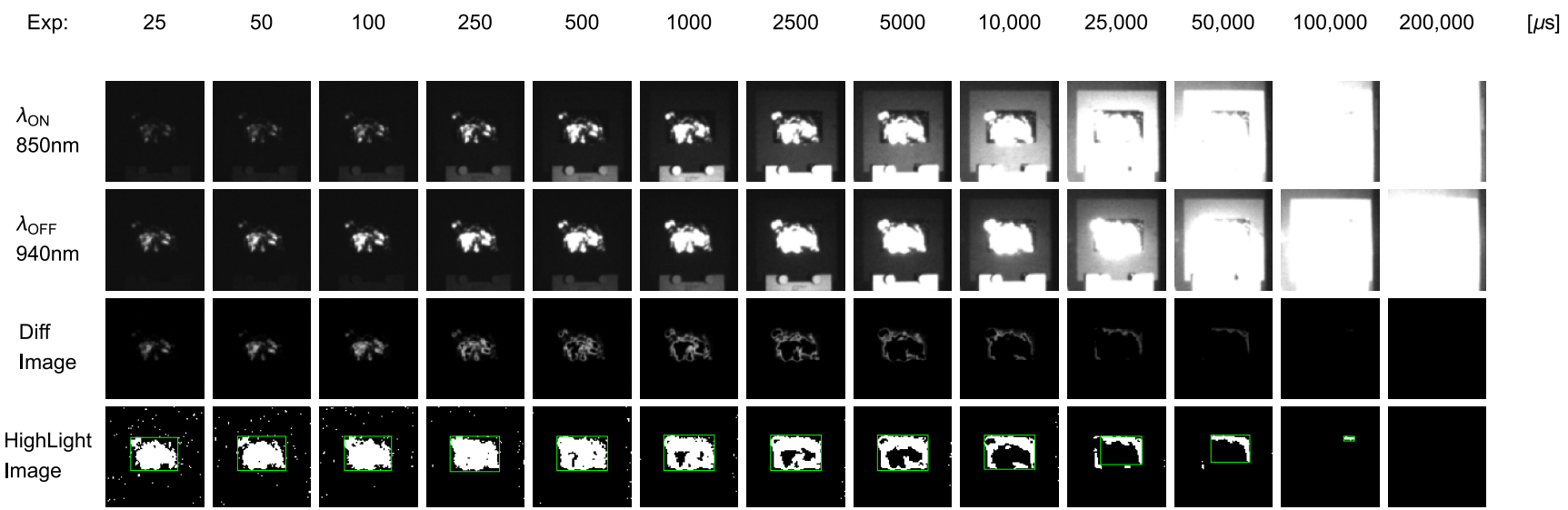


Figure 4-42 Examples of solar cell detection.

From upper row to lower row: λ_{ON} image, λ_{OFF} image, Differential image, Binarized image, Trimming size: 82 × 83 px, Power control status P0. The binarization threshold was set to 1/255. Exposure time: 25, 50, 100, 250, 500, 1000, 2500, 5000, 10,000, 25,000, 50,000, 100,000, 200,000 μs. The binarized image's highlight represents the boundary rectangle of connected components which has the largest area. This example shows the case of the rotatable stage angle ϕ = 100 degrees, and the solar cell is stably detected from exposure time 25 μs.

References 4

1. Differential Absorption Lidar | Elsevier Enhanced Reader Available online: https://reader.elsevier.com/reader/sd/pii/B9780123822253002048?token=ACBBE2F8761774F5628FC13C0F6B8E339140949E50BF9DE9F5063F95873CC081FB2353E862E10CA4576416252562C600&originRegion=us-east-1&originCreation=20220824035349 (accessed on 24 August 2022).
2. Dual-Wavelength Measurements Compensate for Optical Interference | May 7, 2004 Available online: https://www.biotek.com/resources/technical-notes/dual-wavelength-measurements-compensate-for-optical-interference/ (accessed on 24 August 2022).
3. Herrlin, K.; Tillman, C.; Grätz, M.; Olsson, C.; Pettersson, H.; Svahn, G.; Wahlström, C.G.; Svanberg, S. Contrast-Enhanced Radiography by Differential Absorption, Using a Laser-Produced x-Ray Source. *Invest Radiol* **1997**, *32*, 306–310, doi:10.1097/00004424-199705000-00009.
4. Intel *Intel® RealSense™ D400 Series Data Sheet*;
5. Intel® RealSense™ Available online: https://www.intelrealsense.com/sdk-2/ (accessed on 24 August 2022).
6. Open CV Available online: https://opencv.org/ (accessed on 23 August 2022).
7. Welcome to Python.Org Available online: https://www.python.org/ (accessed on 24 August 2022).
8. Otsu, N. A Threshold Selection Method from Gray-Level Histograms. *IEEE Transactions on Systems, Man, and Cybernetics* **1979**, *9*, 62–66, doi:10.1109/TSMC.1979.4310076.
9. Binarize Wolfram Language Documentation Available online: https://reference.wolfram.com/language/ref/Binarize.html.en?source=footer (accessed on 15 August 2022).
10. Asaba, K.; Miyamoto, T. System Level Requirement Analysis of Beam Alignment and Shaping for Optical Wireless Power Transmission System by Semi–Empirical Simulation. *Photonics* **2022**, *9*, 452.
11. Mori, N. Design of Projection System for Optical Wireless Power Transmission Using Multiple Laser Light Sources, Fly-Eye Lenses, and Zoom Lens. *OWPT2019* **2019**, OWPT-4-02.
12. Katsuta, Y.; Miyamoto, T. Characterization and Optimization of Fly-Eye Lens System in Optical Wireless Power Transmission. In Proceedings of the 2019 24th Microoptics Conference (MOC); IEEE: Toyama, Japan, November 2019; pp. 288–289.
13. GPS.Gov: GPS Accuracy Available online: https://www.gps.gov/systems/gps/performance/accuracy/ (accessed on 9 May 2022).

14. Industrial Cameras: Spectral Sensitivity Available online: https://s1-dl.theimagingsource.com/api/2.5/packages/publications/whitepapers-cameras/wpspectsens/a5cb0f39-fea8-56ae-8e04-ec20ab4e72c9/wpspectsens_1.30.en_US.pdf (accessed on 29 December 2022).
15. OS13CA5111A Available online: https://www.optosupply.com/uppic/20211028118028.pdf (accessed on 29 December 2022).
16. OSI5FU511C-40 Available online: https://akizukidenshi.com/download/OSI5FU5111C-40.pdf (accessed on 29 December 2022).
17. Wolfram Mathematica: Modern Technical Computing Available online: https://www.wolfram.com/mathematica/ (accessed on 15 August 2022).
18. Corporate Profile | AXT, Inc. Available online: http://axtinc.gcs-web.com/ (accessed on 14 February 2023).
19. Asaba, K.; Moriyama, K.; Miyamoto, T. Preliminary Characterization of Robust Detection Method of Solar Cell Array for Optical Wireless Power Transmission with Differential Absorption Image Sensing. *Photonics* **2022**, *9*, 861, doi:10.3390/photonics9110861.
20. Oren, M.; Nayar, S.K. Generalization of Lambert's Reflectivity Model. In Proceedings of the Proceedings of the 21st annual conference on Computer graphics and interactive techniques - SIGGRAPH '94; ACM Press: Not Known, 1994; pp. 239–246.
21. Torrance, K.E.; Sparrow, E.M. Theory for Off-Specular Reflection From Roughened Surfaces*. *J. Opt. Soc. Am., JOSA* **1967**, *57*, 1105–1114, doi:10.1364/JOSA.57.001105.
22. ロケットや人工衛星等の宇宙開発と人工衛星打上サービスの先端技術研究所 宇宙開発 Available online: https://www.ati-space.com/ATI.files/company.htm (accessed on 15 February 2023).

5. Position and Attitude Estimation of Photovoltaics

As long as the detectability criteria are satisfied, Figures 4-32 and 4-33 show the angular dependence of detectable ranges. Next, we propose a position estimation method expected to accommodate the detectability criteria in a scale-invariant (non-dimensional) way. From a similar discussion in 4.2.2, assuming $\Delta\theta$ varies as $1/R$, pixel coordinates are regarded as scale invariant. Therefore, we discuss experiments in Sections 5 and 6 using scale-invariant parameters such as pixel coordinates, SNR (equivalent to Exp: exposure time), and other inherent lengths to make the discussion in such a way except discussion in the real 2D experiment space in which $\Delta\theta$ is fixed at a certain value. Note that we estimate that relative position between the camera and the target.

5.1. The Positioning Experiments using a GaAs Substrate

5.1.1. The Experiment Configuration and the Coordinate System Definition

In the concept-proof experiments, targets were alternately illuminated by different wavelength LEDs of λ_{ON} (850 nm) and λ_{OFF} (940 nm) and captured by a single camera. Figure 5-1 shows the layout of the positioning experiments.

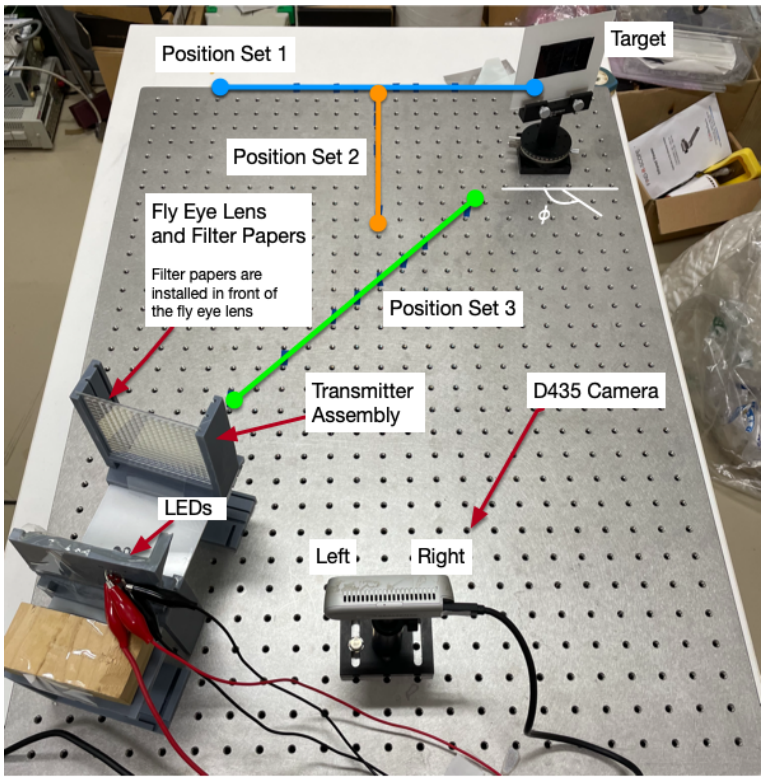


Figure 5-1 Layout of the experiments on position information.

The transmitter assembly consists of 850 nm and 940 nm LEDs, both of which are two 2 mW LEDs connected in series [19,20]. Like in the concept-proof experiments, a fly-eye lens was installed in front of the LEDs to expand their beam size to be large enough to cover the target. The beam divergence of the transmitter assembly was estimated to be about 85 deg (full angle, without filter paper). The power reduction by the filter paper was about 50 %/paper, calculated by the brightness of the captured image. As for the infrared camera, an Intel Realsense D435™ depth camera [21,22] was used. Even though it can generate depth information, this function was not used throughout this thesis. Instead, two infrared output streams of the camera were directly inputted into the image processor (PC) and processed by dedicated software. Images were captured with various exposure times. These were 25, 50, 100, 250, 500, 1000, 2500, 5000, 10,000, 25,000, 50,000, 100,000, and 200,000 μs. The camera gain was 240 (maximum value), and the output image size was 640 × 480 px. The rest of the internal parameters were not changed from their default values. As for target assembly, the target in the experiments of the current section was the GaAs substrate used in Section 4. It was fixed on a frost glass, and its attitude was varied by rotating the stage on which it was installed. The angle of the rotatable

stage ϕ increases counterclockwise and is defined as 90 degrees (deg) when the target faces normal to the camera. There are 23 (horizontal) × 31 (vertical) screw holes on the optical bench used in the experiments, and the pitch is 25.4 mm. Positions of these holes were regarded as lattice points of the 2D (x, y) coordinate system on the bench, whose coordinates were defined to vary with $-11 \leq x \leq 11$, $-3 \leq y \leq 27$, respectively. The camera (D435) was installed at the origin (0,0), and its front face was aligned to the +Y direction. In the experiments, the positions of the targets were set as the following Position Set 1, 2, and 3 and shown in Figure 5-1.

Position Set 1 = $(-8,27), (-4,27), (-2,27), (-1,27), (0,27), (1,27), (2,27), (4,27), (8,27)$

Position Set 2 = $(0,27), (0,26), (0,25), (0,23), (0,19)$

Position Set 3 = $(-6,9), (-4,11), (-2,13), (-1,14), (0,15), (1,16), (2,17), (4,19), (8,23)$

Typical parameters in this experiment are summarized in Table 5-1

Table 5-1 Parameter in the experiments.

Transmitter Assembly	**Parameters**
LED power	2 mW × 2 for λ = 850 nm and 940 nm
Beam divergence	85 deg (full angle)
Filter paper transmittance	50%/paper(typical)
Target Assembly	
GaAs substrate	2-inch diameter
GaAs PV	6 cm × 4 cm
Distance from the camera assembly	660 mm(typical)
Attitude angle	43~123 deg (typical)
Camera Assembly	
Camera	D435 × 2
Exposure time	25, 50, 100, 250, 500, 1000, 2500, 5000, 10,000, 25,000, 50,000, 100,000 and 200,000 μs
Image size	640 × 480 px

Figure 5-2 shows the procedure for generating the range information, which is the Y-coordinate of the target on the 2D plane. The target images from the left and right sensors were generated by differentiation and binarization of the ones from the two infrared streams. From the center coordinates of the target detected in each image, its range (the Y-coordinate) was estimated from the parallax between them. Finally, the X-coordinate of the target was determined from the

range and the center coordinate. The mathematical formulation of this position estimation is summarized in A.5.1.

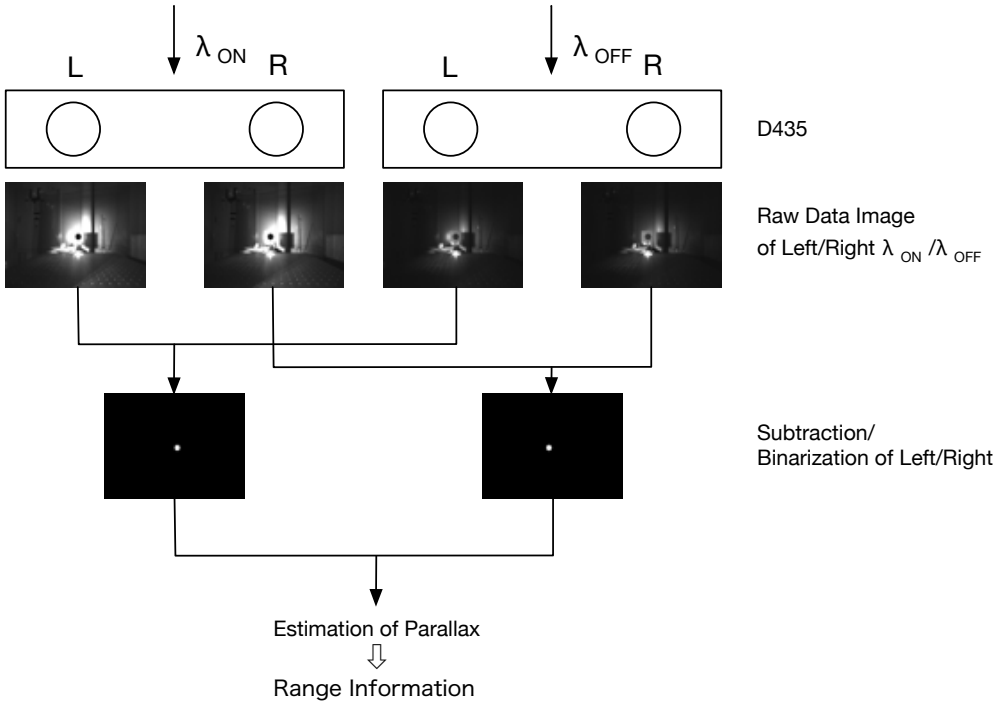


Figure 5-2 Procedure of generating range information from left/right differential images.

5.1.2. Integrity Measure

Available exposure time settings of D435 range from 25 to 200,000 μs for its infrared streams. The accuracy of the center coordinates and the area size estimation are affected by this exposure time. To obtain a reasonable estimation accuracy, the necessary exposure time for the target should be determined. Although this depends on the configuration and the measurement system, a set of conditions can be defined that determines the minimum necessary exposure time. Since this is derived from the consistency consideration of the stereo imagery and it reflects the integrity of positioning, this is referred to as the ”integrity measure” in this thesis.

- First condition (C1)

  Figure 5-3 shows the target, two optical axes of the camera, and three regions in the 2D real space, with symbols representing the following: T: target; LL’: the optical axis of the left image sensor; RR’: the optical axis of the right image sensor. The plane is divided into three zones: Zone 1 is to the right of RR’, Zone 2 is between RR’

and LL', and Zone 3 is to the left of LL'. Assume that the target is found at (ξ_L, η_L) and (ξ_R, η_R) in the pixel coordinate system of the images captured by the left and the right image sensors, respectively. Since the width of the captured image is 640 px, $0 < (\xi_R - 320) < (\xi_L - 320)$ holds in Zone1, $(\xi_R - 320) < 0 < (\xi_L - 320)$ in Zone2, and $(\xi_R - 320) < (\xi_L - 320) < 0$ in Zone3. Thus, $(\xi_L - 320) - (\xi_R - 320) > 0$ holds in every zone. Note that this condition guarantees the positiveness of the estimated Y-coordinates ($y > 0$) in (5-32).

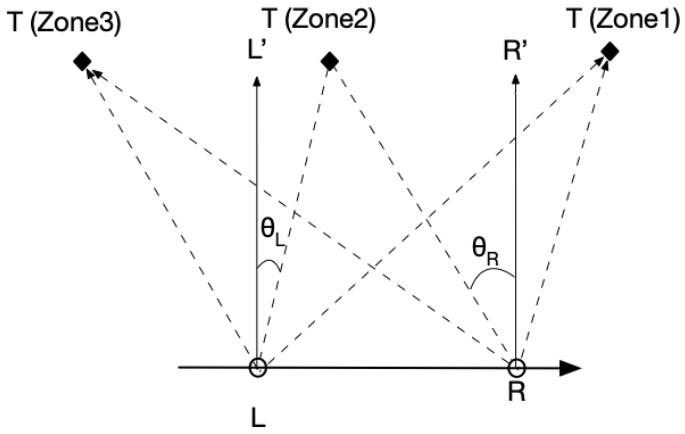


Figure 5-3 Integrity measure C1.

- Second condition (C2)

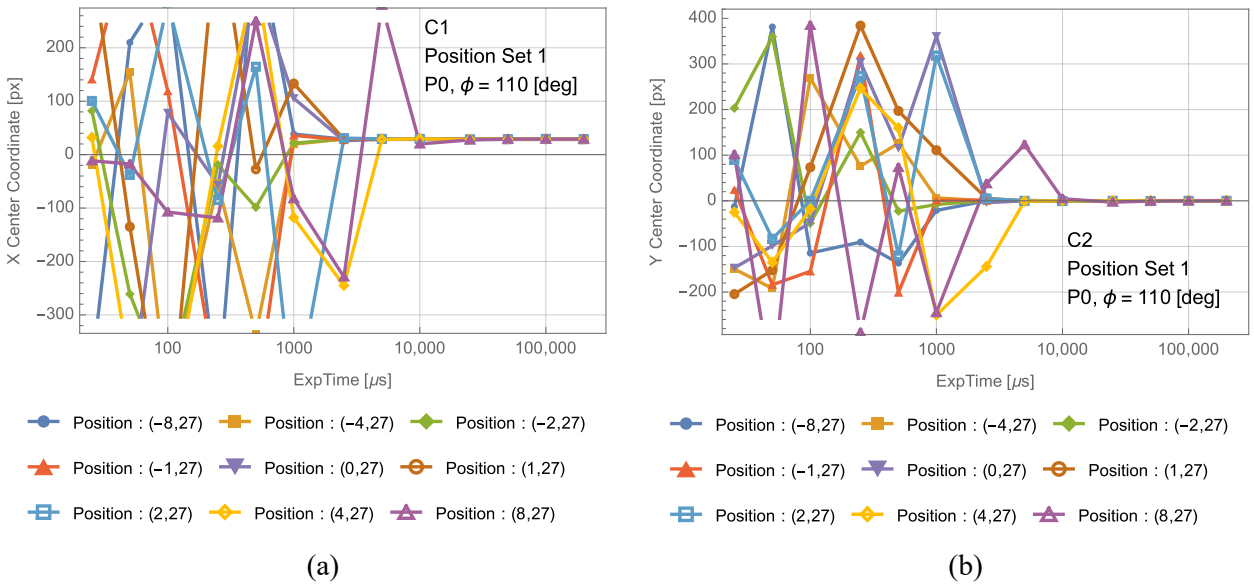
  Since the two optical axes of the left and the right image sensors are on the same plane, the vertical component of the center coordinate of the target detected by the left sensor is equal to the one detected by the right. Therefore, $\eta_R = \eta_L$ holds.

These are the necessary conditions for the two coordinates determined by the left and right sensors to represent the same point in the target. From the above discussions, the following conditions are adopted as the "integrity measure". It is worth noting that, since these requirements are written by pixel coordinates, they are scale-invariant.

$$\text{C1: } \xi_L - \xi_R > 0 \tag{5-1}$$

$$\text{C2: } \eta_L - \eta_R = 0 \tag{5-2}$$

In Figure 5-4, C1 and C2 are plotted for each position of Position Set 1 against the exposure time. The attitude angle of the target was set Off-axis (ϕ = 110 deg) to the target to avoid excessive received power. Similar plots were obtained for both Position Sets 2 and 3 as well.



(a) (b)

Figure 5-4 Integrity measure of Position Set 1 (GaAs substrate). (a) C1 ($\xi_L - \xi_R$) against exposure time; (b) C2 ($\eta_R - \eta_L$) against exposure time.

As the exposure time increases, the fluctuations in both C1 and C2 rapidly disappear, and they converge. C2 was implemented as in (5-3), using the ”Vertical Threshold” parameter in the image processing software developed for the experiments.

$$|\eta_L - \eta_R| \leq Vertical\ Threshold \tag{5-3}$$

Figure 5-5 shows plots representing the relationship between the integrity measure and the estimated positioning accuracy for Position Set 1. Similar results were obtained for Position Sets 2 and 3. The “Mean Error” in the vertical axis is the mean positioning error averaged over Position Set 1, and data that did not satisfy (5-3) were removed.

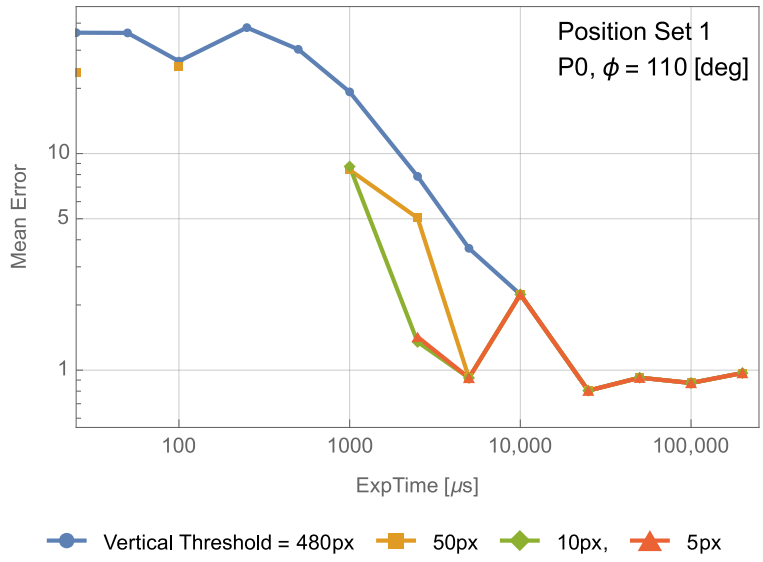


Figure 5-5 Mean positioning error along Position Sets 1, 2, and 3.

Comparing Figure 5-4 and Figure 5-5, the minimum exposure time of the integrity measure convergence in Figure 5-4 is correlated with that of the positioning accuracy convergence in Figure 5-5. Thus, convergence of the integrity measure can be identified as that of the positioning accuracy. Also, from Figure 5-5, once the integrity measure converges, the positioning accuracy is not affected by the Vertical Threshold. Since a larger value is desirable to avoid unnecessary data rejection, Vertical Threshold = 50 was set for the following discussions.

5.2. Positioning Experiments using a GaAs Substrate

Figure 5-6 shows the position estimation results of a GaAs substrate for Position Sets 1, 2, and 3. Both the vertical and horizontal lines are plotted using the lattice coordinates normalized by the screw hole pitch = 25.4 mm, and the solid gray dots and lines in the figures represent the true values.

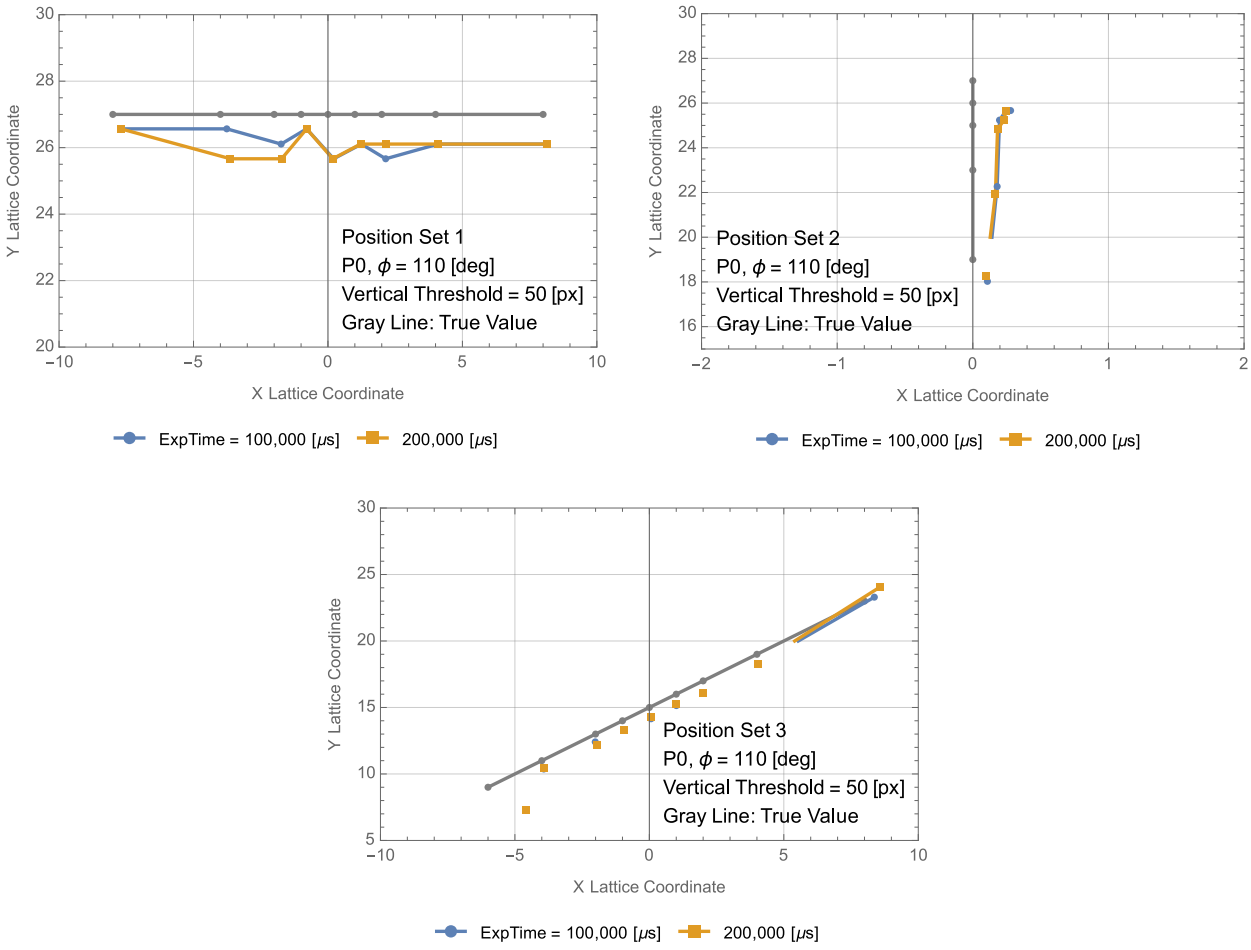


Figure 5-6 Estimated position of the GaAs substrate.

Position estimation consists of range and direction estimation. The estimated direction (azimuth angle) in the 2D plane ψ defined by (5-4) is plotted in Figure 5-7.

$$\psi = tan^{-1}\left(\frac{x}{y}\right) \tag{5-4}$$

The error limit of the estimation is defined such that the irradiated beam marginally hits the target when it deviates an angle ε from its true value ψ (deg). Let ϕ (deg) the target's attitude, L be its full width, and R be its range. Then, ε can be expressed by (5-5).

$$\varepsilon = tan^{-1}\frac{d\ cos(\psi + \phi - 90)}{R - \frac{L}{2}\ sin(\psi + \phi - 90)} \tag{5-5}$$

Let $(\Delta x, \Delta y)$ be positioning errors, then the direction estimation error of the target Δψ can be expressed as

$$\Delta\psi = \frac{y\,\Delta x - x\,\Delta y}{x^2 + y^2} \tag{5-6}$$

Using dimensions of the experiments in these experiments, $\Delta\psi$ is suppressed by the factors of order $\mathcal{O}(10^{-1}) \sim \mathcal{O}(10^{-2})$. Thus, direction can be more accurately estimated than range.

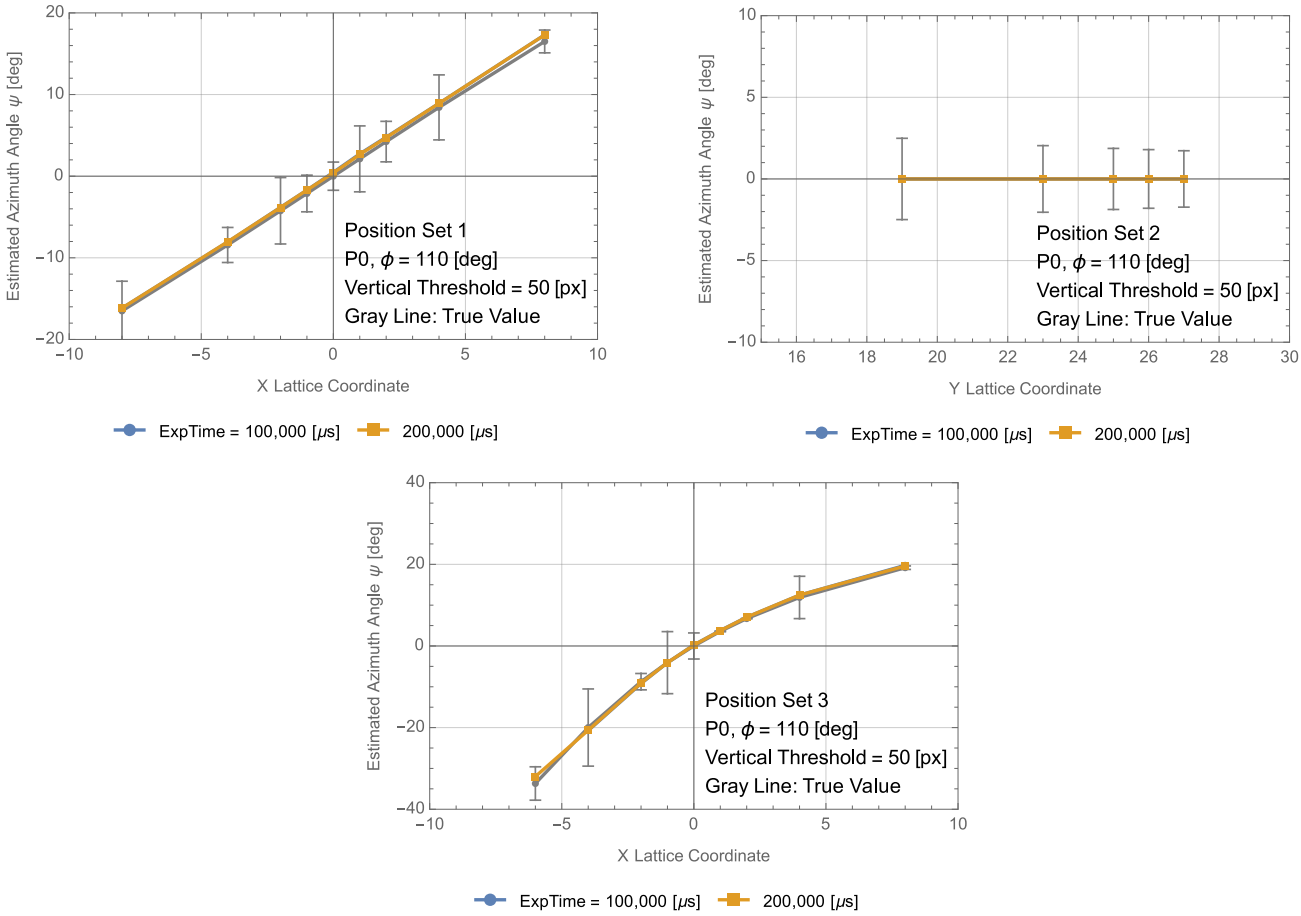


Figure 5-7 Estimated direction of the GaAs substrate. The error bars are defined by (5-5).

5.2.1. Introducing The Coaxial Optics

In the experiments of Figure 5-1, the target was alternately illuminated by λ_{ON} and λ_{OFF}, and the images of these wavelengths were also alternately captured by the camera. This means that, in the case of moving targets, the target position in each wavelength image is different. To avoid this issue, the following measurement equipment with two coaxial optics was introduced into the experiments. This equipment will be advantageous for moving target detection. The drawings of the equipment are shown in Figure 5-8(a), (b), (c). Internal configuration is shown in Figure 5-9(a),(b). It has two coaxial optics inside. After the received lights are separated into

50% and 50% by the beam splitters shown in Figure 5-8(b), (c), λ_{ON} and λ_{OFF} are separated by the wavelength filters [28,29] shown in Figure 5-8(c).

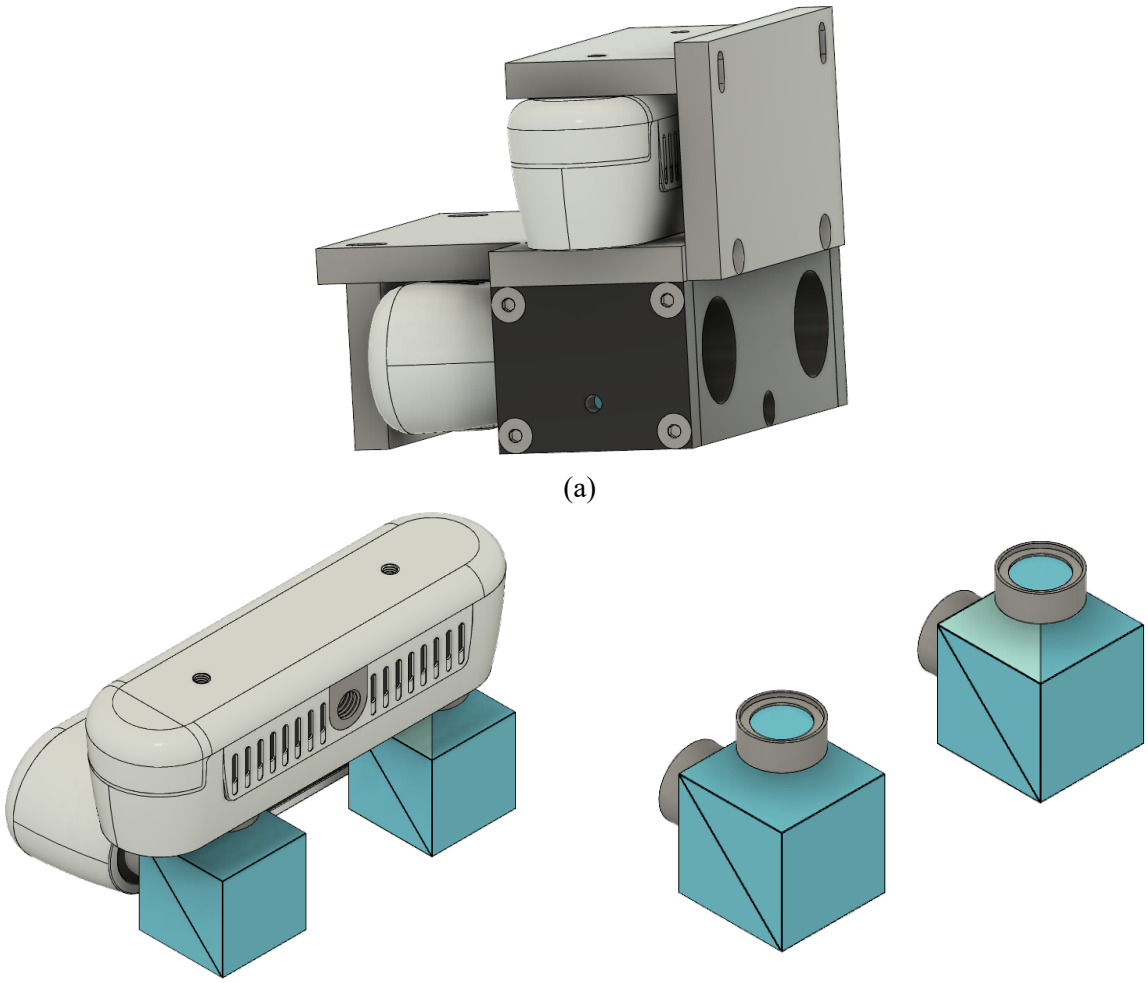


Figure 5-8 The coaxial optics. (a) External view; (b) Internal view(Beam Splitters and Cameras); (c) Internal view(Beam Splitters and Filters).

Figure 5-9(a) is a left-side view, and Figure 5-9(b) is a bottom view.

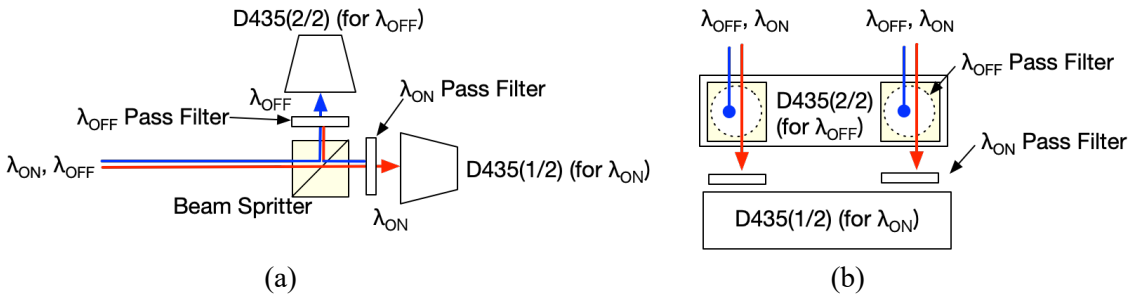


Figure 5-9 Internal configuration of the coaxial optics. (a) Left-side view. (b) Bottom view.

The left and the right image sensors of D435 (1/2) and D435 (2/2) capture time-synchronized images of λ_{ON} and λ_{OFF}, respectively. The transmission efficiency of the filters was estimated by measuring the ratio of the brightness of the frost glass image with and without the filter. The results are summarized in Table 5-2.

Table 5-2 Transmittance of λ_{ON} pass filter and λ_{OFF} pass filter.

	Transmittance at λ_{ON}	**Transmittance at λ_{OFF}**
λ_{ON} pass filter	0.54	0
λ_{OFF} pass filter	0	0.27

The efficiency of the coaxial optics was obtained from the value in Table 5-2 multiplied by the reflectivity (transmittance) of the beam splitter (= 0.5) and was estimated as 0.27 for λ_{ON} and 0.135 for λ_{OFF}. The experiment layout including the coaxial optics is shown in Figure 5-10.

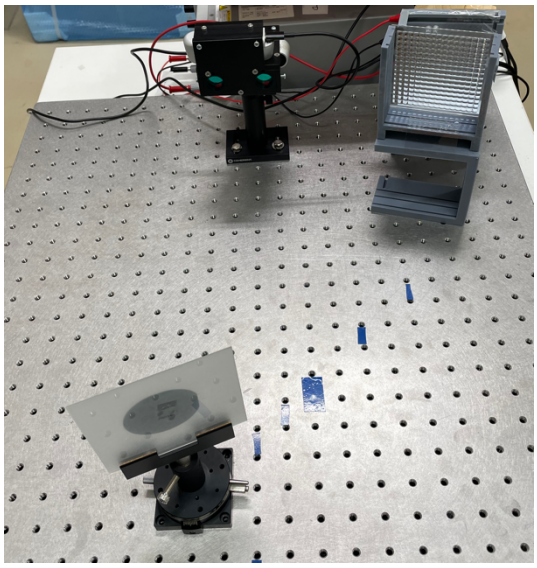
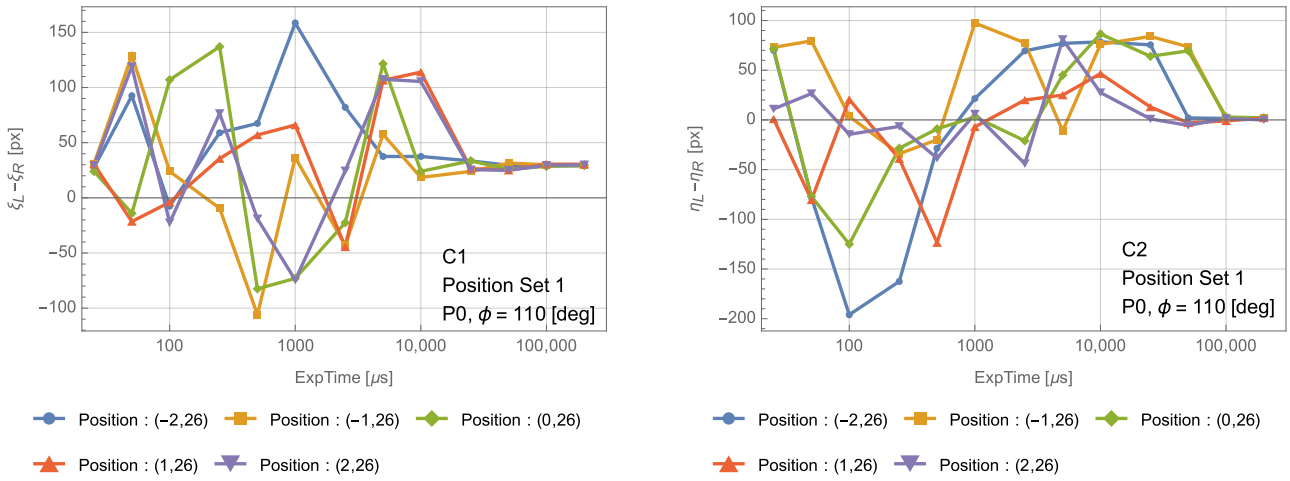


Figure 5-10 The Experiment layout of GaAs target position estimation with coaxial optics

Figure 5-11 shows plots of the integrity measure data of the GaAs substrate experiment using the coaxial optics. Like in Figure 5-4, similar plots were obtained for both Position Sets 2 and 3. Compared with Figure 5-4, the minimum exposure time of convergence for both C1 and C2 became longer. As shown in the later section (5.5.2.3), since the integrity measure and the detectability threshold are regarded as equivalent, the threshold equation predicts that the ratio of the integrity measure convergence time in Figure 5-11 to those in Figure 5-4 gives the λ_{OFF}

transmission efficiency of the equipment. The mean value over Position Sets 1, 2, and 3 is 0.124, close to the above-estimation 0.135.



(a) (b)

Figure 5-11 Integrity measure of Position Sets 1 (GaAs substrate). (a) C1; (b) C2.

The coaxial optics' field of view (FOV) is limited by the size of the wavelength pass filters (ϕ12.5 mm). The angle observable by both the left and right image sensors is about 17 deg.

5.2.2. GaAs Substrate Experiments Using the Coaxial Optics

Positions and directions of the GaAs substrate were estimated with the coaxial optics. Like in Figure 5-6 and Figure 5-7, the results for Position Sets 1, 2, and 3 are shown in Figure 5-12 and Figure 5-13.

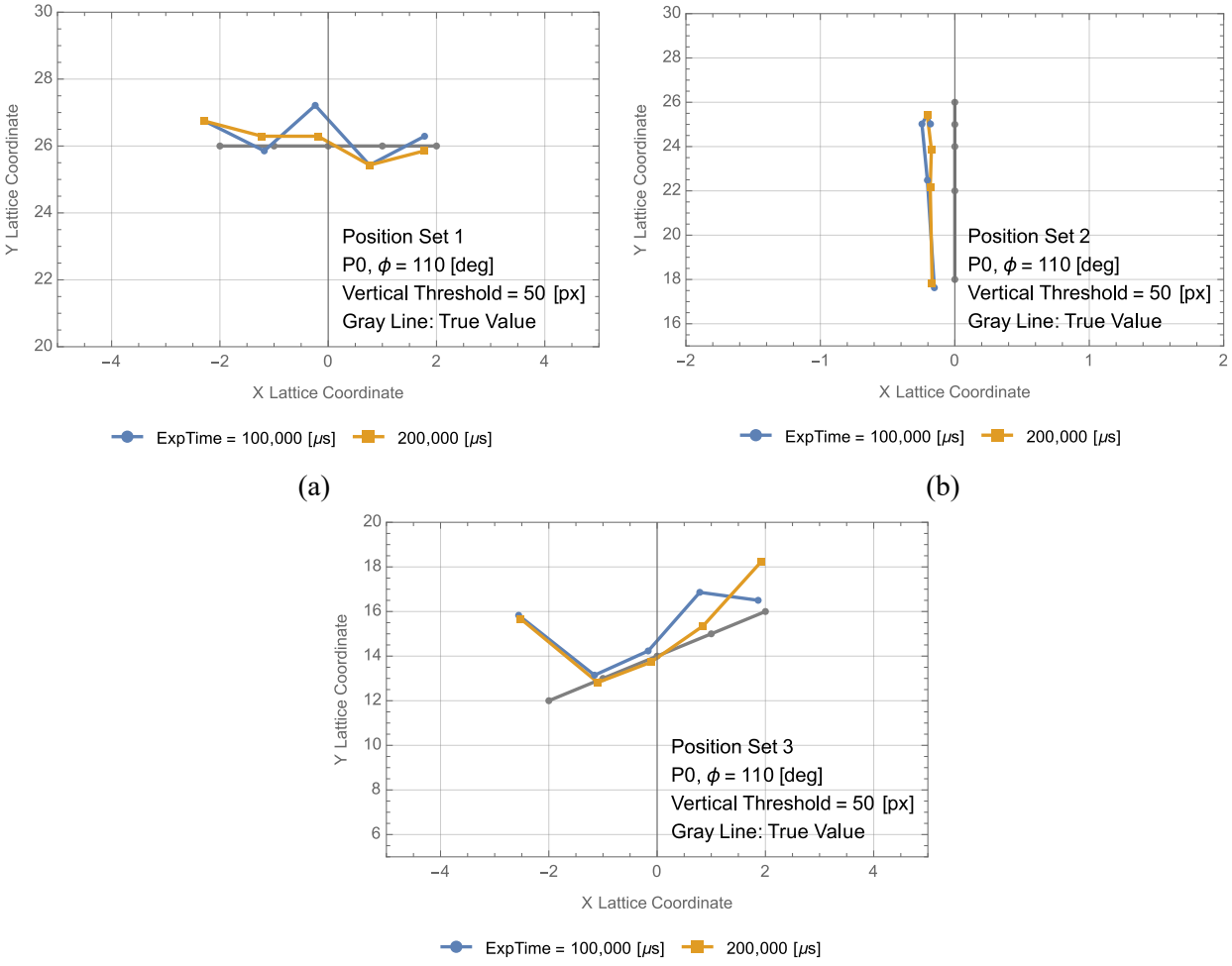


Figure 5-12 Estimated position of the GaAs substrate. (a) Position Set 1; (b) Position Set 2; (c) Position Set 3.

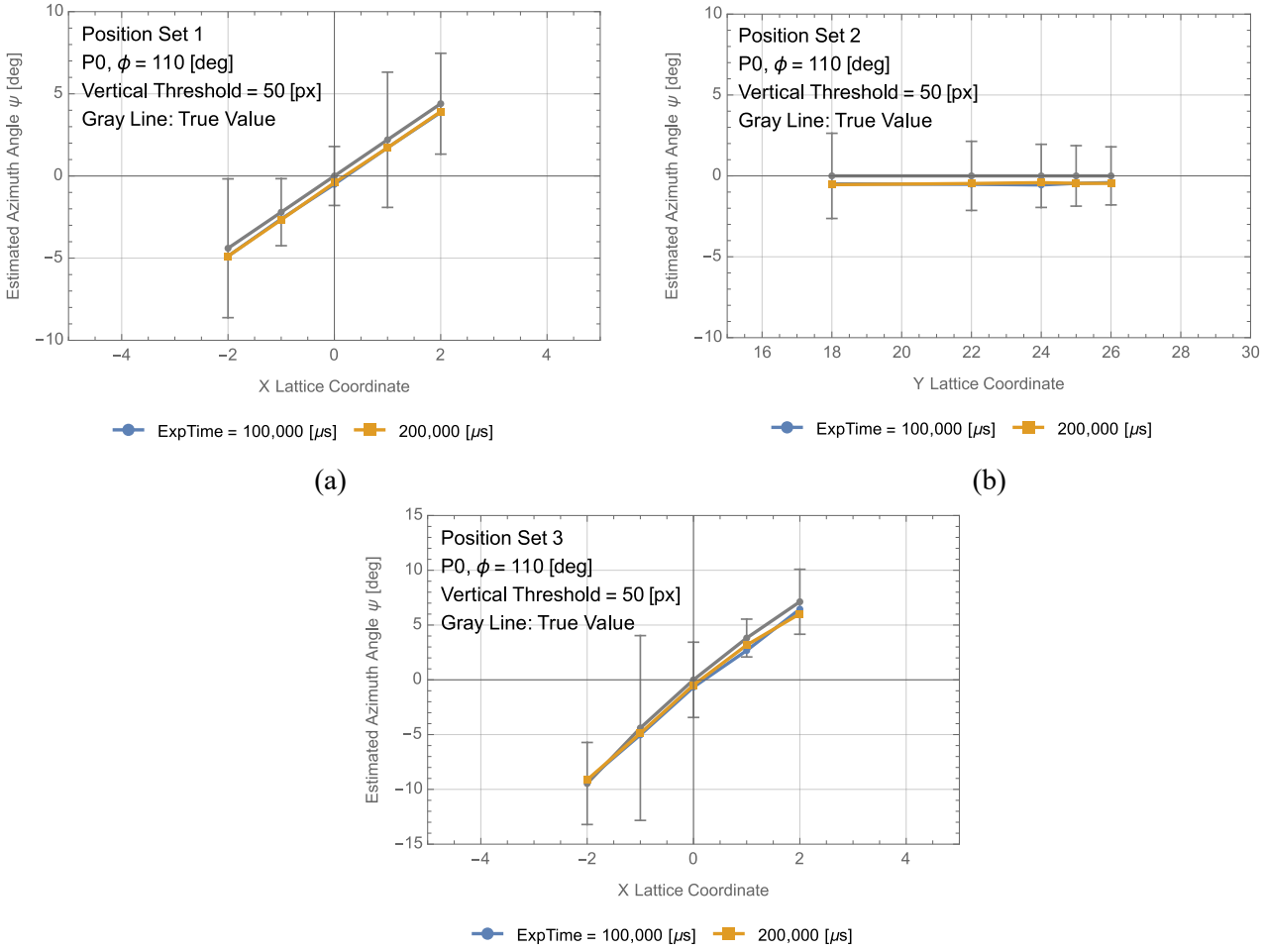


Figure 5-13 Estimated direction of the GaAs substrate. The error bars are defined by Equation (5). (a) Position Set 1; (b) Position Set 2; (c) Position Set 3.

Position estimation accuracies degraded at both endpoints in Figure 5-12 due to the eclipse of the target, which is partially outside the FOV. For other points, the results obtained for both position and direction were like those from the experiments without the coaxial optics shown in Figure 5-6 and Figure 5-7.

5.3. PV Positioning Experiments

Like the GaAs substrate, position and direction estimations were conducted for the GaAs PV used in Section 4 using the coaxial optics equipment. In the concept-proof GaAs detection experiments, the target's center coordinates, and area size could be stably estimated within a wide angular range for the substrate. On the other hand, for the PV, the estimation was limited

to within the neighborhood of its normal. Such a difference affects the position determination characteristics of the PV, which are different from the substrates as described below.

5.3.1. Positioning of the PV at a Fixed Position

Position estimation was conducted with a fixed target at (0, 27) for various ϕ. Results are shown in Figure 5-14. Positioning errors for each axis are expressed as $(\Delta x, \Delta y)$, and $\sqrt{\Delta x^2 + \Delta y^2}$ are plotted for the vertical axis with the target's attitude angle ϕ for the horizontal axis. It decreases in the range $78 \leq \phi \leq 98$ deg and rapidly increases in both outer sides.

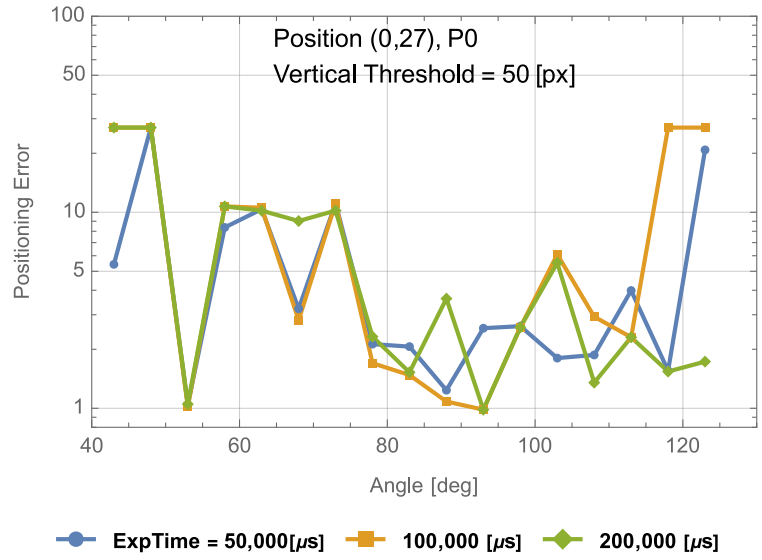
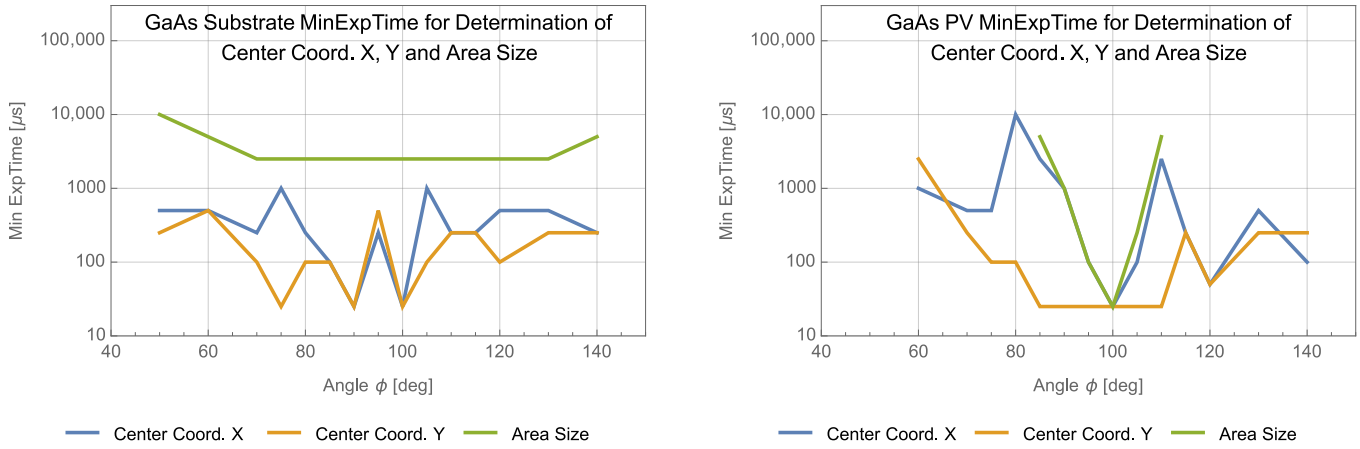


Figure 5-14 Position estimation error of the fixed target at (0,27) (stereo imagery, with coaxial optics).

Figure 5-15 shows the angular characteristics for determining the center coordinates and the area size in the pixel coordinates of the image sensor, based on the data from Section 4. The plots show the angular dependence of the minimum exposure time (vertical axis) to determine the X and Y center coordinates and the area size.

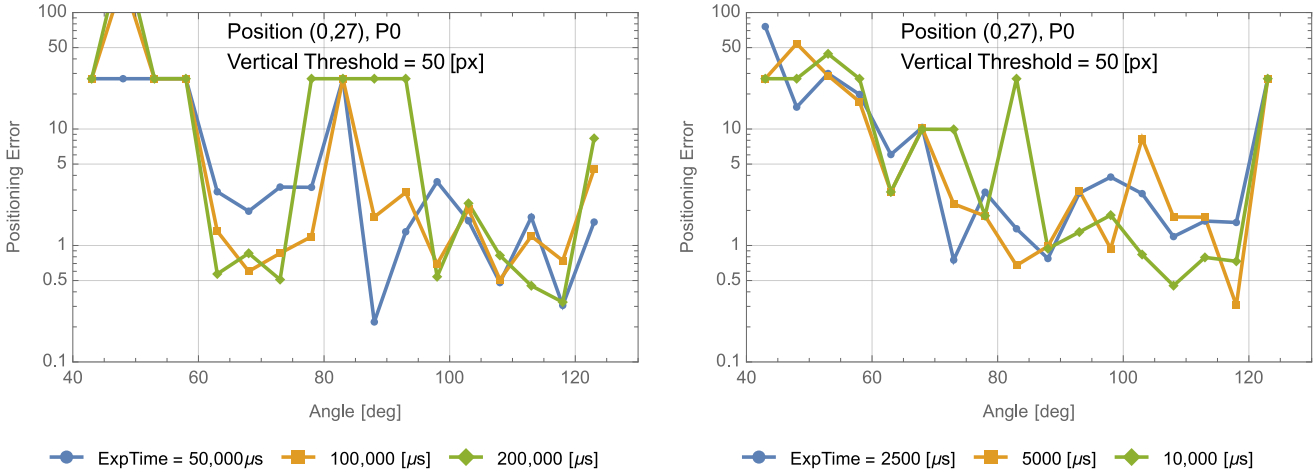


(a) (b)

Figure 5-15 Angular characteristics of center coordinates and area size determination in the pixel coordinates of the image sensor for the GaAs substrate and PV. (a) GaAs substrate; (b) GaAs PV.

Figure 5-15(a) indicates that the center coordinates of the substrate are stably determined in a wide angular range. On the other hand, regarding the minimum exposure time for detection of the center coordinates of the PV, Figure 5-15(b) shows that the value around the neighborhood of the normal differs from the one outside of it. For the positioning of the PV, determination of the X-coordinate of its center is necessary. The resultant positioning accuracies of the PV reflect this steep angular characteristic of the X-coordinate determination, thus, the positioning accuracies are strongly affected by the reflection characteristics of the targets.

Figure 5-16 shows the results of a similar experiment in which the coaxial optics were removed to increase the power received by the camera. As explained in 5.2.1, the received power differs about 8-fold between Figure 5-14 and Figure 5-16. Comparing Figure 5-14 and Figure 5-16(a), positioning accuracies were improved at both sides of the $78 \leq \phi \leq 98$ deg range. They are degraded around the normal, however, from Figure 5-16(b), this can be avoided by limiting the exposure time appropriately. Thus, positioning accuracy can be improved in the $63 \leq \phi \leq 118$ deg range by increasing the received power.



(a) (b)

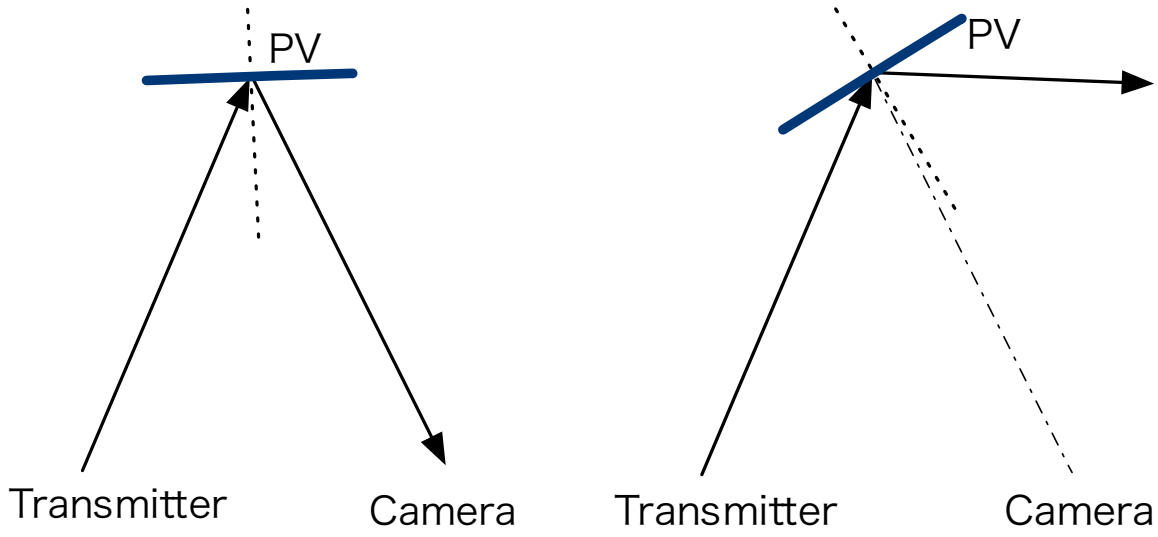
Figure 5-16 Position estimation error of the fixed target at (0,27) (stereo imagery, without coaxial optics). The received power in this figure is greater than Figure 13 about 8-fold. (a) Exposure Time: 50,000 μs, 100,000 μs, 200,000 μs ; (b) Exposure Time: 2500 μs, 5000 μs, 10,000 μs.

5.3.2. Positioning of the PV at Position Sets 1, 2, and 3

In the experiment with the substrate, the angle of the rotatable table (= attitude angle of the target) was ϕ = 110 deg. When the irradiated beam is reflected by the target and directly enters the camera like in Figure 16a, its attitude angle ϕ depends on the position and satisfies (5-7).

$$\phi = cos^{-1}\frac{(\boldsymbol{P}+\boldsymbol{B})\cdot\boldsymbol{N}}{|\boldsymbol{P}+\boldsymbol{B}||\boldsymbol{N}|} \tag{5-7}$$

where $\boldsymbol{P}$ is the position vector of the target, $\boldsymbol{B}$ is the directional vector of the irradiated beam, and $\boldsymbol{N}$ is the directional vector of the camera facing normal. This angle ϕ is referred to as the "on-axis angle" throughout this report.



(a) (b)

Figure 5-17 On-axis configuration and off-axis configuration. (a) On-axis. (b) Off-axis.

Using the lattice coordinates and from the experiment layout, $\boldsymbol{B} = (1,4)$ and $\boldsymbol{N} = (0,1)$. The on-axis angle ranges from 79 to 87 deg angular range for the target in Position Sets 1, 2, and 3. Two kinds of experiments were conducted for the PV. One was where ϕ was always adjusted to the on-axis angle of the target's position like in Figure 5-17(a), which is referred to as the "on-axis experiment". The other was like in Figure 5-17(b), where ϕ was fixed at the same angle, which is different from the on-axis angle. This is referred to as the "off-axis experiment".

Some results of the on-axis P0 and P1 GaAs PV position estimations are excerpted and shown in Figure 5-18. The rest are summarized in A.5.3.1.

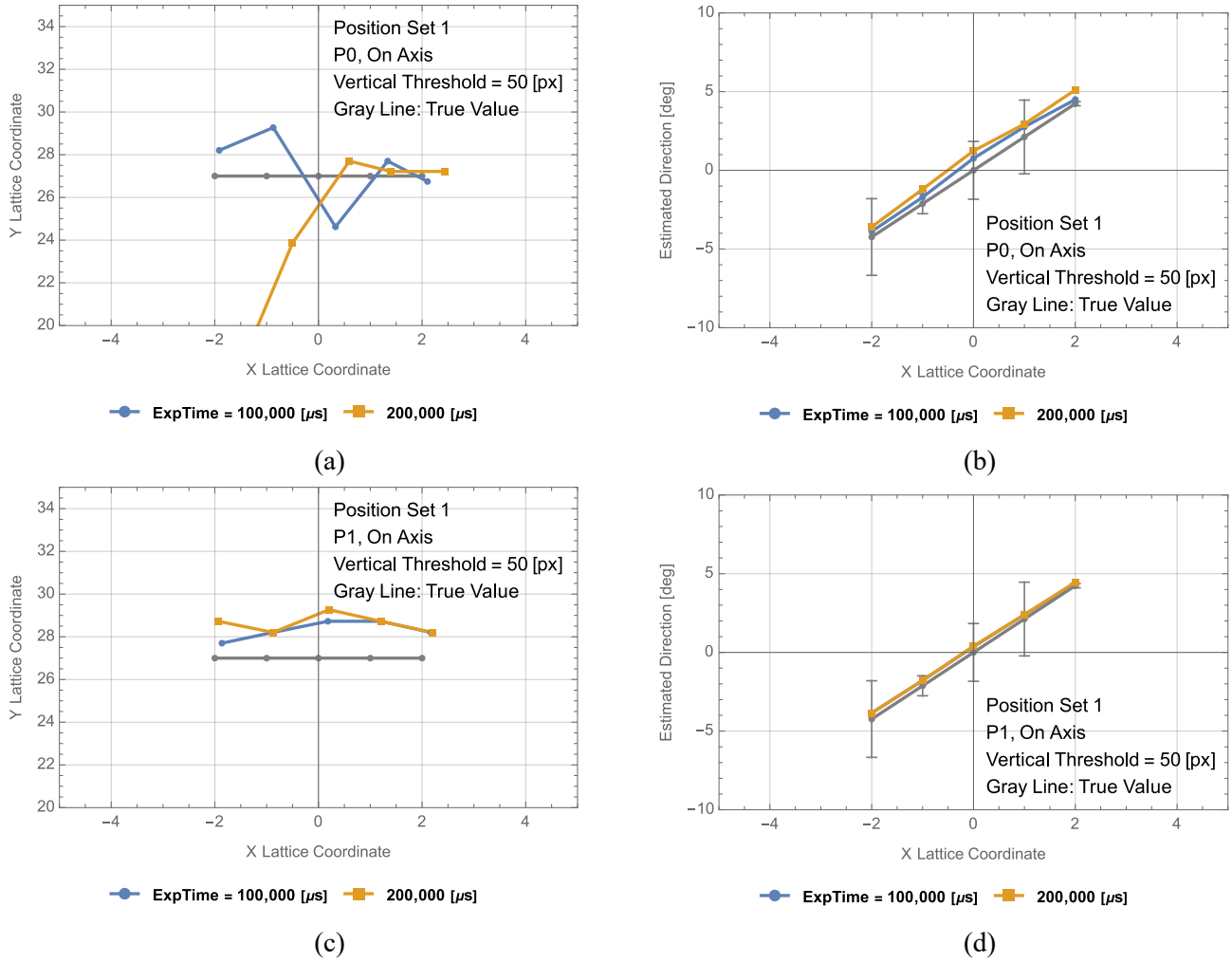


Figure 5-18 Estimated position and direction of the GaAs PV (on-axis P0 and P1). (a) Position (P0). (b) Direction (P0). (c) Position (P1). (d) Direction (P1).

Even though the directions were stably estimated in Figure 5-13, degraded results of position accuracies were obtained for every position set for P0. In the P0 on-axis experiments, the light input to the camera is excessive and, due to scattering by the filter holder and partial saturation of the image at the sensors, this causes accuracy degradation. These issues were relaxed in P1, and its estimation accuracies were better than those of P0. Off-axis experiments were conducted by varying the attitude angle ϕ (referred to as the "off-axis angle") to 45, 65, 105, or 125 deg. Some results are shown in Figure 5-19. The rest are shown inA.5.3.2.

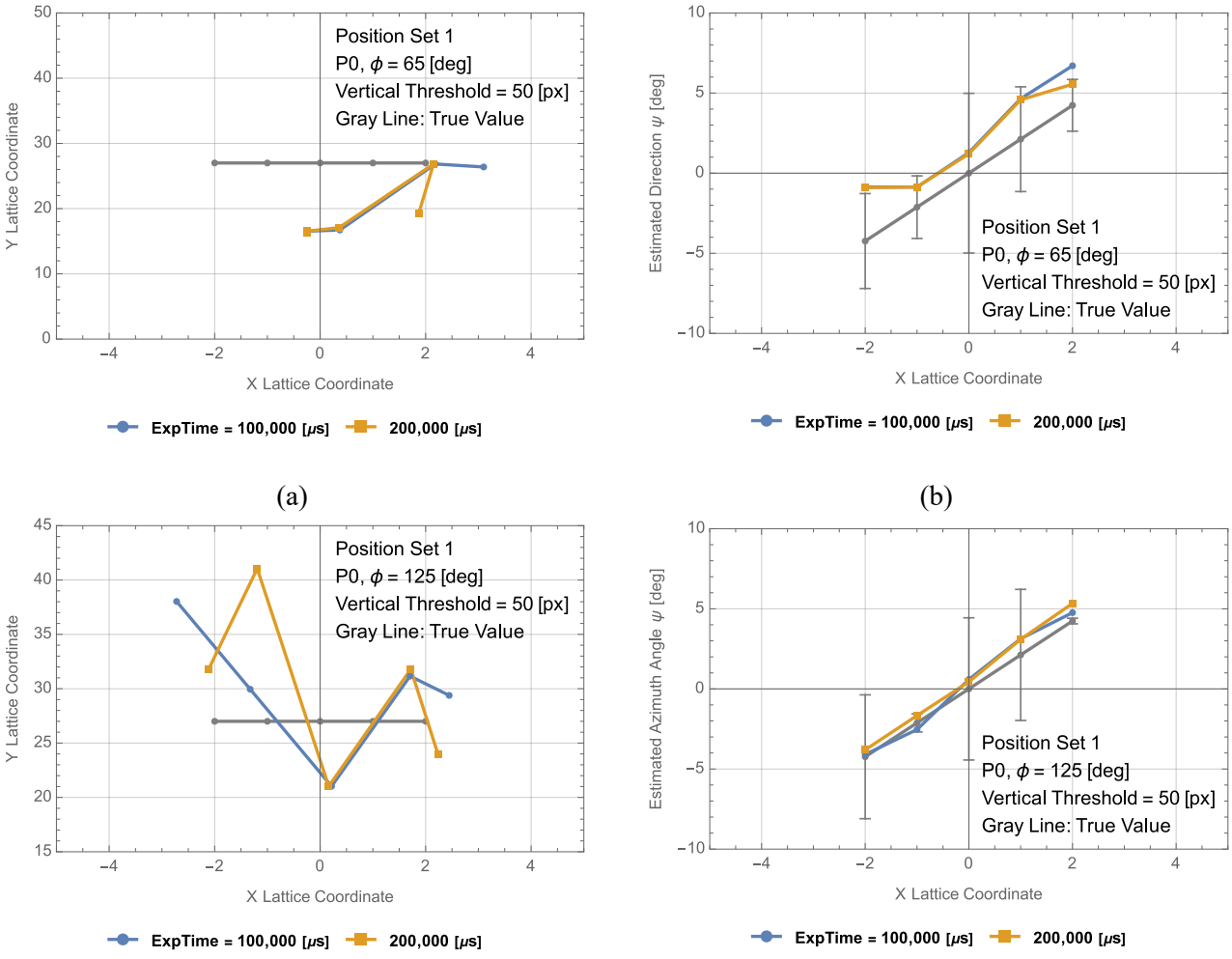


Figure 5-19 Estimated position and direction of the GaAs PV (off-axis P0 ϕ = 65, 125 deg). The error bars in (b) and (d) are defined by Equation (5). (a) Position (65 deg). (b) Direction (65 deg). (c) Position (125 deg). (d) Direction (125 deg).

Since the layout in Figure 5-1 was asymmetric about the optical axis of the camera, accuracies at ϕ = 105, 125 deg were better than those at ϕ = 45, 65 deg. Compared with the on-axis experiments, accuracies were degraded in the off-axis case. In contrast, from data in Figure 5-36 and Figure 5-37, the estimated direction is well estimated, at least in the $65 \leq \phi \leq 125$ deg range, and it can be determined in more than a 60 deg full angular range even in off-axis conditions. Since the results of the on-axis and off-axis experiments are qualitatively consistent with Figure 5-14, the figure can be regarded as the representative data of the on-axis and off-axis experiments, and the discussion in 5.3.1 also holds for the results in this section.

In the substrate experiments in 5.2.2, the attitude angle was ϕ = 110 deg. Comparing the results of the substrate experiments with the PV results (ϕ = 105 deg), even though the attitude angles of these two are close to each other, the positioning accuracies are better in the substrate experiments in which the reflection characteristic is mainly diffuse than in the PV case, whose dominant component is specular.

5.4. Position Estimation by the methods other than the Stereo Imagery

5.4.1. Position Estimation by the Apparent Size of the Target

In OWPT, the design and operation of the system are strongly affected by the position determination of the PV. In stereo imagery, since the necessary width between left and right sensors is proportional to the range of the target, the size of the image sensor unit would be an issue for a distant target. This issue would diminish when the range is determined by another method. Assuming the target size is known, its range can be estimated by measuring its apparent size. This method was investigated using data from the right image sensor and sizes of the target (substrate: ϕ50.8 mm, PV: 60 mm $\times$ 40 mm). Estimating direction using the same data, the position was then determined by these two factors. The mathematical formulation is simple and included in A.5.2.

5.4.1.1. GaAs Substrate

Results of the position and direction estimations are shown in Figure 5-20 and Figure 5-21.

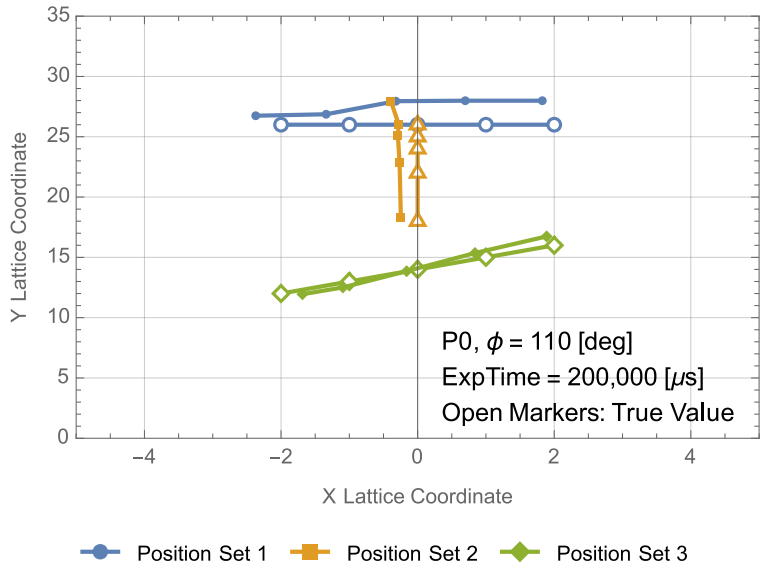
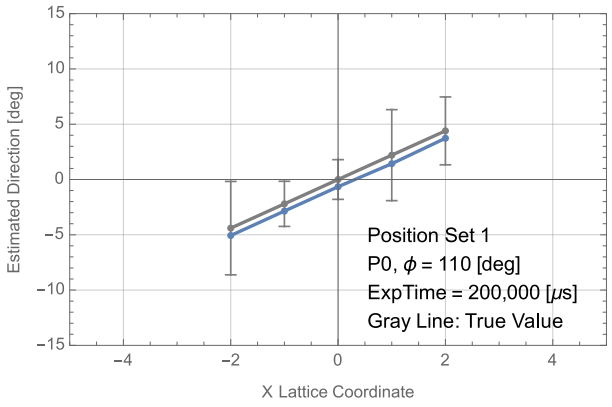
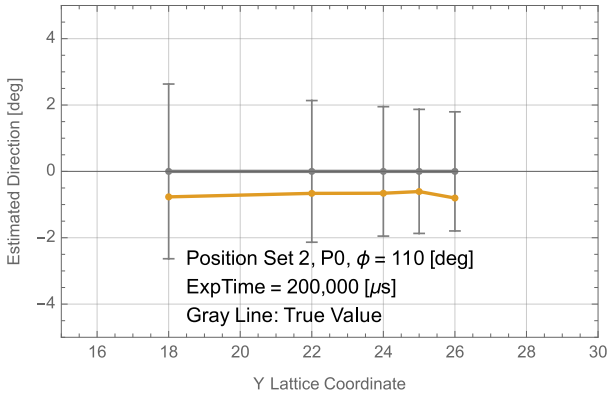


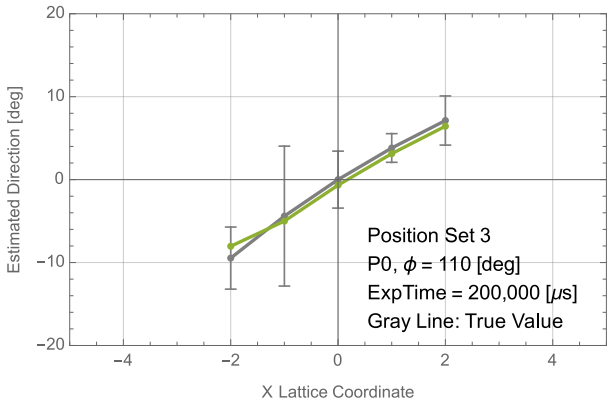
Figure 5-20 Estimated position of the GaAs substrate (ϕ = 110 deg).



(a)



(b)



(c)

Figure 5-21 Estimated direction of the GaAs substrate (ϕ = 110 deg). The error bars are defined by Equation (5). (a) Position Set 1; (b) Position Set 2; (c) Position Set 3.

Comparing these figures with Figure 5-12 and Figure 5-13, these results are similar in the substrate experiments, the performance difference between the stereo imagery and the apparent size method is small.

5.4.1.2. GaAs PV

5.4.1.2.1. Positioning of the PV at a Fixed Position

As in Figure 5-14, the target was fixed at (0, 27) and was estimated with the attitude angle as the horizontal axis. The results are shown in Figure 5-22.

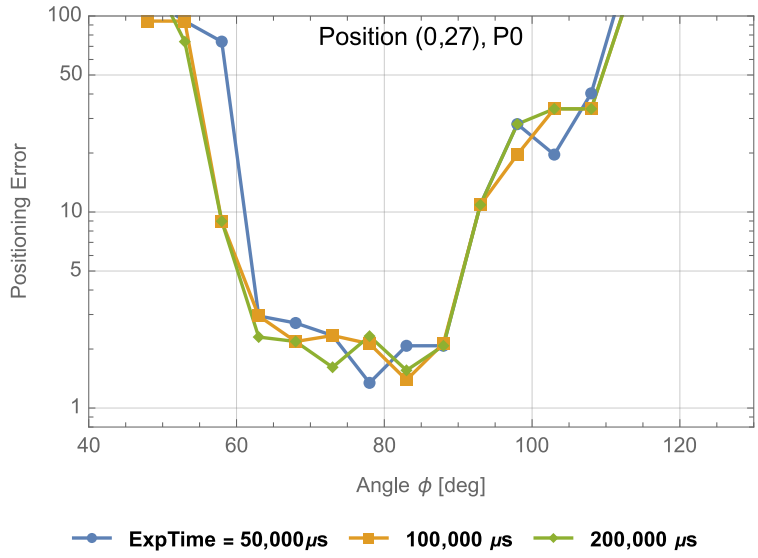
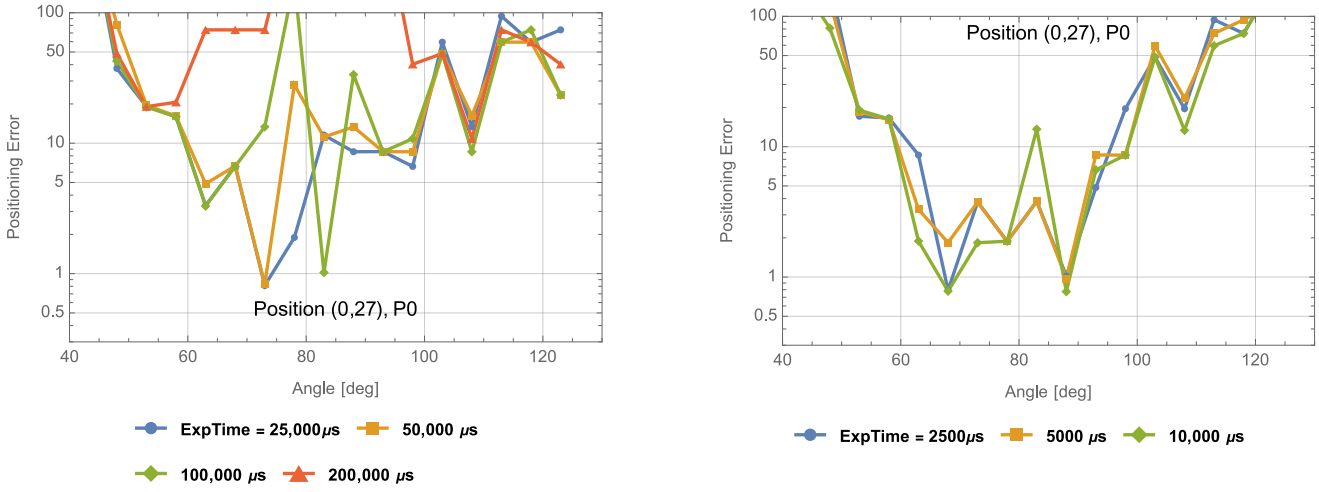


Figure 5-22 Position estimation error of the fixed target at (0,27) (apparent target size, with coaxial optics).

The position error decreases within the 63≤ ϕ ≤88 deg range and rapidly increases outside of it. The full width of the angular range is 25 deg, which is also close to the full angular width of the area size determination in Figure 5-15(b). This is because the vertical target size was used for the position estimation in Figure 5-22, and capturing the whole vertical image of the target is necessary to estimate its vertical size. Like in Figure 5-16, position estimation results for the fixed target at (0, 27) without the coaxial optics are shown in Figure 5-23.



(a) (b)

Figure 5-23 Position estimation error of the fixed target at (0,27) (apparent target size, without coaxial optics). The received power in this figure is greater than in Figure 5- 21 about 8-fold. (a) Exposure time = 25,000 μs, 50,000 μs, 100,000 μs, 200,000 μs. (b) Exposure time = 2500 μs, 5000 μs, 10,000 μs.

Even though some accuracy improvements can be seen on both sides of the on-axis angle in this case, compared with those in Figure 5-16, the improvements in Figure 5-23 are limited. This can be explained by a similar discussion to the one in 5.3.1. Generally, increasing the received power is equivalent to enlarging the irradiated power. In this case, it is the same as the elongation of the exposure time in Figure 5-15. In Figure 5-14, stereo imagery positioning was based on the X-coordinate estimation and the X-coordinate plot in Figure 5-15(b). In contrast, Figure 5-23 is based on area size estimation and the area size plot in Figure 5-15(b). Even though the angular characteristics of the area size and the X-coordinate are similar about the normal, they are quite different outside of it. Thus, the angular characteristic of Figure 5-22 which has relationship with the area size is not the same as that of Figure 5-14 with the X-coordinate. The detectability concept can be applied to also position estimations. Figure 5-15(b),

the detectability data, provides qualitative explanations for the difference between Figure 5-16 and Figure 5-23.

5.4.1.2.2. Positioning of the PV at Position Sets 1, 2, and 3

Excerpted on-axis results are shown in Figure 5-24(a). The rest are included in Figure 5-42 and Figure 5-43. Figure 5-24(b), (c), and Figure 5-44 and Figure 5-45 show the off-axis results. Comparing these results with Figure 5-18 and Figure 5-19 like in the substrate experiments, the two methods provided similar results also for the PV. Like in 5.3.2, these results are consistent with Figure 5-22, thus, it can be regarded as the representative data of the on-axis and off-axis experiments.

Close investigation and comparison of the positioning error between the stereo imagery and the apparent size measurement show that their angular characteristics are similar in the on-axis neighborhood and different in the off-axis range. In (5-8), the position estimation error $\sqrt{\Delta x^2 + \Delta y^2}$ is expressed using 2D polar coordinate variables (range R, azimuth angle (direction) ψ) and their errors ($\Delta R, \Delta\psi$).

$$\sqrt{\Delta x^2 + \Delta y^2} = \sqrt{(\Delta R)^2 + (R\,\Delta\psi)^2} \tag{5-8}$$

$\Delta\psi$ can be compared between the stereo imagery off-axis data (Figure 5-19(b), (d), Figure 5-38, Figure 5-39, Figure 5-40, and Figure 5-41) and the apparent size measurement (Figure 5-45). Table 5-3summarizes the result for Position Set 1, in which the typical value of $R = 27$ is employed.

Table 5-3 Comparison of the off-axis $\Delta\psi$ between stereo imagery and apparent size measurement.

	$\Delta\psi$	$R\,\Delta\psi$ ($R = 27$)
stereo imagery	1 to 3 deg	0.47 to 1.41
apparent size measurement	2 to 5 deg	0.94 to 2.35

Comparing $R\,\Delta\psi$ with the position estimation error of the stereo imagery (Figure 5-19(a),(c), Figure 5-38, and Figure 5-40), and with the apparent size measurement (Figure 5-24(b), (c)), it shows that $\sqrt{\Delta x^2 + \Delta y^2} \gg R\,\Delta\psi$ always holds, which means that ΔR, rather than $R\,\Delta\psi$, dominates the position estimation error. In the apparent size measurement, the off-axis position estimation error of Position Set 1 is so large that some of the data are beyond the plot range (ϕ = 45, 105, 125 deg). Regarding the stereo imagery errors, they are still large but within 5 to 20 units except for ϕ = 45 deg. This observation indicates that the off-axis positioning errors are

affected by the off-axis ΔR, which differs between the stereo imagery and the apparent size measurement, as discussed in 5.4.1.2.1.

Comparing the on-axis case of the stereo imagery (Figure 5-18(a), (c)) and the apparent size measurement (Figure 5-24(a) and Figure 5-42), all the data support $\sqrt{\Delta x^2 + \Delta y^2} \sim \mathcal{O}(R\,\Delta\psi)$. This means that ΔR values are small enough and of the same order as $R\,\Delta\psi$. This observation is consistent with the results of the fixed-point positioning in Figure 5-14 and Figure 5-22.

The difference in the position estimation error in these two methods appears in the off-axis angle range, and it suggests that it is strongly affected by the shape of X-coordinates estimation and area size estimation in Figure 5-15(b). For Position Set 2 and Position Set 3, the same results are obtained.

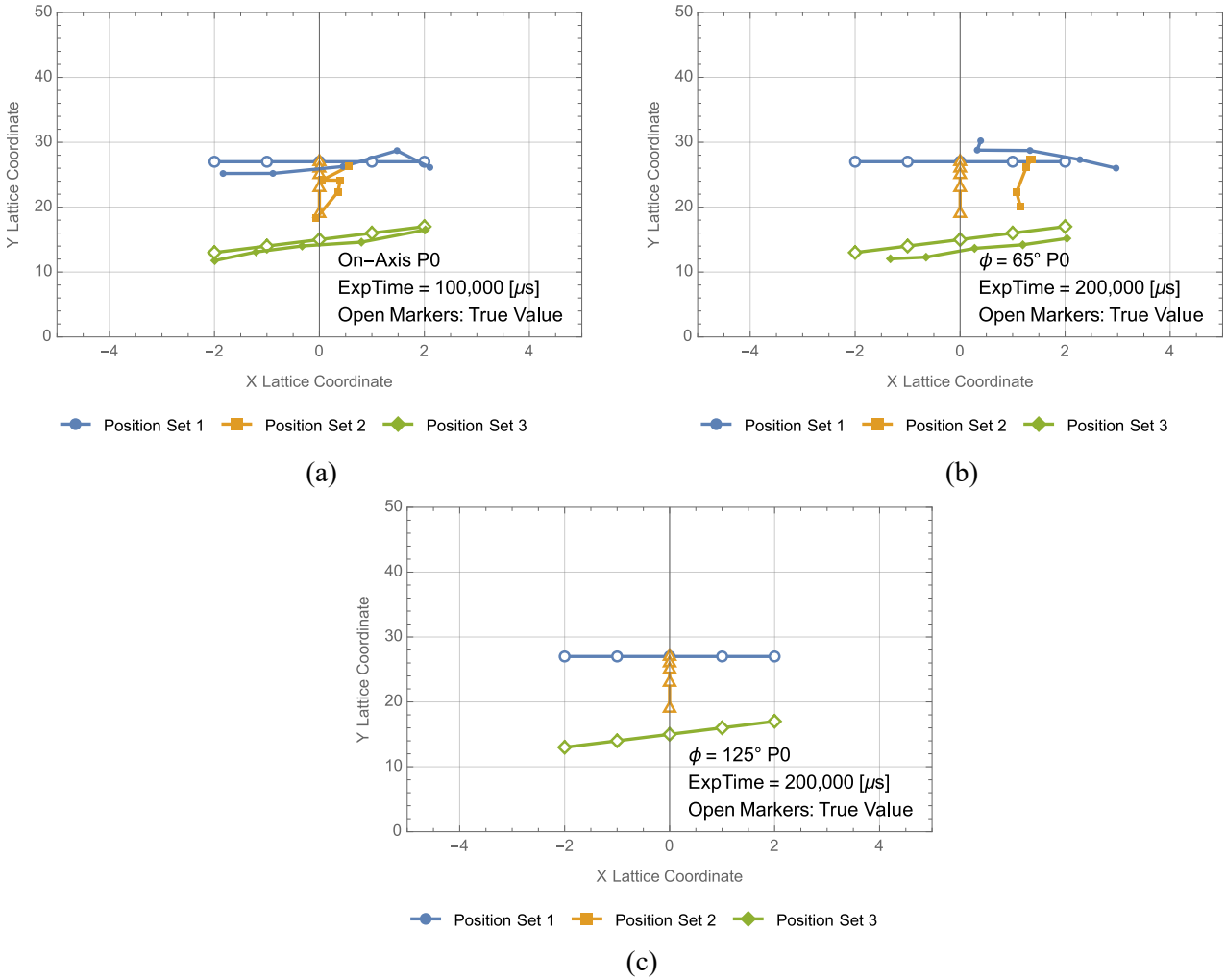
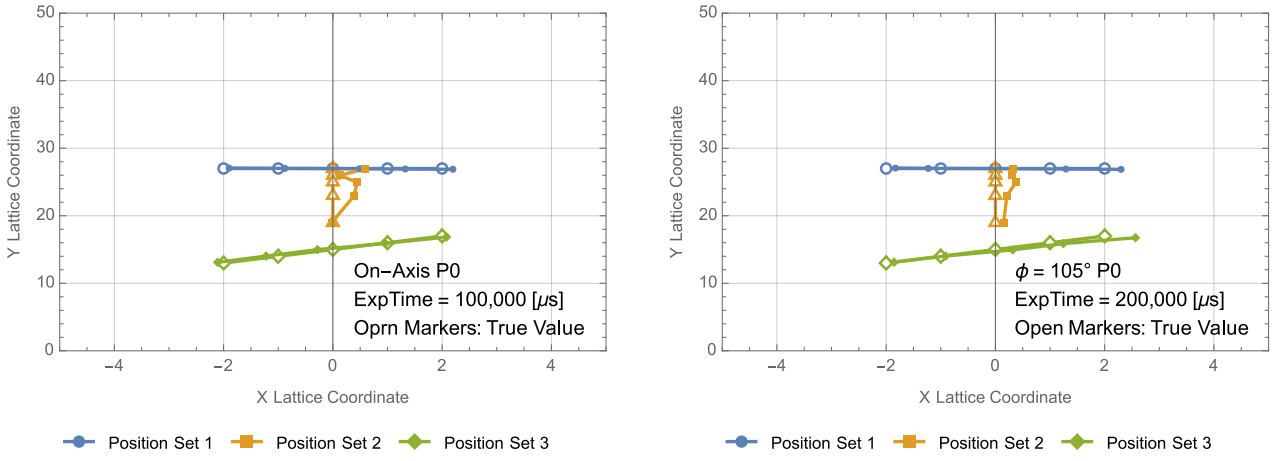


Figure 5-24 Estimated position of the GaAs PV. (a) On-axis P0. (b) Off-axis ϕ = 65 deg. (c) Off-axis ϕ = 125 deg.

5.4.2. Position Estimation with External Ranging Information

If the exact range data are provided externally, there would be an option to determine the target's position based on range information from the external ranging source combined with the internally estimated direction. The dominant contribution to the positioning error is removed by setting $\Delta R = 0$ in (5-8). Positions were calculated using (exact) range information with the independent direction estimation. Results are shown in Figure 5-25, Figure 5-46, and Figure 5-47. In this case, accurate positioning results were obtained for both on-axis and off-axis conditions.



(a) (b)

Figure 5-25 Excerpts from on-axis and off-axis position and direction estimation with external ranging information. (a) On-axis position. P0. (b) Off-axis position (ϕ = 105 deg). P0

5.5. Attitude Estimation of the GaAs Photovoltaics Target

5.5.1. The Attitude Estimation by the Integrity Measure

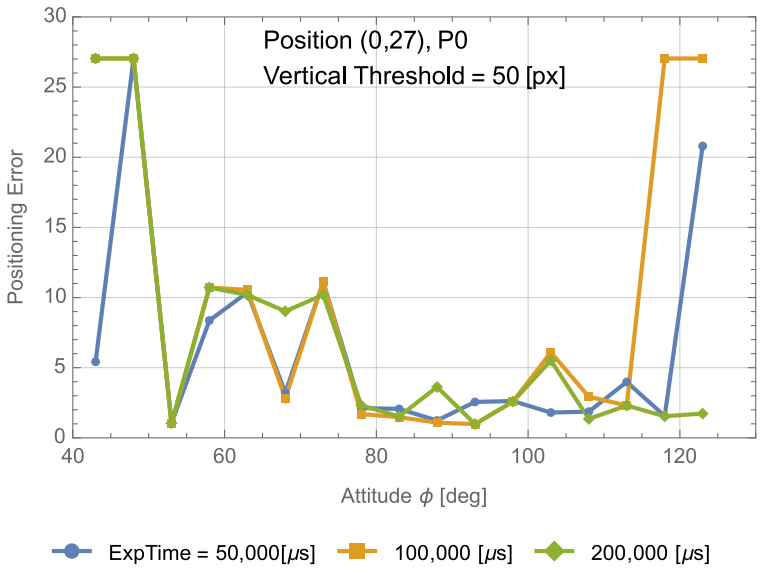


Figure 5-14 Position estimation of the target at (0, 27).

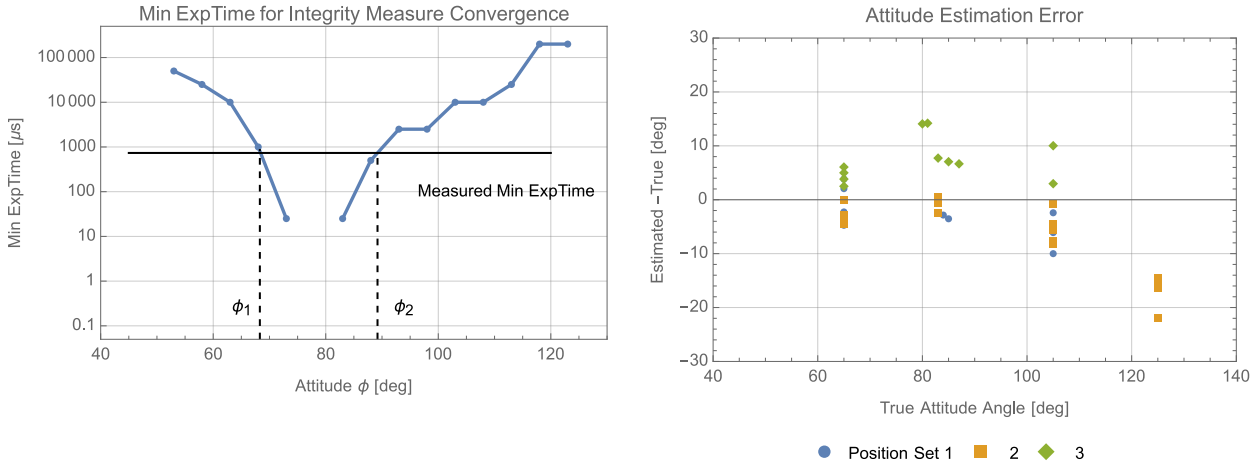
Figure 5-14 shows that the position estimation accuracy depends on the target's attitude angle, Figure 5-4, and Figure 5-5 indicate that the convergence of the position accuracy is related to the convergence exposure time of the integrity measure. Therefore, the target's attitude angle is expected to be estimated using this minimum exposure time.

Using the data from Figure 5-14, it is possible to calculate the minimum exposure time for the integrity measure to converge for each attitude angle of the target placed at (0, 27). The results are shown in Figure 5-26(a). The vertical axis of Figure 5-26(a) represents the minimum exposure time at which both C1 (5-1) and C2 (5-2) are satisfied, and the horizontal axis represents the target's attitude angle. The minimum exposure time shows sharp dependence on the target's attitude angle.

For a target with an unknown attitude angle, by measuring the minimum exposure time of the integrity measure convergence, one can estimate the attitude angle using a curve like that shown in Figure 5-26(a) and the measured minimum exposure time. Although the determined attitude angles from the measured minimum exposure time yield two solutions, ϕ_1 and ϕ_2 shown in

Figure 5-26(a), due to the symmetry, this does not pose any problem for beam shaping performed by the transmitter discussed in Section 3.

At points in Position Set 1, 2, and 3, by obtaining the minimum exposure time from the data and overlaying it on Figure 5-26(a), the plot in Figure 5-26(b) shows that the estimation of the attitude angles at each point of Position Set 1, 2, and 3 are feasible, albeit with some outliers.



(a) (b)

Figure 5-26 Minimum exposure time for integrity measure to converge. (a) Attitude dependence of the target at (0, 27); (b) Attitude estimation of the target at Position Set 1, 2, 3.

Figure 5-26(a) represents the curve of the minimum exposure time for the target fixed at (0, 27). The curve for the minimum exposure time at an arbitrary target position will not be the same as that for the target fixed at (0, 27). Therefore, developing a model for the minimum exposure time corresponding to each target's position and conducting attitude estimation based on it would likely improve the estimation accuracy shown in Figure 5-26(b).

5.5.2. The Physical Model of the Integrity Measure's Minimum Exposure Time and Attitude Estimation

5.5.2.1. Derivation of the Integrity Measure's Minimum Exposure Time

When the integrity measure converges, also the position estimation accuracy. The position estimation accuracy is related to the detectability. Therefore, we try to derive the physical model of the minimum exposure time for the integrity measure based on the detectability threshold equation in the following manner.

The attitude angle of the target (ϕ), the irradiation (incident) angle of the beam (θ_i), and the view angle from the camera (θ_r) are extended to include non-zero values, respectively. The reflection characteristics of the target are extended to include a non-diffuse one. The profile of the irradiation beam is extended to Gaussian. The threshold equation takes the following form when the absorption wavelength is fully absorbed:

$$\left[K\left(\frac{\lambda}{hc}\right)\rho I_t \eta_t \eta_r \eta_Q \frac{\Delta\sigma}{\Delta\Omega}\Delta\omega_r Exp\right]_{threshold} = \Delta I_{diff} \quad (5\text{-}9)$$

Here, η_Q: the quantum efficiency of the camera sensor, $\Delta\sigma/\Delta\Omega$: the differential scattering cross-section of the target, $\Delta\omega_r$: the solid angle of the receiver FOV, I_t: the transmitted beam power density, η_r: the efficiency of the receiving optics, hc/λ: the energy of a λ_{OFF} photon, K: a constant dependent on the experimental setup, and ΔI_{diff}: differential intensity between the target and the background at the threshold.

First, considering θ_r is non-zero, $\Delta\omega_r$ is expressed as follows:

$$\Delta\omega_r = \frac{A_r cos\theta_r}{(R/cos\theta_r)^2} = \frac{A_r}{R^2} cos^3\theta_r \quad (5\text{-}10)$$

Introducing θ_i in addition to this, (5-9) becomes as follows. It should be noted that θ_i and θ_r are functions of the targets attitude angle ϕ.

$$\left[K\left(\frac{\lambda}{hc}\right) f_r I_t\, \eta_t \eta_r \eta_Q \Delta\sigma \frac{A_r}{R^2} cos\theta_i cos^4\theta_r Exp\right]_{threshold} = \Delta I_{diff} \quad (5\text{-}11)$$

(5-11) is the general form of the threshold equation taking θ_i and θ_r into account. Here, f_r is defined as,

$$f_r \equiv \frac{\rho}{\Delta\Omega\ \cos\theta_r} \quad (5\text{-}12)$$

The expression for the minimum exposure time in the experimental setup is derived by considering the irradiation beam's profile and the target's reflectivity characteristics. Considering that the irradiation beam profile is Gaussian with the $1/e^2$ beam radius: w, the irradiation beam power: P_t, and the beam area on the target surface: A_{tr},

$$I_t(r) = I_0 exp\left(-2\frac{r^2}{w^2}\right) = \frac{2\eta_t P_t}{A_{tr}} exp\left(-2\frac{r^2}{w^2}\right) \quad (5\text{-}13)$$

where η_t: is the efficiency of the transmitter optics, w is determined by the measurements of the irradiation beam used in the experiment.and r represents the length of the perpendicular dropped from the target position to the extension of the direction vector of the irradiation beam. Taking R' as the distance from the transmitter, it is measured as,

$$w(R') = -2.95 + 0.65\,R' \tag{5-14}$$

$$\Delta\sigma = \begin{cases} A_{tr} \ \ (if\ A_{SC} \geq A_{tr}) \\ A_{SC}\ (if\ A_{SC} < A_{tr}) \end{cases} \tag{5-15}$$

Therefore, from (5-11), (5-13), and (5-15), we have:

$$\left[2K\left(\frac{\lambda}{hc}\right) Exp\ f_r \eta_t\ \eta_r \eta_Q \frac{A_r}{R^2} F(R) P_t \exp\left(-2\frac{r^2}{w^2}\right) \cos^4\theta_r \cos\theta_i\right]_{threshold} = \Delta I_{diff} \tag{5-16}$$

Here, $F(R)$ is defined as

$$F(R) \equiv \begin{cases} 1 \ \ (if\ A_{SC} \geq A_{tr}) \\ A_{SC}/A_{tr} \ \ (if\ A_{SC} < A_{tr}) \end{cases} \tag{5-17}$$

The factor "Exp" appearing on the left-hand side of (5-16) is the minimum exposure time to be obtained. Therefore,

$$Exp = K' \frac{R^2 R'^2}{f_r \cos^4\theta_r cos\theta_i \exp\left(-2\frac{r^2}{w^2}\right)} \tag{5-18}$$

Here, based on the experimental conditions, the case $A_{SC} < A_{tr}$ was selected in (5-17), and in this case, $F(R)$ is proportional to $F(R) \propto 1/R'^2$. The constants appearing in (5-18) are collectively denoted as K'.

5.5.2.2. Reflectivity model of the PV

The f_r in (5-16) represents the target's reflectivity characteristics, and this depends on the target reflectivity ρ and θ_i, θ_r. The target's reflectivity characteristics are mainly specular accompanied by small diffuse components. To represent this, we introduce the Bidirectional Reflectance Distribution Function (BRDF) and express f_r in the following the Cook–Torrance form [14–17].

$$f_r(\rho, \theta_i, \theta_r) = \frac{D\ G\ F}{4\ cos\theta_i cos\theta_r} \tag{5-19}$$

Here, D is the micro-surface distribution function, and G is the geometrical shadowing-masking function. F represents the Fresnel reflection function, which denotes the target's Fresnel reflectivity and is known for its simplified formula by Schlick [16]. On the other hand, G depends on D [17]. When considering the target as a set of micro surfaces forming a random rough surface, D is a distribution function dependent on the orientation and roughness of the micro surfaces. There are several variations of the micro surface distribution function D, and two representative distribution functions are known. One is the Beckmann distribution, which represents a Gaussian distribution of flat micro surface orientation whose correlation decays exponentially [18].

$$D_B(m) = \frac{exp(-tan^2\theta_m/m^2)}{\pi\ m^2\ cos^4\theta_m} \tag{5-20}$$

Here, θ_m is the angle between the macroscopic normal and the local (microscopic) normal and m is the surface roughness parameter. Another one is the Trowbridge–Reitz distribution [19] (note the Trowbridge–Reitz distribution is denoted as GGX in some literature [17]), which expresses the curved random surface with a quadratic mean m.

$$D_{TR}(m) = \frac{m^2}{\pi\ cos^4\theta_m(m^2 + tan^2\theta_m)^2} \tag{5-21}$$

Here, θ_m and m are parameters like in the Beckmann distribution. For both distributions, a smaller m implies a stronger specular characteristic. Referring to the comparison provided in [16], m is approximately 0.5 for acid-etched glass and around 0.02 for anti-glare glass, and smaller m results in a smaller difference between the Beckmann and the Trowbridge–Reitz distributions. To determine whether $D_B(m)$ or $D_{TR}(m)$ is more suitable as a model representing the reflection characteristics of the PV, the BRDF is computed based on (5-13), (5-14), and (5-15). F and G were calculated using the equations proposed in [16] and [17], respectively. Assuming a strong specular component with m = 0.01, both distributions are plotted against θ_m on the horizontal axis, resulting in the plot depicted in Figure 5-27.

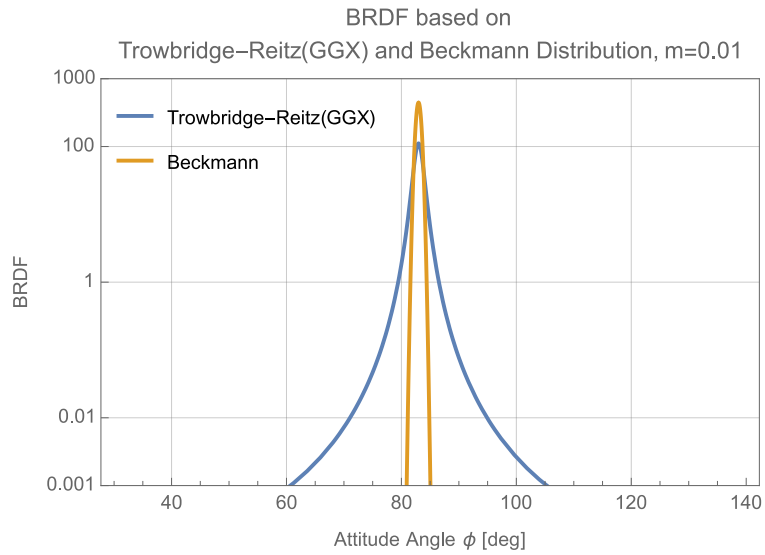


Figure 5-27 Comparison of Trowbridge-Reitz and Beckmann distribution.

Both show minor differences within the range of around $O(10^1)\sim O(10^2)$, but the disparity becomes significant within the range of approximate $O(10^{-2})\sim O(10^{-3})$. In Figure 5-26(a), due to the influence of the diffuse component in the target reflection characteristics, even when the target attitude angles are large, the BDRF needs to be $\leq O(10^{-2})$ considered. Therefore, the Trowbridge–Reitz distribution is appropriate for the PV rather than the Beckmann's. Actually, when attempting to fit the experimental data from Figure 5-26(a) to determine the constant K' in (5-18), successful fitting is achieved with $m = 0.01$ for the Trowbridge–Reitz distribution, however, the Beckmann distribution fails the fitting and its value of m cannot be determined due to its short tail distribution. For both the Beckmann and the Trowbridge–Reitz distributions, when the value of m becomes large, the specular state represented by the BRDF should continuously become a diffuse state. To make such a continuous transition mathematically, the small constant term ρ/π can be included in (5-20) and (5-21) [15,16]. Even when attempting to fit including this additional term, the above results remain unchanged for the PV. When the model for the minimum exposure time derived from the Trowbridge–Reitz distribution is overlaid and plotted in Figure 5-26(a), it appears as shown in Figure 5-28.

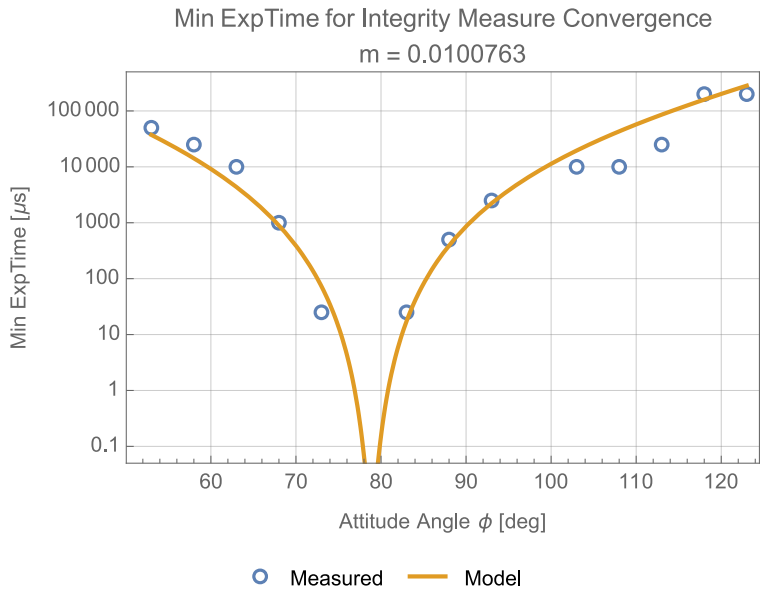


Figure 5-28 Minimum exposure time model for integrity measure convergence.

The estimated errors of the attitude angles at each point of Position Set 1, 2, and 3, based on the model, are illustrated in Figure 5-29. This figure shows that the derived integrity measure model can be used to estimate the target's attitude. The estimation errors are improved from Figure 5-26(b) and remain within the range of 10~15 deg except for the outlier at ϕ = 123 deg.

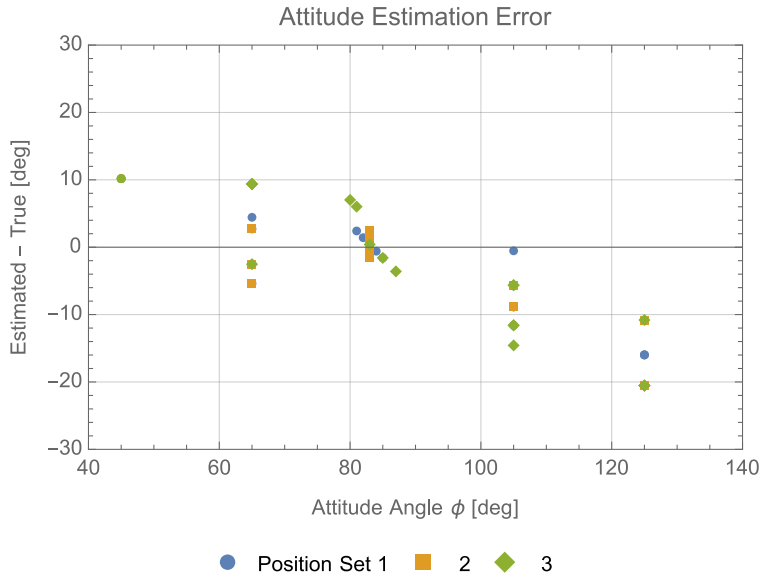


Figure 5-29 Attitude estimation of the points of Position Set 1, 2, and 3 based on the integrity measure model.

5.5.2.3. Relationship of the Integrity Measure with the Detectability

In 5.5.2.1 and 5.5.2.2, the physical model of the minimum exposure time for the integrity measure was derived and integrity measure data were well-fitted with the threshold equation based on the detectability in Figure 5-28. Experimentally, this suggests if the integrity measure (I) is satisfied, the detectability (D) will be satisfied. Symbolically, $(I \subseteq D)$.

The detectability criteria restrict the center coordinates error and that of the area size, and the threshold of its realization depends on the exposure time of the image sensor. If the detectability criteria hold for either the left or the right image, it will be highly probable that the criteria hold for both. While the integrity measure restricts the difference between the center coordinates of the left and the right images, its convergence is equivalent to that of the accuracy of the position estimation and its threshold depends on the exposure time. Thus, since both conditions are indicators of positioning accuracy and their thresholds depend on the exposure time, a close relationship between them is suggested. Unlike the detectability criteria, the integrity measure indicates only the convergence of the position accuracy, not its value. Therefore, it may look like a weaker condition than the detectability criteria. Symbolically, $(D \subseteq I)$.

Then , $I \sim D$ will be conjectured. Figure 5-30 shows the experiment data of the detectability threshold, superimposed with the integrity measure threshold shown in Figure 5-28. While the curve was for the threshold of the integrity measure, it looks fitted also with the detectability threshold. While the Y coordinates do not fit due to the rotational symmetry about the Y axis, X coordinates and the area size fit well. From the figure, the two thresholds are well-fitted by the single curve. This suggests that the two concepts are equivalent up to the adaptation constant K' in (5-18).

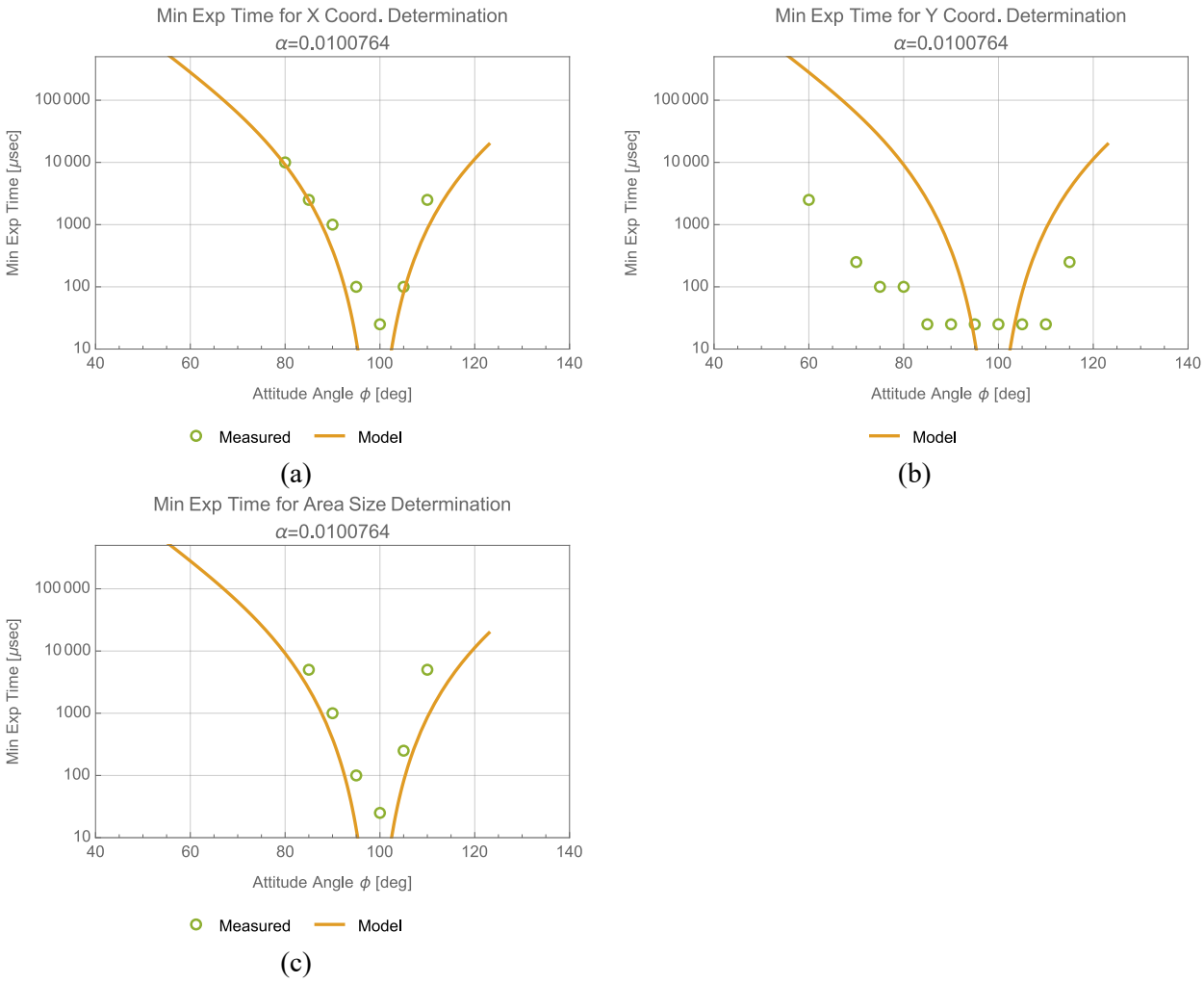


Figure 5-30 The minimum exposure time that the detectability criteria hold, superimposed with the minimum exposure time model of the integrity measure convergence

5.5.2.4. Error Model of the Minimum Exposure Time Method

The error model of this minimum exposure time is constructed using the model developed in 5.5.2.1. The attitude estimation error of this model comes from the measurement error of the minimum exposure time ΔExp. The attitude estimation error $\Delta\phi$ [deg] is expressed by the following equation.

$$Exp + \Delta Exp = \frac{K' R^2 R'^2}{f_r(\phi + \Delta\phi)\cos^4\theta_r(\phi + \Delta\phi)cos\theta_i(\phi + \Delta\phi)\exp\left(-2\frac{r^2}{w^2}\right)} \quad (5\text{-}22)$$

(5-22) is plotted in Figure 5-31 for the case of $\Delta Exp/Exp = -0.3, -0.6, -0.9, -1.0$. In the case that $\Delta Exp/Exp$ is in the range $-0.6 \sim -0.9$, Figure 5-31 agrees with Figure 5-29.

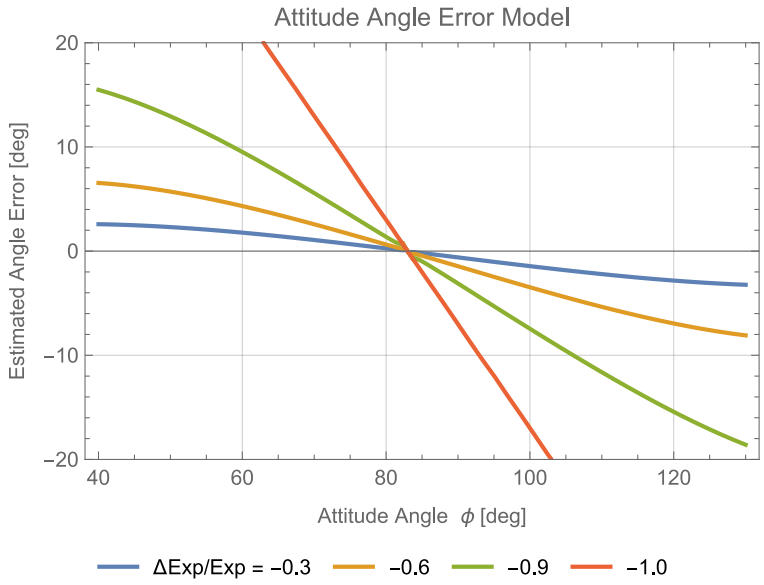


Figure 5-31 Attitude angle error model.

Even though this indicates that the measurement of the minimum exposure time suffered large errors, considering the resolution of the exposure time setting for the camera was coarse as shown in Table 5-1, this can be regarded as allowable. This indicates the validity of the model developed in 5.5.2.

5.5.3. Attitude Estimation by the Apparent Size of the Target

There is another method for estimating the target's angular position based on the variation in the apparent width of the target, aside from the one proposed in the former sections. Let the size of the target be denoted as x_0 and y_0, respectively. Assume the target is tilted around the y-axis, and the measured apparent size at a certain distance is x and y, the change in the target's attitude angle change $\Delta\phi$ from its normal can be expressed as:

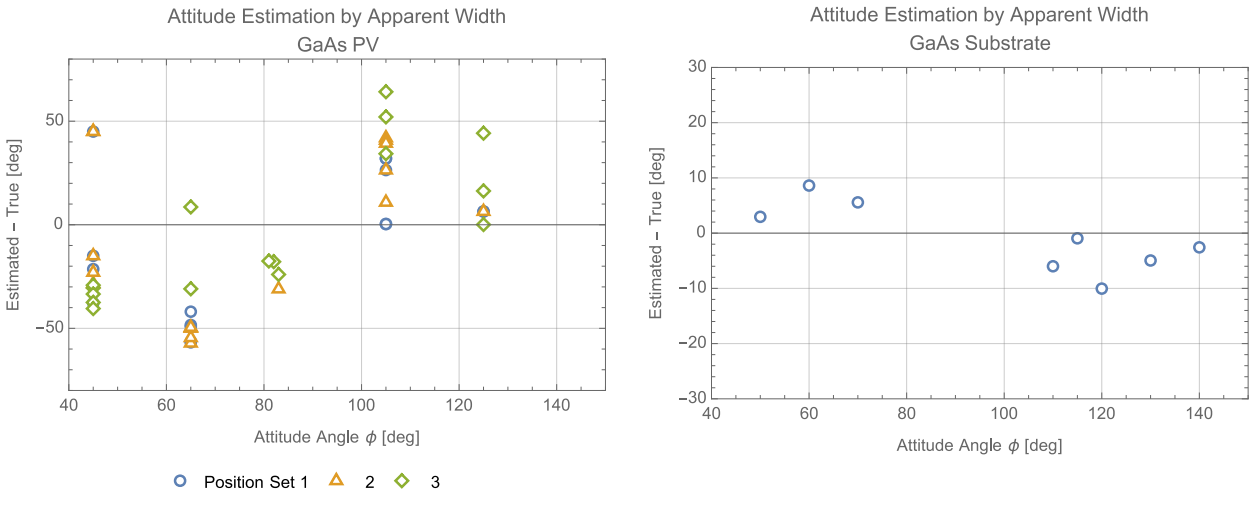
$$\Delta\phi = cos^{-1}\left[\frac{x}{x_0}\left(\frac{y_0}{y}\right)\right] \tag{5-23}$$

The results of the estimation of the attitude of the PV based on this method using the images obtained from the left image sensor are shown in Figure 5-32(a). A comparison with Figure 5-29 reveals a significant increase in estimation error. While Figure 5-29 estimates the attitude based on the estimated left and right center coordinates of the target and their integrity condition, Figure 5-32(a) estimates based on the apparent size of the target. Therefore, when measuring the

apparent size of the target from an incomplete image, the error is expected to increase. On the other hand, when the target is a GaAs substrate that is close to an ideal diffuse reflector, a complete image of the target can be obtained. Figure 5-32(b) was plotted using the data for the GaAs substrate fixed at (0, 27) obtained in the experiments in Section 4. Overall, the errors are smaller, but estimation fails at ±20 degrees around the normal. The estimation limit of $\Delta\phi$ can be estimated as:

$$x_0(1 - cos\Delta\phi) \geq 1\ px \tag{5-24}$$

In the experiment, x_0 was measured to be 35 px, which results in $\Delta\phi \geq 13.8$ deg. The true value of the estimation limit for $\Delta\phi$ in the experiment lies between 15 and 20 deg, which is close to 13.8 deg. Thus, the estimation failure near the normal in Figure 5-32(b) can be understood as the estimation limit imposed by the target's size within the captured image. In summary, when the target's image is incomplete, the method of estimating the target's attitude based on the apparent size of the target, as shown in Figure 5-32(a), results in decreased accuracy. On the other hand, in cases where the target's reflectivity characteristics closely resemble those of an ideal diffusing reflector as depicted in Figure 5-32(b), the constraint is imposed by (5-24).



(a) (b)

Figure 5-32 Attitude estimation based on the apparent width of the target. (a) GaAs PV at the points of Position Set 1, 2, and 3; (b) GaAs substrate at (0, 27).

The photometric method proposed in this section, which utilizes the minimum exposure time associated with the convergence of the integrity measure, enables the estimation of the angular position even from an incomplete image. Moreover, in principle, it is not constrained by the target's size within the captured image. However, this method relies on the steep variation of the minimum exposure time regarding the attitude of the PV. In the case where the target closely resembles an ideal diffusing reflector, this minimum exposure time is expected to exhibit minimal changes regarding the attitude. It is anticipated that such target angular position estimations using this approach could lead to significant errors.

Comparing Figure 5-29 with Figure 5-32(b), the error characteristics of the former are complementary to that of the latter. While in Figure 5-29, the absolute value of the estimation error reaches a minimum in the neighborhood of 80 to 90 deg and increases with angle deviation from the normal, it behaves contrary in Figure 5-32(b). Even though the attitude estimation based on the apparent size change of the target has about a 30-degree (full angle) dead zone around the normal, it can be usable outside the region. According to Table 3-2 in Section 3, the incident (half) angle deviation limits for the fly-eye module are 180 (10.3), 499 (28.6), 245 (14.0) mrad (deg) for Wall-less, 1-Wall, and 2-Wall configurations, respectively. Since the diffuse target simulates the fly-eye module, the apparent size method can be used for the module with more than 1 wall.

Appendix 5

A.5.1. Mathematical Formulation of PV Positioning

A.5.1.1. The Positioning Formula with the Stereo Imagery

Cartesian X, Y, Z axes are defined in real three-dimensional (3D) space as $\vec{Z} = \vec{X} \times \vec{Y}$, and their coordinates are defined as (x, y, z). Assume that the two optical axes of the left and the right image sensors are parallel with each other and that both optical axes are included in the XY plane. Also, assume that the left optical axis and the right optical axis are parallel with the Y-axis. Then, consider that the target is projected onto the XY plane. Lengths and angles in the XY plane are defined as in Figure 5-33.

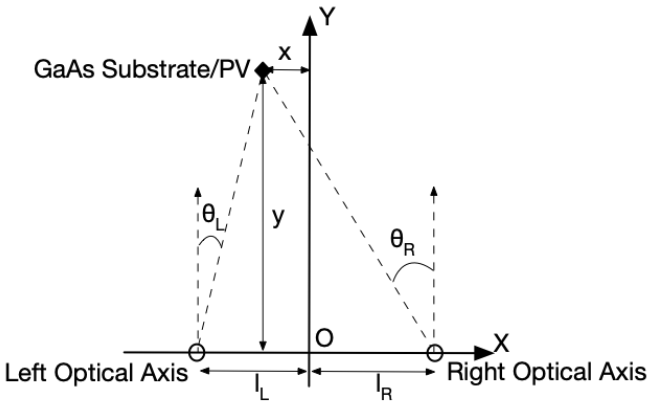


Figure 5-33 Configuration of positioning (stereo imagery).

$$l_L = y\, tan\theta_L \tag{5-25}$$

$$l_R = -y\, tan\theta_R \tag{5-26}$$

From Figure 5-33, since (5-25) and (5-26) hold, coordinates of the target (x, y) are expressed as

$$y = \frac{l_L + l_R}{tan\theta_L - tan\theta_R} \tag{5-27}$$

$$x = y\, tan\theta_L - l_L \tag{5-28}$$

Both l_L and l_R are known parameters and, according to the datasheet of D435, their values are 17.5 mm and 32.5 mm respectively. The image size from D435 was set to 640 × 480 px. The origin of the pixel coordinate system of both image sensors is defined as the bottom-left corner, and pixel coordinates (ξ, η) are defined as $0 \leq \xi \leq 639$, $0 \leq \eta \leq 479$. From (5-2), the

left/right vertical pixel coordinates should be the same ($\eta_L = \eta_L \equiv \eta$), and we assume that the pixel coordinates of the target are (ξ_L, η), (ξ_R, η) in the left and the right sensors respectively. Then θ_L, θ_R are given by (5-29) and (5-30).

$$\theta_L = tan^{-1}[\Delta\theta(\xi_L - 320)] \tag{5-29}$$

$$\theta_R = tan^{-1}[\Delta\theta(\xi_R - 320)] \tag{5-30}$$

From Equations (5-27)–(5-30), (x, y) can be expressed as follows, where $\Delta\theta$ converts the pixel size to an angular size, and it depends on the individual measurement system.

$$x = \frac{(\xi_L - 320)(l_L + l_R)}{(\xi_L - \xi_R)} - l_L \tag{5-31}$$

$$y = \frac{l_L + l_R}{\Delta\theta(\xi_L - 320) - \Delta\theta(\xi_R - 320)} \tag{5-32}$$

$$\Delta\theta = \frac{apparent\ angular\ size}{apparent\ size\ \ in\ pixel} \tag{5-33}$$

It is worth noting that, since l_L and l_R are inherent lengths in D435 camera, (5-31 is scale-invariant. In (5-32, y defines a scale of the system and $\Delta\theta$ y is scale-invariant.

The height of the target ($Z - axis$) is obtained from the vertical pixel coordinate of the target η, above y and $\Delta\theta$.

$$z = \mathrm{y}\tan(\Delta\theta\ \eta) \tag{5-34}$$

A.5.1.2.Estimation of the Constant ($\Delta\theta$) of Pixel (px) to Angle Conversion

$\Delta\theta$ was estimated using (5-33) using a frosted glass target of 100 mm × 100 mm size observed by a camera. The apparent pixel size of the target at fixed positions was measured as below. Since the target was tilted 20 deg to the X-axis (optical axis of the camera), the values in "Apparent size in px" were corrected by multiplying $1/cos(20\ deg) = 1.064$

Table 5-4 Estimation of $\Delta\theta$

Frost Glass Position	Distance (mm)	Apparent Size in px (X)	Apparent Size in px (Y)	Estimated $\Delta\theta$ (X) (mrad/px)	Estimated $\Delta\theta$ (Y) (mrad/px)
(0, 16)	406.4	86 (91.5)	88	2.69	2.80
(0, 21)	533.4	65 (69.1)	67.5	2.71	2.78
(0, 26)	660.4	53 (56.4)	55	2.68	2.75

The mean value of the above six estimations (three estimations for X and Y) is 2.74 mrad/px. Positions in Table 5-4 of the GaAs substrate were estimated using $\Delta\theta = 2.74\ \mathrm{mrad/px}$ as the initial value. To remove experimental errors included in the initial value of $\Delta\theta$, Y-coordinates were fitted with the true positions by fitting $\Delta\theta$. Then, $\Delta\theta = 2.6\ \mathrm{mrad}$ was obtained. Position estimation results are shown inFigure 5-34 for the two values of $\Delta\theta$. The $\Delta\theta = 2.6\ \mathrm{mrad}$ plot indicates that the camera's optical axis was tilted 33 mrad to the X-axis and the X-coordinate error was within 25.4 mm (= 1 lattice unit).

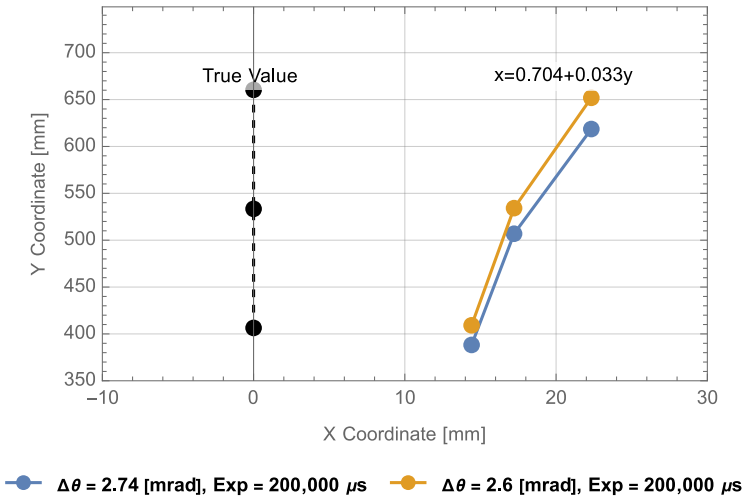


Figure 5-34 $\Delta\theta$ estimation

From the above estimations, the following value is adopted and used for position estimation experiments with (5-32) and (5-33).

$$\Delta\theta = 2.6mrad/px \tag{5-35}$$

A.5.2. The Positioning Formula without the Stereo Imagery

Let R be the range from the image sensor to the target, and consider the configuration in Figure 5-35.

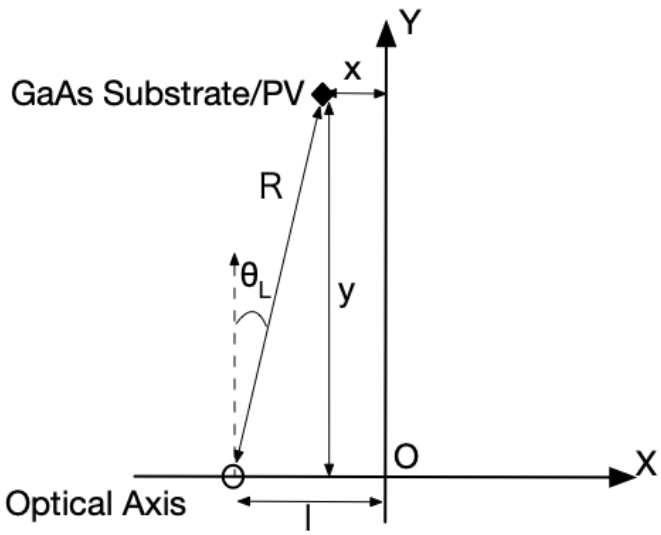


Figure 5-35 Configuration of positioning (mono-axis).

(x, y) is obtained from the estimation of R.

$$x = R\ sin\theta_L - l \tag{5-36}$$

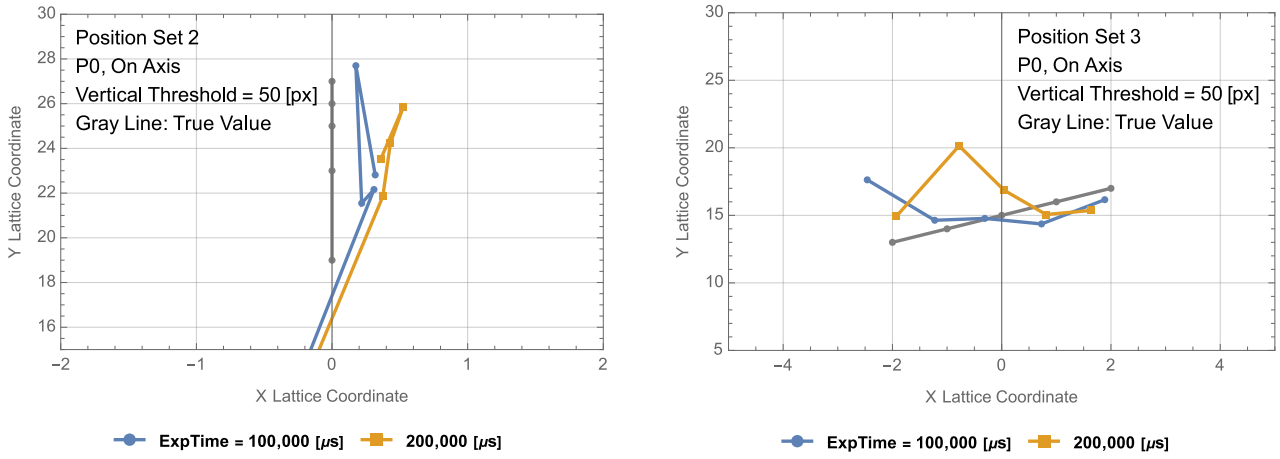
$$y = R\ cos\theta_L \tag{5-37}$$

Like (5-29), θ_L is calculated from pixel coordinates of the target in the pixel coordinate system. Assume that the size of the target D is known, and its apparent pixel size is P_x at range R. Then, R is given by

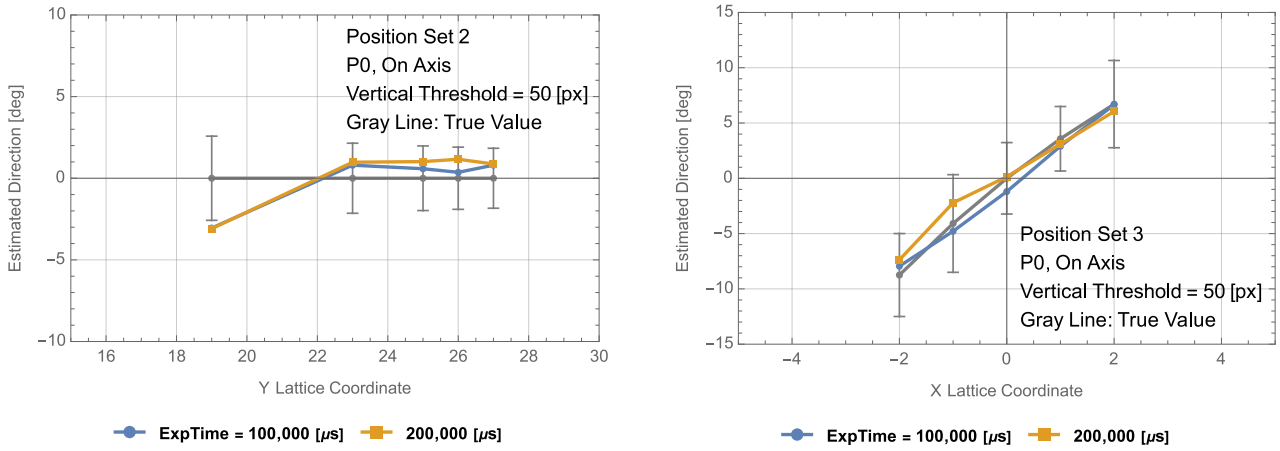
$$R = \frac{D}{tan(\Delta\theta\ P_x)} \tag{5-38}$$

A.5.3. Position and Direction Determination of the GaAs PV (On-Axis and Off-Axis for ϕ = 45 deg, 65 deg, 105 deg, and 125 deg)

A.5.3.1. On-Axis

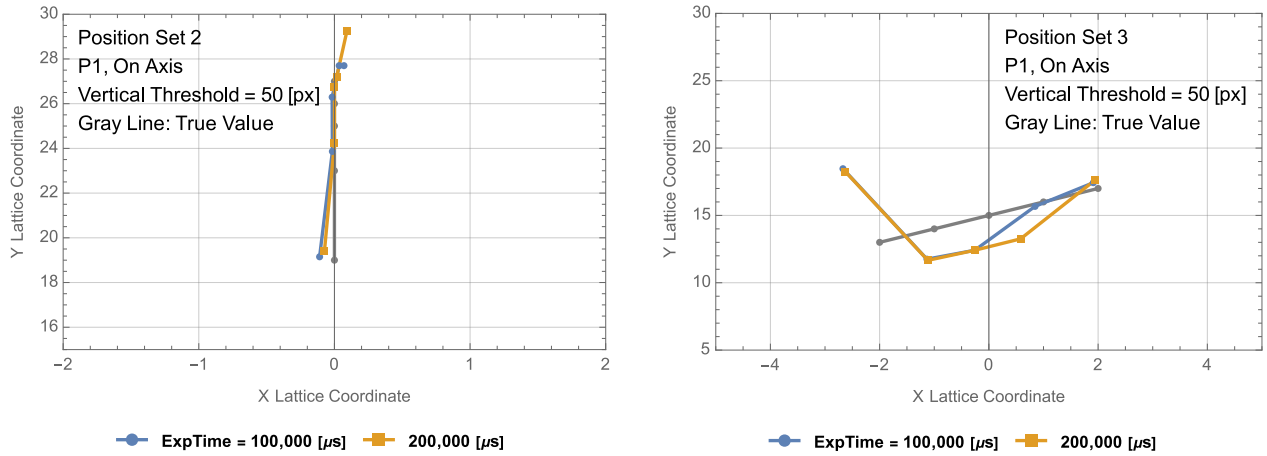


(a)

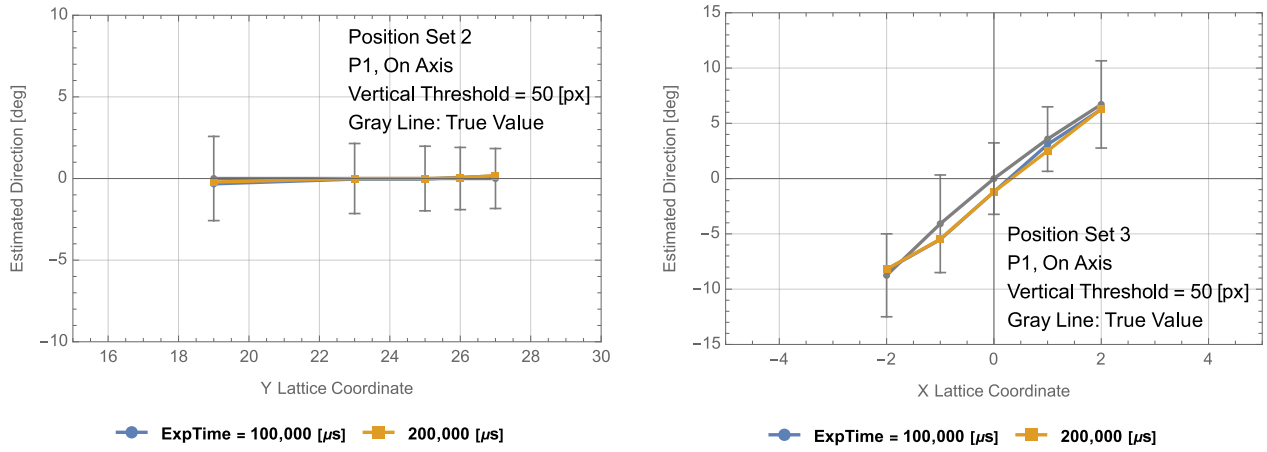


(b)

Figure 5-36 Estimated position and direction of GaAs PV (On-axis P0). The error bars in (b) are defined by Equation (5). (a) Position. (b) Direction.



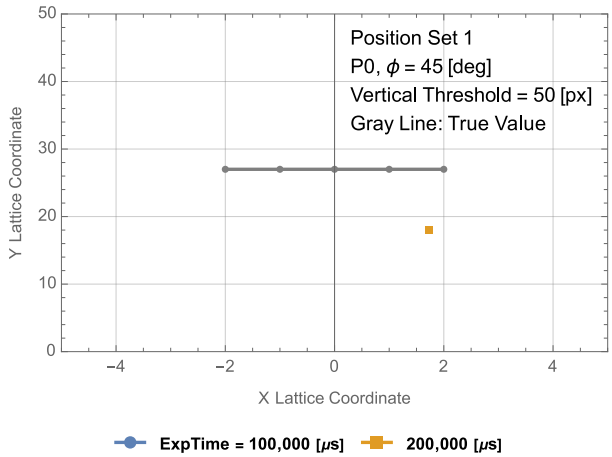
(a)

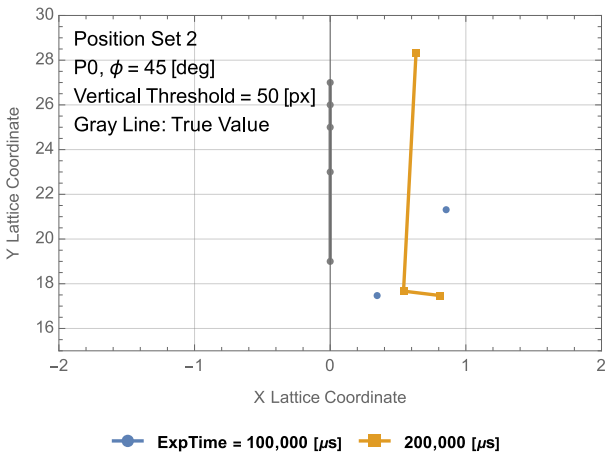


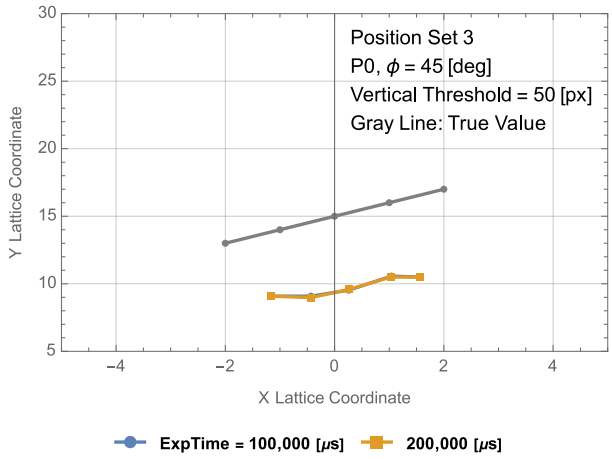
(b)

Figure 5-37 Estimated position and direction of the GaAs PV (On-axis P1). (a) Position. (b) Direction.

A.5.3.2.Off-Axis

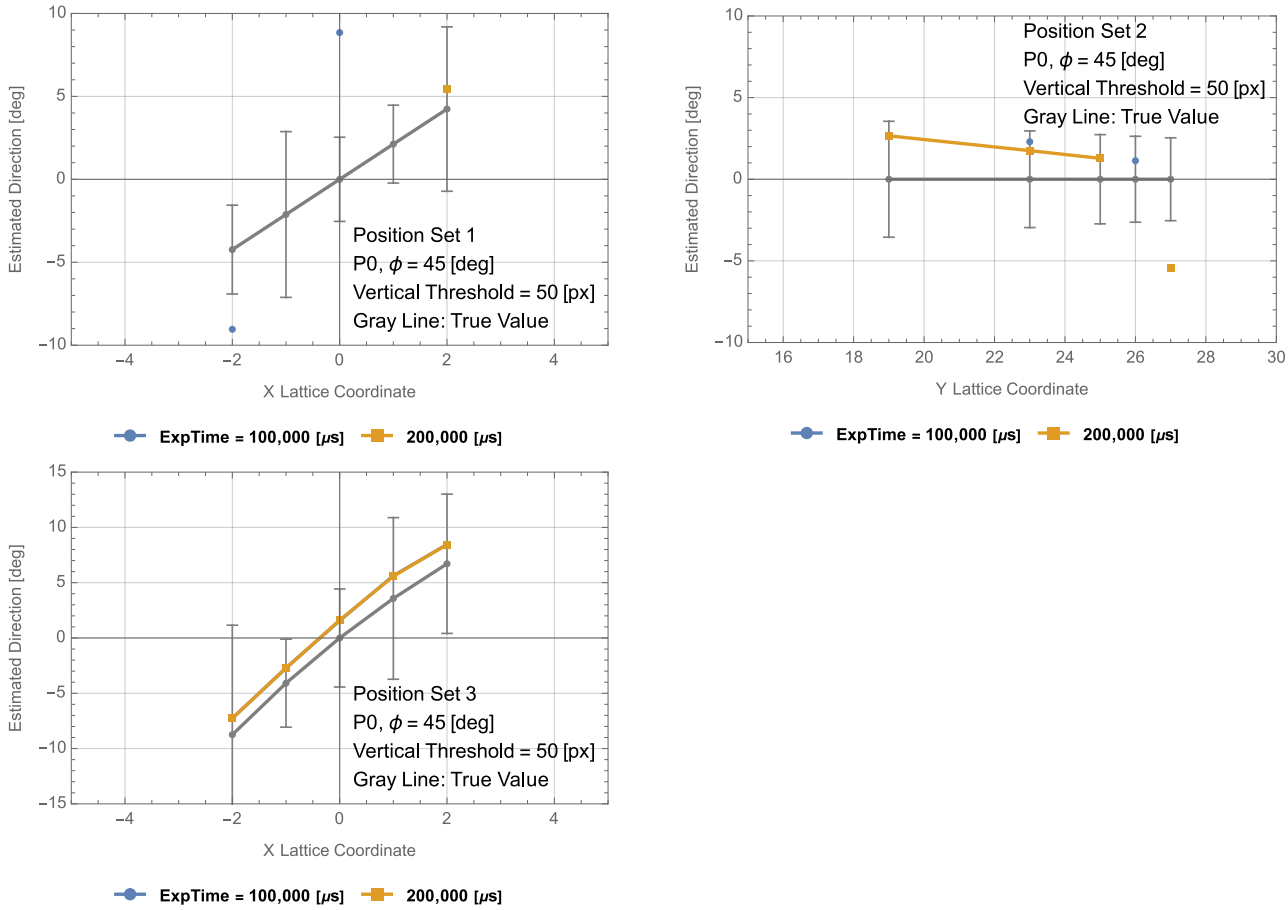






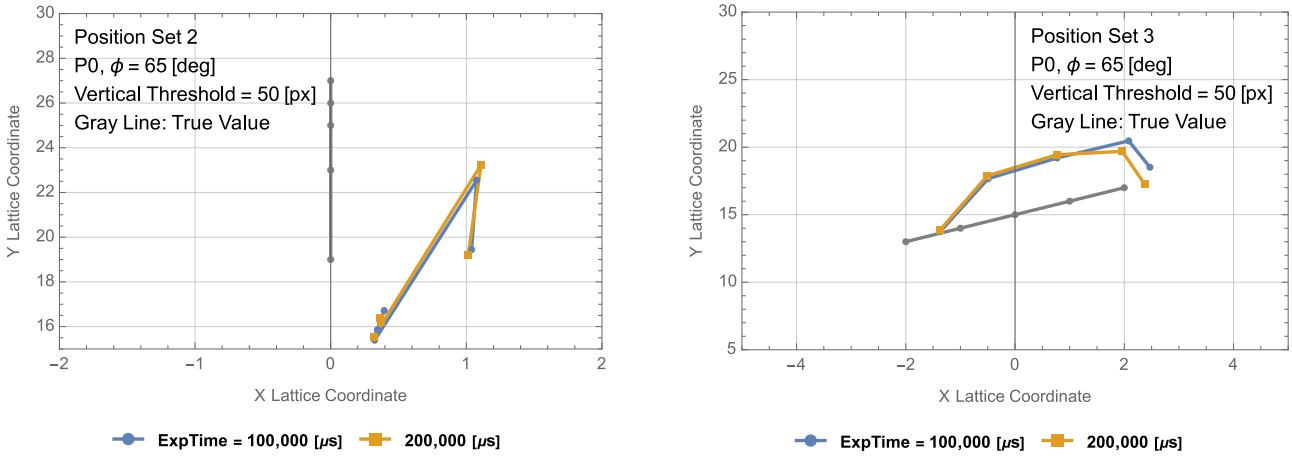
(a)

(Cont)

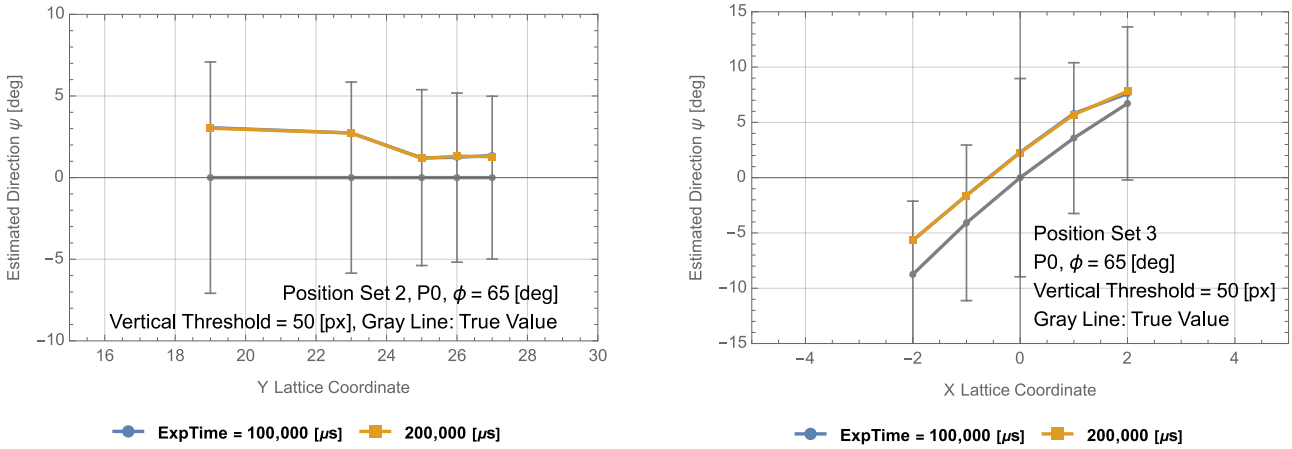


(b)

Figure 5-38 Position, direction determination of GaAs PV by means of stereo imagery for ϕ=45 deg. (a) Position; (b) Direction.

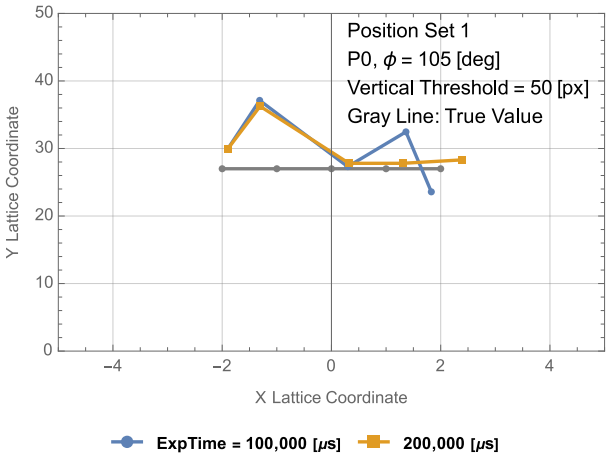


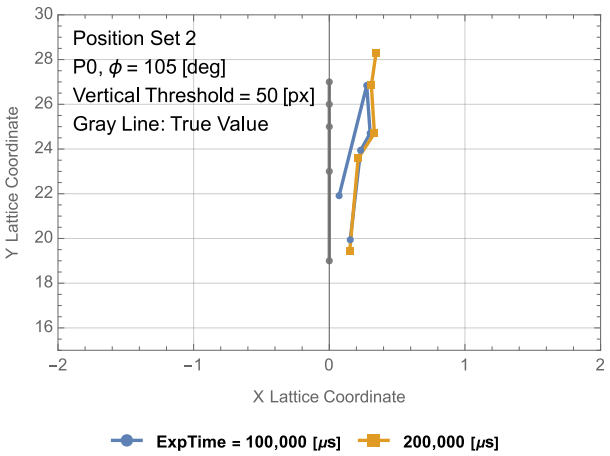
(a)

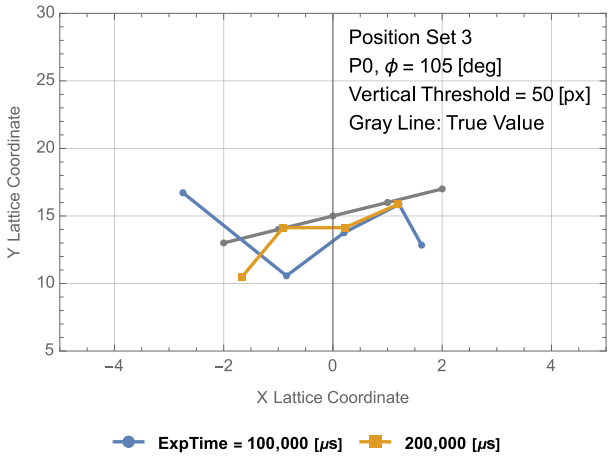


(b)

Figure 5-39 Position and direction determination of the GaAs PV by stereo imagery for ϕ = 65 deg. (a) Position. (b) Direction.

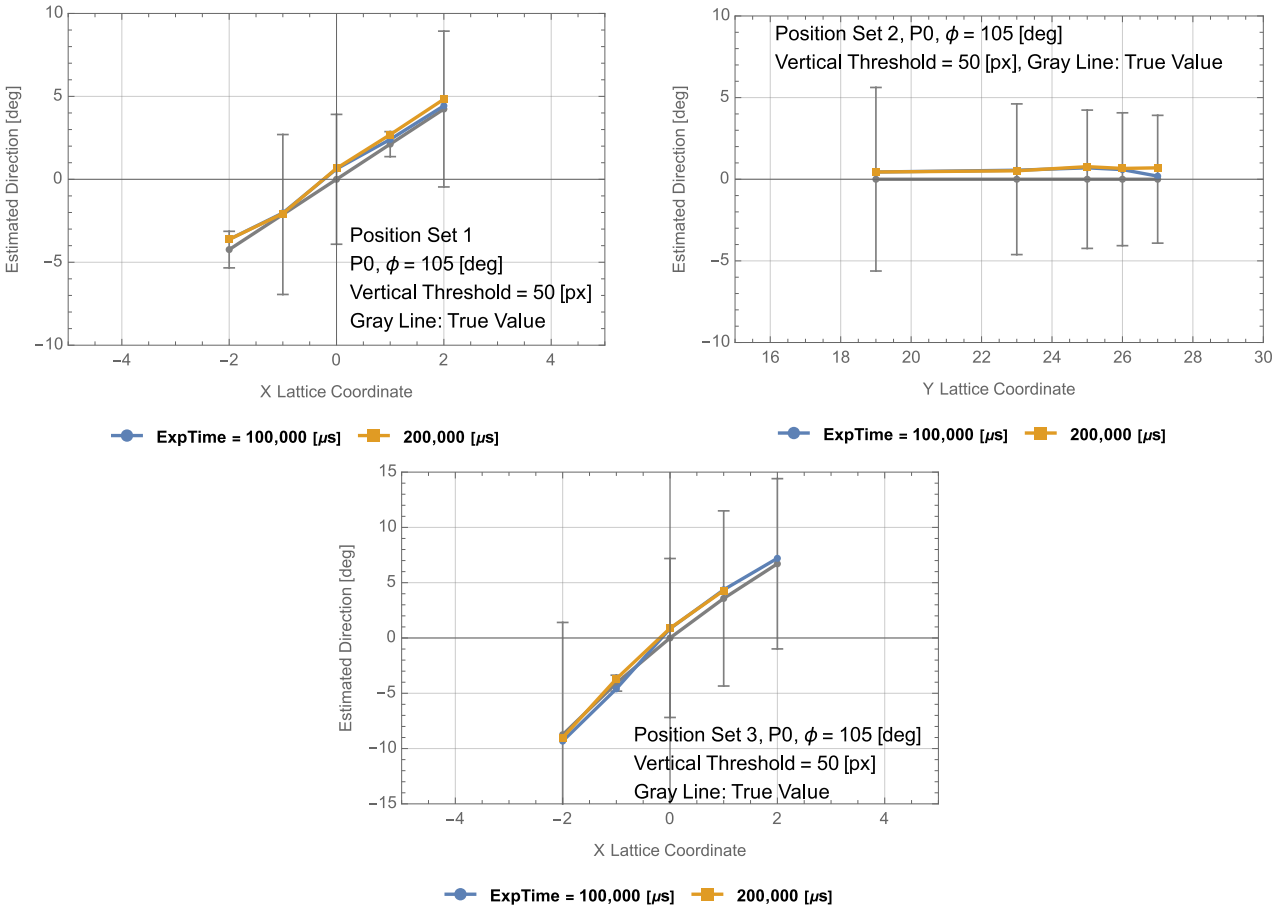

Position Set 1
P0, ϕ = 105 [deg]
Vertical Threshold = 50 [px]
Gray Line: True Value
Y Lattice Coordinate
X Lattice Coordinate
ExpTime = 100,000 [μs]
200,000 [μs]


Position Set 2
P0, ϕ = 105 [deg]
Vertical Threshold = 50 [px]
Gray Line: True Value
Y Lattice Coordinate
X Lattice Coordinate
ExpTime = 100,000 [μs]
200,000 [μs]


Position Set 3
P0, ϕ = 105 [deg]
Vertical Threshold = 50 [px]
Gray Line: True Value
Y Lattice Coordinate
X Lattice Coordinate
ExpTime = 100,000 [μs]
200,000 [μs]

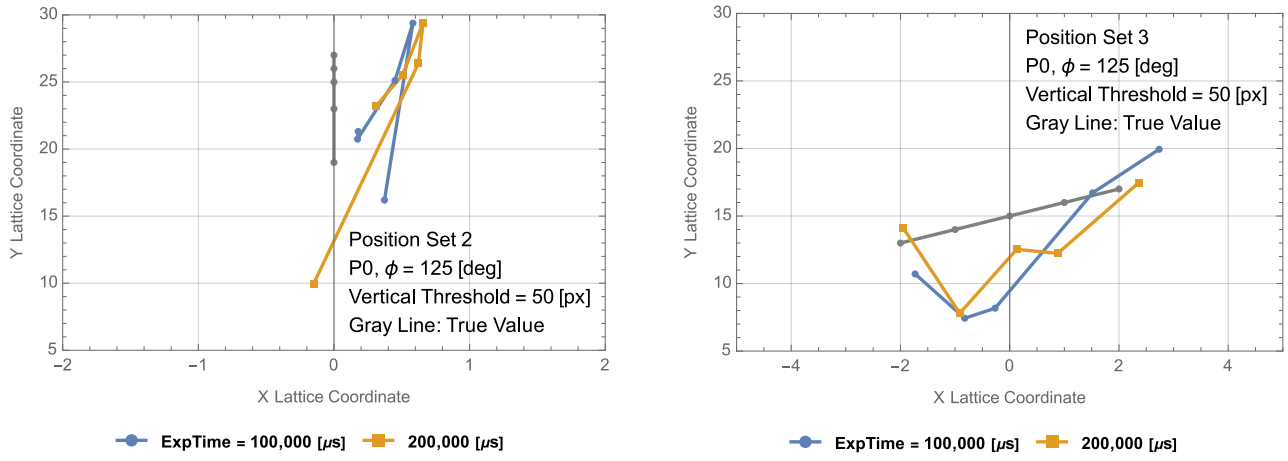
(a)

(Cont)

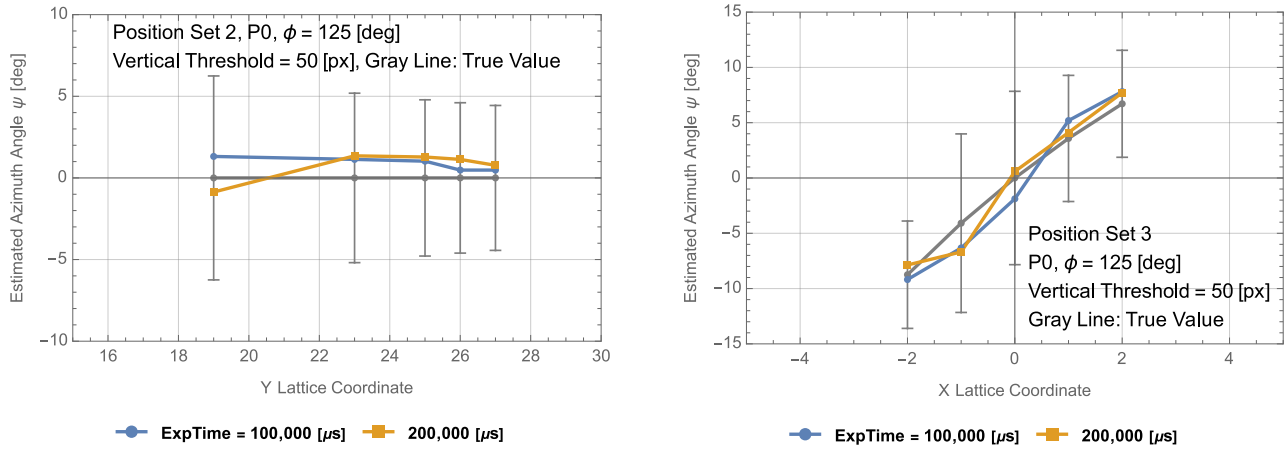


(b)

Figure 5-40 Position, direction determination of GaAs PV by stereo imagery for ϕ=105 deg. (a) Position; (b) Direction.



(a)



(b)

Figure 5-41 Position and direction determination of the GaAs PV by means of stereo imagery for ϕ = 125 deg.

A.5.4. Position Determination based on range estimation by the apparent size of the target combined with direction estimation.

A.5.4.1. On-Axis

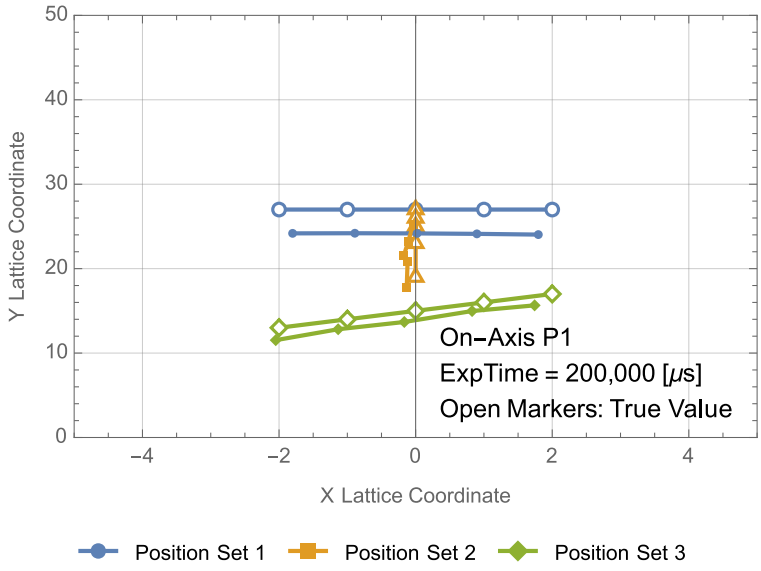
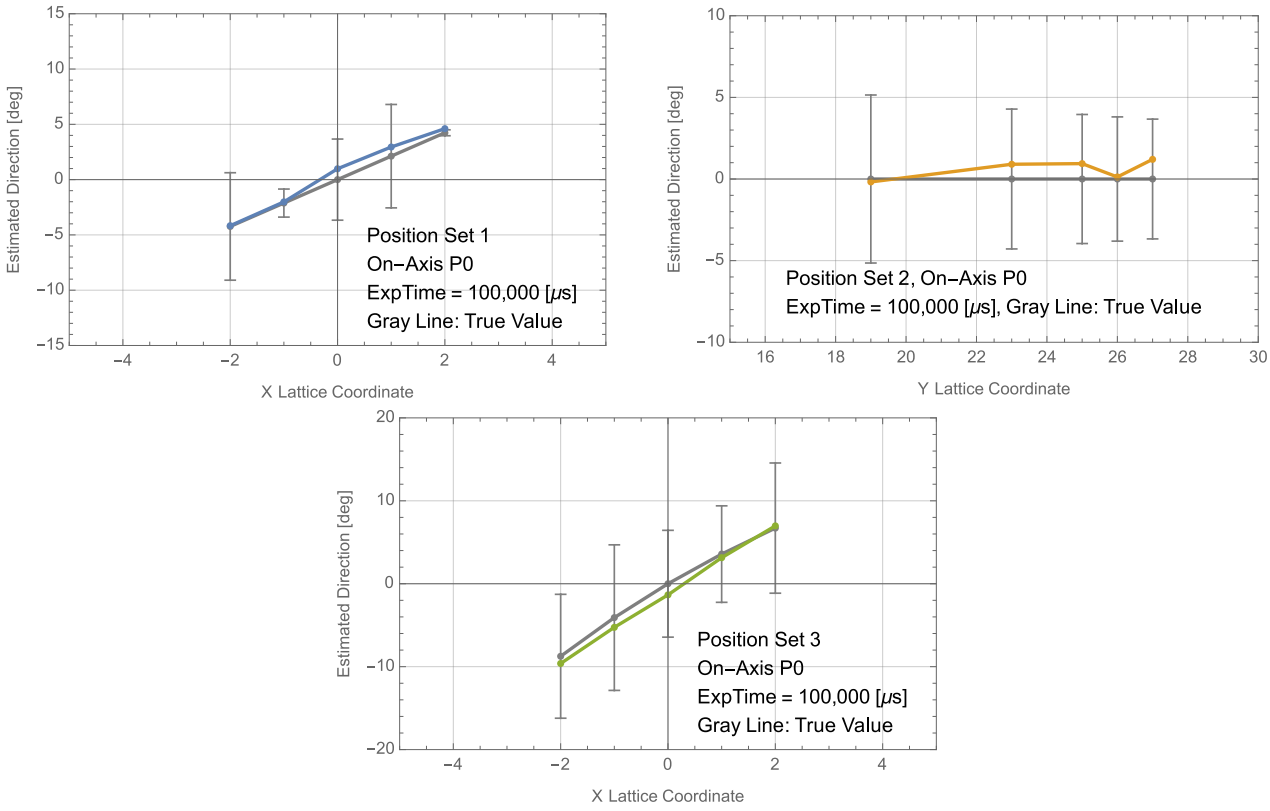
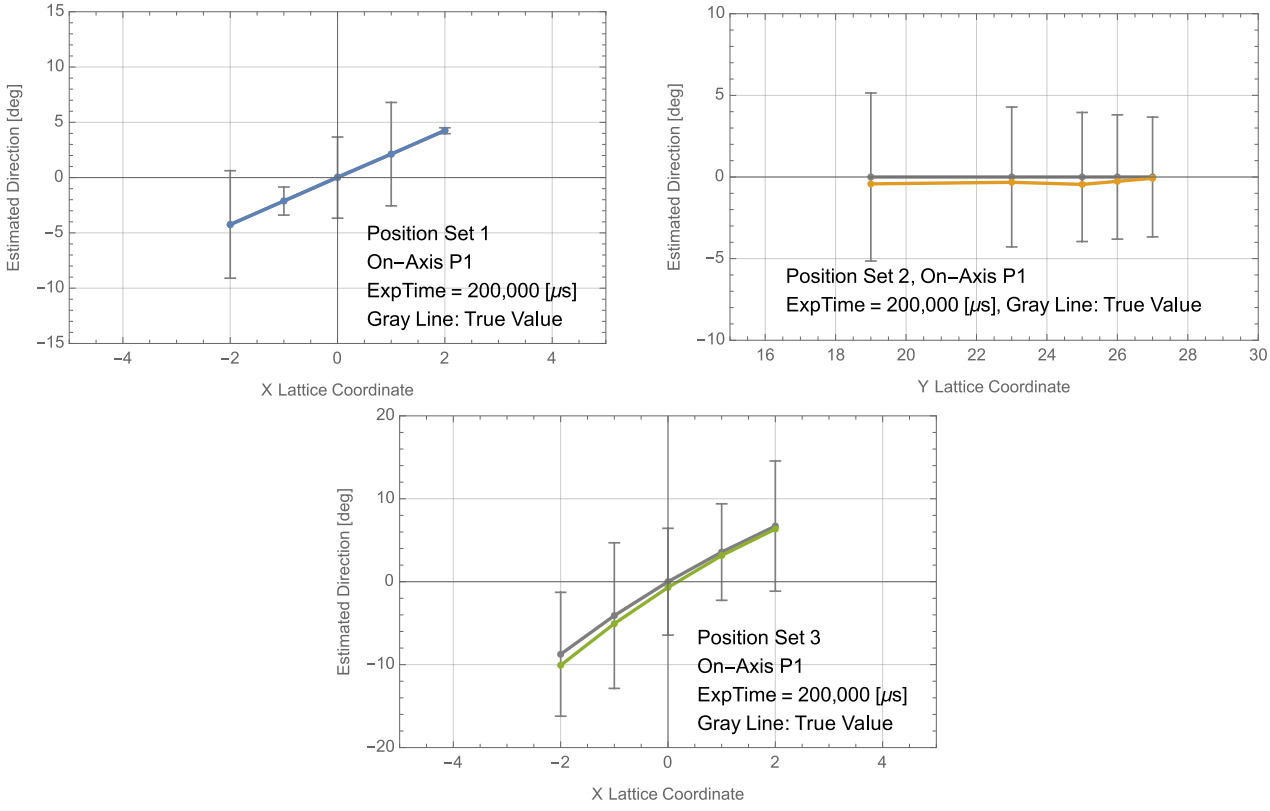


Figure 5-42 Estimated lattice coordinate of the GaAs PV (On-axis P1). Open markers indicate the true value and solid markers are estimations.



(a)



(b)

Figure 5-43 Estimated direction of GaAs PV (On axis P0, P1). (a) P0; (b) P1

A.5.4.2.Off-Axis

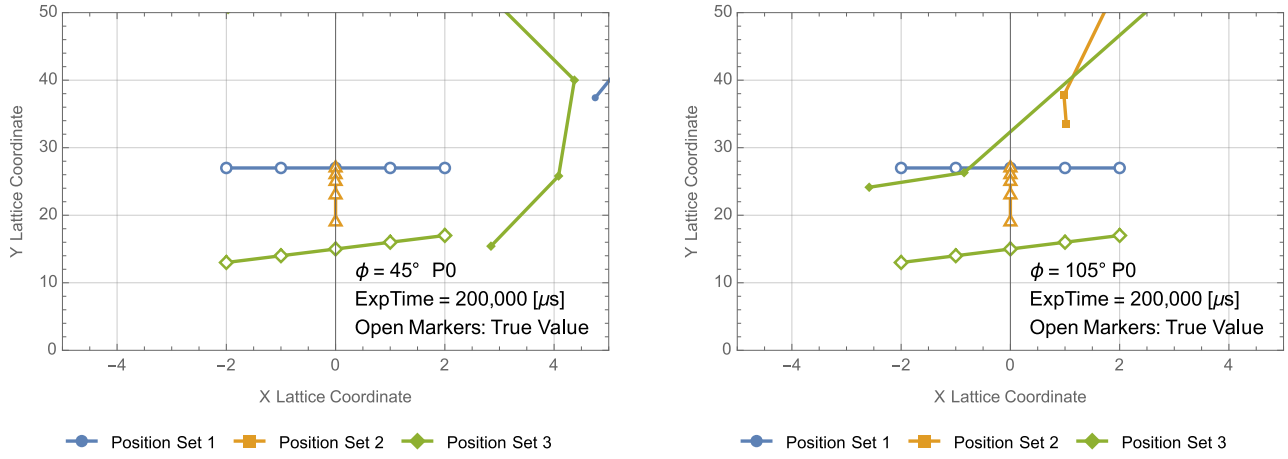
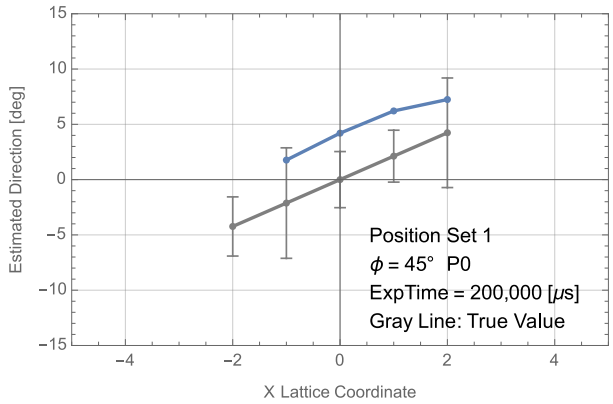
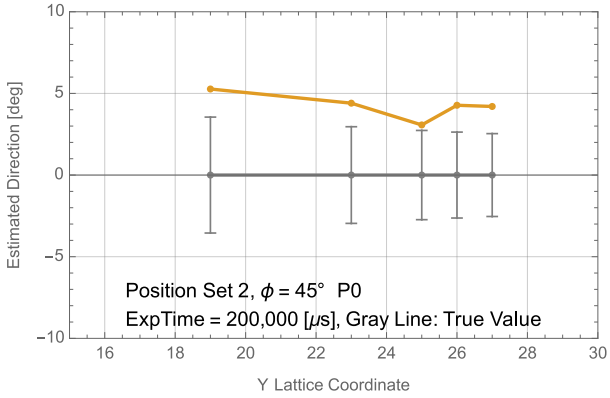
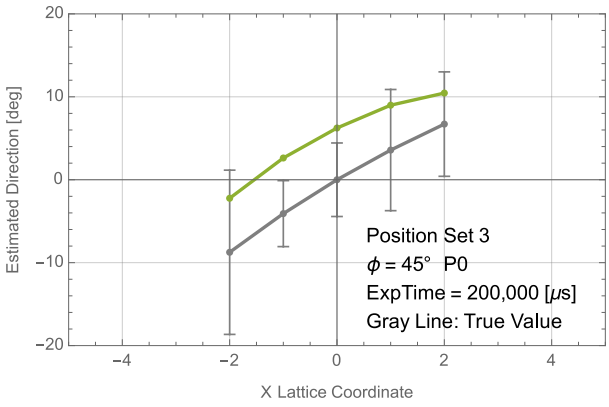


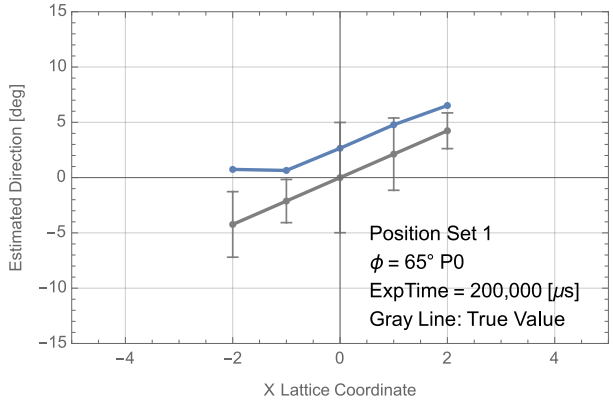
Figure 5-44 Estimated position of the GaAs PV (Off-axis P0). (a) ϕ = 45 deg; (b) ϕ = 105 deg. Open markers indicate the true value and solid markers are estimations.

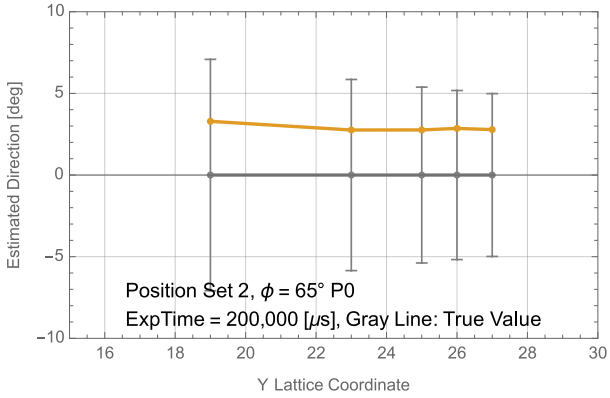

Estimated Direction [deg]
X Lattice Coordinate
Position Set 1
ϕ = 45° P0
ExpTime = 200,000 [μs]
Gray Line: True Value

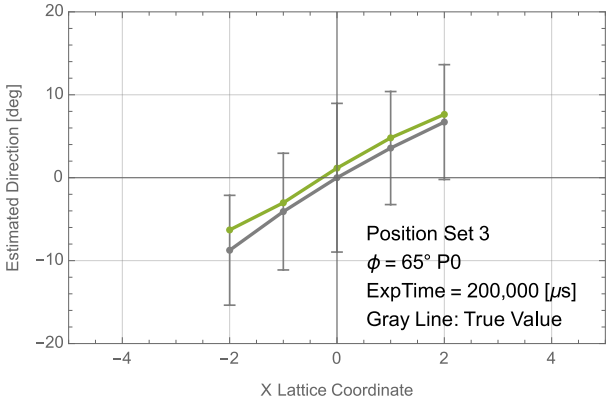

Estimated Direction [deg]
Y Lattice Coordinate
Position Set 2, ϕ = 45° P0
ExpTime = 200,000 [μs], Gray Line: True Value


Estimated Direction [deg]
X Lattice Coordinate
Position Set 3
ϕ = 45° P0
ExpTime = 200,000 [μs]
Gray Line: True Value

(a)

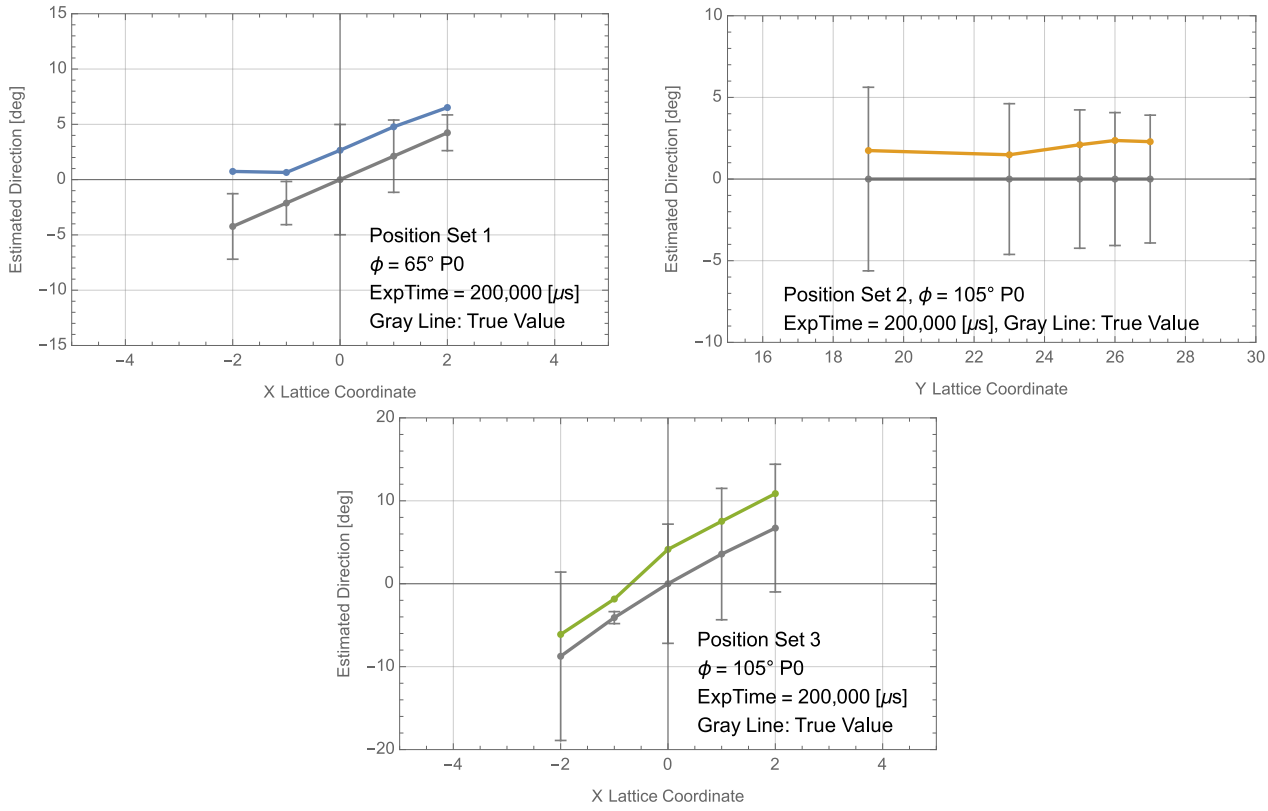

Estimated Direction [deg]
X Lattice Coordinate
Position Set 1
ϕ = 65° P0
ExpTime = 200,000 [μs]
Gray Line: True Value


Estimated Direction [deg]
Y Lattice Coordinate
Position Set 2, ϕ = 65° P0
ExpTime = 200,000 [μs], Gray Line: True Value


Estimated Direction [deg]
X Lattice Coordinate
Position Set 3
ϕ = 65° P0
ExpTime = 200,000 [μs]
Gray Line: True Value

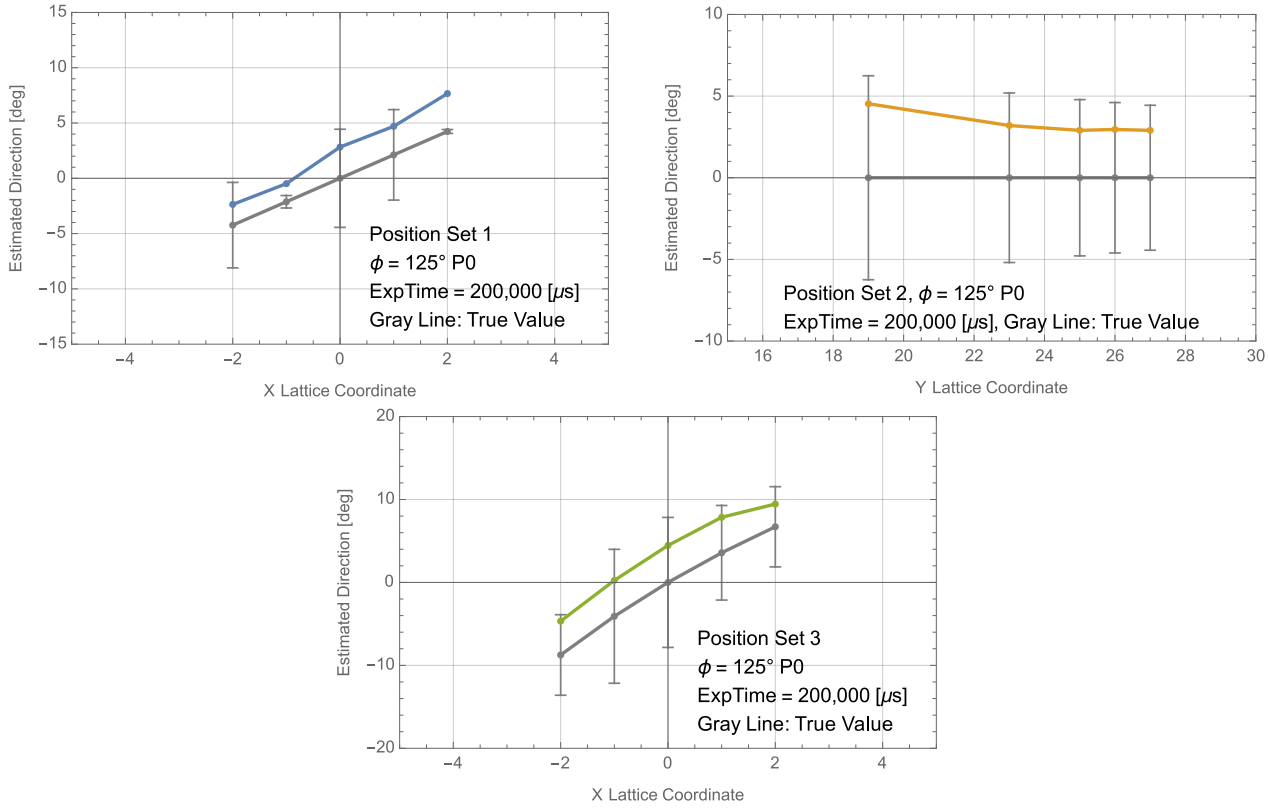
(b)

(Cont)


Estimated Direction [deg]
X Lattice Coordinate
Position Set 1
ϕ = 65° P0
ExpTime = 200,000 [μs]
Gray Line: True Value
Estimated Direction [deg]
Y Lattice Coordinate
Position Set 2, ϕ = 105° P0
ExpTime = 200,000 [μs], Gray Line: True Value
Estimated Direction [deg]
X Lattice Coordinate
Position Set 3
ϕ = 105° P0
ExpTime = 200,000 [μs]
Gray Line: True Value

(c)

(Cont)



(d)

Figure 5-45 Estimated direction of GaAs PV (Off-axis P0). (a) ϕ = 45 deg for Position Set 1,2 3; (b) ϕ = 65 deg; (c) ϕ = 105 deg; (d) ϕ = 125 deg.

A.5.5. Position Determination with External Ranging Information

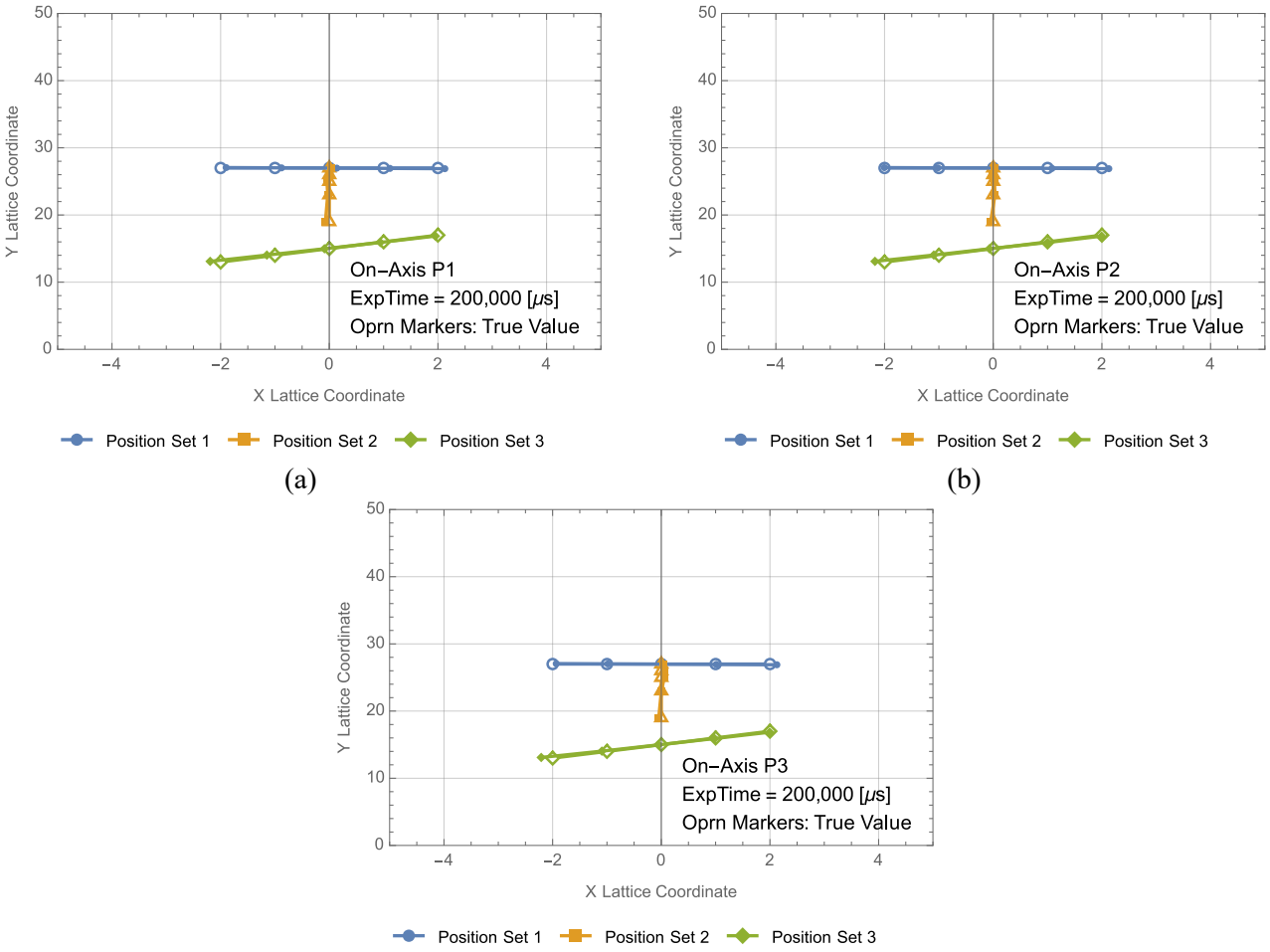


Figure 5-46 On-axis positioning with external ranging information. Open markers indicate the true value and solid markers are estimations. (a) P1 for Position Sets 1,2, and 3; (b) P2; (c) P3.

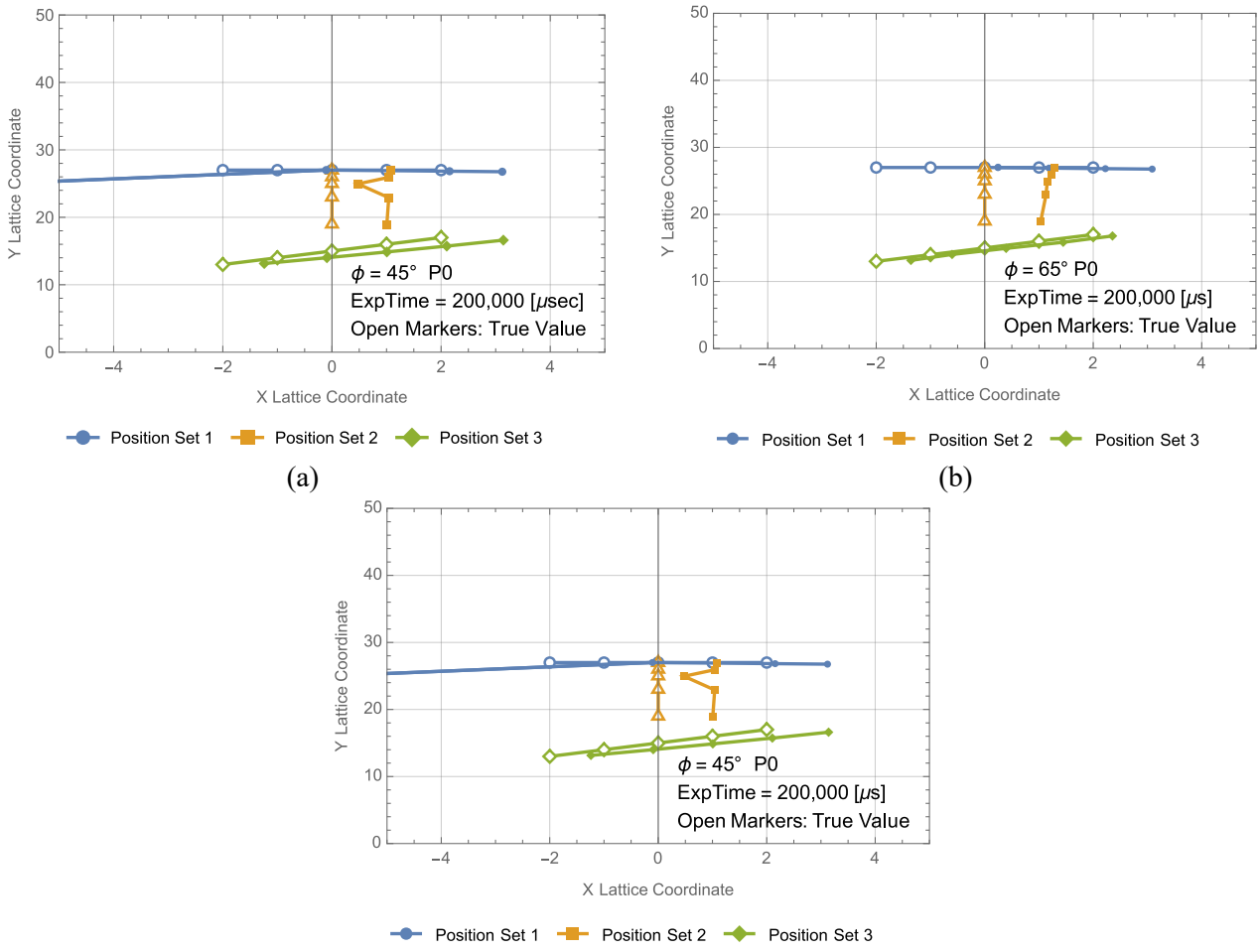


Figure 5-47 Off-axis positioning with external ranging information. Open markers indicate the true value and solid markers are estimations. (a) ϕ = 45 deg for Position Set 1, 2, and 3; (b) ϕ = 65 deg; (c) ϕ = 125 deg.

References 5

1. OS13CA5111A Available online: https://www.optosupply.com/uppic/20211028118028.pdf (accessed on 29 December 2022).
2. OSI5FU511C-40 Available online: https://akizukidenshi.com/download/OSI5FU5111C-40.pdf (accessed on 29 December 2022).
3. Depth Camera D435 Available online: https://www.intelrealsense.com/depth-camera-d435/ (accessed on 15 May 2023).
4. Intel *Intel ® RealSenseTM D400 Series Data Sheet*;
5. Welcome to Python.Org Available online: https://www.python.org/ (accessed on 24 August 2022).
6. Intel® RealSense™ Available online: https://www.intelrealsense.com/sdk-2/ (accessed on 24 August 2022).
7. Open CV Available online: https://opencv.org/ (accessed on 23 August 2022).
8. Wolfram Mathematica: Modern Technical Computing Available online: https://www.wolfram.com/mathematica/ (accessed on 15 August 2022).
9. Home | AXT Inc. Available online: http://www.axt.com/site/index.php?q=node/1 (accessed on 15 May 2023).
10. 850nm CWL, 12.5mm Dia., Hard Coated OD 4.0 10nm Bandpass Filter Available online: https://www.edmundoptics.jp/p/850nm-cwl-125mm-dia-hard-coated-od-4-10nm-bandpass-filter/28574/ (accessed on 24 April 2023).
11. 940nm CWL, 12.5mm Dia., Hard Coated OD 4.0 10nm Bandpass Filter Available online: https://www.edmundoptics.jp/p/940nm-cwl-125mm-dia-hard-coated-od-4-10nm-bandpass-filter/19778/ (accessed on 24 April 2023).
12. Asaba, K.; Miyamoto, T. Solar Cell Detection and Position, Attitude Determination by Differential Absorption Imaging in Optical Wireless Power Transmission. *Photonics* **2023**, *10*, 553, doi:10.3390/photonics10050553.
13. ATI—Advanced Technology Institute, Inc.—BioInformatics/Mathematical Information Engineering Available online: http://www.advanced-tech-inst.co.jp/ (accessed on 14 February 2023).
14. Cook, R.L.; Torrance, K.E. A Reflectance Model for Computer Graphics. *ACM Transactions on Graphics* **1982**, *1*, 7–24.
15. Gregory J. Ward Measuring and Modeling Anisotropic Reflection. *Computer Graphics* **1992**, *26*, 8.
16. Christphe Schlick An Inexpensive BRDF Model for Physically-Based Rendering. *Proc. Eurpgraphics'94, Computer Graphics Forum* **1994**, *13*, 14.

17. Walter, B.; Stephen R. Marschner; Stephen R. Marschner; Hongsong Li; Kenneth E. Torrance Microfacet Models for Refraction through Rough Surfaces. In Proceedings of the Proceedings of the 18th Eurographics conference on Rendering Techniques; Eurographics Association, June 2007; p. 12.
18. Beckmann, P.; Spizzichino, A. *The Scattering of Electromagnetic Wave from Rough Surfaces*; Pargamon Press: New York, 1963;
19. Trowbridge, T.S.; Reitz, K.P. Average Irregularity Representation of a Rough Surface for Ray Reflection. *J. Opt. Soc. Am.* **1975**, *65*, 531, doi:10.1364/JOSA.65.000531.

6. Real-Time Tracking of Photovoltaics

6.1. Experiments of Real-Time Successive Positioning and Attitude Determination of PV

Following position and attitude estimation of the stationary target in the previous section, we progress the investigations toward tracking a moving target.

6.1.1. Experiments Configuration and Tuning of Camera Parameters

The experiments described in this section utilized two D435 cameras designated for receiving λ_{ON} (Camera 1) and λ_{OFF} (Camera 2). Before conducting successive position estimation experiments, it is necessary to determine the maximum data rates available using these two cameras simultaneously, evaluate the latency between them, and estimate the time required for position estimation. The data rate and latency depend intrinsically on D435, while the time for position estimation depends on the PC, the operating system (OS), and the dedicated software used in the experiments. Furthermore, appropriate parameters need to be set in advance. There are two methods for synchronizing the two D435 cameras: hardware synchronization and software synchronization [1]. In this experiment, software synchronization was employed. Data acquisition from Camera 1 and Camera 2 were sequenced as follows and is depicted in Figure 6-1.

1. Initiating Data Stream for Camera 1:

   The data stream for Camera 1 is commenced by issuing the "Wait" command.

   1. Send "Wait" Command for Camera 1:
   2. Upon the data's arrival in the buffer, the timestamp (T1) is obtained.
   3. Following the acquisition of T_1, send a wait command (wait1).

2. Data Acquisition for Camera 2:

   For Camera 2, two options were considered for issuing commands.

   - One option is the "poll" command, which enables obtaining data from Camera 2 buffer and its timestamp (T_2) at T_1+wait1.
   - The other option is the "wait" command to retrieve the subsequent data and timestamp (T'_2) from Camera 2 data stream [2,3].

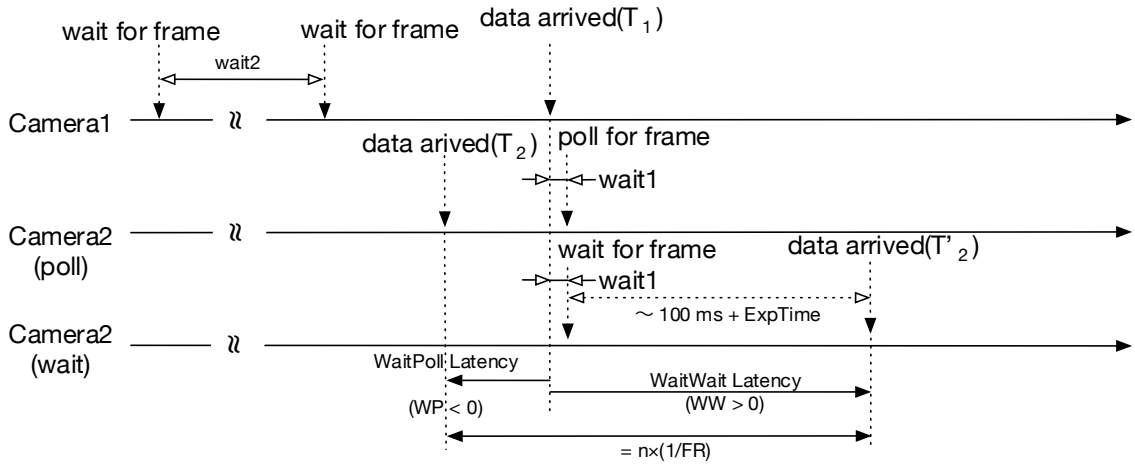


Figure 6-1 Timing chart of Camera 1 and Camera 2

Using the measurement $WP \equiv T_2 - T_1$ taken from the case of using the poll command for Camera 2 and $WW \equiv T'_2 - T_1$ from the case of using the wait command, the camera's internal frame rate (FR) for the camera's exposure time (ExpTime) can be estimated according to (6-1).

$$WW - WP = \left(\left[\frac{100msec + ExpTime}{1/FR}\right] + 1\right)\frac{1}{FR} \tag{6-1}$$

The bracket ([ ]) in (6-1) represents the integer part. The fitting results for FR as an integer based on the measured $WW - WP$ are presented in Figure 6-2.

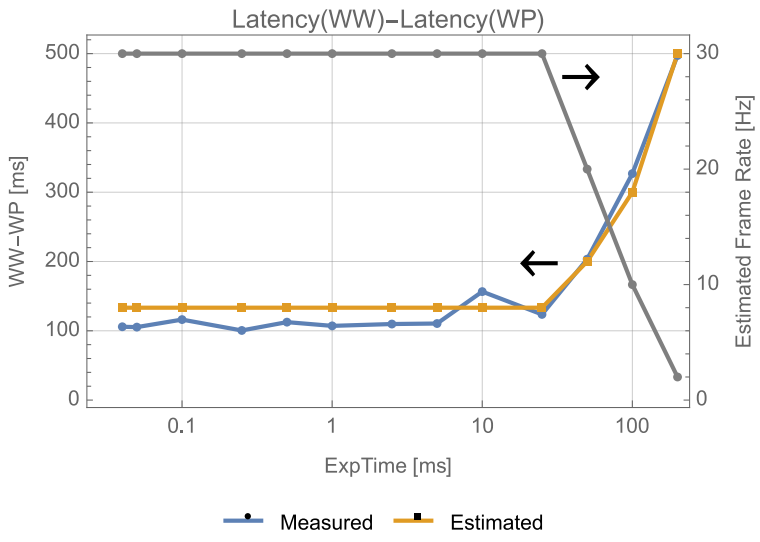
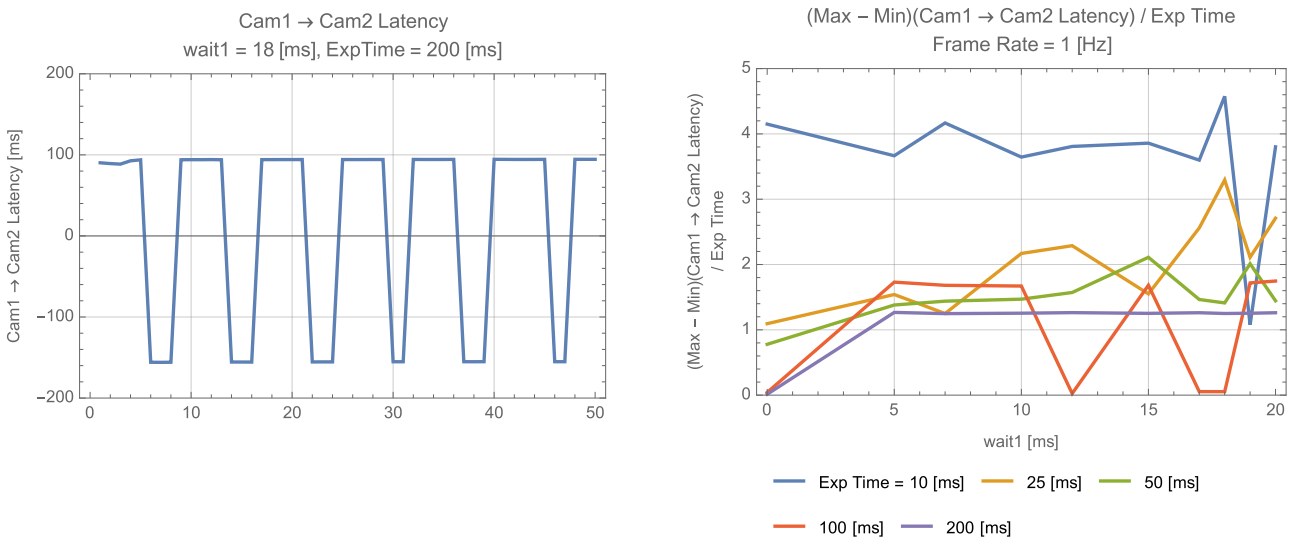


Figure 6-2 Frame Rate Estimation

In the experiments of static target position estimation in the former section, 100 or 200 ms exposure times were significantly important. Considering the frame rate is 2 Hz when the exposure time is 200 ms in Figure 6-2 and the data processing time in PC and OS, a wait time (wait2) in Figure 6-1 was set to 1 s. In addition, the decision was made to utilize Camera 1 with a wait command and Camera 2 with a poll command instead of the wait/wait configuration, as the former was anticipated to result in a smaller latency between Camera 1 and Camera 2. The latency between Camera 1 and Camera 2 was measured by varying wait1 in Figure 6-1, and the results are presented in Figure 6-3.



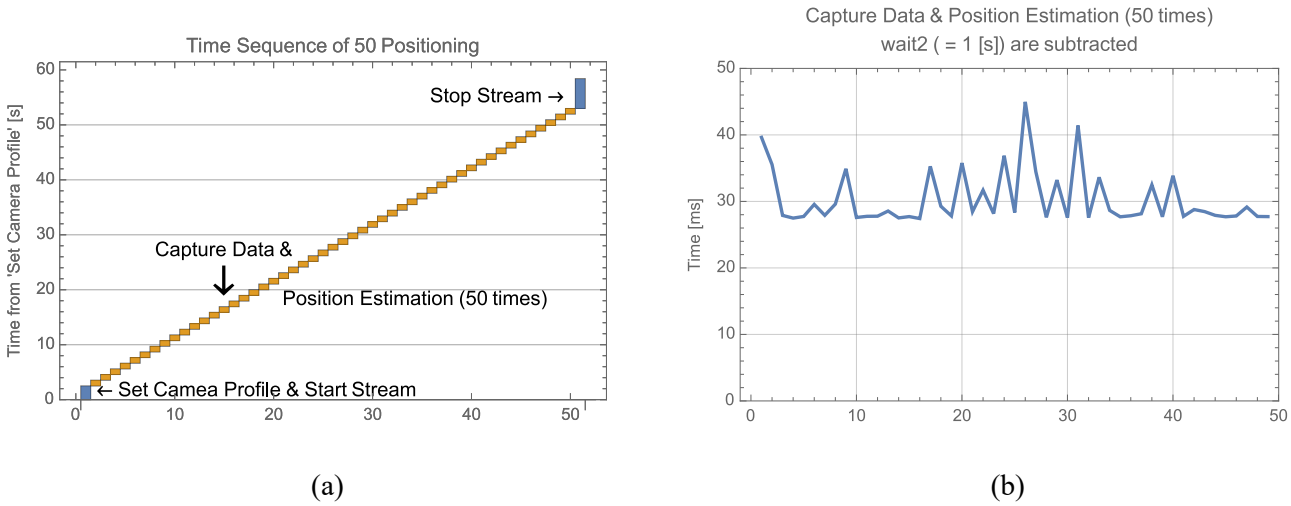
(a) (b)

Figure 6-3 Camera 1→Camera 2 latency, (a) Latency (wait1 = 18 [ms], Exp Time = 200 [ms]); (b) Max – Min latency of successive 50 data normalized by Exp Time

In Figure 6-3(a), the latency for successive 50 data is depicted when wait1 is set to 18 ms and Exp Time (exposure time) is 200 ms. In this case, the latency takes two values: +100 ms and −160 ms. Figure 6-3(b) plots the maximum minus (−) the minimum latency normalized by the camera's exposure time (Exp Time). The clustering of data around 1 on the vertical axis indicates that the latency fluctuates over the entire width corresponding to Exp Time. While the latency does not depend strongly on wait1, wait1 was set to 18 ms for Exp Time = 200 ms and 12 ms for 100 ms in this thesis. The deviation from 1 on the vertical axis of Figure 6-3(b) for shorter Exp Time is due to the time to estimate the position.

Figure 6-4(a) shows the time sequence for 50 consecutive position estimations, revealing that this process took approximately 60 s. It should be noted that about 8 s were allocated for the

initial Set Camera Profile & Start Stream and the final Stop Stream processes. On the other hand, a large portion of time spent on Capture Data & Position Estimation was attributed to wait2 (= 1 s) in Figure 6-4. Figure 6-4(b) displays the net time for Capture Data & Position Estimation, obtained by subtracting wait2 from the total time. The processing time required for position determination was within the range of 30 to 40 ms. It is worth noting that this value depends on the performance of the PC and OS used in the experiments.

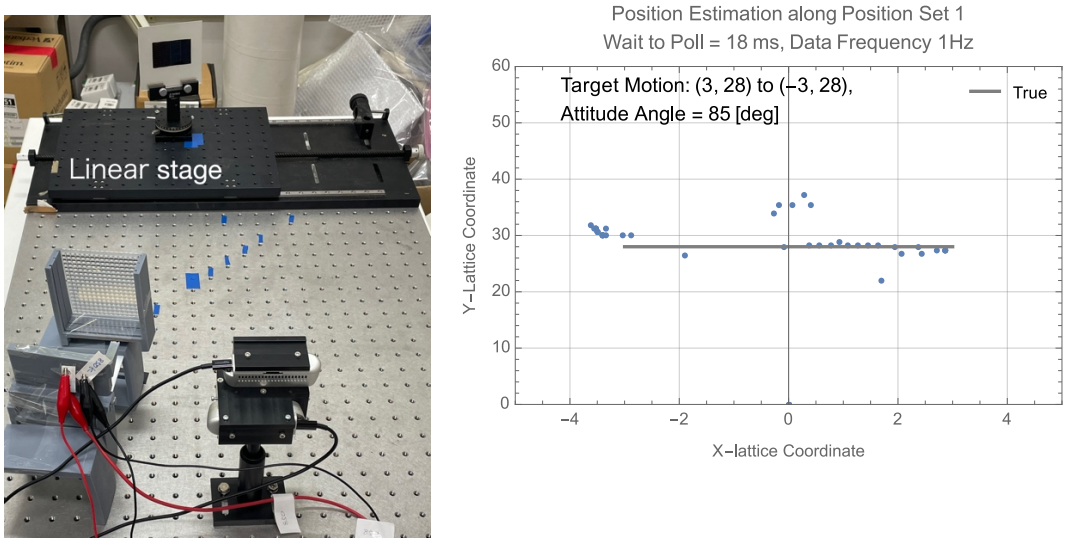


(a) (b)

Figure 6-4 Time sequence of successive 50 position estimation, (a) The whole sequence (wait1 = 18 [ms], Exp Time = 200 [ms]); (b) Time for capture and position estimation (50 data)

6.1.2. Realtime Positioning of PV

The initial experiment of 50 consecutive position estimations was carried out using the setup depicted in Figure 6-5(a). The target mounted on the rotation stage was fixed on the linear stage and translated manually. During experiments involving varying the attitude angles, deviation of the attitude angle from around 90 degrees caused data to fail to meet the integrity measure, consequently leading to a higher data loss rate. The results for Position Set 1 (ϕ = 85 degrees) are shown in Figure 6-5(b). Similar observations were made for Position Sets 2 and 3. These issues are addressed in the later sections.

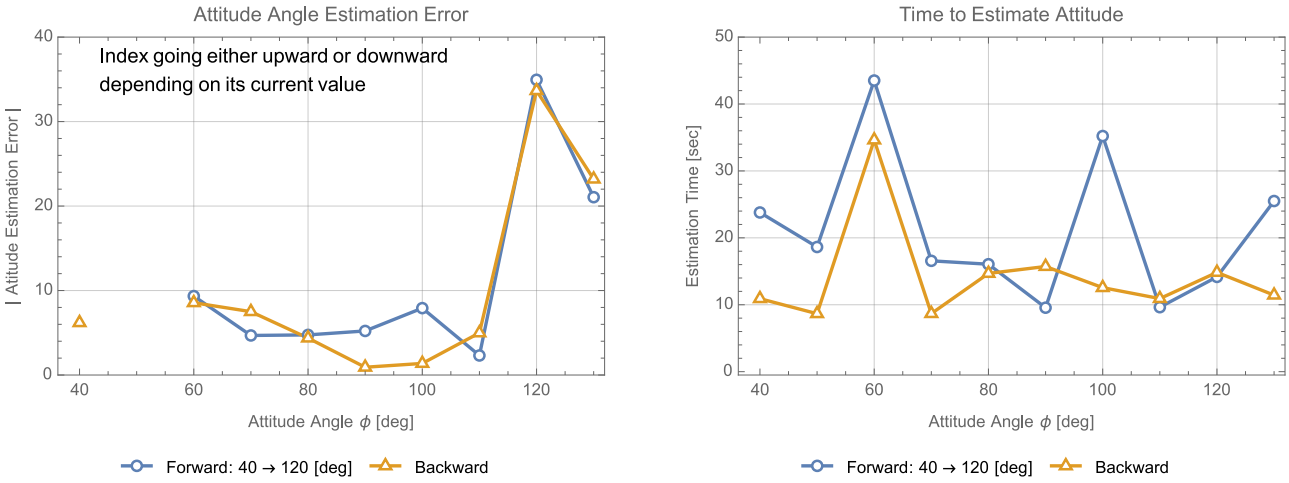


(a) (b)

Figure 6-5 Moving target experiments, (a) Layout of experiments (Position Set 1); (b) Position Set 1 data

6.1.3. Successive Attitude Determination of PV

Like successive position estimation, it is feasible to estimate attitude angles in real time using the method described in Section 5. Figure 6-6 illustrates the outcomes of the attitude angle estimation, while fixing the target at (0,27) and varying its attitude from 40 to 120 degree. To estimate the attitude using the integrity measure, it is necessary to search for the minimum exposure time at which it converges. During the experiment, the current minimum value was searched around the previous value while varying the attitude angles.



(a) (b)

Figure 6-6 Successive Attitude Determination of the PV, (a) The attitude estimation error (b) The time to estimate the attitude

The estimation error was minimized in the neighborhood of the normal direction. The time required for estimation depends on the number of searches conducted for the minimum exposure time and is typically about 10 to 15 s. This duration is explained by Set Camera Profile & Start Stream and Stop Stream which are necessary for each search iteration as illustrated in Figure 6-4(a).

In summary of this subsection, some challenges about successive position and real-time attitude angle estimation are identified. One such challenge is the latency between Camera 1 and Camera 2, as seen in Figure 6-3. However, since the target velocity is roughly 0.1 unit/s, the latency between the two cameras is not an issue in the current experiments. Furthermore, this latency can be minimized by synchronizing the two cameras using hardware. Another challenge is the time required to Set Camera Profile & Start Stream and Stop Streams in Figure 6-4(a). This challenge should be addressed by redesigning the camera system, thereby optimizing the overall

performance of the experiments or system. Using a high-speed PC and compiled application software, the time for positioning would reduce from 30～50 ms to 20 ms or less. If the time for the start frame can be reduced from 2 s to 50 ms and the time for the stop frame from 6 s to 50 ms, respectively, the total time including positioning, and start/stop stream can be less than 120 ms. Since from Figure 8(b), there needs twice search iteration to find the minimum exposure time, this makes the attitude estimation at 4 Hz(= 1 / (2 × 120 ms)). Suppose that attitude angular velocity of the target is 90 deg / 10 s, then, attitude would be measured with 2.25 deg error. Comparing with Figure 6-6(a), this would be acceptable.

6.2. Tracking of the PV

In Figure 6-5(b), there are outliers near the position estimation at $x = 0$, and there is data loss around $x = -1$. Data loss can happen when the attitude angle ϕ deviates from the normal to the transmitter, and when the received light is excessively intense near the normal direction. These causes integrity measure violation and such data were screened. Since Figure 6-5(b) is for data with angles close to the normal direction (ϕ = 85 deg), outliers and data loss were likely caused by excessively intense light.

To address the issue of outliers and missing data, it is necessary to interpolate the raw data, smooth it appropriately, and correct outliers. In this section, three algorithms are discussed for this purpose. A score function is defined based on the true values of the target positions to assess the algorithms.

6.2.1. Tracking Algorithms

Three tracking algorithms are presented. The first one employs a combination of thresholds and an autoregressive (AR) model. It is a supervised anomaly rejection algorithm and requires training before operation. On the other hand, the other two algorithms use Kalman filters for estimation and do not require any training.

6.2.1.1. Autoregressive Model with Threshold (Estimator/Corrector)

The raw data from successive position estimation can be interpreted as time-series data. Analyzing such data using an autoregressive model, including outlier handling, is widely used in various fields [4,5].

1. Raw data (measurement) processing (The primary smoothing)

   Let x_n, x_{n+1} two successive raw data (measurements). If the change from x_n to x_{n+1} does not exceed a predefined threshold, no smoothing nor interpolation is performed. If the change from x_n to x_{n+1} exceeds a predefined threshold T or x_{n+1} is missing, primary smoothing and interpolation of missing data for the (n+1)-th position data x_{n+1} are executed as per (6-2).

$$x_{n+1} = \begin{cases} x_{n+1}, & |x_{n+1} - x_n| \le T \\ \frac{1}{2}(2x_n - x_{n-1} + 2x_{n-2} + x_{n-3}), & x_{n+1}\ is\ missing\ or\ |x_{n+1} - x_n| > T \end{cases} \quad (6\text{-}2)$$

2. Estimator (The secondary smoothing and the primary estimate)

After the primary smoothing, the secondary smoothing is carried out using a Butterworth low-pass filter [6]. The cutoff frequency of the filter is set to $\omega_c = 0.1$ rad/sec, and its order is N = 8. The outcome of this process is referred to as the primary estimate, which is denoted as x'_n.

3. Corrector (The secondary estimate)

The process applies the same procedure to x'_n as per (6-2), then results in the secondary estimates (tracker output) x''_n. The thresholds in this case are denoted as T'.

The above three processes are applied to the X-coordinate and the Y-coordinate estimations. The predefined thresholds for each are $(T_x,\ T_y) = (2,\ 2.3)$ and $(T'_x,\ T'_y) = (1,\ 2)$. Before tracking, the initial data for the AR model and the low-pass filter are needed. The median of 50 consecutive position determinations for the stationary target was used for this purpose, and it was then duplicated as necessary times (4 times for the AR model and 8 times for the low-pass filter). This algorithm requires acquiring data before its operation. It needs optimizing both (T_x, T_y) and (T'_x, T'_y) beforehand.

6.2.1.2. Uniform Motion Model Estimated by Kalman Filter (Kalman)

The algorithm in 6.2.1.1, the Estimator/Corrector, is a supervised model that requires threshold optimization through training. On the other hand, in 6.2.1.2 and 6.2.1.3, models that do not require training are explored.

Assuming no external force on the target, the steady state Kalman filter [7] is used to estimate the position and the velocity of the n-th data point. Let measurement $X_n = (x_n, \dot{x}_n)^T$, and the raw data for $\dot{x}_n$ is given by $\dot{x}_n = (x_n - x_{n-1})/\Delta t$. The prediction for the n-th data using the data up to (n−1)-th estimation is denoted as X'_n, and the estimation for the n-th data using the data up to n-th measurement and the n-th prediction is denoted as X''_n. The corresponding state equation is given by (6-3), (6-4), (6-5), and the observation equation is by (6-6), (6-7).

$$X'_n = FX''_{n-1} + Gw \tag{6-3}$$

$$F = \begin{pmatrix} 1 & \Delta t \\ 0 & 1 \end{pmatrix} \tag{6-4}$$

$$Gw^2G^T = \begin{pmatrix} 0 & 0 \\ 0 & w^2 \end{pmatrix} \tag{6-5}$$

$$x_n = HX_n + R \tag{6-6}$$

$$H = (1, 0) \tag{6-7}$$

In this experiment, that the data rate is 1 Hz implies $\Delta t = 1$. Let $\mathcal{N}(\mu, \sigma)$ a Gaussian distribution with mean μ and standard deviation σ. The system noise w is assumed to be $w \sim \mathcal{N}(0, 0.05)$. Similarly, the measurement noise is assumed to follow $R \sim \mathcal{N}(0, \Sigma)$, where Σ represents the standard deviation during initial value determination. The estimation X''_n can be obtained using the prediction X'_n, the measurement x_n and the Kalman gain K as:

$$X''_n = X'_n + K(x_n - HX'_n) \tag{6-8}$$

1. Raw data processing

   In case of missing raw data, the missing values are interpolated using (6-9) as follows:

   $$X_{raw,n} = FX_{raw,n-1} \tag{6-9}$$

2. Smoothing

   The interpolated raw data $X_{raw,n}$ is inputted to the same Butterworth low pass filter as in 6.2.1.1. The resulting values are denoted as X_n, and X_0 is used for 0-th estimation X''_0.

3. Position estimation (tracker output)

   The n-th prediction X'_n is obtained from (6-3) using the (n−1)-th estimation X''_{n-1}. Along with $x_n = HX_n$, the n-th estimation X''_n is calculated using (6-8). The final tracker output is $x''_n = HX''_n$. This process is applied to both the X-coordinate and the Y-coordinate estimations. The initial values generation process is the same as in 6.2.1.1.

6.2.1.3. Autoregressive Model Estimated by Kalman Filter (AR Kalman)

Also, estimation using a Kalman filter for an AR model is widely employed in the analysis of time-series data [8–10]. The AR model in (6-2) is estimated using a Kalman filter in this algorithm. (6-4), (6-5), (6-7) are replaced by (6-12), (6-13), (6-14).

$$X_n = (x_n, x_{n-1}, x_{n-2}, x_{n-3})^T \tag{6-10}$$

$$X'_n = FX''_{n-1} + Gw \tag{6-11}$$

$$F = \begin{pmatrix} 1 & \frac{1}{2} & 1 & \frac{1}{2} \\ 1 & 0 & 0 & 0 \\ 0 & 1 & 0 & 0 \\ 0 & 0 & 1 & 0 \end{pmatrix} \tag{6-12}$$

$$Gw^2G^T = \begin{pmatrix} 3 \cdot w^2 & 0 & 0 & 0 \\ 0 & w^2 & 0 & 0 \\ 0 & 0 & w^2 & 0 \\ 0 & 0 & 0 & w^2 \end{pmatrix} \tag{6-13}$$

$$H = (1,0,0,0) \tag{6-14}$$

(6-3) is replaced by a similar equation as (6-11). The estimation procedure to obtain the tracker output is $x''_n = HX''_n$, and the initialization method is the same as in 6.2.1.1.

6.2.2. Assessment of the three algorithms

6.2.2.1. Score function and estimation of true position

The algorithms from 6.2.1.1 to 6.2.1.3 enable tracking of the target. An excerpt from the tracking results is shown in Figure 6-7. The procedure to generate the tracking plots in this section is as follows.

1. The Python™ program outputs position data in real-time and each measurement (position determination) is successively stored in a list (List-A).

2. The Mathematica™ program takes measurement data from List-A and estimates its tracked position one by one using the algorithms. Then, each estimation is successively stored in a list (List-B).

The tracking plots are generated from List-B.

It should be noted that, except for the plot generation process using Mathematica, the rest is conducted on an essentially real-time basis. When comparing these algorithms under the same target distance, etc., since the amount of computation is not so different among the three algorithms, the difference appears only in tracking errors.

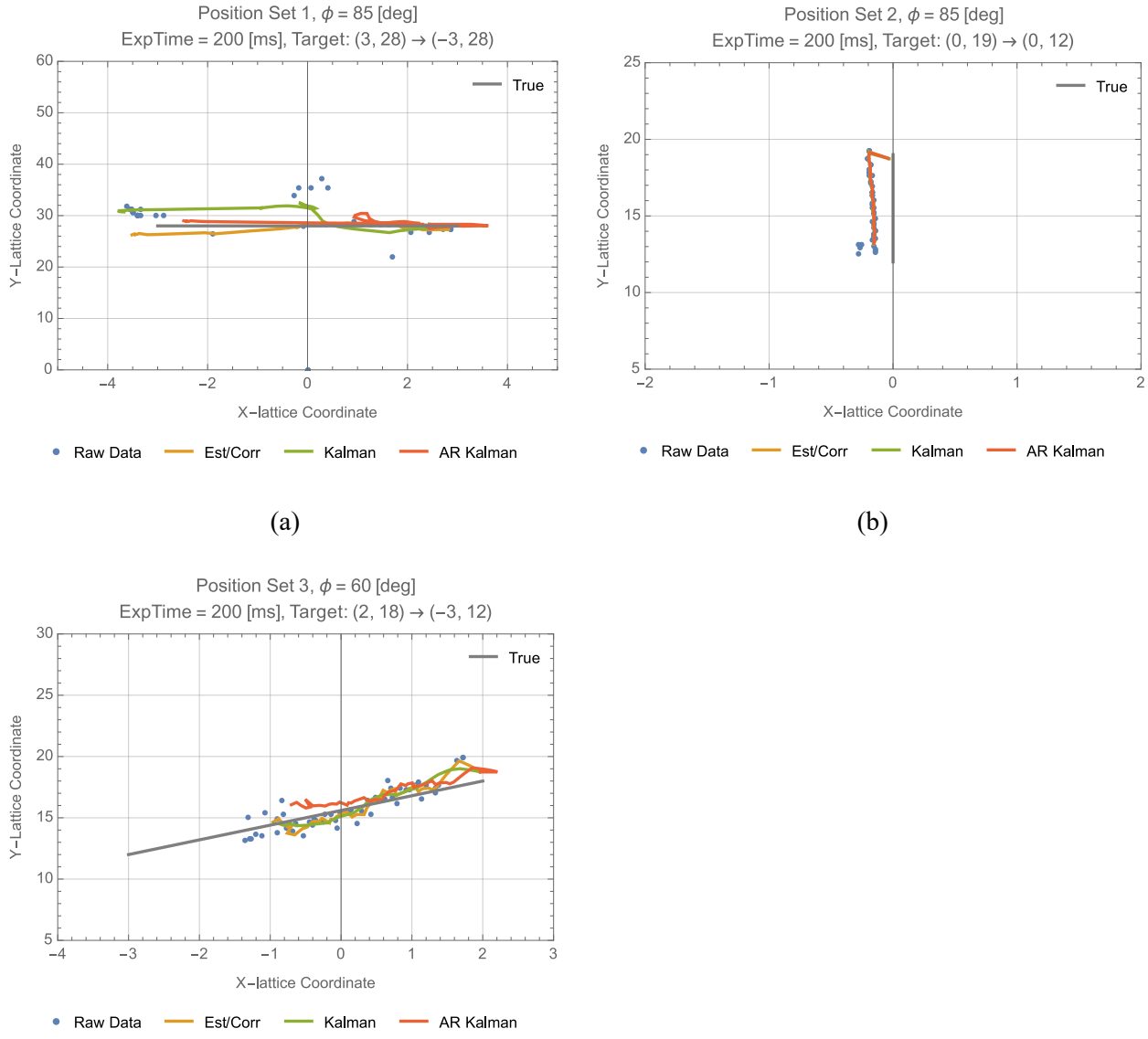


Figure 6-7 Tracking of the PV target, (a), (b), (c) Position Set 1, 2, 3.

To assess the performance of the algorithms, a score function is defined. It quantifies the tracked results.

$$Score = \frac{100}{1+e} \tag{6-15}$$

$$e = \frac{1}{N}\sum_{i=1}^{N} e_i \tag{6-16}$$

e_i denotes a position error associated with each tracked target data, and e represents the mean tracking error over N (=50) data of the tracking process. Each e_i is defined as follows:

$$e_i = \sqrt{\left(x''_i - x_{t,i}\right)^2 + \left(y''_i - y_{t,i}\right)^2} \tag{6-17}$$

x''_i, y''_i are the i-th estimates obtained by the algorithms. On the other hand, $x_{t,i}$, $y_{t,i}$ are the true values of the target, which are generally determined by measuring the target position using an independent device from the experimental setup in Figure 6-5. However, a simpler method to estimate them is proposed.

The score utilizing e_i defined by (6-17) is referred to as the TP (True Position)-Based Score. The former section showed that estimating the direction angle ψ, defined by $tan\psi \equiv x/y$ as more accurate compared to the position estimation (x, y). The direction error $\Delta\psi$ due to position estimation errors Δx, Δy is obtained by (6-18), where $\xi_{L(R)}$ is the horizontal coordinate in the left (right) image sensor of the target, and $\Delta\xi_{L(R)}$ represents its error.

$$\Delta\psi = \frac{y\Delta x - x\Delta y}{x^2+y^2} = \frac{y^2}{x^2+y^2}\frac{\xi_L\Delta\xi_R + \xi_R\Delta\xi_L}{\xi_L+\xi_R}\Delta\theta \tag{6-18}$$

Assuming ξ_L and ξ_R are quantities of the same order, and $\Delta\xi_L$ and $\Delta\xi_R$ are also, the evaluation of $\Delta\psi$ is approximated as $\Delta\psi{\sim}\Delta\theta\Delta\xi_{R(L)} = 2.6\ \text{mrad}\ (0.15\ \text{deg}) \times \Delta\xi_{R(L)}/px$. Re-evaluating the accuracy of the direction angle estimation from the data included in the previous section, Figure 6-8 is obtained where the solid lines represent Exp Time = 200 ms and the dashed lines 100 ms respectively. The actual experimental data included a constant offset that varied from day to day, and this constant offset is due to errors in the daily setup of the experimental apparatus. In Figure 6-8, the accuracy of the direction angle estimation is evaluated by the standard deviation across each Position Set excluding this offset.

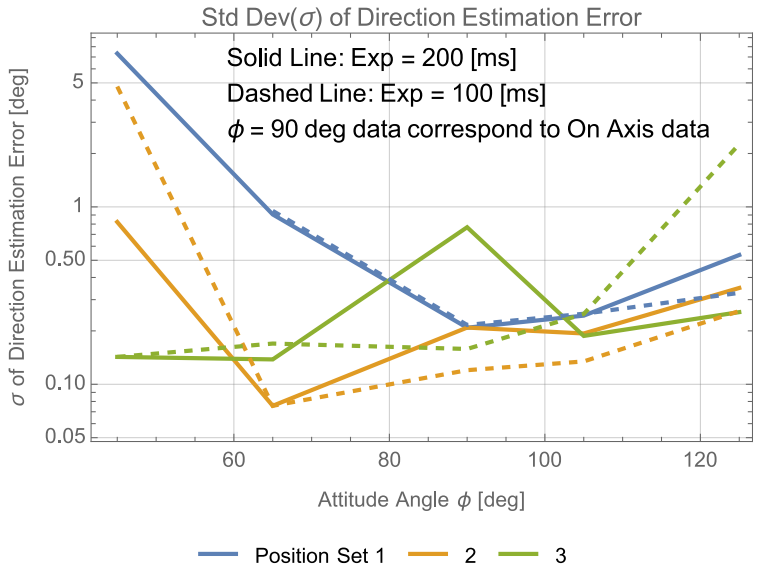


Figure 6-8 Direction angle estimation accuracy

From Figure 6-8, the accuracy of the direction angle ψ estimation varies with the target's attitude angle ϕ, and ψ can be estimated with an accuracy of approximately 0.15 degree when the target is close to the normal direction. From (6-18), this corresponds to about 1 pixel error in the pixel coordinate system, which can be regarded as the measurement limit. Then, the true position can be estimated by the intersection of the true track of the target which is known in the experiments and the line $x_i = y_i tan\psi_i$ as depicted in Figure 6-9. e_i can be calculated from (6-17) as the distance between the estimated position by the algorithm and the estimated true position.

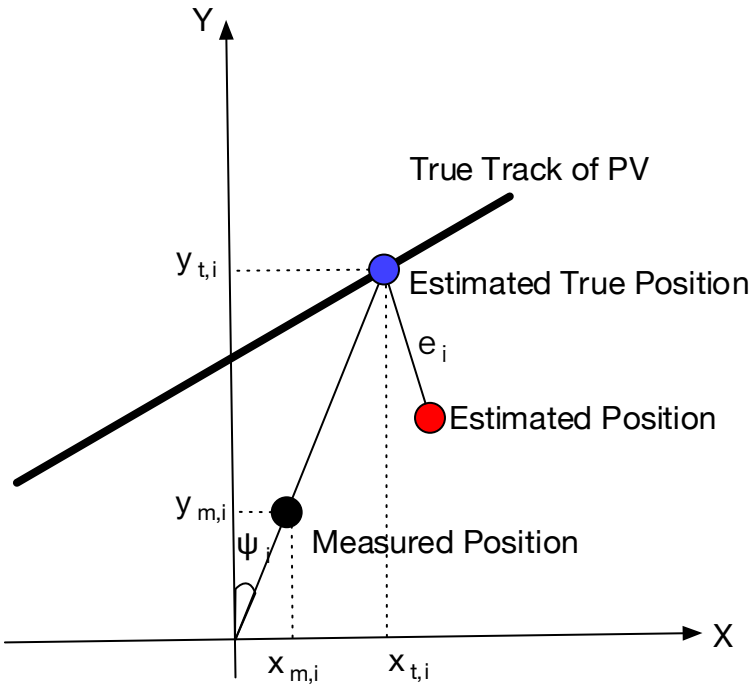


Figure 6-9 True position estimation by direction angle ψ

6.2.2.2. Assessment of the three algorithms

The results of the TP-Based Score are displayed in Figure 6-10 (Position Set 1) and Figure 6-11 (Position Set 3). Along with the score evaluation results, the right vertical axis represents the N(umber) of available data which meets the integrity measure. Based on the plot, it appears that the values on the horizontal axis corresponding to the maximum values (= 50) on the right vertical axis are near the normal direction, and the scores seem to increase there. In Figure 6-10, Position Set 1 shows many outliers and missing data, suggesting that the correction by the algorithm is effective. However, since Position Set 3 data contains fewer outliers and missing data in Figure 6-11, the algorithm correction is limited in comparison with the raw data. Although the evaluation results of the three algorithms do not differ significantly, it seems that the Estimator/Corrector, which requires costs for additional training, behaves slightly superior to (the uniform motion/) Kalman filter and AR (model/) Kalman filter.

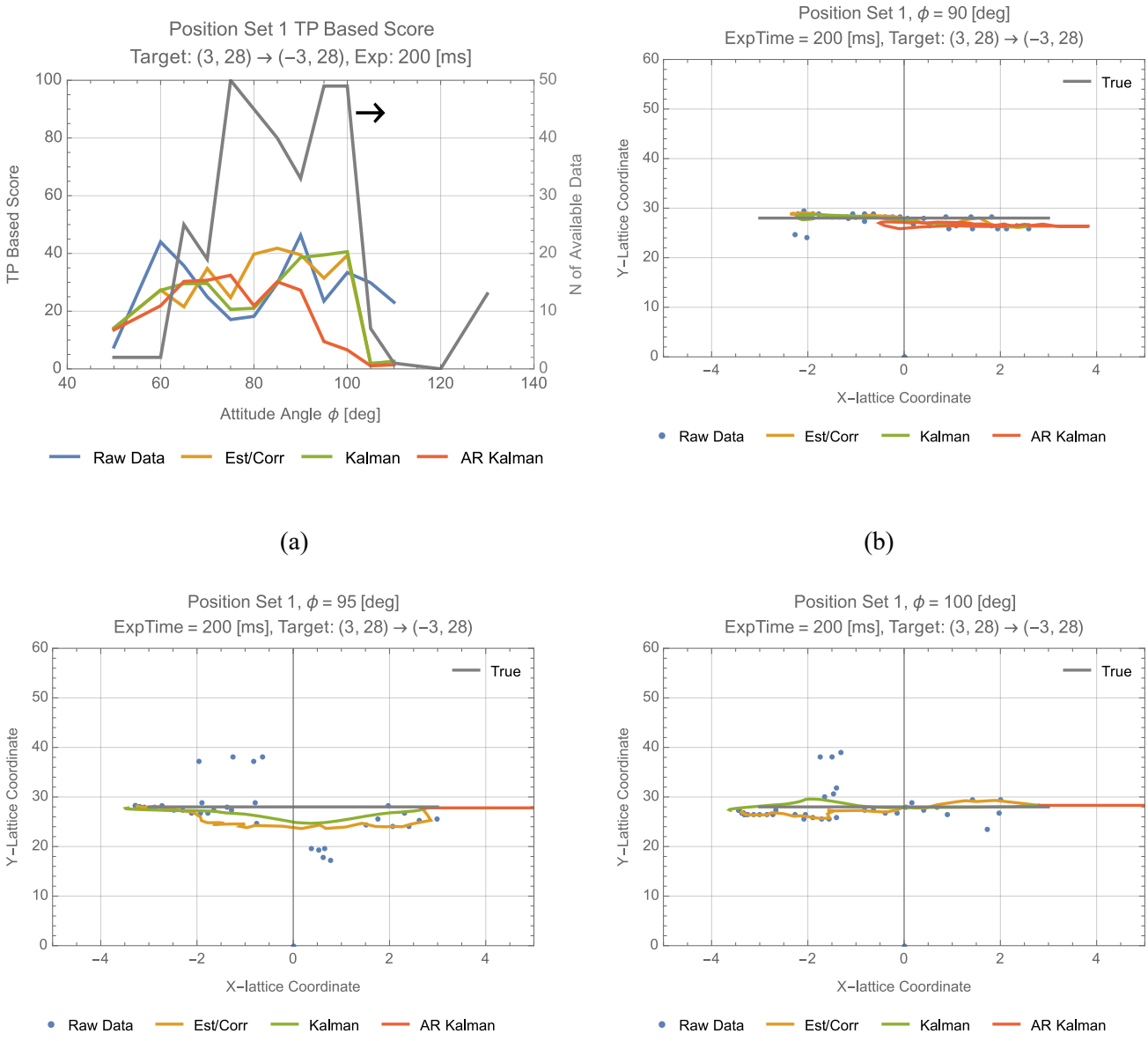


Figure 6-10 Assessment of the three algorithms by TP-Based Score for Position Set 1, (a) TP-Based Score; (b) Data of $\phi = 90$ [deg]; (c) $\phi = 95$ [deg]; (d) $\phi = 100$ [deg]

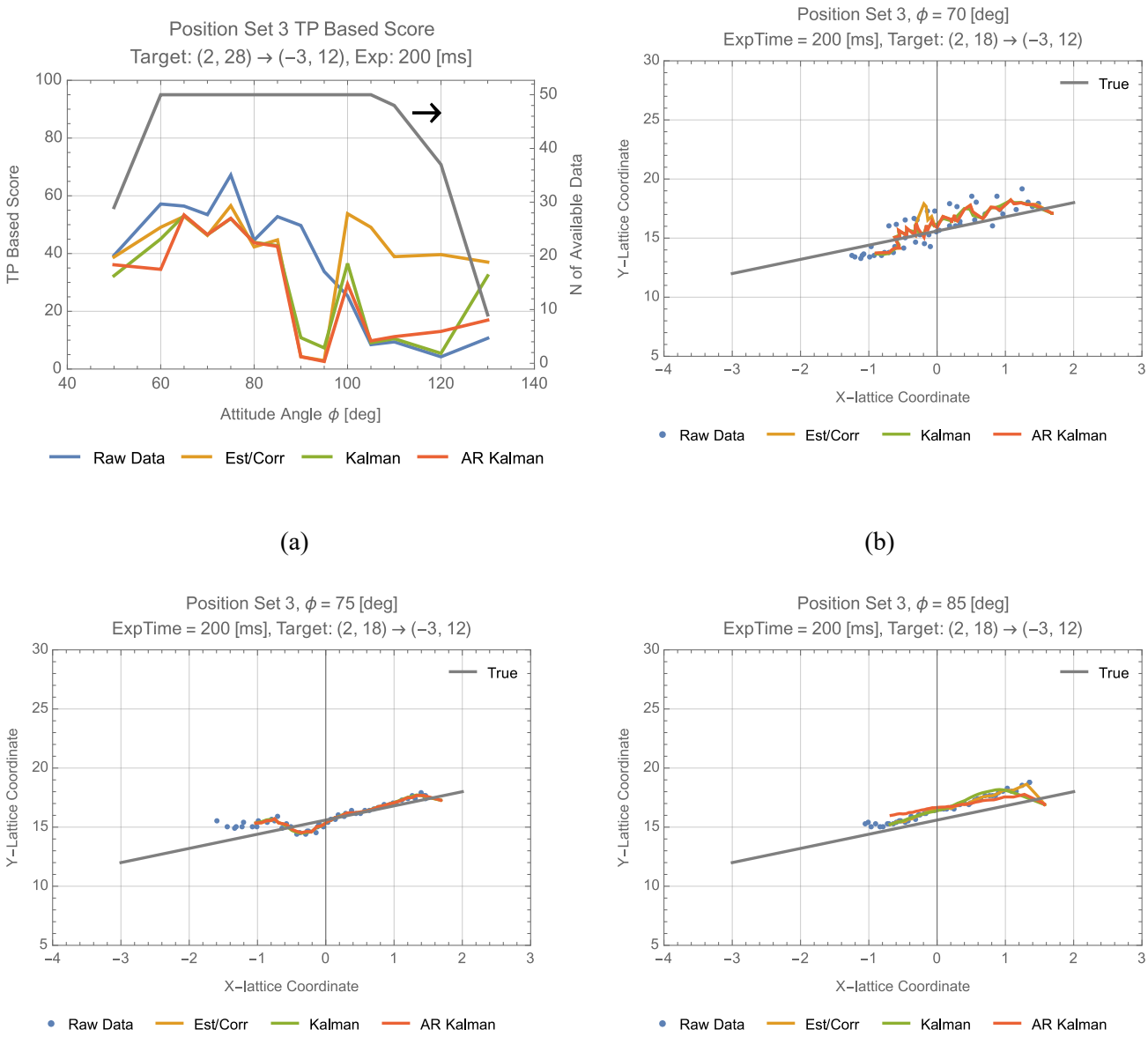


Figure 6-11 Assessment of the three algorithms by TP-Based Score for Position Set 3, (a) TP-Based Score; (b) Data of ϕ = 70 [deg]; (c) ϕ = 75 [deg]; (d) ϕ = 85 [deg]

6.3. Accuracy improvement of the three algorithms

Figure 6-8 suggests that each position measurement accurately estimated ψ_i near the normal, and this fact implies that ψ_i can be regarded as a reliable ($\fallingdotseq$ true) value there. The three algorithms in 6.2.1 estimated two coordinates (x, y) independently for position estimation. On the other hand, if we focus on the Y-coordinate estimation and use it with the "reliable value" ψ to

calculate the X-coordinate by $x_{e,i} = y_{e,i} \tan\psi_i$, as shown in Figure 6-12, this estimation involves one estimation $y_{e,i}$ and one reliable value ψ_i. In this case, improvement in accuracy is expected.

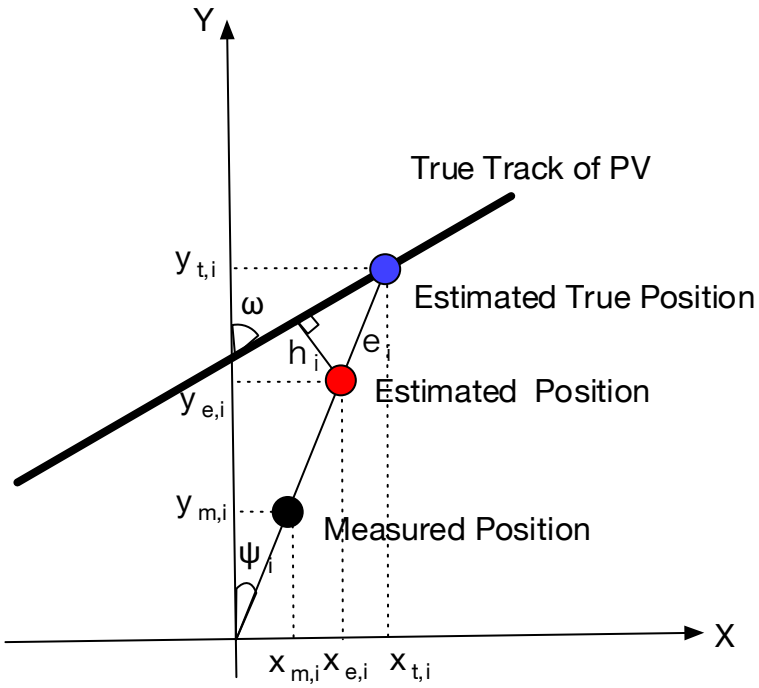
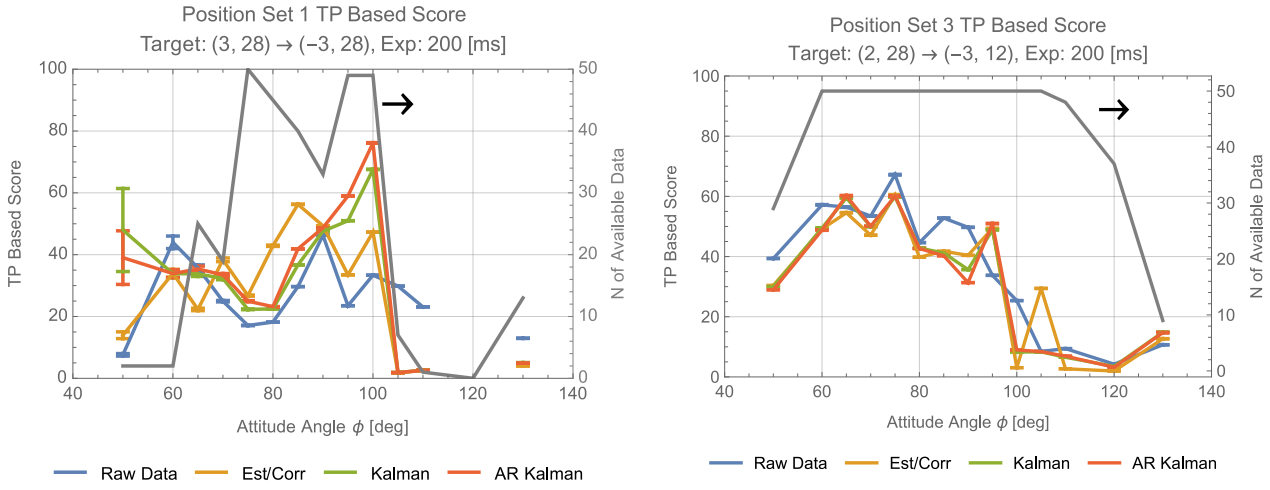


Figure 6-12 Position estimation by direction angle ψ

In this algorithm, the estimation error of ψ ($\Delta\psi$) introduces an error in the score function $Score$ ($\Delta Score$). In situations where there is attitude angle deviation from the normal, the estimation of the direction may be subject to error. $\Delta Score$ can be expressed as:

$$\Delta Score = \frac{Score^2}{100}\frac{1}{N}\sum_{i=1}^{N}(2y_i\, sec\psi\, tan\psi)\,\Delta\psi \tag{6-19}$$

The value of $\Delta\psi$ is known to vary with the attitude angle ϕ, as illustrated in Figure 6-8. To evaluate $Score$ and $\Delta Score$, the results are shown in Figure 6-13, where $\Delta Score$ is represented as error bars.



(a) (b)

Figure 6-13 Assessment of the improved three algorithms by TP-Based Score, (a) Position Set 1; (b) Position Set 3

Comparing Figure 6-13(a) with Figure 6-10(a) and Figure 6-13(b) with Figure 6-11(b), there was a noticeable improvement in the scores for both cases. Despite the ranking of the three algorithms remaining largely consistent, Estimator/Corrector has a better average performance compared to both Kalman Filter and AR Kalman Filter.

6.4. Assessment of the algorithms for Position Set 2

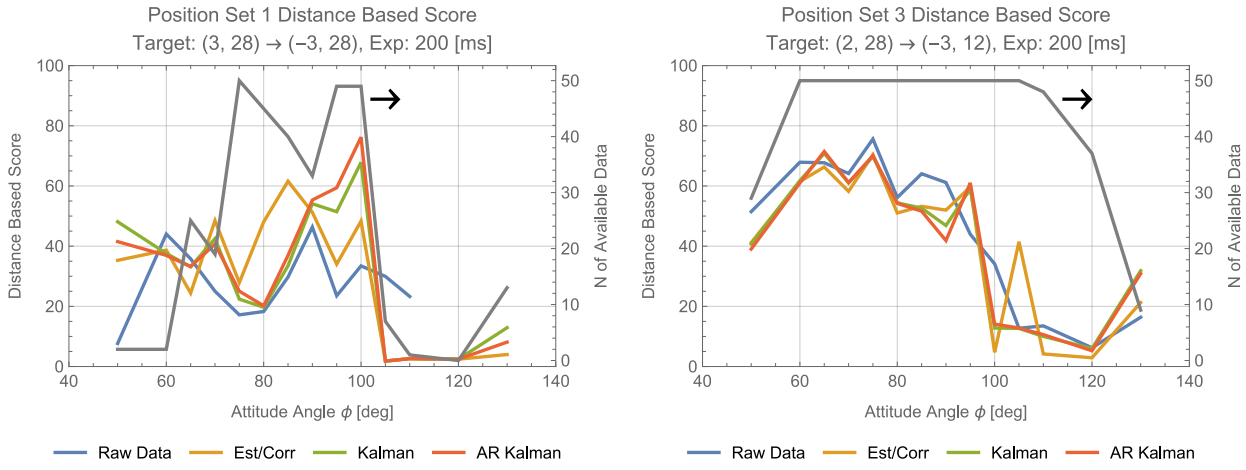
While the conclusion of 6.2.2 is supported by the data of Position Set 1 and 3, there remains a question of if the data of Position Set 2 also supports that.

For Position Set 2, while the improved method in 6.3 is applicable, evaluating the score using the method described in 6.2.2.1 to estimate the true value is not feasible. As an alternative, a possible method is to evaluate the target's position error by measuring the distance between the estimated position and the true track instead of the true position. This method is referred to as Distance-Based Score in this thesis. This corresponds to using $\mathrm{h_i}$ instead of e_i in Figure 6-12, and in other words, evaluating the score based solely on the cross-track error, ignoring the along-track error. From Figure 6-12, the following (6-20) holds:

$$\mathrm{h_i} = e_i sin(\omega - \psi) \tag{6-20}$$

For Position Set 1, where ω = 90 deg and $|\psi|$ < 5.7 [deg] (= 0.1 [rad]), $h_i \approx e_i$, and TP-Based Score and Distance-Based Score are nearly identical. For Position Set 3, $h_i < e_i$, and Distance-Based Score tends to underestimate. The track for Position Set 2 does not allow the application of (6-20).

Figure 6-14 represents the evaluation results of position estimation using the method in 6.3 and the scoring based on Distance-Based Score.



(a) (b)

Figure 6-14 Assessment of the improved three algorithms by Distance Based Score, (a) Position Set 1; (b) Position Set 3

Comparing Figure 6-13, Figure 6-14, it can be concluded that the differences between them are minimal for Position Set 1, 3 data. Figure 6-15 presents the evaluation results of Distance Based Score for Position Set 2 data, where position estimation using the method in 6.3 was applied. Furthermore, the analysis results for additional data are added in the Figure 6-18 and Figure 6-19 in Appendix 6.

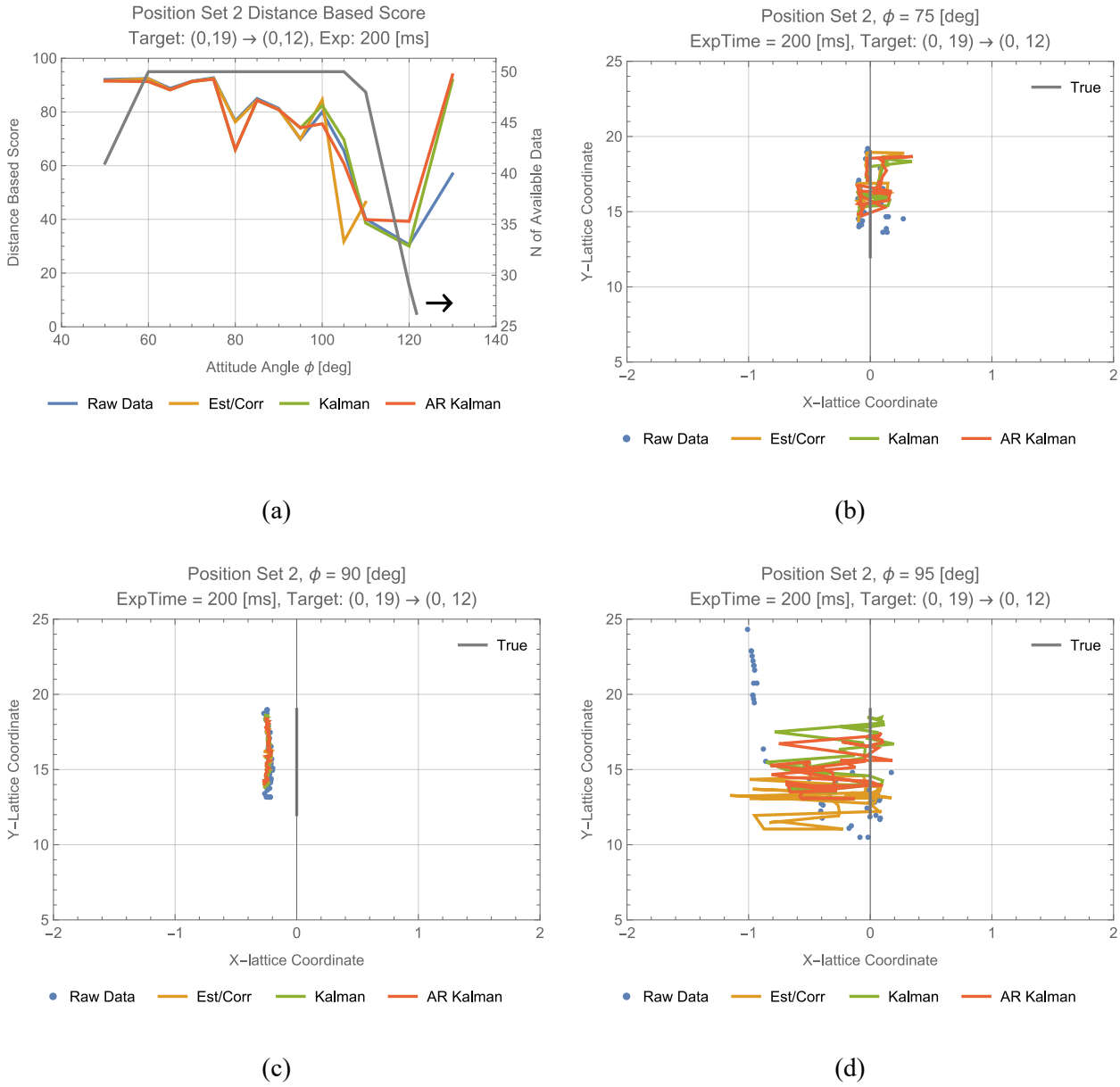


Figure 6-15 Assessment of the three algorithms by Distance Based Score for Position Set 2, (a) Distance Based Score; (b) Data of ϕ = 75 [deg]; (c) ϕ = 90 [deg]; (d) ϕ = 95 [deg]

Paying attention is crucial to the impact of ignoring along-track errors in Distance-Based Score in Position Set 2. A constant X-direction error exists, but any noticeable irregularity in the Y-direction cannot be found in Figure 6-15(c). Similarly, Figure 6-15(b) and (d) show random position errors in the X-direction, but no observable random error in the Y-direction. This suggests the motion of the target along the Y-axis is tracked appropriately. Based on the data, it can be inferred that the impact of ignoring along-track errors in Position Set 2 is allowable. This conclusion is also supported by the data in Figure 6-18 and Figure 6-19. Thus, evaluating the

algorithms using Distance-Based Score in Position Set 2 is reasonable. When the three algorithms modified according to 6.3 are assessed with Distance-Based Score in Position Set 2, there is no significant difference in their performance.

Based on the discussion in 6.2.2.1 and above, it is concluded that when there are many outliers and missing data, such as Position Set1, the correction of outliers and interpolation of missing data by the algorithms are effective. Among the algorithms, Estimator/Corrector, which requires training costs, appears to be the best option as it outperforms both the Kalman filter and AR Kalman filter. On the other hand, where there are fewer outliers and missing data such as in Position Sets 2 and 3, the effect of the correction and the interpolation by the algorithms are limited, and the score of the measurements (raw data) may not be necessarily surpassed by the algorithms. In such cases of fewer outliers and missing data, the performance of the three algorithms can be considered equivalent.

6.5. Demonstration of the PV Tracking Using the Algorithm

PV tracking demonstration combine with the orthogonal cylindrical expander optics discussed in Section 1 was demonstrated by Moriyama, et.al.[11]

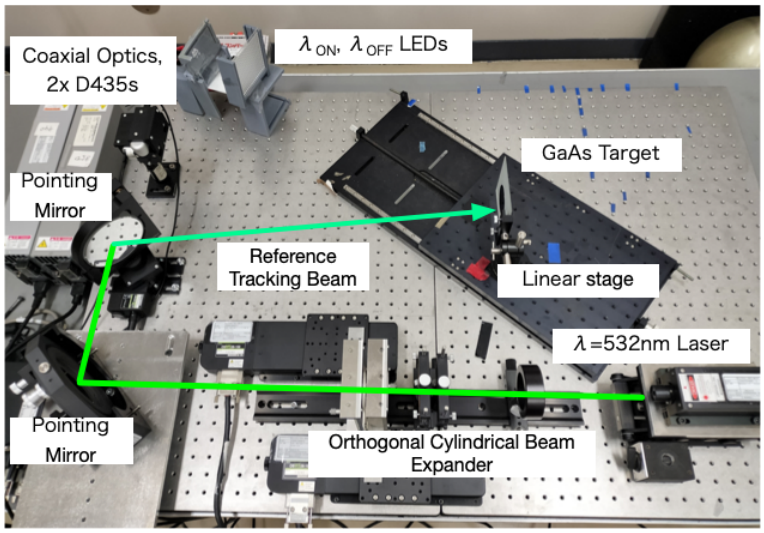


Figure 6-16 The layout of the demonstration of PV tracking

6.6. Consistency between system-level requirement study

The high-level requirement analysis for OWPT beam alignment and shaping was conducted in Section 3. The overall power generation efficiency of the OWPT system (η_{system}) is expressed as:

$$\eta_{system} = \eta_{Light\ Source} \times \eta_{Transmission} \times \eta_{Power\ Generation} \times \eta_{SolarCell} \quad (6\text{-}21)$$

Among the 4 factors of η_{system}, $\eta_{Power\ Generation}$ indicates the proportion of the beam energy incident on the PV that contributes to power generation [12]. The calculation method for $\eta_{Power\ Generation}$ including errors of the transmission optics is explained in Section 3. Figure 6-17 shows the analysis results for the X-direction alignment error and power generation ratio in a cooperative OWPT system with a target size of 100 mm × 100 mm, which is used as a reference size in the former analysis [13]. From Figure 6-14 and Figure 6-15, the alignment error is estimated to be approximately 0.67 units or less. Figure 6-17 shows that the alignment error tolerance on the PV surface does not depend on the target distance, and the power generation ratio can be greater than 55% for the estimated alignment error (≤ 0.67 unit = 17.0 mm).

It is worth noting that the accuracy depends on the exposure time of the image sensor, and there is a minimum exposure time for the positioning accuracy to converge. Since SNR is proportional to exposure time, it can be reworded that there is a minimum SNR for the positioning accuracy to converge. The SNR formula depends on several parameters derived in the former section. Since the target's position is determined in the pixel coordinate system in this method, the resolution of the position estimation is determined by the angle of view of the pixel ($\Delta\theta$ =2.6 mrad/px). The further the target is, the smaller $\Delta\theta$ needs to be, thus the accuracy is limited by this parameter. The value "55%" would be sufficient for an initial acquisition, and a high-resolution camera, a zoom lens, or enlarging the target size will be necessary to improve this.

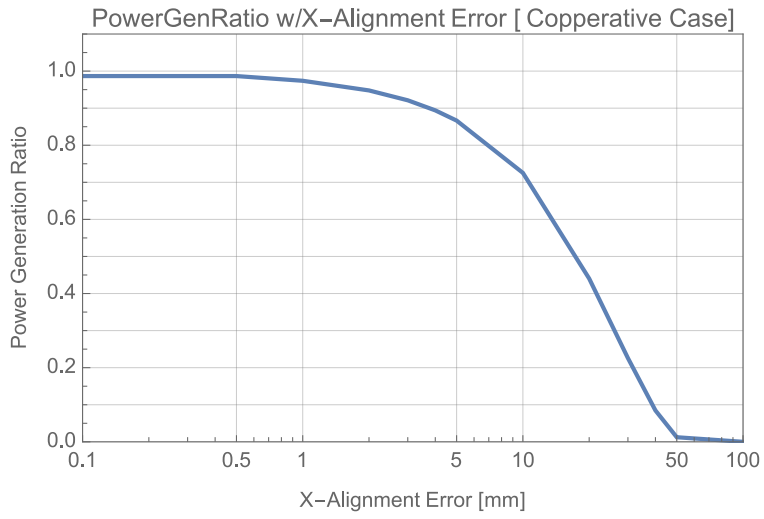
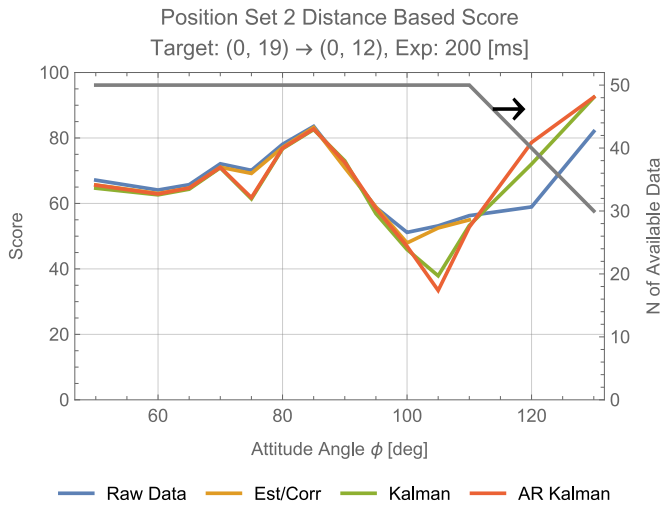


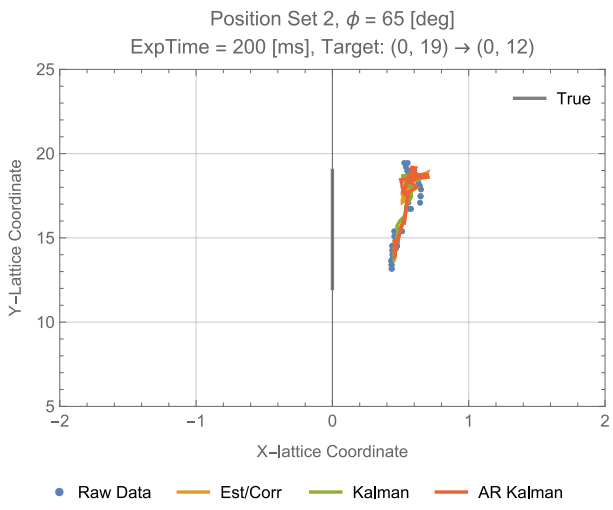
Figure 6-17 Power generation ratio and X-alignment error

Appendix 6

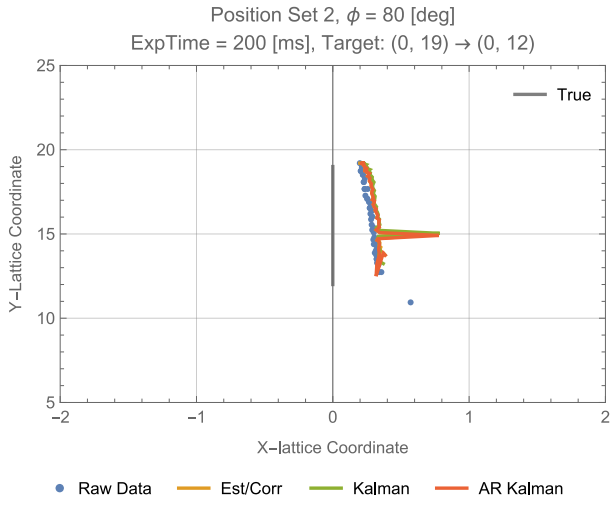
Supporting data of Position Set2.



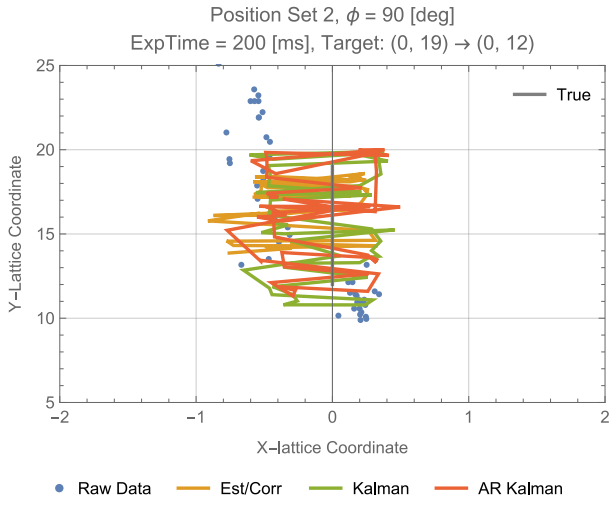
(a)



(b)



(c)



(d)

Figure 6-18 Assessment of Distance-Based Score for Position Set 2 with another data set, Exp Time = 200 [ms], (a) Distance-Based Score; (b) Data of ϕ = 75 [deg]; (c) ϕ = 90 [deg]; (d) ϕ = 95 [deg]

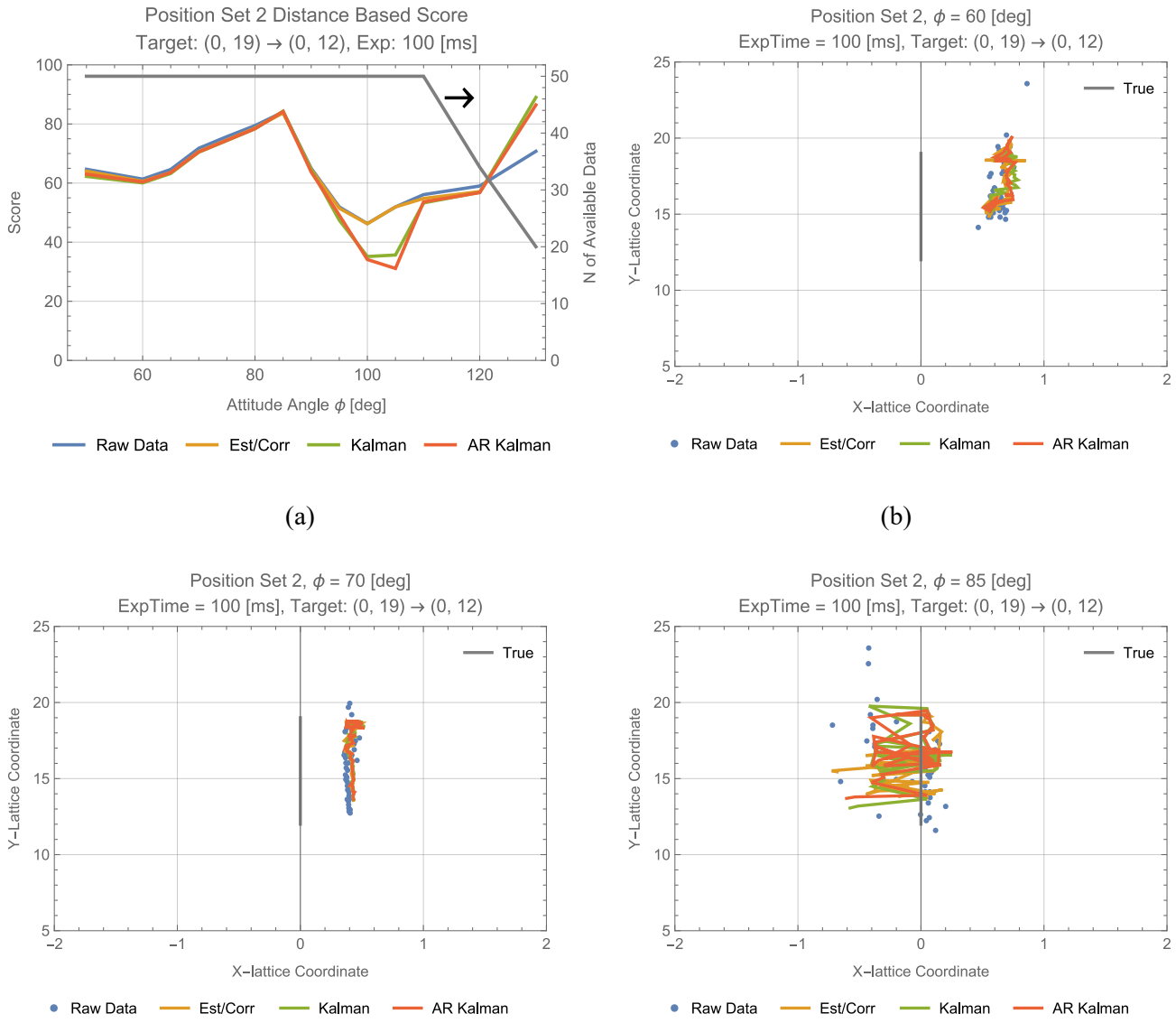


Figure 6-19 Assessment of Distance-Based Score for Position Set 2 with another data set, Exp Time = 100 [ms], (a) Distance-Based Score; (b) Data of ϕ = 60 [deg]; (c) ϕ = 70 [deg]; (d) ϕ = 85 [deg]

References 6

1. Hardware and Software Synchronization - Realsense Multicam · Issue #11669 · IntelRealSense/Librealsense Available online: https://github.com/IntelRealSense/librealsense/issues/11669 (accessed on 10 February 2024).
2. API How-To Available online: https://dev.intelrealsense.com/docs/api-how-to (accessed on 20 February 2024).
3. Difference between `poll_for_frames` and `wait_for_frames` Modes? · Issue #2422 · IntelRealSense/Librealsense · GitHub Available online: https://github.com/IntelRealSense/librealsense/issues/2422 (accessed on 20 February 2024).
4. Montgomery, D., C.; Jennings, C., L.; Kulahci, M. *Introduction to Time Series Analysis and Forecasting*; 2nd ed.; John Wiley & Sons: Hoboke, NJ, USA, 2015; ISBN 978-1-118-74511-3.
5. Chandola, V.; Banerjee, A.; Kumar, V. Anomaly Detection: A Survey. *ACM Comput. Surv.* **2009**, *41*, 1–58, doi:10.1145/1541880.1541882.
6. Oppenheim, A.V.; Schafer, R.W. *Digital Singal Processing*; Prentice-Hall: Englewood Cliffs, N.J., 1975; ISBN 0-13-214635-5.
7. Haykin, S. *Adaptive Filter Theory*; 2nd ed.; Prentice-Hall: Englewood Cliffs, N.J., 1991; ISBN 0-13-005513-1.
8. Maximum Likelihood Fitting of ARMA Models to Time Series with Missing Observations. **2024**, *22*.
9. Xiaobo Zhou; Yunxin Zhao; Xinhua Zhuang Kalman Filter Channel Tracking Algorithm Based on AR Model in WCDMA Systems. In Proceedings of the WCC 2000 - ICSP 2000. 2000 5th International Conference on Signal Processing Proceedings. 16th World Computer Congress 2000; IEEE: Beijing, China, 2000; Vol. 3, pp. 1759–1762.
10. Tatinati, S.; Veluvolu, K.C.; Hong, S.-M.; Latt, W.T.; Ang, W.T. Physiological Tremor Estimation With Autoregressive (AR) Model and Kalman Filter for Robotics Applications. *IEEE Sens. J.* **2013**, *13*, 4977–4985, doi:10.1109/JSEN.2013.2271737.
11. Moriyama, K.; Asaba, K.; Miyamoto, T. Beam Control System for the Moving Target on a Two-Dimensional Plane in OWPT. In Proceedings of the IEICE Society Conference 2024; Saitama, Japan.
12. Tang, J.; Matsunaga, K.; Miyamoto, T. Numerical Analysis of Power Generation Characteristics in Beam Irradiation Control of Indoor OWPT System. *Opt. Rev.* **2020**, *27*, 170–176, doi:10.1007/s10043-020-00590-z.
13. Asaba, K.; Miyamoto, T. System Level Requirement Analysis of Beam Alignment and Shaping for Optical Wireless Power Transmission System by Semi–Empirical Simulation. *Photonics* **2022**, *9*, 452.

7. A Concept of Operations (ConOps) of a Cooperative OWPT System

In this section, a ConOps of OWPT is presented. First, subsystems constitute the system and their functions, interrelationships and operation flow are proposed. The system-level requirements were obtained from the power generation ratio concept in Section 3. In Section 4, the long-range non-diffuse PV detection was predicted by differential absorption imaging. In Sections 5 and 6, positioning accuracies were evaluated for a stationary and a moving target. A remaining question is whether these can fit into a unified picture without discrepancy. Consistency among them is discussed and examples of OWPT system parameters are presented for various ranges.

7.1. A Concept of the Operation of an OWOPT

7.1.1. A ConOps of the cooperative OWPT

Assume that the system consists of the OWPT NW (Net Work), the transmitter, and the receiver subsystems; there can be multiple such transmitter and receiver units in the system but may be one each (in which case the OWPT NW and the transmitter are integrated). These three subsystems have a means of communication with each other.

- OWPT NW

  It has position information, etc. of the transmitters and the receivers, and a communication method to share information among the transmitters and the receivers. It manages their pairing based on the information.

- Transmitter

  It searches the receiver based on instructions from the OWPT NW. While the pairing is valid, position, attitude estimation, beam shaping, and alignment are conducted in real time. When the OWPT NW indicates that the combination with the receiver is terminated, the transmitter will be free and prepares for the next power transmission service.

- Receiver

  It sends a power transmission request to the OWPT NW, which initiates information sharing with the transmitter based on the OWPT NW's instruction. It receives power

transmission service while performing attitude control based on the transmitter's request. If the OWPT NW terminates the pairing with the transmitter, the receiver waits for the instruction to pair with the next transmitter.

From the above the system configuration concept and a derived system functional block diagram in Figure 7-1, a ConOps for a cooperative OWPT system including a beam alignment concept is developed.

- The initial approximate position of the target is assumed to be known in advance as the initial status of the transmitter and the target. By inputting the approximate initial position of the target into the cooperative OWPT system, the initial relative direction of the transmitter and receiver (target) can be estimated.

1 OWPT NW holds paring availability and other information based on the relative range between transmitters and receivers
2 On request from a receiver, OWPT NW requests one of the nearest and available transmitters to communicate with the receivers
3 Paring information is shared between the transmitter and the receiver such as
   - Coordinates of the transmitter optics center
   - The receiver’s position
   - Ready or Not-Ready status, etc.

- The transmitter is pointed in the azimuth and elevation direction of the target, and the relative direction of the transmitter and receiver are aligned with each other using the relative direction information. Like in the initial position information from OWPT NW, the relative attitude also includes an error. Two wavelength beams are irradiated to generate a differential absorption image. The differential absorption image can accurately determine the target's relative direction. Errors in the relative attitude are corrected by attitude angle estimation using differential absorption images. The above procedure enables the transmitter and receiver to pair perfectly. The transmitter optics align and shape the power beam appropriately according to the receiver's position and irradiate the power beam to the receiver.

4 The transmitter acquires the receiver image, recognizes the coordinate of its center, and requests to align its attitude angle
5 The transmitter aligns its beam
6 The transmitter rotates its beam around the optical axis, if necessary
7 The transmitter determines necessary focus adjustment by range information to the receiver
8 The transmitter and the receiver communicate and conduct precise adjustments (fine tuning) to maximize the generated power on the receiver's side by the receiver, if necessary

- For a moving target, the above process is repeated in real time. The direction of the transmitter optics is corrected according to changes in the target position, and beam alignment is repeated. When the target attitude is deviated, the relative attitude is corrected.

9 OWPT NW and the transmitter share and hold the Go/No-Go status of transmission based on paring info and safety information
   - If No-Go, then the transmitter stops power transmission to the receiver
10 OWPT NW cancels the paring between the transmitter and the receiver and saves the receiver's position for hands-over to another transmitter

7.1.2. Consistency between Detectability Criteria and Differential Absorption Imaging

We proposed the method to estimate position, attitude, and tracking in Section 5 and Section 6 based on the requirement of integrity measures discussed in Section 5. A discussion of consistency between the detectability criteria and the proposed position estimation method is necessary to accommodate the above discussion.

Based on the ConOps and derived system-level requirements in Section 3, a beam alignment accuracy for a cooperative OWPT based on the detectability criteria discussed in Section 4 is evaluated.

The representative target distance in Section 6 is $\mathbf{L \equiv 28\ units \times 25.4\ mm = 711.2\ mm}$.

Following the discussion in 4.1.1.2, the detectability criteria for GaAs PV is ±7.6 px. From the angular resolution of the camera (2.6 mrad/px) and L (711.2 mm), the detectability criteria is

obtained as $\pm 7.6\ px \times 2.6\ mrad/px \times 711.2\ mm = \pm 5.0\ mm$. The requirement for the area size is ±20% of the area from 4.1.1.2. The requirements for the Fly-Eye module, are obtained from Table 3-2, the requirement for X(Y) deviation is 34 mrad ($34\ mrad \times 711.2\ mm = 24.2\ mm$) for Wall-less and 1-Wall configuration and 117 mrad ($117\ mrad \times 711.2\ mm = 83.2\ mm$) for 2-Wall configuration, respectively. From the discussion in 4.2.1.1, the requirement for the area determination can be allocated as ±40% of the area.

The tracking error is obtained from 6.4 and 6.5, and it is $0.67\ units \times 25.4\ mm / 711.2\ mm = 24\ mrad$, which means 9.2 px (24 mrad/2.6 mrad/px).

Table 7-1 Comparison of Tracking Error with the Detectability Criteria

	Detectability Criteria		Tracking Error	
	X coordinates	Area size	X coordinates	Area size
GaAs PV w/o the Fly-Eye Module	±5.0mm	±20%	16.5mm	28.3%
GaAs Substrate w/ the Fly-Eye Module				
Wall-less	24.2mm	±40%	16.5mm	28.3%
1-Wall	24.2mm	±40%		
2-Wall	83.2mm	±40%		

The fly-eye module satisfies the detectability criteria for the X-coordinate of the target center. For the area, the error in the X coordinate is 28.3% (17mm/60mm) of the PV size, and considering that there is no error in the Y coordinate, an area estimation error of 28.3% can be obtained. Since the detectability criterion for area estimation error is 40%, the fly-eye module satisfies the criterion for area estimation error. In Section 5, the position estimation for diffuse targets was more accurate than non-diffuse targets. Considering that the experiments in Section 6 were conducted for a non-diffuse target, the tracking errors in Table 7-1 w/ the Fly-Eye Module will be smaller for a diffuse target. On the other hand, w/o the fly-eye module, the detectability criteria are not satisfied, especially for the X coordinate. In such a case, fine-tuning is needed in the precise alignment (step 8 in 7.1) of the previous procedure. On the other hand, this may be a limitation of the camera hardware used in the experiment, as we estimated the angle of view per pixel to be $\Delta\theta$ = 2.6 mrad/px in Section 5. If a higher-resolution camera with

a smaller $\Delta\theta$ value is available, the detectability criteria may be satisfied by the cooperative OWPT w/o the fly-eye module.

The tracking error of the GaAs PV in the 2D plane can be considered acceptable for the detectability criteria. Since the detectability criteria were derived from the system-level requirement analysis, as far as the experiments conducted in the study, the discussions from the system-level requirements analysis and the PV tracking based on the infrared differential absorption imaging in the thesis are consistent in the proposed ConOps.

7.2. Scalability of OWPT Systems

7.2.1. Designing OWPT Systems of Various Power Transmission Ranges

As stated in 4.2.2, using the error requirement in pixel units for error requirements and SNR expression for detectability, we can formulate a detectability discussion in a scale-invariant way. Regarding position and attitude estimation and tracking, their formulations were in pixels for accuracy and exposure time for consistency (integrity measure). Since exposure time is equivalent to SNR, the position and attitude estimation and tracking formulations were the essentially scale-invariant. Therefore, the consistency between detectability criteria and position estimation is a scale-invariant nature. Since they were consistent at the scale of the experiments, this also holds for the other scales. Thus, scale transformations can be used to design different scale OWPT systems from the experiments conducted in this study.

7.2.2. Scale Transformation of OWPT System Parameters

Even though the experiments in this study were conducted at about 0.7 m, the systems assumed in this study were focused on scales ranging from tens of meters to several kilometers. According to the discussions in 4.2.2, the SNR determines the detectability and is given by the threshold equation valid at the thresholds of the detectability criteria. If the parameters of the threshold equation are scale-transformed so that the SNR, which is equivalent to the number of signal electrons, is invariant, a new OWPT system with the scaled parameters will meet the same detectability criteria as in the experiments conducted in this study. The parameters of the threshold equation for the experiment are denoted by α, the scale-transformed parameters by α', and so on. Considering that $\eta_r, \eta_t, \eta_Q, \rho$ remain unchanged before and after the scale transformation, the following equations can be obtained from (4-34)

(7-1), (7-2). Assuming the effective diameter of the receiver to be D, $A_r = \pi D^2/4$. The following equation is obtained by taking the target area as L×L and considering (4-30). The other symbols are defined in Appendix 4 A.4.1.

In case the irradiated beam size $\leq$ the target size,

$$\frac{P_t}{P'_t}\frac{\eta_t}{\eta'_t}\frac{Exp}{Exp'}\left(\frac{D}{D'}\right)^2\left(\frac{R'}{R}\right)^2 = 1 \qquad (7\text{-}1)$$

In case the irradiated beam size $>$ the target size,

$$\frac{P_t}{P'_t}\frac{\eta_t}{\eta'_t}\frac{Exp}{Exp'}\left(\frac{D}{D'}\right)^2\left(\frac{L}{L'}\right)^2\left(\frac{R'}{R}\right)^4 = 1 \quad (7\text{-}2)$$

The transformation coefficient $\Delta\theta$ from (5-33) is used in the transformation to real 2D coordinates, so it is necessary to determine the change in $\Delta\theta$ due to the scale transformation. Following the discussion in 4.2.2, we require $\Delta\theta \propto 1/R$ to make our whole theory scale-invariant. Then, pixel coordinates and their differentials(Δpx) can be considered as invariant in the scale transformation when $\Delta\theta/\Delta\theta' = R'/R$. If one zooms the target, or enlarges the target size, one can apparently improve the angular resolution of the camera. Considering the target size L and the zoom lens magnification M in the receiving optical system, for a physical (real) angular resolution $\Delta\theta'$ and $\Delta\theta'$, the requirement for apparent angular resolution of the camera (length/pixel) corrected by the target size and magnification is written as,

$$\frac{1}{L'M'}\Delta\theta'R' = \frac{1}{L\,M}\Delta\theta R \quad (7\text{-}3)$$

, and the accuracy of the center coordinate estimation is obtained by setting $\Delta px' = 9.2px$ from 7.1.2,

$$\Delta L = 9.2 \times \frac{1}{M'}\Delta\theta'R' \quad (7\text{-}4)$$

7.2.3. Maximum Detectable Range of the GaAs Substrate and the PV

7.2.3.1. The Maximum Detectable Range of the PV in Cooperative OWPT

This cases are equivalent to the ones of without the Fly-Eye Module. As long as the detectability criteria are satisfied, or equivalently, SNR is greater than the threshold SNR discussed in 4.2.2, the transmitter can determine the target's accurate position and size appropriately. The maximum detectable range is given by the SNR discussion in 4.3.4 by extending the exposure time to the maximum value 25,000μs. When the transmitter specifications in the experiments were as follows: 4mW λ_{OFF} = 940 nm output, transmitter optics efficiency ~50 %, receiver optics transmittance ~13.5 %, the GaAs PV target is detectable up to 20m for a receiver effective diameter ϕ0.94 cm and up to 150 m for ϕ50 mm. When the illuminating beam divergence is controlled so that the beam size at the target is

smaller than the target, the target range is detectable about 400 m with a receiver effective diameter of ϕ0.94 cm and about 20 km with a receiver effective diameter of ϕ50 mm.

7.2.3.2. The Maximum Detectable Range of the Substrate in Cooperative OWPT

This cases are equivalent to the ones of with the Fly-Eye Module. Also, from the discussion in 4.3.4, a GaAs substrate is detectable up to about 6m, and ϕ50 mm up to about 40 m by simply extending the exposure time to its maximum value. When controlling the beam divergence angle, the detection range is 40 m for a receiver effective diameter of ϕ0.94 cm and 2 km for a receiver effective diameter of ϕ50 mm. The trade-off in system design is whether to use the fly-eye module and emphasize beam alignment mitigation and position estimation accuracy using the diffuse reflection targets or to use the non-diffuse reflection targets and emphasize the long-range detectable range without the module.

The results of 7.2.3.1 and 7.2.3.2 are summarized in the table below.

Table 7-2 Maximum Detectable Range of GaAs PV and Substrate

	D= 0.94 mm		D= 50 mm	
	w/o Beam Div Ctrl (R^{-4} dependency)	w/ Beam Div Ctrl (R^{-2} dependency)	w/o Beam Div Ctrl (R^{-4} dependency)	w/ Beam Div Ctrl (R^{-2} dependency)
GaAs PV (w/o Fly-Eye Module)	20 m	400 m	150 m	20 km
GaAs Substrate (w/ Fly-Eye Module)	6 m	40 m	40 m	2 km

7.2.4. Examples of OWPT System Design with Scale Transformation

Examples of OWPT design with scale transformation based on (7-1) and (7-2) are presented. Examples are given in Tables 7-2 and 7-3 for the case where the irradiation beam size is adjusted to the target size (Equation (7-1)) and the case where the irradiation beam is not adjusted (Equation (7-2)), respectively. The accuracy of estimating the center coordinate (ΔL) is calculated using (7-3) and (7-4).]

Table 7-3 Examples of OWPT System Design, Scaled by Equation (7-1)

	Experiments	Scaled by Equation (7-1)			
R: Range (m)	0.711	10	100	1000	10,000
P: Irradiated Power (W)	4×10^{-3}	4×10^{-3}	4×10^{-3}	4×10^{-3}	1×10^{-1}
Exp: Exposure Time (s)	25×10^{-6}	300×10^{-6}	300×10^{-6}	250×10^{-6}	1×10^{-3}
D: Receiver Diameter (m)	0.94×10^{-3}	0.94×10^{-3}	50×10^{-3}	100×10^{-3}	100×10^{-3}
L: Target Size (m)	5×10^{-2}	5×10^{-2}	5×10^{-1}	1	5
Equation (7-1) value	1	0.989	1.079	1.049	1.049
M: Zoom	1	10	10	69	140
$\Delta\theta'$ (rad) Equation (7-3)	2.6×10^{-3}	1.89×10^{-3}	1.89×10^{-3}	2.6×10^{-3}	2.64×10^{-3}
ΔL (m) Equation (7-4)	1.74×10^{-2}	1.74×10^{-2}	1.74×10^{-1}	3.47×10^{-1}	1.74

Table 7-4 Examples of OWPT System Design, Scaled by Equation (7-2)

	Experiments	Scaled by Equation (7-2)			
R: Range (m)	0.711	10	100	1000	10,000
P: Irradiated Power (W)	4×10^{-3}	8×10^{-3}	10×10^{-3}	50×10^{-3}	5×10^{-1}
Exp: Exposure Time (s)	25×10^{-6}	30×10^{-3}	30×10^{-3}	1×10^{-3}	250×10^{-3}
D: Receiver Diameter (m)	0.94×10^{-3}	0.94×10^{-3}	50×10^{-3}	1	1
L: Target Size (m)	5×10^{-2}	5×10^{-2}	5×10^{-1}	1	5
Equation (7-2) value	1	0.94	0.996	0.996	0.996
M: Zoom	1	10	10	69	140
$\Delta\theta'$ (rad) Equation (7-3)	2.6×10^{-3}	1.89×10^{-3}	1.89×10^{-3}	2.64×10^{-3}	2.64×10^{-3}
ΔL (m) Equation (7-4)	1.74×10^{-2}	1.74×10^{-2}	1.74×10^{-1}	3.47×10^{-1}	1.74

The results show that the target detection and position estimation by differential absorption imagery is effective for OWPT of 10 km operation distances. The system size tends to increase as the distance increases. The value of $\Delta\theta$ decreases as the distance increases. $\Delta\theta$ is the angular resolution of the image sensor in the experiment and is a requirement for the camera hardware development.

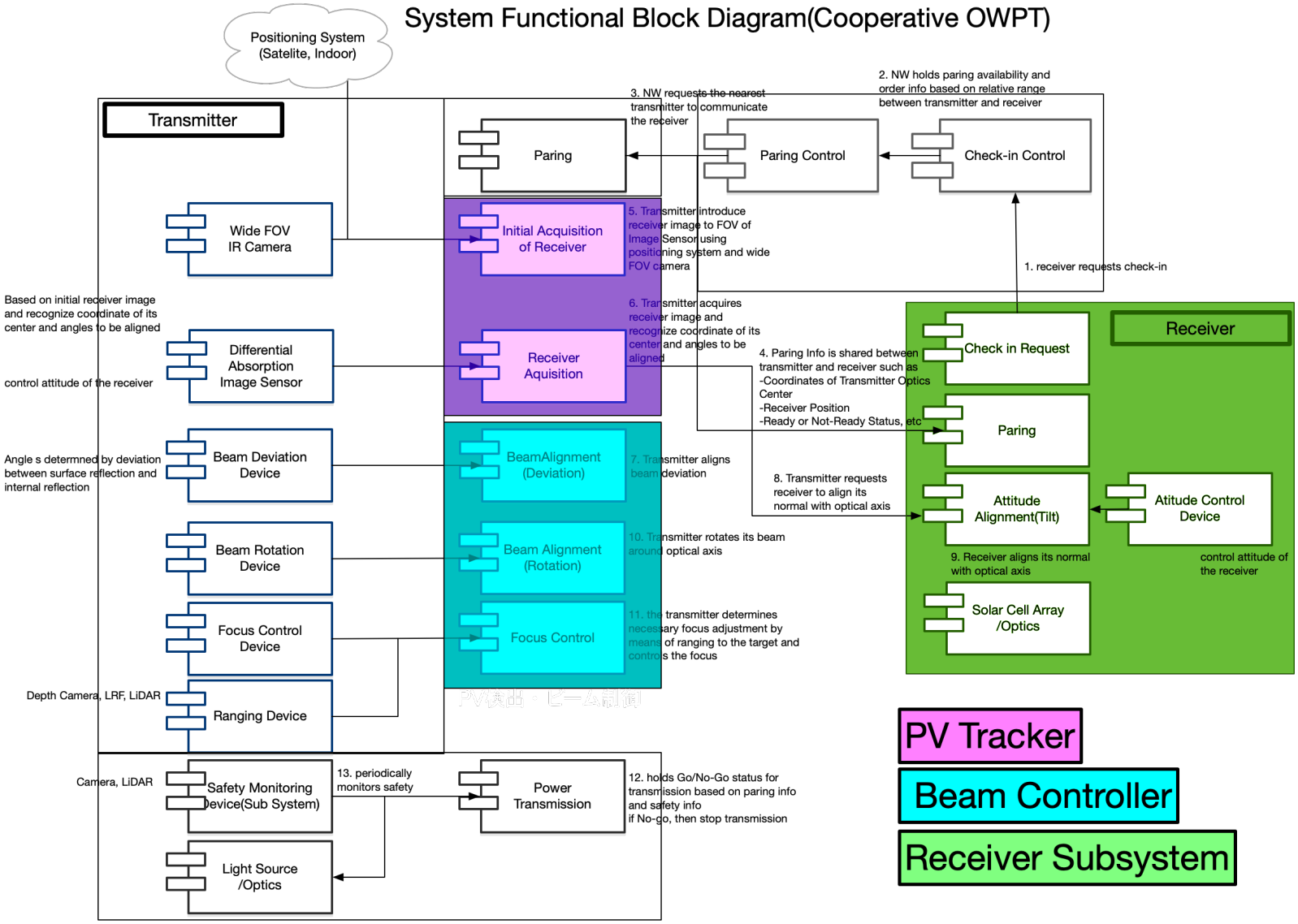


Figure 7-1 A Cooperative OWPT System Functional Block Diagram

8. Conclusion

Among the wireless power transmission technologies, Optical Wireless Power Transmission (OWPT) has the strength of its directivity due to short-wavelength electromagnetic waves. Besides that, future technological development trends such as long-distance inter-satellite optical communications in space will provide an opportunity for OWPT and such trends will strongly influence the future of OWPT. In this thesis, to maximize the value of OWPT, such strength and opportunity were focused on, and long-range and high-power cooperative OWPT was investigated. To minimize the weakness and the threat discussed in Section 1, the fields of application are supposed to be space and military. However, as the policy of investigation throughout the thesis was to be as scalable as possible, each result of the subtheme can be applied to small or mid-scale systems.

In this thesis, requirement development and a basic concept validation were conducted. This thesis presents a comprehensive and consistent discussion of OWPT systems including a business case study, a system-level requirement study, and a proposal for a PV detection and tracking method for stationary and moving targets. The system-level requirement study, and the proposal for the detection, positioning, and tracking of a PV target using differential absorption imaging constitute a unified system picture without discrepancy. Since they are discussed in a scale-invariant way in this thesis, the system-level requirement study, differential absorption imaging, and the ConOps were shown to be usable for designing OWPT operational systems of various scales.

A methodology to consolidate system-level requirements for OWPT in terms of the power generation ratio was proposed. Regarding beam shaping and alignment, system-level requirements for non-cooperative and cooperative OWPT were analyzed in general configuration using a simple geometry and the orthogonally arranged cylindrical beam expander optics. The derived requirements for the non-cooperative OWPT model were generally one or two orders stronger than for the cooperative system, and the longer the distance to the PV, the stronger these requirements were. Since these would make it seriously difficult to build robust and practical non-cooperative OWPT systems, especially when they support long-range power transmission, it would be a realistic option for the feasibility and cost of a system to adopt a cooperative system to relax the requirements. On the other hand, a cooperative OWPT needs

real-time control of the PV array to face the transmitter. Relaxation of the system-level requirement of a cooperative OWPT system is realized with a module utilizing the fly-eye lens surrounded by reflective walls (the fly-eye module). When the irradiated beam size is smaller than the PV size at the entrance of the module, the beam homogeneously irradiates the whole area of the PV. In a cooperative OWPT utilizing such a module, the transmitter optics focus and rotation adjustment around the optical axis are largely relaxed. Furthermore, the requirement for beam incident angle and beam position was relaxed by the surrounding reflective wall configuration of the module.

Once the beam alignment and shaping requirements are derived, the next issue is detecting the PV satisfying the requirements. It is important in OWPT to stably recognize PV and estimate its position and attitude under varying illuminating conditions. This study proposed differential absorption imaging. The concept validation experiment was conducted employing a Si substrate simulating diffusely reflective PV, and it was detected using single λ = 532 nm visible light. The “detectability criteria” were defined as the accuracy requirements for X, and Y center coordinates and area size derived from the system-level requirements study. The “threshold equation”, which holds at a threshold regardless of wavelength, was derived and verified by experiments. This equation was generalized to include non-diffuse reflection characteristics of the PV and was used to estimate the attitude angle of the PV. The “detectable range” was defined as the performance limit of this image sensor. Enlarging the effective diameter of camera optics or beam divergence control of the transmitter will improve the performance. The concept validation was followed by conducting with a GaAs substrate and a real thin-film GaAs PV, in which two infrared wavelengths 850nm and 940nm were used. A GaAs substrate, which had a diffuse reflection characteristic, was used in the experiments. The target was “detectable” within a wide angular range. It is worth noting that the diffuse target simulated the reflection from the fly-eye module. The copper metalized rear surface of the real GaAs PV used in the experiments mainly has a vital non-diffuse reflection characteristic accompanied by a small diffuse one. The detectability criteria for the PV were satisfied within ±10 degrees around its normal.

Regarding the detectable range limit, there are two issues to be addressed. One is the camera resolution, the other is to lower the binarization threshold. The latter was solved by introducing the over-subtraction technique with a longer exposure time. This could reduce the threshold to

the minimum, and noise reduction in the differential image occurred even for a full-size one by the over-subtraction technique. It should be noted that, by the over-subtraction with long exposure time, the detectable range is limited only by the resolution of the acquired images, which can be improved by increasing the resolution of the camera or by utilizing a zoom lens.

Based on these PV detection studies, position estimation using differential absorption imaging was investigated using two methods. One was the stereo imagery, the other was based on range estimation by the apparent size of the target combined with direction estimation. For the stereo imagery, the results depended on the angular characteristics of reflection by the target. Position determination is not strongly affected by its attitude angle in the GaAs substrate experiments, whereas, in the GaAs PV case, the results were quite different. Position estimation accuracy was strongly affected by the target's attitude, however, its direction was not. This feature was utilized to improve the tracking algorithms later.

A condition, the "integrity measure", was defined to avoid inconsistencies between the center coordinates estimations by the left/right optical sensors. It was suggested experimentally that the integrity measure is closely related to the detectability. The integrity measure rapidly converges when the exposure time of the image sensor exceeds a certain threshold, and this minimum exposure time depends on the target's attitude angle. When the target is non-diffuse, the characteristic becomes sharp. Using this characteristic of the minimum exposure time, the target's attitude angles for the non-diffuse target were estimated within a range of approximately 60 degrees including its normal. A physical model for determining the minimum exposure time under general conditions was derived based on the threshold equation. Another method of estimating the target's attitude is measuring the change in the apparent size of the target with its attitude angle. When using this method to estimate the attitude of a diffuse GaAs substrate, the attitude estimation has a dead zone around the normal. The error characteristics of the one suitable for a non-diffuse target are complementary to the one for a diffuse target.

To investigate tracking moving non-diffuse GaAs PV targets, three algorithms were evaluated. They were, the Estimator/Corrector, a supervised model using AR models and thresholds, the Kalman filter to estimate the position with a uniform motion model, and the method of the AR model with the Kalman filter. To compare the performances of the three algorithms, a score function was defined based on the mean position estimation error over tracking. The

Estimator/Corrector was generally superior, a supervised model using AR models and thresholds. There was little difference between the Kalman filter to estimate the position with a uniform motion model and the AR model with the Kalman filter. The feature that the target's direction can be accurately estimated was used to improve position estimation accuracy. As a result, within the experiment set of 660 × 200 mm size, real-time tracking of the PV confirmed that the target positions were estimated within 16.5 mm error and that its attitude error was within 10 deg error around the normal. The choice of tracking algorithm depends on the system design. If a system allows for the training of a supervised algorithm, then choosing the Estimator/Corrector would yield generally superior results, particularly near the normal position. If training is not an option, choosing one of the algorithms using the Kalman filter should suffice.

This accuracy depends on the camera's resolution used in the experiments, and using a higher-resolution camera, etc. will improve it. The other challenges were identified. One is hardware-based synchronization between the cameras, and the other is minimizing the time to start/stop frame. Such improvement with a high-speed PC will generate attitude estimation data up to 4 Hz.

A concept of operation (ConOps) for a cooperative OWPT system was proposed, and it was shown that it was harmonized with the requirements developed in Section 3. The simulation predicts that the vital directional reflection from the non-diffuse PV supports a much longer detectable range than the diffuse substrate. It revealed that the choice of with and without the fly-eye module depends on considering which is more important for the system to be developed. One is the relaxation of beam focusing and alignment accuracies, the other is the long detectable range. Using the scalability of the discussion of the thesis, some examples of OWPT system design were presented by means of scale transformation from the experimental results.

A few issues were identified in this study project. The Fly-Eye module size will be an issue for a small size application. The miniaturization of the fly-eye module including the reflective walls would be feasible by integrating miniaturized solar cell arrays. Even though such miniature module can generate small amount of electrical current, necessary number of parallel connected such modules would both generate enough current and achieve compactification of the whole OWPT system. Also the camera issue was identified. The time required to Set Camera Profile &

Start Stream and Stop Streams takes 5～6 s for the D435 used in the experiments. This would be addressed by redesigning the camera system. If the time for the start frame can be reduced from 2 s to 50 ms and the time for the stop frame from 6 s to 50 ms, respectively, this makes the attitude estimation at 4 Hz. Finally, the PV accuracy issue was identified. This would be improved by introducing a high-resolution camera or zoom lens. In the ConOps, there is the fine-tuning option in the beam-shaping phase which is equivalent to closed-loop feedback control of the receiver and the transmitter.

Image recognition of tilted PVs would be improved by integrating the position and attitude estimation proposed in this thesis with machine learning technology. As this would improve the inputs to the position/attitude determination, positioning accuracy would be improved.

Since discussions in this thesis are conducted in a scalable way, OWPT system parameters at a different scale can be derived from a scale transformation. Some examples of up to 10 km range were presented. It should be noted that this theoretical conclusion should be verified in experiments.

The model in the thesis depends on parameters such as the beam divergence angle and the PV size. The values used in the analysis depend on the conditions and apparatus in the experiment study. Moreover, there would be an OWPT system that utilizes other PV materials. However, the methodologies in this thesis are general and they easily derive new models, and values accommodating a new experiment and its apparatus.

As described in Section 1, system engineering in OWPT is not mature. Even though the detection and estimation of PV targets' position and attitude angles are crucial for implementing OWPT systems, there have not been many studies about the robust detection and positioning of targets in the OWPT system. Even though this work is a basic-level proposal for such system engineering in OWPT, the author hopes that there will be works to address the issues identified above and this work will exhibit an advancement towards the practical implementation of OWPT systems.

Acknowledgments

First, the author is very grateful to his supervisor, Associate Professor Dr. Miyamoto, who provided him with research instruction during the doctoral course in the past 3 years. The author also wishes to thank Kenta Moriyama for design, conducting experiments, and data analysis for the orthogonal cylindrical beam expander optics and its demonstration. The author also thanks members of the T. Miyamoto Lab for discussion and assistance, and Yota Suzuki of the Open Facility Center of Institute of Science Tokyo for design support and manufacturing of the equipment for the experiments.

List of Publications

1. Published Journal Papers

    1. Asaba, K.; Miyamoto, T. System Level Requirement Analysis of Beam Alignment and Shaping for Optical Wireless Power Transmission System by Semi–Empirical Simulation. Photonics 2022, 9, 452. https://doi.org/10.3390/ photonics9070452

    2. Asaba, K.; Moriyama, K.; Miyamoto, T. Preliminary Characterization of Robust Detection Method of Solar Cell Array for Optical Wireless Power Transmission with Differential Absorption Image Sensing. Photonics 2022, 9, 861. https:// doi.org/10.3390/photonics9110861

    3. Asaba, K.; Miyamoto, T. Relaxation of Beam Irradiation Accuracy of Cooperative Optical Wireless Power Transmission in Terms of Fly Eye Module with Beam Confinement Mechanism. Photonics 2022, 9, 995. https://doi.org/10.3390/ photonics9120995

    4. Asaba, K.; Miyamoto, T. Solar Cell Detection and Position, Attitude Determination by Differential Absorption Imaging in Optical Wireless Power Transmission. Photonics 2023, 10, 553. https:// doi.org/10.3390/photonics10050553

    5. Asaba, K.; Miyamoto, T. Positioning of a Photovoltaic Device on a Real Two-Dimensional Plane in Optical Wireless Power Transmission by Means of Infrared Differential Absorption Imaging. Photonics 2023, 10, 1111. https://doi.org/10.3390/ photonics10101111

    6. Asaba, K.; Miyamoto, T. Attitude Determination of Photovoltaic Device by Means of Differential Absorption Imaging. Photonics 2024, 11, 32. https:// doi.org/10.3390/photonics11010032

    7. Asaba, K.; Miyamoto, T. Real-Time Tracking of Photovoltaics by Differential Absorption Imaging in Optical Wireless Power Transmission. Photonics 2024, 11, 490. https:// doi.org/10.3390/photonics11060490

2. International Conferences

1. Asaba, K.; Miyamoto, T. Beam Deformation Correction using Orthogonal Cylindrical Beam Expander. In Proceedings of the 4th Optical Wireless and Fiber Power Transmission Conference (OWPT2022), Hybrid, Yokohama, Japan, 18–21 April 2022; p. OWPTp-03.

2. Asaba, K.; Miyamoto, T. Solar Cell Detection by Differential Absorption Image Sensor for OWPT. In Proceedings of the 5th Optical Wireless and Fiber Power Transmission Conference (OWPT2023), Hybrid, Yokohama, Japan, 18–21 April 2023; p. OWPT6-04.

3. Asaba, K.; Miyamoto, T. Asaba, K.; Miyamoto, T. Solar Cell Position, Attitude Determination by Differential Absorption Imaging in Optical Wireless Power Transmission. In Proceedings of the Physics, Simulation, and Photonic Engineering of Photovoltaic Devices XIII, SPIE OPTO, San Francisco, CA, USA, 29–30 January 2024; p. 12881, 128810B.

4. Asaba, K.; Miyamoto, T. Asaba, K.; Miyamoto, T. Solar Cell Detection by Differential Absorption Image Sensor for OWPT. In Proceedings of the 6th Optical Wireless and Fiber Power Transmission Conference (OWPT2024), Hybrid, Yokohama, Japan, 23-26 April 2024; p. OWPTp-01.

3. Domestic Conferences

1. 浅葉薫、宮本智之 発電効率を元にした光無線給電のシステム要求解析 電子情報通信学会 2022 ソサィエティ大会, 6–9 September 2022, C-3/4-3.

2. 浅葉薫、宮本智之 光無線給電における赤外差分吸収画像を用いた太陽電池検出 電子情報通信学会 2023 総合大会, 7–10 March 2023, C-3/4-45.

3. 浅葉薫、宮本智之 光無線給電における差分吸収画像を用いた太陽電池位置・姿勢決定 第 41 回レーザセンシングシンポジウム , 6–8 September 2023, B6.

4. 浅葉薫、宮本智之光無線給電における差分吸収画像を用いた太陽電池位置・姿勢決定 電子情報通信学会 2023 ソサィエティ大会, 12–15 September 2023, C-3/4-30.

5. 浅葉薫、宮本智之 光無線給電における赤外差分吸収画像を用いた太陽電池の連続的な位置推定・姿勢推定 電子情報通信学会 2024 総合大会, 4–8 March 2023, C-3/4-31.

6. 浅葉薫、宮本智之 光無線給電における赤外差分吸収画像を用いた長距離太陽電池検出 電子情報通信学会 2023 ソサィエティ大会, 10–13 September 2024, C-3/4-38

4. Meetings

1. 浅葉薫 光無線給電のビーム制御におけるシステム要求解析 第 44 回光通信研究会, 22–24 August 2022, P-1-7.

2. 浅葉薫 Solar Cell Position, Attitude Determination by Differential Absorption Imaging in OWPT 第 45 回光通信研究会, 22–24 August 2023, P-2-31.

3. 浅葉薫 光無線給電における赤外差分吸収画像を用いた長距離太陽電池検出, 第一回末松カンファレンス, 29-31 August 2024, P-1-10